Coupled deformation-diffusion-fracture theories for solids: application to polymeric gels and hydrogen embrittlement in steels

by

Yunwei Mao

B.S., Xi'an Jiaotong University, China (2011)
M.S., Xi'an Jiaotong University, China (2014)

Submitted to the Department of Mechanical Engineering
in partial fulfillment of the requirements for the degree of

Doctor of Philosophy

at the

Massachusetts Institute of Technology

June 2018

Signature redacted

Author .....
Department of Mechanical Engineering
May 9, 2018

Signature redacted

Certified by .....
Lallit Anand
Rohsenow Professor of Mechanical Engineering
Thesis Supervisor

Signature redacted

Accepted by .....
Rohan Abeyaratne
Chairman, Department Committee on Graduate Students

Coupled deformation-diffusion-fracture theories for solids: application to polymeric gels and hydrogen embrittlement in steels

by
Yunwei Mao

Submitted to the Department of Mechanical Engineering
on May 9, 2018, in partial fulfillment of the
requirements for the degree of
Doctor of Philosophy

Abstract

Solids with deformation-diffusion coupling are ubiquitous in engineering applications. Understanding and modeling the fracture of such solids is vitally important. This thesis addresses the theoretical formulation, numerical implementation, and application of fully-coupled deformation-diffusion-damage theories for two different classes of materials: (i) polymeric gels and (ii) hydrogen embrittlement in steels, as elaborated below.

(i) *Fracture of polymeric gels*: We first introduce a field called "stretch of Kuhn segments and/or crosslinks", which is necessary for understanding and modeling of the fracture in polymeric materials. Together with this newly introduced field, we formulate a thermodynamically consistent phase-field type theory for fracture of gels. A central feature of our theory is the recognition that the free energy of polymeric materials is not entirely entropic in nature, there is also an energetic contribution from the deformation of the backbone bonds in a chain and/or the crosslinks. It is this energetic part of the free energy that drives the progressive damage and fracture of polymeric materials. We have implemented our theory in a finite element code, and used this simulation capability to study some interesting phenomena in failure of elastomers and gels.

(ii) *Fracture of steels due to hydrogen embrittlement*: We have formulated a thermodynamically consistent theory for the diffusion of hydrogen coupled with the large elastic-plastic deformations, and a phase-field type theory to model ductile fracture of metals. The theory accounts for the macroscopic effects due to the generation and agglomeration of microscopic hydrogen-vacancy complexes. We have implemented our fully coupled theory in a finite element program, and calibrated the material parameters in the theory by using experimental data available in the literature. Finally we have utilized our simulation capability to study the process of fracture due to hydrogen embrittlement in some technically relevant notched-components made from steel.

Thesis Supervisor: Lallit Anand
Title: Rohsenow Professor of Mechanical Engineering

Acknowledgments

My graduate career has been completed with the support of many people.

I would like to first express my gratitude to Professor Lallit Anand for his direction and financial support during the past years. We have a fruitful four-year period. On one hand, we collaborate together to generate several profound ideas and decent research publications. On the other hand, during these four years, the myriad discussions that I had with Professor Anand sharpened my research philosophy. Professor Anand imparted me with great tools for conducting research in solid mechanics, and taught me patiently on how to disentangle the various aspects of research. He has taught me to always conduct research at the highest standard, and to value quality and integrity above all. His teachings will continue to inspire me throughout my career, and his dedication to the field of mechanics & materials and the integrity of his research will be a standard for me.

I would also like to thank my thesis committee members, Professor David Parks, Professor Ju Li, and Professor Xuanhe Zhao, for their invaluable suggestions and guidance throughout my research. A great thanks to Christina Spinelli and Pierce Hayward, who throughout my years have provided all of the necessary support to ensure that I could focus on producing the best research. I would also like to thanks Leslie Reagan for her support. Meanwhile, I would also like to thank Professor Jing Kong in EECS at MIT for her David-and-Jonathan type friendship and encouragement during the past years.

During my time at MIT I have had the pleasure of working with incredibly talented individuals. I would like to thank my friends and colleagues Shaoting Lin, Teng Zhang, Hyunwoo Yuk, Juner Zhu, Shenghua Wu, Zhantao Chen, and Pedro Reis, for their inspiring discussions and support. Finally, I would like to thank Brandon Talamini, who has been my closest collaborator ever. Our heated discussion are invaluable.

I would like to thank my parents who have shown me unwavering support throughout all my years. This thesis is dedicated to my wife Junyan, who inspires me to be a better person. Thank you for standing besides me for everything during the past years. Finally, to my daughter Yanyi. Thank you for teaching me so many things that I did not know.

Contents

List of Figures

List of Tables

Chapter 1

Introduction

1.1 Background

The materials used in revolutionary engineering innovations have a common salient feature: operated in the situations that coupled with multiple physical fields. Examples include polymeric gels used in biological applications, and metallic materials for energy storage. The drug-releasing polymeric materials usually interact with pH and concentration fields. They undergo gradual polymer chain degradation on the microscopic-mesoscopic scale and final matrices rupture on the macroscopic scale. The steel pipes used for oil transportation communicate with chemical and pressure fields. In this situation, microscopic-mesoscopic defects development and final macroscopic failures, are all inevitable. For these two cases, the multi-physics nature of the materials not only complicates the understanding of the fundamental failure mechanisms, but also makes it challenging to build useful theoretical and numerical tools for failure analysis of materials.

Generally, fracture mechanics, or the failure analysis of materials, attempts to answer the following questions for a specific material:

1. When does a pre-existing crack start to grow?

2. What is the direction of crack propagation?

The field of fracture mechanics has its foundations in a classical paper by Griffith (1921). Classical theories based on asymptotic solutions with one-parameter fracture criteria, like the critical energy release rate G_c (or equilvently K_c) (Griffith, 1921; Lawn, 1993), the generalized critical energy release rate J_c (Rice, 1968), the strain energy density and related energy density factor (Sih, 2012), the crack tip open distance (Tracey, 1976) and the critical distance (Taylor, 2010), try to answer the first question. The classical $K_{\mathrm{II}} = 0$ criteria in mixed mode loadings and atomistic simulations (Buehler et al., 2003; Karma et al., 2001) try to answer the second problem for brittle solids. During the past century, these theories have been

applied to understand the fracture of brittle solids (Griffith, 1921; Lawn, 1993), viscoelastic media (Schapery, 1984; Slepyan, 2012), elasto-plastic solids (Rice, 1968; Hutchinson, 1968; Rice and Rosengren, 1968; McMeeking, 1977; McMeeking and Parks, 1979), and the interface between solids (Hutchinson and Suo, 1991). These myriad applications based on the classical fracture mechanics highlights its great success.

However, this existing fracture mechanics and analysis is barely useful for materials coupling with multiple physical fields. The major reasons are

- These coupling fields will make the fracture properties of materials inhomogeneous. For example, an inhomogeneous deformation field induces an inhomogeneous chemical potential field, which leads to an inhomogeneous concentration of the fluid because of diffusion within the body; such an inhomogeneous fluid concentration leads to an inhomogeneous propensity to fracture within the body.

- A lot of coupling fields are time-dependent, such as diffusion of solvents. These time-dependent fields usually influence the deformation field in a nonlinear way. Thus typically the impact of these fields on the fracture of a sample needs to be examined by a fully coupling theory.

- The coupled multi-physical fields help the evolution of microscopic defects and the accumulation of damage in materials. These developed microscopic defects and accumulated damage have important impacts on the macroscopic fracture behaviors of materials. Thus a fully coupling theory accounting for specific and microscopic features is generally needed for the failure analysis of such materials.

Instead of traditional fracture mechanics and analysis, the recently proposed variational and phase-field approaches to modeling fracture (Francfort and Marigo, 1998; Bourdin et al., 2008; Karma et al., 2001) are very promising, and may provide a unified framework to understand and model fracture of a variety of materials coupled with multi-physical fields. For examples, the above-mentioned two essential questions in fracture mechanics can be answered naturally in these phase-field approaches, by introducing a single scale damage field d and its gradient ∇d. This advantage dramatically simplifies fracture analysis of material samples in complex geometry and environment. Because of this, the phase-field approaches to model fracture become extremely popular in mechanics society during the past 15 years.

However, since the fracture process in materials that couple with multiple fields depends highly on microstructure of materials, a more systematic way to embed the phase field type idea in modeling the fracture of materials coupled multiple fields is needed (Sih and Provan, 2013; Kienzler and Herrmann, 2012; Wang and Li, 2010). In this thesis, we focus on studying the coupled deformation-diffusion-damage behaviors of materials. We study two different classes of materials: (i) polymeric gels and (ii) hydrogen embrittlement in steels. The details of these two classes of materials are discussed in the following subsections.

1.1.1 Polymeric gels

The development of elastomeric materials for engineering applications has ushered a recent revolution in materials. Applications often depend on the great extensibility of elastomeric materials, as well as many other useful properties that gels can possess, including bio-compatibility, self-healing, and novel actuation mechanisms and functions. Elastomeric materials are traditionally found in several diverse applications, such as structural bearings, tires, seals, adhesives, and vibration isolators. In addition to the traditional engineering uses of elastomeric materials, transformative applications are being developed daily, such as soft robotics, scaffolds for drug delivery, adhesives for wound dressing, and stretchable electronics. Many of these applications require the underlying elastomeric materials to be stretchable and yet fracture resistant. This places new importance on understanding the physics of deformation and fracture in these elastomeric materials.

One of the distinguishing features of elastomeric materials, which consist of a network of flexible polymeric chains, is that **the deformation response is dominated by changes in entropy**. Since the deformation process of elastomeric materials is essentially dominated by changes in entropy, they can be easily deformed to a very large strain, either by external fields, such as applied forces and voltages (Treloar, 1975; Mark and Erman, 2007), or swelling in suitable solvents (Yamakawa, 1971). For example, a loosely crosslinked hydrogel can easily deformed to 5 times of its initial length (see Fig. 1-1 (a)), and PDMS can swell to 2.7 times of its initial size in pentane (see Fig. 1-1(b)). Accordingly, most classical theories of rubber-like elasticity (see Treloar (1975); Arruda and Boyce (1993) and the references therein), deformation-diffusion coupling theory of gels (Hong et al., 2008; Duda et al., 2010; Chester and Anand, 2010, 2011) consider only the configurational entropy and neglect any changes in internal energy within polymer chains.

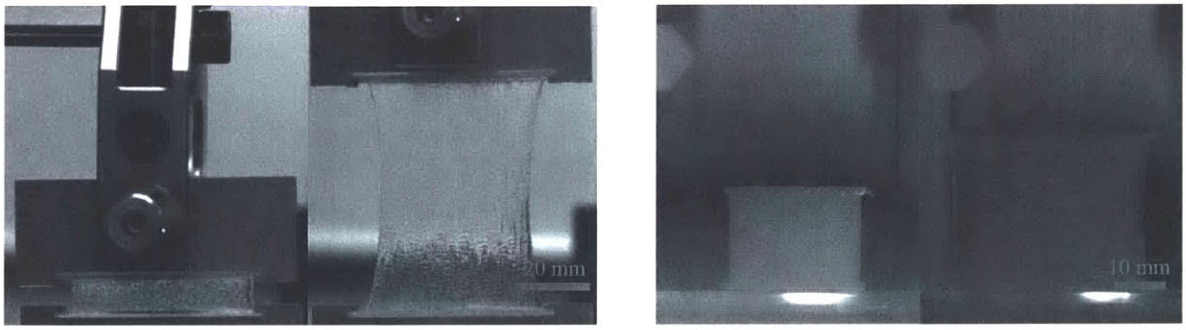

Figure 1-1: (a) Loosely crosslinked polyacrylamide hydrogel can easily be deformed to 5 times of its initial length. (b) PDMS swells to 2.7 times its initial size after being immersed in pentane for 8 hours; from Watson (2015).

Large stretches caused by external fields eventually culminate in fracture. Research on the fracture of polymeric soft materials started more than 70 years ago by Rivlin and Thomas (Rivlin and Thomas, 1997). The high value of the fracture toughness of an elastomer is

explained in the classic model by Lake and Thomas (1967). With reference to Fig. 1-2, the essential point that Lake and Thomas provided in their model is that, if one bond in a polymer chain breaks, the energy stored in the whole chain is dissipated. With ρ_s the number of chains crossing unit area in the reference configuration of the body, n the number of monomer units in a chain, and U_c the energy required to break a covalent bond in the chain, Lake and Thomas estimate the critical energy release rate to have a value of $G_c \sim \rho_s n U_c$. Thus, according to Lake-Thomas model, **the fracture process in an elastomer is dominated by energy released due to chain-scission**.

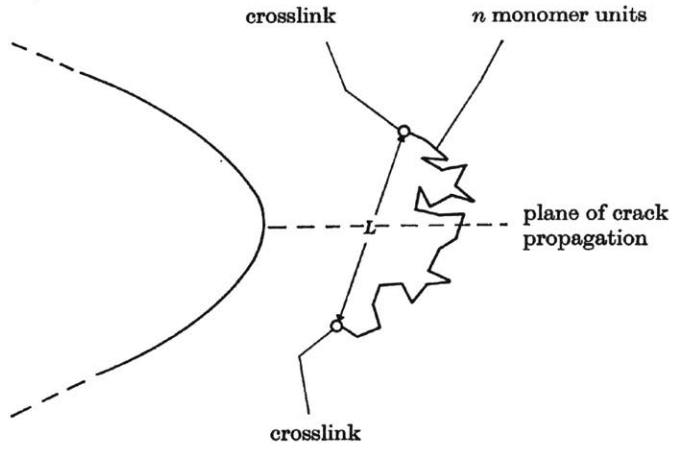

Figure 1-2: Schematic of a polymer chain lying across the plane of crack propagation. Adopted from Lake and Thomas (1967).

There are several problems that we need to address to obtain better understandings on fracture of elastomeric gels. First of all, the inconsistency of deformation and fracture responses of elastomeric gels not only impedes our understandings on these systems, but also prevent us to develop efficient and predictive models for mechanical responses of elastomeric materials. So fundamentally and conceptually we need to resolve this inconsistency first.

Furthermore, we need to consider the migration of solvent as the sample deforms. Since the interaction between the solvent diffusion within the gels, and other rates imposed on the soft materials by surrounding environment, such as stretch rate and evaporation rate, can cause a lot of interesting phenomena, such as delayed fracture, in these materials. These behaviors cannot be fully understood or modeled by classical fracture mechanics. As we said before, phase-field type theory is very promising for modeling the fracture in materials coupled with multiple physical fields. However, to build a predictive phase-field type theory, we need to include the microscopic features of the system. In elastomeric gels, the most important microscopic feature is the polymer chain, the polymer network, and the diffusive species. How to properly include such microscopic features in continuum-level model is a difficult task.

1.1.2 Hydrogen embrittlement in steels

Atomic hydrogen readily dissolves in and permeates through most materials. The deleterious effects of hydrogen on the mechanical response of iron and steel are well-known (Hirth, 1980). Several mechanisms for hydrogen embrittlement have been proposed (Dadfarnia et al., 2009, 2010):

1. **Hydrogen-enhanced decohesion (HEDE)**: This mechanism posits that the accumulation of hydrogen reduces the cohesive strength of a solid along crystallographic planes, grain boundaries, or particle/matrix interfaces, giving rise to a reduced fracture toughness (Troiano, 1960; Oriani, 1972).

2. **Hydrogen-enhanced localized plasticity (HELP)** (references (Beachem, 1972; Birnbaum and Sofronis, 1994)): This mechanism posits that hydrogen redistribution occurs around dislocations, reduces the elastic interaction energy between dislocations and thereby decreases the lattice Peierls stress — material softening then ensues. See Song and Curtin (2014) for a recent perceptive discussion of this mechanism. However, note that this mechanism by itself does not say how final fracture occurs.

3. **Hydrogen-enhanced strain-induced vacancy stabilization (HESIV)**: Nagumo et al. (Nagumo et al., 2003; Nagumo, 2004) have suggested that vacancies play a crucial role in hydrogen embrittlement. The presence of vacancies was demonstrated by positron annihilation and thermal desorption spectroscopic techniques. By plastically deforming and subsequently heating, with and without hydrogen, these authors determined that vacancy-based hydrogen traps were created during plastic deformation, and that their creation was significantly accelerated by the presence of hydrogen. However, these defects could be apparently removed by annealing. They interpreted these trap sites as vacancies created by dislocation interactions, which were stabilized by the presence of hydrogen. They proposed that hydrogen accelerated the formation of these vacancies by lowering the formation energy and by accelerating dislocation interaction processes. They suggested that clustering of atomic vacancies could act as a potential source of fracture initiation by destabilizing the process zone ahead of a crack tip by "amorphization."

In spite of the long history of study into the embrittlement of metals by hydrogen, there is little consensus as to the mechanism by which hydrogen degrades their mechanical response. The microscopic mechanisms by which hydrogen embrittles steels are still not very well understood or modeled.

Recently, Neeraj et al. (2012) and Srinivasan and Neeraj (2014) have reported on their experiments at ExxonMobil which have identified evidence for nano-void coalescence as a failure pathway for steels in the presence of hydrogen; cf. Fig. 1-3 for a schematic from their paper. In addition, atomistic simulations conducted by researchers have helped provide support for the following observations/hypotheses:

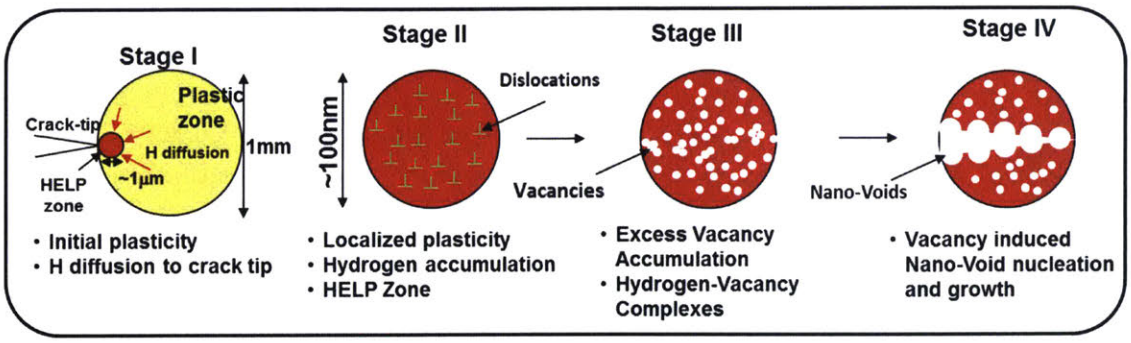

Figure 1-3: Schematic of stages associated with the nano-void coalescence mechanism.

- That hydrogen stabilizes vacancies in Fe by both lowering the vacancy formation energies and by reducing the mobility of vacancies.

- Plastic deformation leads to transient injection of (beyond-thermal-equilibrium) vacancies, which are usually swept away quickly by moving dislocations, but in the presence of hydrogen are stabilized as hydrogen-vacancy complexes that cannot be swept away by moving dislocations.

- Hydrogen vacancy complexes can grow to nucleate nanovoids which might eventually lead to fracture.

However, there are gaps in understanding how these atomic-level defects lead to failure at the macroscopic scale. A coupled deformation-diffusion continuum-level model has been proposed (Di Leo and Anand, 2013; Anand, 2011), however, extension of this model to capture the fracture/failure of materials incorporating the underlying atomic-level principles and understandings has not yet been done. As discussed in previous sections, phase field methods are promising for modeling fracture phenomena. However, the hydrogen-embrittlement of steels also highly depends on micro-defects, so a more systematic way to embed the phase field type idea in modeling fracture of hydrogen embrittled steels is needed.

1.2 Contributions of thesis and related publications

This thesis is comprised of two major parts:

(i) Modeling of fracture of polymeric gels;

(ii) Modeling of hydrogen embrittlement in steels.

Each part is discussed in more details in the following sections, and publications in peer-reviewed journals related to each part are listed.

1.2.1 Modeling of fracture in polymeric gels

A polymeric gel is a cross-linked polymer network swollen with a solvent. If the concentration of the solvent or the deformation is increased to substantial levels, especially in the presence of flaws, then the gel may rupture. Although various theoretical aspects of coupling of fluid permeation with large deformation of polymeric gels are reasonably well-understood and modeled in the literature, the understanding and modeling of the effects of fluid diffusion on the damage and fracture of polymeric gels is still in its infancy.

The first contribution of this part is introducing a new field related with stretch of Kuhn segments, to bridge the deformation of polymers and the fracture of polymers consistently. We provide a rational yet simple model for deformation and fracture of cross-linked polymers, based on two ingredients: (i) a non-Gaussian statistical mechanics model of polymer chains that accounts for the increase in energy due to the deformation of molecular bonds; (ii) a chain scission criterion based on the bond deformation energy attaining a critical value. Using this model, we can estimate the rupture stretch of elastomeric materials from fundamental quantities describing the polymer network. We use this model to relate the flaw sensitivity of elastomers to an intrinsic material length scale related to the network structure.

- Mao, Y., Talamini, B. , Anand L., 2017. Rupture of polymers by chain scission. *Extreme Mechanics Letters.* 13, 17-24.

The second contribution of this part is building a thermodynamically-consistent theory for fracture of polymeric gels. — a theory which accounts for the coupled effects of fluid diffusion, large deformations, damage, and also the gradient effects of damage. The particular constitutive equations for fracture of a gel proposed in our paper, contain two essential new ingredients: (i) Our constitutive equation for the change in free energy of a polymer network accounts for not only changes in the entropy, but also changes in the internal energy due the stretching of the Kuhn segments of the polymer chains in the network. (ii) The damage and failure of the polymer network is taken to occur by chain-scission, a process which is driven by the changes in the internal energy of the stretched polymer chains in the network, and not directly by changes in the configurational entropy of the polymer chains. The theory developed in this paper is numerically implemented in an open-source finite element code MOOSE, by writing our own application. Using this simulation capability we

- study the fracture of elastomers by crosslink failure and chain scission, and
- report on our study of the fracture of a polymeric gel, and some interesting phenomena which show the importance of the diffusion of the fluid on fracture response of the gel are highlighted.

- Talamini, B., Mao, Y. , Anand L., 2018. Progressive damage and rupture in polymers. *Journal of the Mechanics and Physics of Solids.* 111, 434-457.

- Mao, Y. and Anand L., 2018. Fracture of elastomeric materials by crosslink failure. *Journal of Applied Mechanics.* in press.

- Mao, Y. and Anand L., 2018. A theory for fracture of polymeric gels. *Journal of the Mechanics and Physics of Solids.* 115, 30-53.

1.2.2 Modeling of fracture in steels due to hydrogen embrittlement

Based on these recent experimental obervations, and guided by the hydrogen embrittlement mechanism proposed by Li et al. (2015), we have formulated a continuum theory for the diffusion of hydrogen coupled with the elastic-viscoplastic response of metals, together with an accounting for microscopic effects due to trapping of hydrogen in hydrogen-vacancy complexes, culminating in eventual fracture. We postulate that when the hydrogen which is trapped in hydrogen-vacancy complexes reach a critical concentration, then there is a change in mechanism of inelastic deformation from standard plastic flow by dislocation glide to plastic flow by a *quasi-cleavage* type mechanism — a change in mechanism which is reminiscent of a transition between "shear-yielding" and "crazing" in amorphous polymers. We have formulated a criterion for this change in mechanism together with an attendant dilatant craze-plasticity flow rule, and a corresponding damage theory to model hydrogen embrittlement of ferritic line-pipe steels.

We have numerically implemented our coupled diffusion-deformation-failure theory in a finite element program Abaqus by writing a user element subroutines (UEL), and we present representative numerical examples which show the ability of the simulation to qualitatively replicate the failure due to hydrogen embrittlement in some technically relevant geometries.

- Anand L., Mao, Y., and Talamini, B., 2018. On modeling fracture of ferritic steels due to hydrogen embrittlement. *Journal of the Mechanics and Physics of Solids.* Submitted.

Part I

Fracture of polymeric gels

Chapter 2

Introduction

There are numerous polymeric materials which have a crosslinked network and which can absorb large quantities of suitable fluids without the essential skeletal network structure of the polymer being disrupted by the absorbed fluid. Such a polymeric network, together with the fluid molecules, forms a swollen aggregate called a polymeric gel. When the fluid is water, the gel is known as a hydrogel. Gels may be designed to swell by several hundred percent, and — depending on the precise constitution of a gel — the amount of swelling may be controlled by varying external stimuli. Stimuli-responsive polymeric gels have the ability to swell and deswell in response to changes in the environmental conditions such as mechanical forces, temperature, solvent-type, pH, electric field, and also light. Because of their unique characteristics, polymer gels are found in several diverse applications, such as carriers for drug delivery, scaffolds for tissue engineering, soft actuators, smart optical systems, as well as packers for sealing in oil-wells. Living organisms are largely made of polymer gels; this facilitates the transport of ions and molecules within the organism while keeping its solidity (shape). Hydrogels are commonly considered as proxies for soft biological tissues and are thus the subject of intense theoretical and experimental investigations.

There have been several (essentially-similar) recent publications regarding modeling of the coupled diffusion-deformation response of polymeric gels (Hong et al., 2008; Doi, 2009; Duda et al., 2010; Chester and Anand, 2010). Several papers related to the numerical implementation of these theories for solving coupled diffusion-deformation boundary value problems for gels have also been recently published (Chester and Anand, 2011; Lucantonio et al., 2013; Chester et al., 2015; Broger et al., 2017a).

In order to develop a robust simulation capability for the use of polymer gels in applications, one also needs to be able to model the damage and fracture of these materials. A difficulty in modeling the fracture of gels comes from the influence of the amount of fluid on the propensity to fracture of a gel. Generally, an inhomogeneous deformation field induces an inhomogeneous chemical potential field, which leads to an inhomgeneous concentration of the fluid because of diffusion within the body; such an inhomogeneous fluid concentration

leads to an inhomogeneous propensity to fracture within the body. According to the classical arguments of Lake and Thomas (1967), regions of higher fluid concentration (and therefore lower polymer volume fraction) have an increased propensity to damage and failure because of the lower number of highly stretched polymer chains. Further, because of the diffusion, the damage process zone in the vicinity of a crack — when compared to the overall geometry of a body — is not always small, and classical notions of "small-scale process zone" often do not hold. The heterogenous propensity to fracture and large damage process zones makes classical fracture mechanics criteria — like the energy release rate reaching a critical value — inapplicable. Also, since diffusion of the fluid relative to the polymer network is a dissipative process, classical fracture mechanics models which are based entirely on Lake-Thomas-type energetic arguments, and which do not account for the dissipation due to diffusion, will underestimate the fracture resistance of polymeric gels.

Thus a theory and a numerical simulation capability which couples diffusion of the fluid with the large deformation, damage and fracture of polymeric gels is needed. Most of the existing studies on the fracture of gels have limited their attention to conditions under which the characteristic time-scale for deformation is much smaller than the time-scale for diffusion, so that the diffusion of the fluid may be neglected (Brown, 2007; Tanaka, 2007; Zhang et al., 2015). However, there are many important operating conditions under which the fluid diffusion cannot be ignored. One such set of conditions occurs when a notched-specimen is stretched to a sub-critical level and thereafter the stretch is held constant; after a sufficient incubation time damage initiates, accumulates, and eventually fracture occurs — a phenomenon known as "delayed-fracture"; this phenomenon cannot be explained by ignoring the diffusion of the fluid (Bonn et al., 1998; Wang and Hong, 2012; Tang et al., 2017).

There are very few papers in the literature which address the complete coupled diffusion-deformation-fracture problems in gels; the only paper that we are aware of is the very recent paper of Broger et al. (2017b).[1] In their paper these authors propose a diffusion-deformation-fracture theory with a diffuse-crack approximation based on a phase-field/damage variable d.[2] They present a variational framework for their phase-field fracture theory of gels together with a numerical implementation of their variational theory in a finite element program, and show some interesting simulations of crack intiation and propagation during drying of hydrogels.

The purpose of this part is also to address the coupled diffusion-deformation-fracture problem for an "ideal" single-network polymeric gel. If the cross-linking chemical bonds in such a network are strong then fracture is expected to occur by scission of the chains between the crosslinks, as envisioned in the classical model of Lake and Thomas (1967),

[1]For other previous papers on fracture of polymer gels — papers which are based generalizations of classical fracture mechanics theories and not on phase-field or gradient-damage theories — see, e.g., Wang and Hong (2012), Hui et al. (2013), Bouklas et al. (2015), and Noselli et al. (2016).

[2] The origins of the regularization of a sharp crack discontinuity in their diffuse-crack theory may be traced back to the energy minimization concepts of brittle fracture mechanics proposed in Francfort and Marigo (1998) and Bourdin et al. (2000).

while if the chemical crosslinks are weak then fracture is expected to occur because of the scission of the cross-linking bonds themselves. In this paper we focus our attention networks with strong cross-linking bonds which fail by chain-scission.[3] Further, as in the theory of Broger et al. (2017b), to model the fracture of a gel we introduce a damage variable $d(\mathbf{X}, t) \in [0, 1]$. If $d = 0$ at a point then that point is intact, while if $d = 1$ at some point, then that point is fractured. Values of d between zero and one correspond to partially-fractured material. We assume that d grows montonically so that $\dot{d}(\mathbf{X}, t) \geq 0$, which is a constraint that represents the usual assumption that microstructural changes leading to fracture are irreversible. As in Broger et al. (2017b) our theory also accounts for the gradient of the damage variable, ∇d. However, in contrast to the particular "incremental variational" approach taken by these authors in formulating their theory, we formulate our gradient-damage theory by using Gurtin's pioneering virtual-power approach (Gurtin, 1996, 2002). This approach leads to macroforce and microforce balances for the forces associated with the rate-like kinematical descriptors in the theory. These macro- and microforce balances, together with a free-energy imbalance law under isothermal conditions, when supplemented with a set of thermodynamically-consistent constitutive equations, provide the governing equations for our theory. The particular constitutive equations for fracture of a gel in our paper are based on extensions of a physical model of fracture of dry elastomers presented in our recent papers (Mao et al., 2017b; Talamini et al., 2018) which contain two essential new physical ingredients:

- Our constitutive equation for the change in free energy of a polymer network accounts for not only changes in the entropy, but also changes in the internal energy due to the stretching of the Kuhn segments of the polymer chains in the network. To do so, we introduce a dimensionless positive-valued internal variable, $\lambda_b \in [1, \infty)$, to represent (at the continuum scale) a measure of the stretch of the Kuhn segments. We call λ_b the *effective bond stretch.*

- The damage and failure of a polymer network with strong cross-linking chemical bonds is taken to occur by chain-scission, a process which is driven by the changes in the internal energy of the stretched polymer chains in the network, and not (directly) by changes in the configurational entropy of the polymer chains.

The paper by Broger et al. (2017b) does not consider changes in the internal energy of a polymer newtwork by stretching of the Kuhn segments. Their model for fracture of a gel is based entirely on changes of free energy due to configurational entropy changes, which we believe is not what occurs physically in a polymer network with strong chemical crosslinks.

The plan of this part is follows.

1. We begin in Chapter 3 by discussing more details of the newly-introduced bond stretch field λ_b and its physics consequence. As we state in previous chapter, one of the distinguishing features of elastomeric materials, which consist of a network of flexible

[3]We leave a consideration of interpenetrating-multiple-network gels, as well as materials which exhibit additional non-trivial dissipation mechanisms such as viscoelasticity and Mullins-effect, to future efforts.

polymeric chains, is that the deformation response is dominated by changes in entropy. Accordingly, most classical theories of rubber-like elasticity consider only the entropy and neglect any changes in internal energy. On the other hand, the fracture of strongly cross-linked elastomers is essentially energy dominated, as argued in the well-known Lake-Thomas model for the toughness of elastomers. The newly-introduced bond stretch field λ_b is the exactly the missing piece to resolve the inconsistency of deformation and fracture responses of elastomeric soft materials. We also show that both classical Arruda-Boyce model and the Lake-Thomas arguments can be recovered from our theory with the newly introduced Kuhn segment stretch field λ_b.

2. We then move to Chapter 4 to derive and summarize the continuum-mechanical framework of our theory for fracture of gel, with deformation, diffusion, Kuhn segment stretch, and damage fields. The governing partial differential equations, boundary conditions, and constitutive equations are displayed. We close this chapter by specializing the constitutive equations of our theory and the specialized constitutive equations. The theory developed in this paper is numerically implemented in an open-source finite element code MOOSE (Gaston et al., 2009) by writting our own application.

3. Using this simulation capability, in Chapter 5 we present results for our simulations of fracture of elastomers by suppressing the diffusion within the body. Moreover, we also discuss the case when the elastomers failed by crosslink failure instead of Kuhn segments scission. A central feature of our theory is the recognition that the free energy of elastomers is not entirely entropic in nature, there is also an energetic contribution from the deformation of the backbone bonds in a chain and/or the crosslinks. For polymers with weak crosslinks this energetic contribution is mainly from the deformation of the crosslinks. It is this energetic part of the free energy which is the driving force for progressive damage and fracture of elastomeric materials. Moreover, we show that for elastomeric materials in which fracture occurs by crosslink stretching and scission the Lake-Thomas Lake and Thomas (1967) scaling — that the toughness G_c of an elastomeric material is proportional to $1/\sqrt{G_0}$, with $G_0 = Nk_b\vartheta$ the ground-state shear modulus of the material — does not hold. A new scaling is proposed, and some important consequences of this scaling are remarked upon.

4. Using this simulation capability, in Chapter 6 we present results of fracture of gels from our simulations. We first focus on the Mode-I fracture in single-edge-notch and asymmetric-double-edge-notch geometries under plane-stress conditions. Then the single-edge notch geometry is used to explore the consequences of the competition between the characteristic time-scale for deformation and the characteristic time-scale for diffusion by fixing the time scale for deformation, and varying the value of the diffusivity of the fluid. While there are many operating conditions under which the characteristic time-scale for deformation is much smaller than the time-scale for diffusion, so that the diffusion of the fluid may be neglected, there are also operating conditions under which the fluid diffusion cannot be ignored — such as conditions leading to "delayed-fracture"

discussed earlier. We numerically study the phenomenon of "delayed-fracture" in following sessions, and clarify the important role of fluid diffusion in these phenomena. Finally we report on our study of fracture of an asymmetric-double-notched sheet specimen of a gel under Mode-I plane-stress loading. This example shows the capability of our gradient damage theory and its numerical implementation to model merging of two cracks.

5. Finally we close in Chapter 7 with some final remarks.

Chapter 3

The physics of fracture in elastomeric materials

3.1 Introduction

The classical statistical mechanical model of Kuhn and Grün (Kuhn and Grün, 1942) for the deformation response of a single polymer chain is based on the assumption that the change in free energy upon stretching of a long-chain molecule is dominated by the change in configurational entropy, and that any change in internal energy is negligible. A key feature of this model is that it accounts for the finite extensibility of the chain and reproduces the experimentally observed stiffening of the chain as it is highly stretched. This theory is the basis of a number of notable models for the deformation response of polymeric networks (see Treloar (1975); Arruda and Boyce (1993) and the references therein). On the other hand, the fracture behavior of polymers is widely accepted to be adequately described by the model of Lake and Thomas Lake and Thomas (1967), which connects the macroscopic work of fracture (the critical energy release rate G_c) to the energy required to strain and ultimately rupture bonds between monomer units. According to the arguments of Lake and Thomas, the *entropic* contribution to the free energy is negligible at the point of rupture, and the internal energy due to the bond deformation dominates. How can these models—both well accepted—be reconciled? The goal of this chapter is to address this question.

The plan of this chapter is as follows. In Section 3.2, we modify the single chain model of Kuhn and Grün to include an internal energy contribution which we associate with the mechanism of stretching of molecular bonds. In light of the success of the classic freely jointed chain model, any new model should behave similarly at stretch levels below rupture. On the other hand, to be consistent with the arguments of Lake and Thomas, a model should also be able to predict the increase of the internal energy during deformation and describe how it ultimately comes to dominate the free energy at large stretches. Our model satisfies these objectives while introducing only a single adjustable parameter, which has a clear physical

interpretation. Following the introduction of this model, we propose a simple criterion for chain scission based on the attainment of a critical value of bond stretching energy. In Section 3.3 we extend our considerations to deformation and fracture of a macroscopic elastomeric body composed of a network of chains. We use this model to study fracture in continuum bodies composed of elastomeric materials and to connect the flaw sensitivity to an intrinsic material length scale related to the network structure. We show that the proposed model recovers the Lake-Thomas scaling law for the critical energy release rate in the case of macroscopic sized cracks. We close in Section 3.4 with some final remarks.

3.2 Single chain model

The basic postulates of the original freely jointed chain (FJC) theory are as follows: (i) the macromolecule behaves like a chain of freely jointed segments (i.e., Kuhn segments); (ii) every segment in the polymer chain has the same length; (iii) the segments are rigid. Based upon these assumptions, the classic theory states that the free energy ψ of a single chain with n freely jointed segments of length L_b is given by

$$\psi = \hat{\psi}(r) = k_B \vartheta n \left[\frac{r}{nL_b}\beta + \ln\left(\frac{\beta}{\sinh\beta}\right)\right] \quad \text{with } \beta = \mathcal{L}^{-1}\left(\frac{r}{nL_b}\right), \tag{3.1}$$

where r is the current end-to-end length of the chain, ϑ is the absolute temperature, k_B is Boltzmann's constant, and $\mathcal{L}^{-1}$ is the inverse of the Langevin function $\mathcal{L}(x) = \coth x - x^{-1}$. This model captures the pronounced stiffening of polymeric materials at large extensions seen in experiments (see, e.g., Treloar (1975)). As $r \to nL_b$, the chain approaches a fully straightened configuration. Since the links are presumed rigid, the chain can accommodate no further displacement and the free energy diverges. The FJC model is intended for deformations below this level, where the approximation of the free energy as purely entropic is quite good. However, this is an obstacle for investigating chain scission, which usually occurs at large stretches.

We extend this model by relaxing the assumption of segment rigidity, and instead consider L_b to be the *rest* segment length, which may be altered by stretching of the segments in the chain. This idea has been explored in the form of the extended freely joint model (EFJM) of Smith et al. Smith et al. (1996). The EFJM was proposed to improve agreement between the observed mechanical behavior of DNA molecules and predictions from the freely jointed chain model. However, the EJFM is written directly in terms of chain force and displacement, rather than energy, and it is not simple to separate the entropic contribution to the free energy from the internal energy that governs bond rupture. Moreover, the Kuhn length and the number of Kuhn segments are constants in this model, while the effective contour length is allowed to change, which we argue introduces a conceptual inconsistency. In what follows, we consider an alternative model.

We consider the current segment length l_b to relate to the rest length L_b through $l_b = L_b\lambda_b$, where λ_b is a dimensionless stretch (i.e., the Kuhn segment stretch). We use the subsrcipt

"b" here and in the following to suggest "bond", since the extensibility of the Kuhn segments is presumed to come from deformation of the constituent atomic bonds. Then, with $\hat{\varepsilon}_{\mathrm{b}}(\lambda_{\mathrm{b}})$ denoting the change in internal energy associated with the stretching of the segments, we take the free energy to be

$$\psi = \hat{\psi}(r, \lambda_{\mathrm{b}}) = n\hat{\varepsilon}_{\mathrm{b}}(\lambda_{\mathrm{b}}) + k_B\vartheta n\left[\frac{r}{nl_b}\beta + \ln\left(\frac{\beta}{\sinh\beta}\right)\right]. \tag{3.2}$$

It is convenient to rewrite the free energy (3.2) in terms of the overall chain stretch $\lambda = r/r_0$, where $r_0 = \sqrt{n}L_b$ is the unstretched chain length determined from random walk statistics. As in the classical FJC model, we write $\lambda_L := \sqrt{n}$ to represent the chain "locking stretch" in the absence of any bond stretch. Substituting these definitions into (3.2) yields

$$\begin{aligned}\psi = \hat{\psi}(\lambda, \lambda_{\mathrm{b}}) &= \lambda_L^2\hat{\varepsilon}_{\mathrm{b}}(\lambda_{\mathrm{b}}) + k_B\vartheta\lambda_L^2\left(\frac{\lambda}{\lambda_L\lambda_{\mathrm{b}}}\beta + \ln\left(\frac{\beta}{\sinh\beta}\right)\right), \\ \text{with } \beta &= \mathcal{L}^{-1}\left(\frac{\lambda}{\lambda_L\lambda_{\mathrm{b}}}\right).\end{aligned} \tag{3.3}$$

Comparing with the classical FJC model, we see that $\lambda\lambda_{\mathrm{b}}^{-1}$ may be interpreted as the chain stretch due solely to Kuhn segment rearrangement.

At any *fixed* stretch λ, increasing λ_{b} increases the internal energy contribution to the free energy while decreasing the entropic part. This competition induces an optimal value of λ_{b} which will minimize the free energy and will be the actual state adopted by the system. Thus, setting $\partial\psi/\partial\lambda_{\mathrm{b}} = 0$ provides an implicit equation for λ_{b}, which reads

$$\frac{\mathrm{d}\hat{\varepsilon}_{\mathrm{b}}(\lambda_{\mathrm{b}})}{\mathrm{d}\lambda_{\mathrm{b}}}\lambda_{\mathrm{b}} = k_B\vartheta\frac{\lambda}{\lambda_L\lambda_{\mathrm{b}}}\beta. \tag{3.4}$$

As is standard, the force is given by

$$\begin{aligned}F = \frac{\partial\hat{\psi}(\lambda, \lambda_{\mathrm{b}})}{\partial r} &= \frac{1}{\sqrt{n}L_b}\frac{\partial\hat{\psi}(\lambda, \lambda_{\mathrm{b}})}{\partial\lambda} \\ &= \frac{k_B\vartheta}{L_b}\frac{\beta}{\lambda_{\mathrm{b}}},\end{aligned} \tag{3.5}$$

with λ_{b} determined by (3.4). [1]

[1]The intuitive derivation of the equations (3.2)-(3.5) displayed here is actually can be rigorously derived from statistical field theory. The full derivation of the model from statistical field theory is displayed in Appendix A. Essentially, (3.2) is the free energy expression of the mean-field theory by omitting the terms from saddle point approximations. This free energy expression is exact if we pick the quadrature form for internal energy. Equation (3.4) is the result of the saddle point approximation. Finally equation (3.5) is a nature result of thermodynamics.

We can visualize the behavior of this model by selecting a particular form for $\hat{\varepsilon}_{\mathrm{b}}(\lambda_{\mathrm{b}})$. By analogy with finite deformation continuum models of internal energy storage in materials, we choose an energy quadratic in the logarithmic strain, viz.

$$\hat{\varepsilon}_{\mathrm{b}}(\lambda_{\mathrm{b}}) = \frac{1}{2} E_{\mathrm{b}} \left(\ln \lambda_{\mathrm{b}}\right)^2, \tag{3.6}$$

where E_{b}, with dimensions of energy, represents the stiffness of the bonds.[2] With this choice, (3.4) becomes

$$E_{\mathrm{b}} \ln \lambda_{\mathrm{b}} = k_B \vartheta \frac{\lambda}{\lambda_L \lambda_{\mathrm{b}}} \beta. \tag{3.7}$$

Using these expressions, we compare the response of the proposed model with the classical inverse Langevin FJC model in Figure 3-1. In Figure 3-1(a) the force-stretch curves of the proposed model (with $E_{\mathrm{b}} = 1200 k_B \vartheta$) and the inverse Langevin FJC model are plotted. We plot λ_{b} versus the imposed stretch in Figure 3-1b. Since the proposed model degenerates to the classical inverse Langevin FJC model if λ_{b} is fixed at unity, the deviation of λ_{b} from 1 serves as a metric of the difference between the two models.

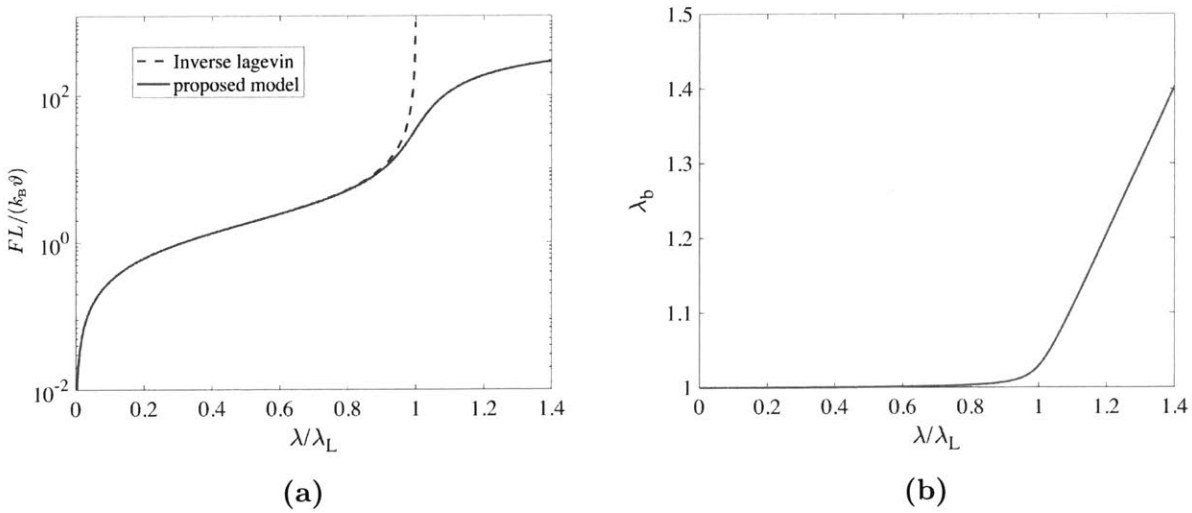

Figure 3-1: (a) Normalized force $FL/(k_B\vartheta)$ versus normalized stretch $\lambda/\lambda_{\mathrm{L}}$. Note that we have used a logarithmic scale for the force axis to emphasize the difference between the two responses. (b) The bond stretch λ_{b} versus normalized stretch $\lambda/\lambda_{\mathrm{L}}$.

The behavior of the present model is virtually indistinguishable from the classic FJC model at stretches $\lambda \leq 0.8\lambda_{\mathrm{L}}$, showing the same progression from Gaussian-like (neo-Hookean) behavior at low stretches, followed by pronounced stiffening at larger stretches

[2]Mathematically $\frac{1}{2} E_{\mathrm{b}} \left(\ln \lambda_{\mathrm{b}}\right)^2$ is not a convex function. This non-convexity of the expression will lead to a softening response of the model. This softening effect will potentially induce an instability in the system for a large λ_b.

as the chains become nearly aligned. However, as $\lambda \to \lambda_L$, the bond stretching becomes significant and the nonphysical singularity of the classic model is avoided.

Another view of the deformation process is depicted in Figure 3-2, where we plot the relative contribution of the new internal energy term ($n\varepsilon_b$) to the total free energy ψ, as a function of the imposed stretch. It can be clearly seen that at stretches below λ_L, entropic chain alignment is the preferred deformation mechanism. However, at larger stretches, segment stretching becomes energetically favorable and prevents the degenerate, fully locked state from being reached. Thus, the model predicts a smooth transition from the entropy dominated regime consistent with the assumption of the classic inverse Langevin FJC model to an internal energy-dominated regime consistent with the assumptions of the Lake-Thomas model. Furthermore, the physical interpretation of the newly introduced parameter E_b is evident in Figure 3-2: for larger values of E_b, free energy increase through the entropic contribution is increasingly favored, and the effect of bond stretching is delayed until larger stretches.

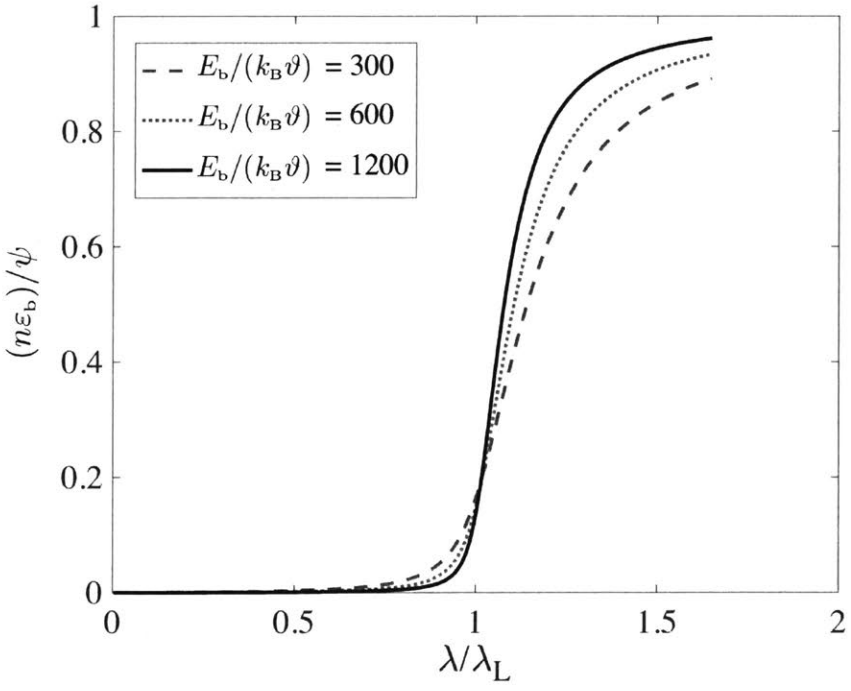

Figure 3-2: Contribution of the new internal energy of bond stretching to the total free energy, as a function of the normalized stretch λ/λ_L.

3.2.1 Scission of a single chain

With separate accounting of the configurational entropy and the segment stretching energy, we can make a connection between the deformation process and the scission process in polymers.

We postulate that scission of a chain occurs when the internal energy reaches a critical value, which for strongly cross-linked polymers is expected to be the binding energy between backbone units. We will use the symbol $\varepsilon_{\mathrm{b}}^{f}$ for the critical value of the energy for a single segment. Note that through the model above, this critical energy can also be translated into a critical value of stretch or a critical value of the free energy. The stiffness of the Kuhn segment E_{b} and the binding energy of a Kuhn segment $\varepsilon_{\mathrm{b}}^{f}$ are both related to the respective values of the underlying atomic bonds. If we consider only the contributions of bond stretching (neglecting contributions from bond angle rotation, van der Waals interactions, etc.), then the stiffness and binding energy of the Kuhn segment are the same as those of the bonds between the monomers.

To get a sense of the range of the model parameters E_{b} and $\varepsilon_{\mathrm{b}}^{f}$, consider the behavior of a single chain whose repeat unit is C-C:

- A typical value for the bond dissociation energy is $\varepsilon_{b}^{f} \approx 3.6\,\mathrm{eV}$, which translates to $\varepsilon_{b}^{f}/k_b\vartheta \approx 140$ at 300 K.[3]
- We estimate a value of $E_{\mathrm{b}} = 60$ eV at equilibrium bond length 1.56Å ($E_b/k_b\vartheta \approx 2300$ at 300 K) through *ab initio* calculations in the Vienna Ab initio Simulation Package (VASP) using a plane wave basis (Kresse and Furthmüller, 1996a,b).[4]

Using these values in the constitutive relation (3.6) for the internal energy, our calculations indicate that the polymer chain will undergo scission when $\lambda_{\mathrm{b}}^{f} = 1.4$. Since the stretch of each bond is assumed to be the same with that of the Kuhn segment, then $\lambda_{\mathrm{b}}^{f} = 1.4$ is also the failure stretch of the Kuhn segment (i.e., a nominal strain of 40%). This is in reasonable agreement with other estimates of the amount of stretch sustainable by atomic bonds. For crystalline materials and hard amorphous materials, a commonly used estimate of the ideal cohesive strength is $E/5$, or a nominal failure strain of $\sim 20\%$. Graphene, which has a similar type of bond as the C-C, still can sustain significant force at strains of $\sim 40\%$, see Liu et al. (2007).

Using the proposed relation for the free energy, this indicates that the polymer chain will break at $\lambda \approx 1.41\lambda_{\mathrm{L}}$ at room temperature, which exceeds the locking stretch of the classical model considerably.[5] Furthermore, the internal energy of bond stretching constitutes 95%

[3]Bond dissociation energies are widely available in the literature (see, e.g., deB. Darwent (1970); Huheey et al. (1993)).

[4]We were unable to locate published characterizations of the C-C bond stiffness. The ab initio calculations simultaneously yield a prediction of the equilibrium bond length, which is in agreement with the references above, providing a measure of confidence in the stiffness calculation.

[5]This also provide a fact that on the failure point, the normalized stretch of the polymer chain $\frac{\lambda}{\lambda_L\lambda_b}$ is actually very close to 1. In current case, $\frac{\lambda}{\lambda_L\lambda_b} = 0.99$.

of the total free energy at the point of scission, which agrees with the assumption of Lake and Thomas (Lake and Thomas, 1967).

3.3 Deformation and fracture of a macroscopic elastomeric body

In this section, we extend our considerations of a single chain to treat fracture in a continuum body composed of a network of chains. First, we extend the single chain deformation model to a continuum theory by using the eight-chain network model of Arruda and Boyce (Arruda and Boyce, 1993) in Section 3.3.1. Next, in Section 3.3.2, we generalize the single chain scission criterion proposed above to the continuum.

As recently emphasized by Chen et al. (Chen et al., 2016), the rupture of elastomeric materials is insensitive to "small" cracks or cuts, but beyond a certain size, the stretch to rupture decreases markedly with increasing crack length. In Section 3.3.3, we show that this behavior can be reproduced by our network deformation model and rupture criterion, and thus this model may offer some physical insight into the flaw sensitivity of elastomeric bodies.

As in the single chain scission criterion, the network rupture criterion is based directly on the energetics of bond deformation, and not on the classical critical energy release rate approach. However, we show in Section 3.3.4 that it agrees with the critical energy release rate approach in the limit of macroscopic-scale flaws. Finally, in Section 3.3.5 we demonstrate that in the large flaw size limit, the critical energy release rate predicted by our model obeys the well-known and experimentally supported scaling law predicted by Lake and Thomas (Lake and Thomas, 1967).

3.3.1 Extension of single chain model to the network

A simple way to extend the single chain model to the continuum level is to use the eight-chain network model of Arruda and Boyce (Arruda and Boyce, 1993). Mathematically, this boils down to replacing the single chain stretch λ with an *effective distortional stretch* $\bar{\lambda}$, defined by Anand as (Anand, 1996)

$$\bar{\lambda} \overset{\text{def}}{=} \sqrt{\frac{\operatorname{tr}\bar{\mathbf{C}}}{3}}, \tag{3.8}$$

where $\operatorname{tr}(\cdot)$ represents the trace of a second order tensor, $\bar{\mathbf{C}} = \bar{\mathbf{F}}^{\top}\bar{\mathbf{F}}$ is the distortional right Cauchy-Green tensor, and $\bar{\mathbf{F}} = (\det \mathbf{F})^{-1/3}\mathbf{F}$ is the distortional part of the deformation gradient.

Using the logarithmic strain form of the internal energy of bond stretching, the distortional free energy density per unit reference volume is

$$\psi_{\mathrm{R}} = \hat{\psi}_{\mathrm{R}}(\bar{\lambda}, \lambda_{\mathrm{b}}) = \frac{1}{2}\lambda_L^2 N E_{\mathrm{b}} \left(\ln \lambda_{\mathrm{b}}\right)^2 + N k_B \vartheta \lambda_L^2 \left[\frac{\bar{\lambda}}{\lambda_L \lambda_{\mathrm{b}}}\beta + \ln\left(\frac{\beta}{\sinh \beta}\right)\right], \tag{3.9}$$

with N the number of chains per unit reference volume and $\beta = \mathcal{L}^{-1}\left(\bar{\lambda}/(\lambda_L \lambda_{\mathrm{b}})\right)$. We denote by

$$\varepsilon_{\mathrm{R}} = \hat{\varepsilon}_{\mathrm{R}}(\lambda_{\mathrm{b}}) = N n \hat{\varepsilon}_{\mathrm{b}}(\lambda_{\mathrm{b}}) = \frac{1}{2}\lambda_L^2 N E_{\mathrm{b}} \left(\ln \lambda_{\mathrm{b}}\right)^2, \tag{3.10}$$

the internal energy due to bond stretching. In this case the implicit equation for λ_{b} becomes

$$E_{\mathrm{b}} \ln \lambda_{\mathrm{b}} = k_B \vartheta \frac{\bar{\lambda}}{\lambda_L \lambda_{\mathrm{b}}}\beta. \tag{3.11}$$

It is convenient to define the bulk material parameters $\mu = N k_B \vartheta$ and $E = N E_{\mathrm{b}}$, and to rewrite (3.9) as

$$\psi_{\mathrm{R}} = \hat{\psi}_{\mathrm{R}}(\bar{\lambda}, \lambda_{\mathrm{b}}) = \frac{1}{2}\lambda_L^2 E \left(\ln \lambda_{\mathrm{b}}\right)^2 + \mu \lambda_L^2 \left[\frac{\bar{\lambda}}{\lambda_L \lambda_{\mathrm{b}}}\beta + \ln\left(\frac{\beta}{\sinh \beta}\right)\right]. \tag{3.12}$$

Similarly, equation (3.11) becomes

$$E \ln \lambda_{\mathrm{b}} = \mu \frac{\bar{\lambda}}{\lambda_L \lambda_{\mathrm{b}}}\beta. \tag{3.13}$$

In the limit $\mu/E \to 0$ the original eight chain model is recovered.

Since $E/\mu = E_b/(k_B\vartheta)$, by estimating E_b and μ at a specific temperature, we can estimate E. For a specific material, μ can be determined as usual from standard macroscopic experiments. The bond stiffness E_b can be estimated from *ab initio* calculations, or possibly estimated from AFM measurements of single chains as attempted in Smith et al. (1996); Li et al. (1999); Ghatak et al. (2000).

In order to take the slight compressibility of elastomers into account, following Anand (Anand, 1996), we append a volumetric internal energy term to the free energy, giving

$$\psi_{\mathrm{R}} = \tilde{\psi}_{\mathrm{R}}(\bar{\lambda}, \lambda_{\mathrm{b}}, J) = \frac{1}{2}\lambda_L^2 E \left(\ln \lambda_{\mathrm{b}}\right)^2 + \mu \lambda_L^2 \left[\frac{\bar{\lambda}}{\lambda_L \lambda_{\mathrm{b}}}\beta + \ln\left(\frac{\beta}{\sinh \beta}\right)\right] + \frac{1}{2}K(\ln J)^2, \tag{3.14}$$

where $J = \det \mathbf{F}$ and K is the bulk modulus. Thus

$$\varepsilon_{\mathrm{R,tot}} = \hat{\varepsilon}_{\mathrm{R,tot}}(\lambda_{\mathrm{b}}, J) = \frac{1}{2}\lambda_L^2 E \left(\ln \lambda_{\mathrm{b}}\right)^2 + \frac{1}{2}K(\ln J)^2 \tag{3.15}$$

represents the total internal energy per unit volume.

Remark. The idea developed in this paper can also be extended to other rubber elasticity models, such as the model of Gent (Gent, 1996). Since the Gent model is phenomenological, we cannot derive it from statistical mechanics. However, $\lambda_{\rm b}$ can be introduced to serve the same purpose as in the current modified eight-chain model, inducing a competition between the internal energy and entropy that will determine a preferred Kuhn segment stretch at each level of deformation. For example, one can write

$$\psi_{\rm R} = \hat{\psi}_{\rm R}(\bar{I}_1, \lambda_{\rm b}, J) = \hat{\varepsilon}_{\rm R,tot}(\lambda_{\rm b}, J) - \frac{1}{2}\mu I_m \ln\left(1 - \frac{\bar{I}_1\lambda_{\rm b}^{-2} - 3}{I_m}\right), \tag{3.16}$$

where $\hat{\varepsilon}_{\rm R,tot}(\lambda_{\rm b}, J)$ is the chosen constitutive relation for the internal energy of Kuhn segment stretching and volumetric deformation, and $\bar{I}_1 = \mathrm{tr}\,\bar{\mathbf{C}}$ and I_m are material parameters of the Gent model.

□

3.3.2 Criterion for extension of a crack in an elastomeric body

Next, we scale up the criterion for scission of a single chain to a criterion for crack propagation in an elastomeric body at the continuum level. Our objective is to create a fracture criterion that is rooted in the micro-mechanics of polymer networks, and yet is consistent with fracture mechanics in the limit of macroscopic sized flaws. Fracture is a size-dependent phenomenon, so we expect a length scale to play a role in the generalization from the single chain picture.

From the macroscopic perspective, a natural length scale is associated with the critical energy release rate approach to fracture of elastomers Rivlin and Thomas (1952); Thomas (1955). Presume that the critical energy release rate G_c is a fixed material property, and that the free energy density in the vicinity of the crack tip reaches a critical value $\psi_{\rm R}^f$ at the point of crack propagation. Then as noted by Thomas Thomas (1955), a length scale

$$\ell \simeq G_c/\psi_{\rm R}^f, \tag{3.17}$$

emerges. (Such a relation clearly proceeds from purely dimensional arguments).[6]

Consider now a body with an existing crack-like flaw. Consistent with the length scale observation above, we postulate that

- crack propagation will occur when the internal energy due to segment stretching $\varepsilon_{\rm R} = \hat{\varepsilon}_{\rm R}(\lambda_{\rm b})$ reaches a critical value $\varepsilon_{\rm R}^f$ at a material point P located at a distance ℓ ahead of the crack in the reference configuration (see Figure 5-2).

Expressed mathematically, this is

$$\varepsilon_{\rm R}|_{\mathbf{X}=P} = \varepsilon_{\rm R}^f, \tag{3.18}$$

where

$$\varepsilon_{\rm R}^f = N\,n\,\varepsilon_b^f \tag{3.19}$$

[6] Here and in the following, we define the relation $a \simeq b$ to mean $\frac{a}{b} = O(1)$.

is the critical bond energy per unit volume.

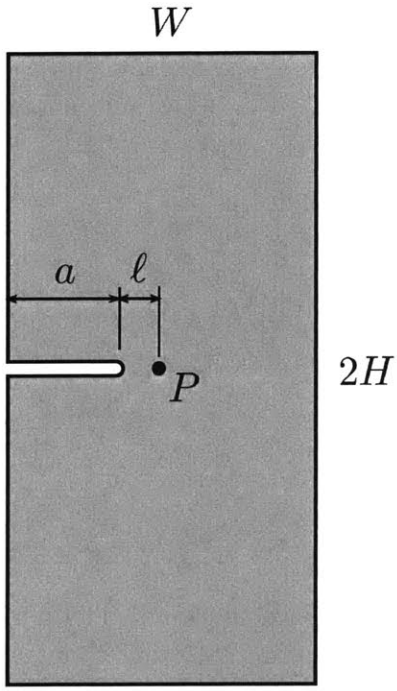

Figure 3-3: Schematic of geometry used in finite element calculations. The bond stretch failure criterion is applied at the point P, located at a distance ℓ ahead of the crack root.

From the microscopic perspective, the only intrinsic length scale comes from the microstructure of the material, which for the ideal elastomers under consideration, is the rest distance between cross-links $r_0 = \sqrt{n}L_b$. Thus, for materials with no other dissipation mechanisms besides chain scission (i.e., true elastomers), one expects $\ell \simeq r_0$. This distance is in the nanometer range for typical polymeric networks. According to this point of view, the region within a distance ℓ of the crack root is the fracture process zone, within which the continuum hypothesis breaks down and the details of the physics are inaccessible to a continuum model. As usual in fracture mechanics, we posit that at a sufficient distance ahead of a flaw, the continuum picture still uniquely characterizes the response of the cracked body.

For polymeric materials besides pure elastomers, ℓ can be much larger than r_0, as shown by the experiments of Chen et. al. (Chen et al., 2016). This is due to the presence of additional dissipation mechanisms, such as viscoelasticity, the Mullins effect, and embedded sacrificial networks (Slepyan, 2012; Zhao, 2014; Zhang et al., 2015).

3.3.3 Role of flaw size on fracture of an ideal elastomer

With the network model and rupture initiation criterion in hand, we are in a position to study the role of flaw size on fracture in elastomers. To this end, we implemented our model in the commercial finite element simulation tool Abaqus Dassault Systèmes (v. 6.14), and

applied it to the problem of plane stress, mode I loading of a body with an edge crack.The problem configuration is shown in Figure 5-2. The specimen is defined by the width W, height $2H$, with a single edge crack of length a and root radius ρ. The crack length is taken to vary over the range $1 \leq a/r_0 \leq 10^5$. For each crack size, we scale the overall sample dimensions so that $W/a = 10$ and $H/a = 20$. We take $\ell/r_0 = 1$. We focus attention on sharp crackes and take $\rho/r_0 = 1$ (it is clear from consideration of the microstructure that in the sharpest limit $\rho \simeq r_0$). The material parameters are given in Table 3.1. For each specimen, we find quasi-static solutions under increasing far-field stretching until the bond rupture criterion (3.18) is met. Additional details of the simulation are located in the Appendix.

Table 3.1: Material parameters for fracture simulations.

$E/\mu = E_b/k_b\vartheta$	$\lambda_L = \sqrt{n}$	K/μ	$\varepsilon_{\mathrm{R}}^f/\lambda_L^2\mu = \varepsilon_b^f/k_B\vartheta$
2.5×10^3	5	2.5×10^5	100

The results are summarized in Figure 3-4, where we plot the failure stretch λ^f against the normalized crack size a/r_0. The failure stretch is normalized by a factor of $(\sqrt{3}\lambda_L)$, which is an approximation of the limiting stretch in uniaxial tension of the classic 8-chain model.[7]

This figure clearly shows that the stretchability is relatively insensitive to small cracks ($a/r_0 \lessapprox 500$). It is noteworthy that with small cracks, the maximum attainable stretch can exceed the limiting value of the classic entropic elasticity model $\sqrt{3}\lambda_L$. With decreasing crack size, the stretchability increases until it approaches a plateau at the *ideal rupture stretch* (shown as a dotted line).[8] In contrast, for large cracks, ($a/r_0 \gtrapprox 500$), the stretchability reduces markedly as the crack size gets larger. These results are supported by the recently published experimental results of Chen et al. (Chen et al., 2016); cf. their Figures 3.

Another way of visualizing the size dependent behavior is shown in Figure 3-5. Contours of $\varepsilon_{\mathrm{R}}/\psi_{\mathrm{R}}$, the ratio of the internal energy density to the total free energy density, are plotted for a small crack ($a/r_0 = 5.25$) and a larger crack ($a/r_0 = 300$). The contours are shown at the point of incipient fracture and are drawn on the reference configuration. For the short crack, most of the specimen is well into the internal energy-dominated regime at the point of incipient fracture, and the crack itself has little effect on the overall response. On the other hand, for the longer crack, only a small region near the crack has any appreciable bond stretching, while the rest of the specimen is still in the entropic elasticity-dominated regime.

[7] For an incompressible material under uniaxial stretch λ, $\bar{\lambda} = \sqrt{(\lambda^2 + 2/\lambda)/3} \approx \lambda/\sqrt{3}$ when $\lambda \gg 1$. Setting $\bar{\lambda} = \lambda_L$ yields the above estimate.

[8] The ideal rupture stretch value was computed by a uniaxial tension computation of a specimen with no flaw.

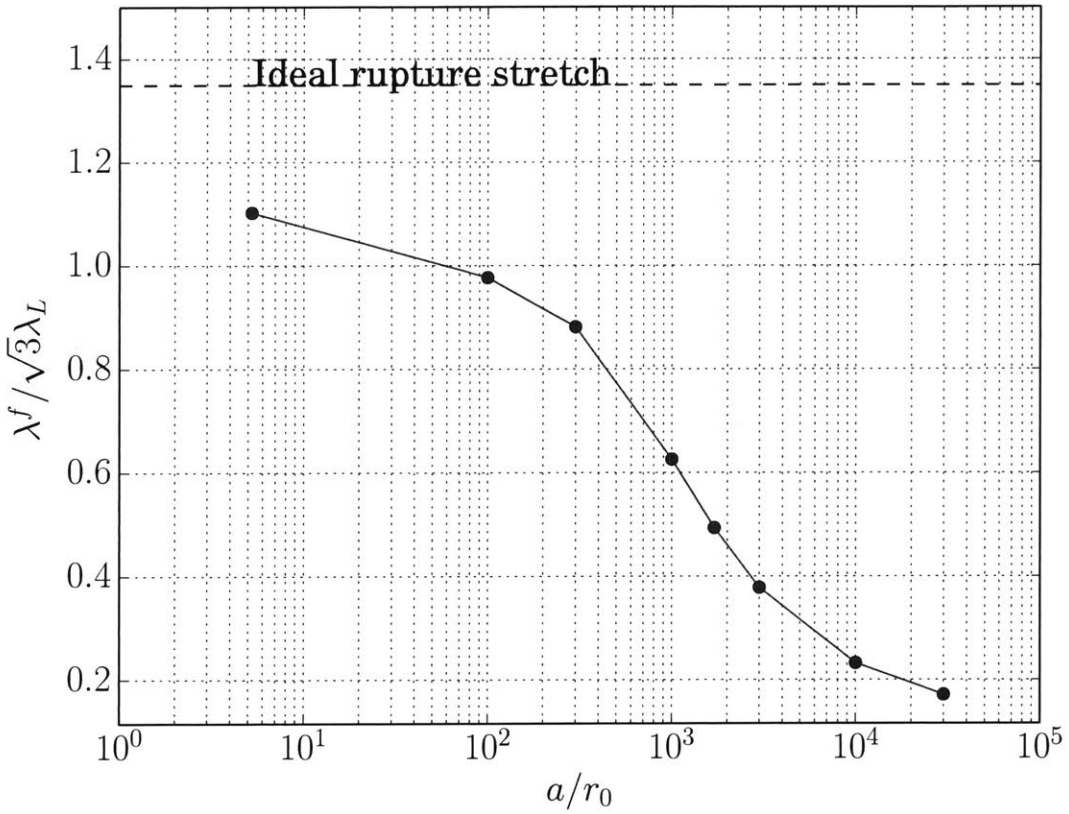

Figure 3-4: Computed normalized failure stretch, $\lambda^f/\sqrt{3}\lambda_L$, at the point of bond failure as a function of a/r_0. For small cracks ($a/r_0 < 500$), the stretchability is relatively insensitive to flaw size, but it decreases markedly for larger flaws. The ideal rupture stretch (in the absence of a flaw) is shown as a dashed line.

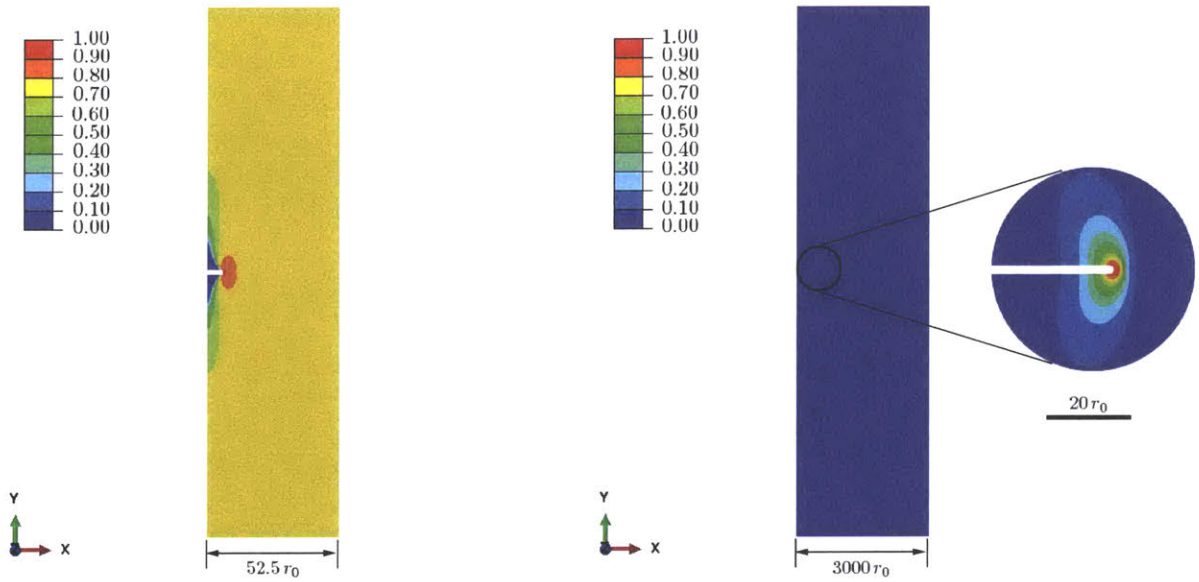

(a) (b)

Figure 3-5: Contours of ε_R/ψ_R, the ratio of internal energy density to the total free energy density, at the point of incipient rupture. The magnitude of bond stretching is strongly affected by crack size. (a) Small crack, $a/r_0 = 5.25$. The crack does not strongly concentrate energy, and the entire specimen undergoes significant bond stretch by the point of rupture. (b) Larger crack, $a/r_0 = 300$. The zone of significant bond stretching is confined to the vicinity of the crack.

3.3.4 Comparison of the bond stretch criterion with the critical energy release rate approach

Using the same simulations as above, we compute the energy release rate via the J-integral Rice (1968) at the point of incipient bond failure, which we will denote by G^f.[9] The results of this numerical experiment are shown in Figure 3-6, which plots the normalized energy release rate at the point of bond rupture $G^f/r_0\mu$ versus the normalized crack size a/r_0. From this plot, it is evident that the predictions by the bond stretching criterion (3.18) indeed approach a fixed critical energy release rate G_c in the limit of large flaws, consistent with (3.17). The approximate value of this limit is shown with a dashed line in Figure 3-6. For smaller flaws approaching the microstructural scale, the energy release rate at the point of rupture is less than G_c. This is expected, since in the small flaw limit the process zone occupies a region comparable in scale to the crack, and the thus the scale separation argument used to justify the critical energy release rate criterion no longer applies. This behavior is observed across all of fracture mechanics. A well-known example is furnished by metals, where the small scale yielding condition limits the applicability of linear elastic fracture mechanics.

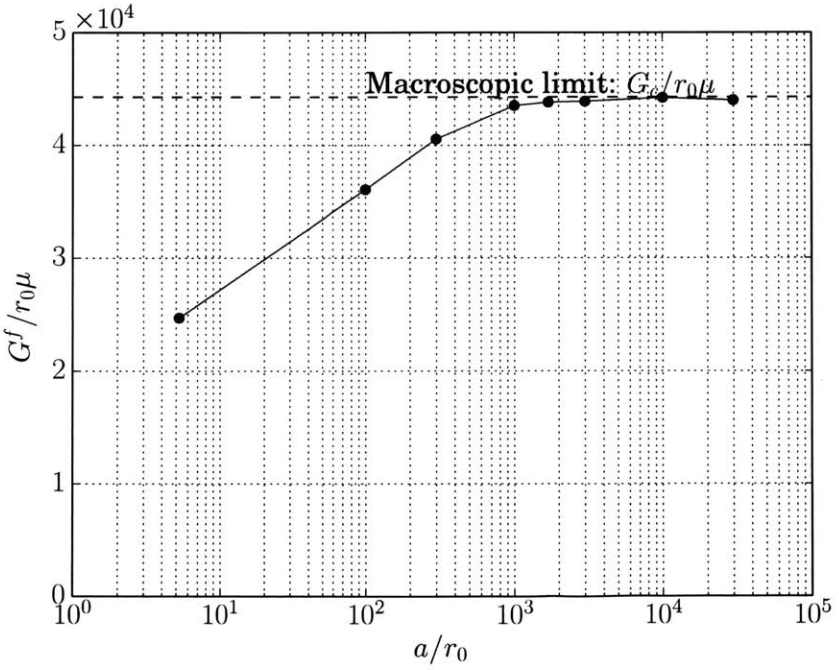

Figure 3-6: Computed normalized energy release rates at the point of bond failure. At large crack lengths approaching macroscopic size $a/r_0 > 500$, the energy release rate G^f tends to a constant value G_c, consistent with the classical energy release rate criterion.

[9]The J-integral is computed using the built-in implementation of Parks's virtual crack extension method Parks (1977) in Abaqus.

3.3.5 Comparison of G_c predictions with scaling law of Lake and Thomas

We now compare our approach with the well-known scaling law for the critical energy release rate of elastomers by Lake and Thomas Lake and Thomas (1967). The scaling law is obtained from a simple and elegant argument: the energy per unit area required to advance a crack a distance ℓ is the product of the chains per unit area ahead of the crack (which goes as $N\ell$) and the total energy stored in a chain when it breaks (approximately $n\varepsilon_b^f$). Then, noting that $\ell \simeq r_0$, the scaling law is

$$G_c \sim N r_0 n \varepsilon_b^f.$$

It can be expressed in dimensionless form as

$$\frac{G_c}{r_0 \mu} \sim \left(\frac{\varepsilon_b^f}{k_b \vartheta} \right) (\lambda_L)^2, \tag{3.20}$$

where we have used the identities $\lambda_L = \sqrt{n}$ and $\mu = N k_B \vartheta$.

To compare our approach with the Lake-Thomas idea, we use numerical simulations with the same setup as in the previous subsection. We use the specimen with $a/r_0 = 10^4$ so that we are considering a system which is well into the large flaw regime where the critical energy release criterion applies. All other parameters are as before.

In the first case, we vary λ_L and plot the results in Figure 3-7a. The quadratic dependence predicted by the Lake-Thomas model is clearly observed (in other words, a linear dependence between G^f and the number of segments per chain n is observed). This agreement is not surprising, since in formulating our model we have assumed that each of the bonds in the chain stores the same amount of energy, which is consistent with the argument that Lake and Thomas make to arrive at (3.20). Next we examine the relation between G_f and $\varepsilon_b^f / k_b \vartheta$. In Figure 3-7b, we plot the normalized energy release rate $G^f / r_0 \mu$ vs. the bond rupture energy $\varepsilon_b^f / k_b \vartheta$. The linear scaling predicted by Lake and Thomas is approached for large values of the bond rupture energy, while for smaller values sub-linear scaling is observed. The deviation from the Lake-Thomas scaling can be understood by noting that for small values of the bond rupture energy, rupture occurs at small stretches where the entropic contribution to the free energy density is still significant. The Lake-Thomas assumption of internal energy dominance does not hold in this case. As one moves to the right of Fig. 3-7b, the assumptions of the Lake-Thomas model are better met, and the observed scaling more closely matches the prediction. Continuing the calculation to larger values of bond rupture energy becomes difficult due to

1. the non-convexity of the internal energy expression

$$\varepsilon_b(\lambda_b) = \frac{1}{2} E_b (\ln \lambda_b)^2 \tag{3.21}$$

that we choice in this work, and

2. high levels of mesh distortion in the vicinity of the notch root.

As we said before, the non-convexity of the internal energy expression will induce an instability in simulation, and such numerical issue as λ_b increases will impede the simulation to converge. To suppress this artificial effect, we can chose a simple quadrature and convex form

$$\varepsilon_b(\lambda_b) = \frac{1}{2}E_b(\lambda_b - 1)^2. \tag{3.22}$$

This form will give better fit with the Lake-Thomas model prediction. Moreover, additional tools, such as mesh adaptivity, could ameliorate this issue, but such complications were not pursued here.

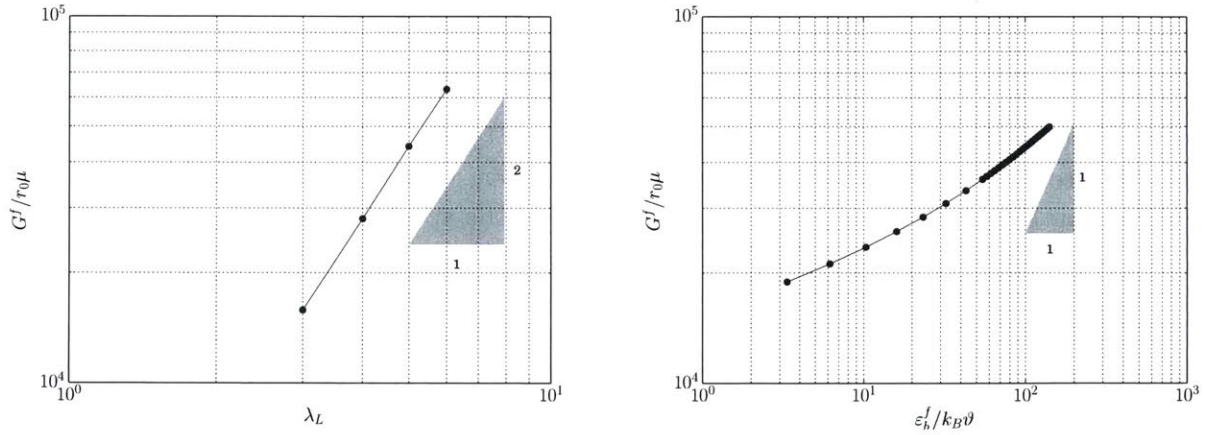

Figure 3-7: Comparison of the bond stretch failure criterion with the Lake-Thomas scaling law for the critical energy release rate. Plotted are the energy release rate at the point of incipient bond failure vs (a) the locking stretch parameter; and (b) the normalized bond rupture energy. The linear relationship assumed by Lake and Thomas holds in the limit of large stretches when the internal energy is much larger than the entropic contribution to the free energy.

3.4 Concluding remarks

We have presented a model which bridges the elastic deformation and the fracture of elastomers. Specifically, we have extended the freely jointed inverse Langevin model (and the corresponding 8-chain Arruda-Boyce model) to account for changes in internal energy due to stretching of the chain segments. Chain scission is postulated to occur upon the attainment of a critical value of this segment stretching internal energy.

We have shown in this chapter that, under appropriate conditions, our model is consistent with two classical models for elastomers: the Arruda-Boyce model for deformation,

and the Lake-Thomas model for fracture. We have used this model to relate the flaw sensitivity of elastomers to an intrinsic material length scale related to the network structure. This approach may be useful for considering small devices made by highly stretchable soft materials.

Substantial effort is needed to extend our current model to describe materials with other dissipation mechanisms, as well as cross-link failure and cavitation mechanisms.

Chapter 4

A theory for fracture of polymeric gels

4.1 Basic kinematics

Consider a fluid-containing (wet) macroscopically-homogeneous body made from an elastomeric gel. In what follows, the spatially-continuous fields that define our continuum theory represent averages meant to apply at length scales which are large compared to the length scales associated with the molecular network and its microscopic-scale free-volume. We identify such a macroscopically-homogeneous body B with the region of space it occupies in a fixed *reference configuration*, and denote by $\mathbf{X}$ an arbitrary material point of B.[1] A motion of B is a smooth one-to-one mapping $\mathbf{x} = \boldsymbol{\chi}(\mathbf{X}, t)$ with deformation gradient, velocity, and velocity gradient given by

$$\mathbf{F} = \nabla\boldsymbol{\chi}, \quad \mathbf{v} = \dot{\boldsymbol{\chi}}, \quad \mathbf{L} = \operatorname{grad}\mathbf{v} = \dot{\mathbf{F}}\mathbf{F}^{-1}. \tag{4.1}$$

We base the theory on a multiplicative decomposition of the deformation gradient

$$\mathbf{F} = \mathbf{F}^e\mathbf{F}^s, \tag{4.2}$$

where,

- $\mathbf{F}^s$ represents the local distortion of the material neighborhood of $\mathbf{X}$ due to the insertion/extraction of the fluid molecules due to the diffusion of the fluid; and

[1] Notation: We use standard notation of modern continuum mechanics (Gurtin et al., 2010). Specifically: ∇ and Div denote the gradient and divergence with respect to the material point $\mathbf{X}$ in the reference configuration, and $\Delta = \operatorname{Div}\nabla$ denotes the referential Laplace operator; grad, div, and div grad denote these operators with respect to the point $\mathbf{x} = \boldsymbol{\chi}(\mathbf{X}, t)$ in the deformed body; a superposed dot denotes the material time-derivative. Throughout, we write $\mathbf{F}^{e-1} = (\mathbf{F}^e)^{-1}$, $\mathbf{F}^{e-\top} = (\mathbf{F}^e)^{-\top}$, etc. We write $\operatorname{tr}\mathbf{A}$, $\operatorname{sym}\mathbf{A}$, $\operatorname{skw}\mathbf{A}$, $\mathbf{A}_0$, and $\operatorname{sym}_0\mathbf{A}$ respectively, for the trace, symmetric, skew, deviatoric, and symmetric-deviatoric parts of a tensor $\mathbf{A}$. Also, the inner product of tensors $\mathbf{A}$ and $\mathbf{B}$ is denoted by $\mathbf{A}:\mathbf{B}$, and the magnitude of $\mathbf{A}$ by $|\mathbf{A}| = \sqrt{\mathbf{A}:\mathbf{A}}$.

- $\mathbf{F}^e$ represents the subsequent stretching and rotation of this coherent fluid-distorted material neighborhood, and thereby represents a corresponding mechanical distortion.

We refer to $\mathbf{F}^s$ and $\mathbf{F}^e$ as the swelling and mechanical distortions, respectively. We write

$$J = \det \mathbf{F} > 0, \tag{4.3}$$

and hence we have

$$J = J^e J^s, \quad \text{and we assume that} \quad J^e = \det \mathbf{F}^e > 0, \quad \text{and} \quad J^s = \det \mathbf{F}^s > 0, \tag{4.4}$$

so that $\mathbf{F}^e$ and $\mathbf{F}^s$ are invertible.

The total and elastic right Cauchy-Green deformation tensors are given by

$$\mathbf{C} = \mathbf{F}^\top \mathbf{F} \qquad \text{and} \qquad \mathbf{C}^e = \mathbf{F}^{e\top} \mathbf{F}^e, \tag{4.5}$$

respectively. Next, by the definition $(4.1)_3$, we have

$$\mathbf{L} = \mathbf{L}^e + \mathbf{F}^e \mathbf{L}^s \mathbf{F}^{e-1}, \quad \text{with} \quad \mathbf{L}^e = \dot{\mathbf{F}}^e \mathbf{F}^{e-1}, \quad \text{and} \quad \mathbf{L}^s = \dot{\mathbf{F}}^s \mathbf{F}^{s-1}, \tag{4.6}$$

where $\mathbf{L}^s$ represents a distortion rate due to insertion/extraction of the fluid molecules. As is standard, we define the elastic and swelling stretching and spin tensors through

$$\mathbf{D}^e = \operatorname{sym} \mathbf{L}^e, \quad \mathbf{W}^e = \operatorname{skw} \mathbf{L}^e, \quad \mathbf{D}^s = \operatorname{sym} \mathbf{L}^s, \quad \mathbf{W}^s = \operatorname{skw} \mathbf{L}^s, \tag{4.7}$$

so that $\mathbf{L}^e = \mathbf{D}^e + \mathbf{W}^e$, and $\mathbf{L}^s = \mathbf{D}^s + \mathbf{W}^s$.

We assume that the swelling distortion $\mathbf{F}^s$ is isotropic and given by,

$$\mathbf{F}^s = \lambda^s \mathbf{1}, \quad \lambda^s = (J^s)^{1/3} > 0; \tag{4.8}$$

we call λ^s the swell-stretch. Further, from the definitions of $\mathbf{D}^s$ and $\mathbf{W}^s$ in (4.7), the definition of $\mathbf{L}^s$ in (4.6), and the specific expression for $\mathbf{F}^s$ in (4.8), we have,

$$\mathbf{D}^s = (\dot{\lambda}^s \lambda^{s-1}) \mathbf{1}, \quad \text{and} \quad \mathbf{W}^s = \mathbf{0}; \tag{4.9}$$

and since $\dot{J}^s = J^s \operatorname{tr} \mathbf{D}^s$, we have

$$\mathbf{D}^s = \frac{1}{3} (\dot{J}^s J^{s-1}) \mathbf{1}. \tag{4.10}$$

Finally, throughout we denote by P an arbitrary part of the reference body B with $\mathbf{n}_{\mathrm{R}}$ the outward unit normal on the boundary $\partial \mathrm{P}$ of P. Also, we denote by $\mathcal{P}_t = \boldsymbol{\chi}(\mathrm{P}, t)$ the image of P in the deformed body $\mathcal{B}_t = \boldsymbol{\chi}(\mathrm{B}, t)$, with $\mathbf{n}$ the outward unit normal on the boundary $\partial \mathcal{P}_t$ of $\mathcal{P}_t$.

4.2 Effective bond stretch

Following Mao et al. (2017b) and the previous chapter we introduce a dimensionless positive-valued internal variable,

$$\lambda_b \in [1, \infty),$$

to represent (at the continuum scale) a measure of the stretch of the Kuhn segments of the polymer chains of the elastomeric gel. We call λ_b the effective bond stretch.

4.3 Damage variable

To describe damage and fracture of the gel we introduce an damage variable or phase-field,

$$d(\mathbf{X}, t) \in [0, 1]. \tag{4.11}$$

If $d = 0$ at a point then that point is intact, while if $d = 1$ at some point, then that point is fractured. Values of d between zero and one correspond to partially-fractured material. We assume that d grows monotonically so that

$$\dot{d}(\mathbf{X}, t) \geq 0, \tag{4.12}$$

which is a constraint that represents the usual assumption that microstructural changes leading to fracture are irreversible.

4.4 Fluid content. Balance law for the fluid content

Let

$$c_{\mathrm{R}}(\mathbf{X}, t) \tag{4.13}$$

denote the number of moles of fluid molecules absorbed by the elastomer, reckoned per unit volume of the dry elastomer. We call c_{R} the fluid content. The initial value of c_{R} in the wet elastomeric gel is denoted by c_{R0}.

Define a fluid flux $\mathbf{j}_{\mathrm{R}}$, measured per unit area, per unit time, so that $-\int_{\partial \mathrm{P}} \mathbf{j}_{\mathrm{R}} \cdot \mathbf{n}_{\mathrm{R}} da_{\mathrm{R}}$ represents the number of moles of fluid entering P across ∂P, per unit time. In this case the balance law for fluid content takes the form

$$\dot{\int_{\mathrm{P}} (c_{\mathrm{R}} - c_{\mathrm{R0}})\, dv_{\mathrm{R}}} = -\int_{\partial \mathrm{P}} \mathbf{j}_{\mathrm{R}} \cdot \mathbf{n}_{\mathrm{R}}\, da_{\mathrm{R}}, \tag{4.14}$$

for every part P. Bringing the time derivative in (4.14) inside the integral and using the divergence theorem on the integral over ∂P, and localization the result leads to the following (local) balance law for the fluid content,

$$\dot{c}_{\mathrm{R}} = -\mathrm{Div}\mathbf{j}_{\mathrm{R}}. \tag{4.15}$$

4.5 Kinematical constitutive relation between J^s and c_{R}

Now, $(J^s - 1)$ represents the change in volume per unit reference volume due to swelling. We assume that this change arises entirely due to the change in the fluid content, so that with Ω denoting the volume of a mole of fluid molecules (presumed to be constant) we have the important swelling constraint

$$J^s = 1 + \upsilon c_{\mathrm{R}}. \tag{4.16}$$

Note that on account of (4.8), the constraint (4.16) may also be stated as

$$\lambda^s = (1 + \upsilon c_{\mathrm{R}})^{1/3}. \tag{4.17}$$

Finally, using (4.1) and (4.16) we may write $(4.6)_1$, for future use, as

$$(\nabla \dot{\boldsymbol{\chi}})\mathbf{F}^{-1} = \dot{\mathbf{F}}^e \mathbf{F}^{e-1} + \frac{1}{3}\Theta(c_{\mathrm{R}}, c_{\mathrm{R0}})\dot{c}_{\mathrm{R}}\mathbf{1}, \tag{4.18}$$

where

$$\Theta(c_{\mathrm{R}}, c_{\mathrm{R0}}) \stackrel{\text{def}}{=} \frac{\Omega}{1 + \Omega(c_{\mathrm{R}} - c_{\mathrm{R0}})} = J^{s-1}\Omega. \tag{4.19}$$

4.6 Principle of virtual power. Balance of forces

We follow Gurtin et al. (2010) and Anand (2012) to derive macroscopic and microscopic force balances via the principle of virtual power. In developing our theory we take the "rate-like" kinematical descriptors to be $\dot{\boldsymbol{\chi}}$, $\dot{\mathbf{F}}^e$, $\dot{c}_{\mathrm{R}}$, $\dot{\lambda}_b$, and $\dot{d}$, and also the gradient $\nabla\dot{d}$. In exploiting the principle of virtual power we note that the rates $(\dot{\boldsymbol{\chi}}, \dot{\mathbf{F}}^e, \dot{c}_{\mathrm{R}})$ are not independent- they are constrained by eq. (4.18).

With each evolution of the body we associate macroscopic and microscopic force systems. The macroscopic system is defined by: (a) A traction $\mathbf{t}_{\mathrm{R}}(\mathbf{n}_{\mathrm{R}})$ that expends power over the velocity $\dot{\boldsymbol{\chi}}$. (b) A body force $\mathbf{b}_{\mathrm{R}}$ that also expends power over $\dot{\boldsymbol{\chi}}$. Regarding the body force, since time scales associated with the fluid diffusion are usually considerably longer than those associated with wave propagation, we neglect all inertial effects. (c) A stress $\mathbf{S}^e$ that expends power over the elastic distortion rate $\dot{\mathbf{F}}^e$.

The microscopic force system, which is non-standard, is defined by: (a) A scalar microscopic stress π that expend power over the rate $\dot{c}_{\mathrm{R}}$. (b) A scalar microscopic force f that expends power over the rate $\dot{\lambda}_b$. (c) A scalar microscopic stress ϖ that expends power over the rate $\dot{d}$. (d) A vector microscopic stress $\boldsymbol{\xi}$ that expends power over the gradient $\nabla\dot{d}$. (e) And a scalar microscopic traction $\xi(\mathbf{n}_{\mathrm{R}})$ that expends power over $\dot{d}$.

We characterize the force system through the manner in which these forces expend power. That is, given any part P, through the specification of $\mathcal{W}_{\text{ext}}(\mathrm{P})$, the power expended on P by material external to P, and $\mathcal{W}_{\text{int}}(\mathrm{P})$, a concomitant expenditure of power within P. Specifically,

$$\begin{aligned}\mathcal{W}_{\text{ext}}(\mathrm{P}) &= \int_{\partial \mathrm{P}} \mathbf{t}_{\mathrm{R}}(\mathbf{n}_{\mathrm{R}}) \cdot \dot{\boldsymbol{\chi}} \mathrm{d}a_{\mathrm{R}} + \int_{\mathrm{P}} \mathbf{b}_{\mathrm{R}} \cdot \dot{\boldsymbol{\chi}} \mathrm{d}v_{\mathrm{R}} + \int_{\partial \mathrm{P}} \xi(\mathbf{n}_{\mathrm{R}}) \dot{d}\, da_{\mathrm{R}}, \\ \mathcal{W}_{\text{int}}(\mathrm{P}) &= \int_{\mathrm{P}} \left(\mathbf{S}^e : \dot{\mathbf{F}}^e + \pi \dot{c}_{\mathrm{R}} + f \dot{\lambda}_b + \varpi \dot{d} + \boldsymbol{\xi} \cdot \nabla \dot{d} \right) \mathrm{d}v_{\mathrm{R}},\end{aligned} \tag{4.20}$$

where $\mathbf{S}^e$, π, f, ϖ, $\boldsymbol{\xi}$ are defined over the body for all time.

Assume that, at some arbitrarily chosen but *fixed time*, the fields $\boldsymbol{\chi}, \mathbf{F}, \mathbf{F}^e, c_{\mathrm{R}}, \lambda_b$, and d are known, and consider the fields $\dot{\boldsymbol{\chi}}, \dot{\mathbf{F}}^e, \dot{c}_{\mathrm{R}}, \dot{\lambda}_b$, and $\dot{d}$ are virtual velocities to be specified independently in a manner consistent with the constraint (4.18), i.e., denoting the virtual fields by $\tilde{\boldsymbol{\chi}}, \tilde{\mathbf{F}}^e, \tilde{c}_{\mathrm{R}}, \tilde{\lambda}_b$ and $\tilde{d}$ to differentiate them from fields asccociated with the actual evolution of the body, we require that

$$(\nabla \tilde{\boldsymbol{\chi}}) \mathbf{F}^{-1} = \tilde{\mathbf{F}}^e \mathbf{F}^{e-1} + \frac{1}{3} \Theta(c_{\mathrm{R}}, c_{\mathrm{R}0}) \tilde{c}_{\mathrm{R}} \mathbf{1}. \tag{4.21}$$

Further, we define a generalized virtual velocity to be a list

$$\mathcal{V} = (\tilde{\boldsymbol{\chi}}, \tilde{\mathbf{F}}^e, \tilde{c}_{\mathrm{R}}, \tilde{\lambda}_b, \tilde{d}), \tag{4.22}$$

consistent with (4.21). Also, we refer to a macroscopic virtual field $\mathcal{V}$ as rigid if it satisfies

$$(\nabla \tilde{\boldsymbol{\chi}}) = \tilde{\mathbf{F}} = \boldsymbol{\Omega} \mathbf{F} \qquad \text{together with} \qquad \tilde{\mathbf{F}} = \tilde{\mathbf{F}}^e, \qquad \tilde{c}_{\mathrm{R}} = 0, \qquad \tilde{\lambda}_b = 0, \qquad \tilde{d} = 0, \tag{4.23}$$

with $\boldsymbol{\Omega}$ a spatially constant skew tensor.

Writing

$$\begin{aligned}\mathcal{W}_{\text{ext}}(\mathrm{P}) &= \int_{\partial \mathrm{P}} \mathbf{t}_{\mathrm{R}}(\mathbf{n}_{\mathrm{R}}) \cdot \tilde{\boldsymbol{\chi}} \mathrm{d}a_{\mathrm{R}} + \int_{\mathrm{P}} \mathbf{b}_{\mathrm{R}} \cdot \tilde{\boldsymbol{\chi}} \mathrm{d}v_{\mathrm{R}} + \int_{\partial \mathrm{P}} \xi(\mathbf{n}_{\mathrm{R}}) \tilde{d}\, da_{\mathrm{R}}, \\ \mathcal{W}_{\text{int}}(\mathrm{P}) &= \int_{\mathrm{P}} \left(\mathbf{S}^e : \tilde{\mathbf{F}}^e + \pi \tilde{c}_{\mathrm{R}} + f \tilde{\lambda}_b + \varpi \tilde{d} + \boldsymbol{\xi} \cdot \nabla \tilde{d} \right) \mathrm{d}v_{\mathrm{R}},\end{aligned} \tag{4.24}$$

respectively, for the external and internal expenditures of virtual power, the principle of virtual power consists of two basic requirements:

(V1) Given any part P,

$$\mathcal{W}_{\text{ext}}(\mathrm{P}, \mathcal{V}) = \mathcal{W}_{\text{int}}(\mathrm{P}, \mathcal{V}) \quad \text{for all generalized virtual velocities } \mathcal{V}. \tag{4.25}$$

(V2) Given any part P and a rigid virtual velocity $\mathcal{V}$,

$$\mathcal{W}_{\text{int}}(\mathrm{P}, \mathcal{V}) = 0 \quad \text{whenever } \mathcal{V} \text{ is a rigid macroscopic virtual velocity.} \tag{4.26}$$

4.6.1 Consequences of the principle of virtual power

The virtual-power principle has the following consequences:

(a) The stress

$$\mathbf{T}_{\mathrm{R}} \stackrel{\mathrm{def}}{=} \mathbf{S}^e \mathbf{F}^{s-\mathsf{T}}, \tag{4.27}$$

is consistent with a macroscopic force balance and a macroscopic traction condition,

$$\mathrm{Div}\, \mathbf{T}_{\mathrm{R}} + \mathbf{b}_{\mathrm{R}} = \mathbf{0} \qquad \text{and} \qquad \mathbf{t}_{\mathrm{R}}(\mathbf{n}_{\mathrm{R}}) = \mathbf{T}_{\mathrm{R}} \mathbf{n}_{\mathrm{R}}, \tag{4.28}$$

and $\mathbf{T}_{\mathrm{R}} \mathbf{F}^{\mathsf{T}}$ is symmetric,

$$\mathbf{T}_{\mathrm{R}} \mathbf{F}^{\mathsf{T}} = \mathbf{F} \mathbf{T}_{\mathrm{R}}^{\mathsf{T}}. \tag{4.29}$$

In view of (4.28) and (4.29) the stress $\mathbf{T}_{\mathrm{R}}$ represents the classical Piola stress, with (4.28) and (4.29) representing the local macroscopic force and moment balances in the reference body.

As is standard, the Piola stress $\mathbf{T}_{\mathrm{R}}$ is related to the symmetric Cauchy stress $\mathbf{T}$ in the deformed body by

$$\mathbf{T}_{\mathrm{R}} = J \mathbf{T} \mathbf{F}^{-\mathsf{T}}, \tag{4.30}$$

so that

$$\mathbf{T} = J^{-1} \mathbf{T}_{\mathrm{R}} \mathbf{F}^{\mathsf{T}}. \tag{4.31}$$

It is convenient to introduce two new stress measures:

- The elastic second Piola stress,

$$\mathbf{T}^e \stackrel{\mathrm{def}}{=} J^e \mathbf{F}^{e-1} \mathbf{T} \mathbf{F}^{e-\mathsf{T}}, \tag{4.32}$$

  which is symmetric on account of the symmetry of the Cauchy stress $\mathbf{T}$.

- The Mandel stress,

$$\mathbf{M}^e \stackrel{\mathrm{def}}{=} \mathbf{C}^e \mathbf{T}^e = J^e \mathbf{F}^{e\mathsf{T}} \mathbf{T} \mathbf{F}^{e-\mathsf{T}}. \tag{4.33}$$

  which in general is not symmetric.

Using (4.27), (4.30), and (9.2) we find that

$$\mathbf{S}^e = J \mathbf{T} \mathbf{F}^{e-\mathsf{T}}. \tag{4.34}$$

Thus, using the definitions (9.44) and (9.45) we find that

$$\mathbf{F}^{e-1} \mathbf{S}^e = J^s \mathbf{T}^e, \quad \text{and} \quad \mathbf{F}^{e\mathsf{T}} \mathbf{S}^e = J^s \mathbf{M}^e. \tag{4.35}$$

(b) The microscopic force balance

$$\pi = \frac{1}{3} \Theta(c_{\mathrm{R}}, c_{\mathrm{R}0})\, J^s \mathrm{tr}\, \mathbf{M}^e = \Omega\left(\frac{1}{3} \mathrm{tr}\, \mathbf{M}^e\right), \tag{4.36}$$

where in writing the last of (4.36) we have used (4.19).

(c) The microstresses $\boldsymbol{\xi}$ and ϖ are consistent with the microforce balance and microtraction condition,

$$\text{Div}\,\boldsymbol{\xi} - \varpi = 0, \qquad \text{and} \qquad \xi(\mathbf{n}_{\mathrm{R}}) = \boldsymbol{\xi}\cdot\mathbf{n}_{\mathrm{R}}. \tag{4.37}$$

(d) The microscopic force f which is conjugate to $\dot{\lambda}_b$ satisfies,

$$f = 0. \tag{4.38}$$

The requirement that $f = 0$ implies that a variation of λ_b expends no internal power. At first blush it appears that the "microforce balance" (4.38) is devoid of physical content. However, it does have physical content, which is revealed later when we consider our thermodynamically consistent constitutive theory. As we shall see (4.38) will imply an internal constraint equation between λ_b and the right Cauchy-Green tensor $\mathbf{C}$ and other constitutive variables of the form $f(\mathbf{C}^e, C, \lambda_b, d, \nabla d) = 0$, which will serve as an implicit equation for determining λ_b in terms of the other constitutive variables.

Finally, using the traction conditions $(4.28)_2$ and $(9.59)_2$, the actual external expenditure of power is

$$\mathcal{W}_{\text{ext}}(\mathrm{P}) = \int_{\partial\mathrm{P}} (\mathbf{T}_{\mathrm{R}}\mathbf{n}_{\mathrm{R}})\cdot\dot{\boldsymbol{\chi}}\, da_{\mathrm{R}} + \int_{\mathrm{P}} \mathbf{b}_{\mathrm{R}}\cdot\dot{\boldsymbol{\chi}}\, dv_{\mathrm{R}} + \int_{\partial\mathrm{P}} (\boldsymbol{\xi}\cdot\mathbf{n}_{\mathrm{R}})\,\dot{d}\, da_{\mathrm{R}}. \tag{4.39}$$

Also, using $(9.47)_1$ and $(4.5)_2$ the stress power $\mathbf{S}^e : \dot{\mathbf{F}}^e$ may be alternatively written as

$$\mathbf{S}^e : \dot{\mathbf{F}}^e = (J^s\mathbf{T}^e) : (\mathbf{F}^{e\mathsf{T}}\dot{\mathbf{F}}^e) = \frac{1}{2}(J^s\mathbf{T}^e) : \dot{\mathbf{C}}^e. \tag{4.40}$$

Thus the corresponding internal expenditure of power may be written as

$$\mathcal{W}_{\text{int}}(\mathrm{P}) = \int_{\mathrm{P}} \left(\frac{1}{2}(J^s\mathbf{T}^e) : \dot{\mathbf{C}}^e + \pi\dot{c}_{\mathrm{R}} + f\dot{\lambda}_b + \varpi\dot{d} + \boldsymbol{\xi}\cdot\nabla\dot{d}\right) \mathrm{d}v_{\mathrm{R}}. \tag{4.41}$$

4.7 Free energy imbalance

Our discussion of thermodynamics involves the following fields: (i) ε_{R}, the internal energy density per unit reference volume; (ii) η_{R}, the entropy density per unit reference volume; (iii) $\mathbf{q}_{\mathrm{R}}$, the heat flux per unit reference area; (iv) q_{R}, the external heat supply per unit reference volume; (v) ϑ, the absolute temperature ($\vartheta > 0$); (vi) μ_{R}, the chemical potential, and follows the discussion of Gurtin (1996) and Gurtin et al. (2010, § 64).

Consider a material region P. Then, consistent with our omission of inertial effects, we neglect kinetic energy, and take the balance law for energy as,

$$\overline{\int_{\mathrm{P}} \varepsilon_{\mathrm{R}}\, dv_{\mathrm{R}}}^{\cdot} = -\int_{\partial \mathrm{P}} \mathbf{q}_{\mathrm{R}} \cdot \mathbf{n}_{\mathrm{R}}\, da_{\mathrm{R}} + \int_{\mathrm{P}} q_{\mathrm{R}}\, dv_{\mathrm{R}} + \mathcal{W}_{\mathrm{ext}}(\mathrm{P}) - \int_{\partial \mathrm{P}} \mu_{\mathrm{R}} \mathbf{j}_{\mathrm{R}} \cdot \mathbf{n}_{\mathrm{R}} da_{\mathrm{R}}, \tag{4.42}$$

where the last term in (4.42) represents the flux of energy carried into P by the flux $\mathbf{j}_{\mathrm{R}}$ of the diffusing fluid. Also, the second law takes the form of an entropy imbalance

$$\overline{\int_{\mathrm{P}} \eta_{\mathrm{R}}\, dv_{\mathrm{R}}}^{\cdot} \geq -\int_{\partial \mathrm{P}} \frac{\mathbf{q}_{\mathrm{R}} \cdot \mathbf{n}_{\mathrm{R}}}{\vartheta}\, da_{\mathrm{R}} + \int_{\mathrm{P}} \frac{q_{\mathrm{R}}}{\vartheta}\, dv_{\mathrm{R}}. \tag{4.43}$$

Assume now that isothermal conditions prevail, so that $\vartheta \equiv$ constant, and introduce the Helmholtz free energy per unit reference volume defined by $\psi_{\mathrm{R}} = \varepsilon_{\mathrm{R}} - \vartheta \eta_{\mathrm{R}}$. Then, upon multiplying the entropy imbalance (9.78) by ϑ and subtracting the result from the energy balance (4.42) yields the free energy imbalance

$$\overline{\int_{\mathrm{P}} \psi_{\mathrm{R}}\, dv_{\mathrm{R}}}^{\cdot} \leq \mathcal{W}_{\mathrm{ext}}(\mathrm{P}) - \int_{\partial \mathrm{P}} \mu_{\mathrm{R}} \mathbf{j}_{\mathrm{R}} \cdot \mathbf{n}_{\mathrm{R}} da_{\mathrm{R}}. \tag{4.44}$$

We henceforth restrict attention to isothermal processes and for that reason base the theory on the free energy imbalance (4.44).

Thus, since $\mathcal{W}_{\mathrm{ext}}(\mathrm{P}) = \mathcal{W}_{\mathrm{int}}(\mathrm{P})$, upon recalling (9.61) and applying the divergence theorem to the term in (4.44) involving an integral over the boundary $\partial \mathrm{P}$ of P, use of the balance law (4.15), and localizing the expression gives the following local form of the free energy imbalance,

$$\dot{\psi}_{\mathrm{R}} - \frac{1}{2}(J^s \mathbf{T}^e) : \dot{\mathbf{C}}^e - \mu_{\mathrm{R}}^{\mathrm{net}} \dot{c}_{\mathrm{R}} - f \dot{\lambda}_b - \varpi \dot{d} - \boldsymbol{\xi} \cdot \nabla \dot{d} + \mathbf{j}_{\mathrm{R}} \cdot \nabla \mu_{\mathrm{R}} \leq 0\,, \tag{4.45}$$

where we have written

$$\mu_{\mathrm{R}}^{\mathrm{net}} \stackrel{\mathrm{def}}{=} \mu_{\mathrm{R}} + \pi \tag{4.46}$$

for a net chemical potential.

For later use we define the dissipation density $\mathcal{D} \geq 0$ per unit volume per unit time by

$$\mathcal{D} = \frac{1}{2}(J^s \mathbf{T}^e) : \dot{\mathbf{C}}^e + \mu_{\mathrm{R}}^{\mathrm{net}} \dot{c}_{\mathrm{R}} + f \dot{\lambda}_b + \varpi \dot{d} + \boldsymbol{\xi} \cdot \nabla \dot{d} - \mathbf{j}_{\mathrm{R}} \cdot \nabla \mu_{\mathrm{R}} - \dot{\psi}_{\mathrm{R}} \geq 0. \tag{4.47}$$

Remark. For brevity we have not discussed the transformation properties under a change in frame of the various fields appearing in our theory. Here, we simply note that all quantities in the free energy imbalance (4.45) are invariant under a change in frame (Gurtin et al., 2010). □

4.8 Constitutive theory

Let $\mathbf{\Lambda}$ represent the list

$$\mathbf{\Lambda} = \{\mathbf{C}^e, c_{\mathrm{R}}, \lambda_b\,, d, \nabla d\}. \tag{4.48}$$

Guided by(4.45), we beginning by assuming constitutive equations for the free energy ψ_{R}, the stress $\mathbf{T}^e$, and the net chemical potential $\mu_{\mathrm{R}}^{\mathrm{net}}$ are given by the constitutive equations

$$\psi_{\mathrm{R}} = \hat{\psi}_{\mathrm{R}}(\mathbf{\Lambda}), \qquad \mathbf{T}^e = \hat{\mathbf{T}}^e(\mathbf{\Lambda}), \qquad \mu_{\mathrm{R}}^{\mathrm{net}} = \hat{\mu}_{\mathrm{R}}^{\mathrm{net}}(\mathbf{\Lambda}), \tag{4.49}$$

Then,

$$\dot{\psi}_{\mathrm{R}} = \frac{\partial\hat{\psi}_{\mathrm{R}}(\mathbf{\Lambda})}{\partial\mathbf{C}^e} : \dot{\mathbf{C}}^e + \frac{\partial\hat{\psi}_{\mathrm{R}}(\mathbf{\Lambda})}{\partial C}\dot{c}_{\mathrm{R}} + \frac{\partial\hat{\psi}_{\mathrm{R}}(\mathbf{\Lambda})}{\partial\lambda_b}\dot{\lambda}_b + \frac{\partial\hat{\psi}_{\mathrm{R}}(\mathbf{\Lambda})}{\partial d}\dot{d} + \frac{\partial\hat{\psi}_{\mathrm{R}}(\mathbf{\Lambda})}{\partial\nabla d}\cdot\nabla\dot{d}. \tag{4.50}$$

Using (4.50) and substituting the constitutive equations (4.49) into the free-energy imbalance (4.45), we find that it may then be written as

$$\begin{aligned}&\left[\frac{\partial\hat{\psi}_{\mathrm{R}}(\mathbf{\Lambda})}{\partial\mathbf{C}^e} - \frac{1}{2}J^s\hat{\mathbf{T}}^e(\mathbf{\Lambda})\right] : \dot{\mathbf{C}}^e + \left[\frac{\partial\hat{\psi}_{\mathrm{R}}(\mathbf{\Lambda})}{\partial C} - \hat{\mu}_{\mathrm{R}}^{\mathrm{net}}(\mathbf{\Lambda})\right]\dot{c}_{\mathrm{R}}\\ &+ \left[\frac{\partial\hat{\psi}_{\mathrm{R}}(\mathbf{\Lambda})}{\partial\lambda_b} - \hat{f}(\mathbf{\Lambda})\right]\dot{\lambda}_b + \left[\frac{\partial\hat{\psi}_{\mathrm{R}}(\mathbf{\Lambda})}{\partial d} - \varpi\right]\dot{d} + \left[\frac{\partial\hat{\psi}_{\mathrm{R}}(\mathbf{\Lambda})}{\partial\nabla d} - \boldsymbol{\xi}\right]\cdot\nabla\dot{d} + \mathbf{j}_{\mathrm{R}}\cdot\nabla\mu_{\mathrm{R}} \leq 0.\end{aligned} \tag{4.51}$$

We assume, constitutively, that the free-energy delivers the stress $\mathbf{T}^e$ and the net chemical potential through the state relations

$$\mathbf{T}^e = 2J^{s-1}\frac{\partial\hat{\psi}_{\mathrm{R}}(\mathbf{\Lambda})}{\partial\mathbf{C}^e}, \qquad \text{and} \qquad \mu_{\mathrm{R}}^{\mathrm{net}} = \frac{\partial\hat{\psi}_{\mathrm{R}}(\mathbf{\Lambda})}{\partial c_{\mathrm{R}}}. \tag{4.52}$$

Further, we introduce an energetic microforce f_{en}, and energetic microstresses ϖ_{en} and $\boldsymbol{\xi}_{\mathrm{en}}$ through

$$f_{\mathrm{en}} \stackrel{\mathrm{def}}{=} \frac{\partial\hat{\psi}_{\mathrm{R}}(\mathbf{\Lambda})}{\partial\lambda_b}, \qquad \varpi_{\mathrm{en}} \stackrel{\mathrm{def}}{=} \frac{\partial\hat{\psi}_{\mathrm{R}}(\mathbf{\Lambda})}{\partial d}, \qquad \boldsymbol{\xi}_{\mathrm{en}} \stackrel{\mathrm{def}}{=} \frac{\partial\hat{\psi}_{\mathrm{R}}(\mathbf{\Lambda})}{\partial\nabla d}, \tag{4.53}$$

respectively, and guided by (4.51) also introduce a dissipative microforce f_{dis}, and dissipative microstresses ϖ_{dis} and $\boldsymbol{\xi}_{\mathrm{dis}}$ through

$$f_{\mathrm{dis}} \stackrel{\mathrm{def}}{=} f - f_{\mathrm{en}}, \qquad \varpi_{\mathrm{dis}} \stackrel{\mathrm{def}}{=} \varpi - \varpi_{\mathrm{en}}, \qquad \boldsymbol{\xi}_{\mathrm{dis}} \stackrel{\mathrm{def}}{=} \boldsymbol{\xi} - \boldsymbol{\xi}_{\mathrm{en}}. \tag{4.54}$$

Using (4.52), (4.53) and (4.54), leads to the following reduced dissipation inequality

$$\mathcal{D} = f_{\mathrm{dis}}\,\dot{\lambda}_b + \varpi_{\mathrm{dis}}\,\dot{d} + \boldsymbol{\xi}_{\mathrm{dis}}\cdot\nabla\dot{d} - \mathbf{j}_{\mathrm{R}}\cdot\nabla\mu_{\mathrm{R}} \geq 0. \tag{4.55}$$

Next, we assume that the vector microstress $\boldsymbol{\xi}$ is purely energetic so that

$$\boldsymbol{\xi}_{\text{dis}} = \mathbf{0}. \tag{4.56}$$

Further, in order to satisfy (9.213) we assume that each of the terms separately satisfy dissipation inequalities of the form,

$$\begin{aligned} f_{\text{dis}}\,\dot{\lambda}_b > 0 \quad &\text{for} \quad \dot{\lambda}_b > 0, \\ \varpi_{\text{dis}}\,\dot{d} > 0 \quad &\text{for} \quad \dot{d} > 0, \\ -\mathbf{j}_{\text{R}} \cdot \nabla\mu_{\text{R}} > 0 \quad &\text{for} \quad \nabla\mu_{\text{R}} \neq \mathbf{0}. \end{aligned} \tag{4.57}$$

Next, we assume that ϖ_{diss} is given by

$$\varpi_{\text{diss}} = \alpha + \zeta\,\dot{d}, \qquad \text{with} \qquad \alpha = \hat{\alpha}(\boldsymbol{\Lambda}) > 0 \quad \text{and} \quad \zeta = \hat{\zeta}_{\text{dam}}(\boldsymbol{\Lambda}) > 0, \tag{4.58}$$

so that the dissipation inequality $(4.57)_1$ is satisfied, in the sense that

$$\left(\alpha + \zeta\,\dot{d}\right)\dot{d} > 0 \quad \text{whenever} \quad \dot{d} > 0. \tag{4.59}$$

Further, we assume that f_{dis} is given by

$$f_{\text{dis}} = \kappa_b\,\dot{\lambda}_b, \qquad \text{with} \qquad \kappa_b = \hat{\kappa}_b(\boldsymbol{\Lambda}) > 0, \tag{4.60}$$

so that the dissipation inequality $(4.57)_2$ is satisfied, in the sense that

$$\left(\kappa_b\,\dot{\lambda}_b\right)\dot{\lambda}_b > 0 \quad \text{whenever} \quad \dot{\lambda}_b > 0. \tag{4.61}$$

Thus summarizing, from the equations above we have the following thermodynamically-consistent constitutive equations for the microforce f and the microstresses ϖ and $\boldsymbol{\xi}$:

$$f = \frac{\partial\hat{\psi}_{\text{R}}(\boldsymbol{\Lambda})}{\partial\lambda_b} + \hat{\kappa}_b(\boldsymbol{\Lambda})\,\dot{\lambda}_b, \qquad \varpi = \frac{\partial\hat{\psi}_{\text{R}}(\boldsymbol{\Lambda})}{\partial d} + \hat{\alpha}(\boldsymbol{\Lambda}) + \hat{\zeta}(\boldsymbol{\Lambda})\,\dot{d}, \qquad \boldsymbol{\xi} = \frac{\partial\hat{\psi}_{\text{R}}(\boldsymbol{\Lambda})}{\partial\nabla d}. \tag{4.62}$$

Finally, we assume that the the fluid flux $\mathbf{j}_{\text{R}}$ obeys a Fick-type relation in the sense that the fluid flux $\mathbf{j}_{\text{R}}$ depends linearly on the gradient of the chemical potential,

$$\mathbf{j}_{\text{R}} = -\mathbf{M}(\boldsymbol{\Lambda})\,\nabla\mu_{\text{R}}, \tag{4.63}$$

where $\mathbf{M}$ is a mobility tensor. Note that on account of $(4.57)_2$, the mobility tensor is positive definite.

4.9 Chemical potential

The microforce balance (4.36), when combined with the thermodynamically consistent constitutive equation $(4.52)_2$, together with the definition (4.46) of $\mu_{\mathrm{R}}^{\mathrm{net}}$, gives the following important expression for the chemical potential in the theory,

$$\mu_{\mathrm{R}} = \frac{\partial \hat{\psi}_{\mathrm{R}}(\mathbf{\Lambda})}{\partial C} - \Omega \left(\frac{1}{3} \mathrm{tr} \mathbf{M}^e \right) . \tag{4.64}$$

4.10 Evolution equation for the bond stretch

The microforce balance (4.38), viz.

$$f = 0, \tag{4.65}$$

together with the constitutive equation $(4.62)_1$ gives the important thermodynamically-consistent Ginzburg-Landau-type equation,

$$\hat{\kappa}_b(\mathbf{\Lambda})\, \dot{\lambda}_b = -\frac{\partial \hat{\psi}_{\mathrm{R}}(\mathbf{\Lambda})}{\partial \lambda_b}, \tag{4.66}$$

which serves as an evolution equation for λ_b.

4.11 Evolution equation for the damage variable

The microforce balance (9.59), viz.

$$\mathrm{Div}\, \boldsymbol{\xi} - \varpi = 0, \tag{4.67}$$

together with the constitutive equations $(4.62)_{2,3}$ gives the evolution equation for the damage variable d as

$$\begin{aligned} &\hat{\zeta}(\mathbf{\Lambda}) \dot{d} = F(\mathbf{\Lambda}) \qquad \text{for} \qquad \dot{d} > 0, \\ &\text{where} \quad F(\mathbf{\Lambda}) \stackrel{\text{def}}{=} \left[-\frac{\partial \hat{\psi}_{\mathrm{R}}(\mathbf{\Lambda})}{\partial d} + \mathrm{Div} \left(\frac{\partial \hat{\psi}_{\mathrm{R}}(\mathbf{\Lambda})}{\partial \nabla d} \right) \right] - \hat{\alpha}(\mathbf{\Lambda}). \end{aligned} \tag{4.68}$$

Since ζ is positive-valued, F must be positive for $\dot{d}$ to be positive, and the damage to increase.

4.12 Boundary and initial conditions

We also need boundary and initial conditions to complete the theory.

1. **Boundary conditions for the partial differential equation (pde) governing the evolution of the motion $\boldsymbol{\chi}$:**

   Let $\mathcal{S}_{\boldsymbol{\chi}}$ and $\mathcal{S}_{\mathbf{t}_\mathrm{R}}$ be complementary subsurfaces of the boundary $\partial\mathrm{B}$ of the body B. Then for a time interval $t \in [0,T]$ we consider a pair of boundary conditions in which the motion is specified on $\mathcal{S}_{\boldsymbol{\chi}}$ and the surface traction on $\mathcal{S}_{\mathbf{t}_\mathrm{R}}$:

   $$\boldsymbol{\chi} = \breve{\boldsymbol{\chi}} \quad \text{on } \mathcal{S}_{\boldsymbol{\chi}} \times [0,T], \qquad \text{and} \qquad \mathbf{T}_\mathrm{R}\mathbf{n}_\mathrm{R} = \breve{\mathbf{t}}_\mathrm{R} \quad \text{on } \mathcal{S}_{\mathbf{t}_\mathrm{R}} \times [0,T], \tag{4.69}$$

   where $\breve{\boldsymbol{\chi}}$ and $\breve{\mathbf{t}}_\mathrm{R}$ are prescribed functions of $\mathbf{X}$ and t.

2. **Boundary conditions for the pde governing the evolution of μ_R:**

   Using (4.63) and (4.64) the balance equation (4.15) for C may be stated as a balance equation for the chemical potential μ_R. Let $\mathcal{S}_{\mu_\mathrm{R}}$ and $\mathcal{S}_{\mathbf{j}_\mathrm{R}}$ be complementary subsurfaces of the boundary $\partial\mathrm{B}$ of the body B. Then for a time interval $t \in [0,T]$ we consider a pair of boundary conditions in which the chemical potential is specified on $\mathcal{S}_{\mu_\mathrm{R}}$ and the fluid flux on $\mathcal{S}_{\mathbf{j}_\mathrm{R}}$:

   $$\mu_\mathrm{R} = \breve{\mu}_\mathrm{R} \quad \text{on } \mathcal{S}_{\mu_\mathrm{R}} \times [0,T], \qquad \text{and} \qquad \mathbf{j}_\mathrm{R} \cdot \mathbf{n}_\mathrm{R} = \breve{j}_\mathrm{R} \quad \text{on } \mathcal{S}_{\mathbf{j}_\mathrm{R}} \times [0,T], \tag{4.70}$$

   where $\breve{\mu}_\mathrm{R}$ and $\breve{j}_\mathrm{R}$ are prescribed functions of $\mathbf{X}$ and t.

3. **Boundary conditions for the pde governing the evolution of d:**

   The presence of microscopic stresses $\boldsymbol{\xi}$ results in an expenditure of power

   $$\int_{\partial\mathrm{B}} (\boldsymbol{\xi} \cdot \mathbf{n}_\mathrm{R}) \dot{d} \, \mathrm{d}a_\mathrm{R}$$

   by the material in contact with the body, and this necessitates a consideration of boundary conditions on $\partial\mathrm{B}$ involving the microscopic tractions $\boldsymbol{\xi} \cdot \mathbf{n}_\mathrm{R}$ and the rate of change of the damage variable $\dot{d}$.

   - We restrict attention to the simplest set of boundary conditions that result in a null expenditure of microscopic power in the sense that $(\boldsymbol{\xi} \cdot \mathbf{n}_\mathrm{R})\dot{d} = 0$.

   A set of boundary conditions which satisfies this requirement is,

   $$\dot{d} = 0 \quad \text{on } \mathcal{S}_d \times [0,T], \qquad \text{and} \qquad \boldsymbol{\xi} \cdot \mathbf{n}_\mathrm{R} = 0 \quad \text{on } \partial\mathrm{B} \setminus \mathcal{S}_d \times [0,T], \tag{4.71}$$

   with the microforce $\boldsymbol{\xi}$ given by $(4.62)_3$.

The initial conditions for the motion, chemical potential, and damage are taken as,

$$\boldsymbol{\chi}(\mathbf{X},0) = \mathbf{X}, \quad \mu_\mathrm{R}(\mathbf{X},0) = \mu_{\mathrm{R}0}(\mathbf{X}) \quad \text{and} \quad d(\mathbf{X},0) = 0. \quad \text{in} \quad \mathrm{B}. \tag{4.72}$$

4.13 Specialization of the constitutive equations

4.13.1 Specialized form for the free energy ψ_{R}

Specialized form for the free energy with no bond stretch and no damage

We begin by recalling and extending a set of specialized equations proposed by Chester and Anand for an elastomeric gel in which there are no energetic effects due to bond-stretch and there is no damage (Chester and Anand, 2010, 2011). Limiting our considerations to isotropic materials under isothermal conditions, we begin by assuming that the free energy ψ_{R} may be written in a separable form as

$$\tilde{\psi}_{\mathrm{R}}(\mathcal{I}_{\mathbf{C}^e}, c_{\mathrm{R}}, \vartheta) = \mu^0_{\mathrm{R}} c_{\mathrm{R}} + \psi^{\mathrm{mix}}_{\mathrm{R}}(c_{\mathrm{R}}, \vartheta) + \psi^{\mathrm{mech}}_{\mathrm{R}}(\mathcal{I}_{\mathbf{C}^e}, c_{\mathrm{R}}, \vartheta), \tag{4.73}$$

where $\mathcal{I}_{\mathbf{C}^e}$ are the principal invariants of $\mathbf{C}^e$, μ^0_{R} is the chemical potential of the unmixed pure solvent, $\psi^{\mathrm{mix}}_{\mathrm{R}}(c_{\mathrm{R}}, \vartheta)$ is the change in free energy due to mixing of the solvent with the polymer network, $\psi^{\mathrm{mech}}_{\mathrm{R}}(\mathcal{I}_{\mathbf{C}^e}, c_{\mathrm{R}}, \vartheta)$ is the contribution to the change in the free energy due to the deformation of the polymer network.

Polymer volume fraction

In the literature on swelling of elastomers, the quantity

$$\phi \stackrel{\mathrm{def}}{=} \frac{1 - \Omega c_{\mathrm{R}0}}{1 + \upsilon c_{\mathrm{R}}} = (1 - \Omega c_{\mathrm{R}0})(\lambda^s)^{-3} = (1 - \Omega c_{\mathrm{R}0}) J^{s-1}, \tag{4.74}$$

is called the polymer volume fraction, with $\phi_0 \stackrel{\mathrm{def}}{=} 1 - \Omega c_{\mathrm{R}0}$ the initial volume fraction of the polymer. If the elastomer is dry, that is $c_{\mathrm{R}0} = 0$, then $\phi_0 = 1$.[2]

Estimate for $\psi^{\mathrm{mix}}_{\mathrm{R}}$

Next, we adopt the following classical from of the theory for the contribution to the free energy due to mixing (Flory, 1942; Huggins, 1942; Flory and Rehner, 1943),

$$\psi^{\mathrm{mix}}_{\mathrm{R}} = \frac{R\vartheta}{\Omega}\left[\frac{\phi_0}{\phi}\Big((1-\phi)\ln(1-\phi) + \chi\phi(1-\phi)\Big)\right], \tag{4.75}$$

where R is the universal gas constant, and χ is a dimensionless parameter (called the χ-parameter, or Flory-Huggins interaction parameter), which represents the dis-affinity between the polymer and the fluid:

- a low value of χ favors swelling, while a high value of χ favours de-swelling.

[2]Note that while C is positive, it has no upper bound. However, the polymer volume fraction is constrained to lie in the range $\phi \in [0, 1]$; this is a useful feature of ϕ in numerical computations.

Estimate for $\psi_{\mathrm{R}}^{\mathrm{mech}}$

In elastomeric materials, the major part of $\psi_{\mathrm{R}}^{\mathrm{mech}}$ arises from an entropic contribution. Let

$$\bar{\lambda} \stackrel{\text{def}}{=} \frac{1}{\sqrt{3}}\sqrt{\mathrm{tr}\,\mathbf{C}} = \frac{1}{\sqrt{3}}\sqrt{(\mathrm{tr}\,\mathbf{C}^e)(1+\Omega c_{\mathrm{R}})^{2/3}} \tag{4.76}$$

define an effective total stretch. If we introduce an effective elastic stretch by

$$\bar{\lambda}^e \stackrel{\text{def}}{=} \frac{1}{\sqrt{3}}\sqrt{\mathrm{tr}\,\mathbf{C}^e}, \tag{4.77}$$

then recalling (4.17), the effective total stretch is given by the product of the swelling stretch and the effective elastic stretch,

$$\bar{\lambda} = \bar{\lambda}^e \lambda^s. \tag{4.78}$$

The classical statistical-mechanical models of rubber elasticity which use non-Gaussian statistics to account for the limited extensibility of the polymer chains, provide the following estimates for the entropy change due to mechanical stretching (cf., e.g., Treloar, 1975; Arruda and Boyce, 1993),

$$\eta_{\mathrm{R}}^{\mathrm{mech}} = -Nk_B n\left[\left(\frac{\bar{\lambda}}{\sqrt{n}}\right)\beta + \ln\left(\frac{\beta}{\sinh\beta}\right)\right] + Nk_B\left(\frac{\sqrt{n}}{3}\beta_0\right)\ln J, \tag{4.79}$$

with k_B Boltzmann's constant,

$$\beta \stackrel{\text{def}}{=} \mathcal{L}^{-1}\left(\frac{\bar{\lambda}}{\sqrt{n}}\right), \qquad \text{and} \qquad \beta_0 \stackrel{\text{def}}{=} \mathcal{L}^{-1}\left(\frac{1}{\sqrt{n}}\right), \tag{4.80}$$

where $\mathcal{L}^{-1}$ is the inverse of the Langevin function $\mathcal{L}(x) = \coth(x) - (x)^{-1}$. This functional form for the change in entropy involves two material parameters: (i) N, the number of polymer chains per unit reference volume, and (ii) n the number of links in a freely-jointed chain.

To account for the interaction between the polymer chains and to account for a slight compressibility of the gel, Chester and Anand (2011) also introduced an energetic component,

$$\varepsilon_{\mathrm{Rvol}} = \hat{\varepsilon}_{\mathrm{Rvol}}(J^e), \tag{4.81}$$

to the free energy.

Then, using (4.79), (4.79), and (4.81), we obtain the estimate

$$\begin{aligned}\psi_{\mathrm{R}}^{\mathrm{mech}}(\mathcal{I}_{\mathbf{C}^e}, c_{\mathrm{R}}, \vartheta) =& (Nk_B\vartheta)\, n\left[\left(\frac{\bar{\lambda}}{\sqrt{n}}\right)\beta + \ln\left(\frac{\beta}{\sinh\beta}\right)\right] - (Nk_B\vartheta)\left(\frac{\sqrt{n}}{3}\beta_0\right)\ln J \\ &+ \hat{\varepsilon}_{\mathrm{Rvol}}(J^e),\end{aligned} \tag{4.82}$$

with $\bar{\lambda}$ defined in (4.76).

Thus, using (4.75) and (4.82) in (4.73), a particular form of the free energy function which accounts for the combined effects of mixing, swelling, and elastic stretching proposed by Chester and Anand (2010, 2011) is

$$\begin{aligned}\psi_{\mathrm{R}} = \mu_{\mathrm{R}}^{0} c_{\mathrm{R}} + \frac{R\vartheta}{\Omega}\left[\frac{\phi_0}{\phi}\Big((1-\phi)\ln(1-\phi) + \chi\phi(1-\phi)\Big)\right] \\ + (Nk_B\vartheta)\, n\left[\left(\frac{\bar{\lambda}}{\sqrt{n}}\right)\beta + \ln\left(\frac{\beta}{\sinh\beta}\right)\right] - (Nk_B\vartheta)\left(\frac{\sqrt{n}}{3}\beta_0\right)\ln J + \hat{\varepsilon}_{\mathrm{Rvol}}(J^e).\end{aligned} \tag{4.83}$$

Specialized form for the free energy accounting for bond stretch

In a recent paper Mao et al. (2017b) proposed a model for both deformation and fracture of elastomeric materials; their model is consistent with Arruda-Boyce model for deformation of elastomers (Arruda and Boyce, 1993), and the Lake-Thomas proposal for fracture of elastomers due to the scission of the Kuhn segments of polymer chains (Lake and Thomas, 1967).

Consider a single polymer chain. The essential idea in the paper by Mao et al. (2017b) is to assume that the Kuhn segments in a polymer chain are not rigid but is stretchable. Thus, let

$$\lambda_b \text{ denote the stretch of a Kuhn segment,}$$

and for simplicity assume that each Kuhn segment in a chain stretches by the same amount. Every stretchable Kuhn segment can store an internal energy, which we denote by

$$\varepsilon_b = \hat{\varepsilon}_b(\lambda_b). \tag{4.84}$$

Under this assumption the change in entropy η of a chain has the same form as given by the classical inverse-Langevin formula, but instead of a constant Kuhn segment length L, the Kuhn segment length is

$$l_b = \lambda_b L_b,$$

and the expression for the change in entropy of a single chain according to the Langevin statistics becomes,

$$\eta = -n\, k_B\left[\left(\frac{\lambda\lambda_b^{-1}}{\sqrt{n}}\right)\beta + \ln\left(\frac{\beta}{\sinh\beta}\right)\right] \qquad \text{with} \qquad \beta = \mathcal{L}^{-1}\left(\frac{\lambda\lambda_b{}^{-1}}{\sqrt{n}}\right), \tag{4.85}$$

where n is the number of Kuhn segments in a chain, and where λ is the overall stretch of the polymer chain. Using (4.84) and (4.85), the free energy a single chain with stretchable Kuhn segments is then given by

$$\psi = n\hat{\varepsilon}_b(\lambda_b) + nk_B\vartheta\left[\left(\frac{\lambda\lambda_b^{-1}}{\sqrt{n}}\right)\beta + \ln\left(\frac{\beta}{\sinh\beta}\right)\right]. \tag{4.86}$$

Next we generalize this free energy expression for a single polymer chain to a network of chains in an elastomeric gel. Assuming inextensible, strong, covalent crosslinking bonds between the chains, straightforward considerations give the following modification of (4.83):

$$\begin{aligned}\psi_{\mathrm{R}} = \mu_{\mathrm{R}}^{0} c_{\mathrm{R}} + \frac{R\vartheta}{\Omega}\left[\frac{\phi_0}{\phi}\Big((1-\phi)\ln(1-\phi) + \chi\phi(1-\phi)\Big)\right] \\ + (Nk_B\vartheta)\, n\left[\left(\frac{\bar{\lambda}\lambda_b^{-1}}{\sqrt{n}}\right)\beta + \ln\left(\frac{\beta}{\sinh\beta}\right)\right] - (Nk_B\vartheta)\left(\frac{\sqrt{n}}{3\lambda_b}\beta_0\right)\ln J \\ + \Big(Nn\hat{\varepsilon}_b(\lambda_b) + \hat{\varepsilon}_{\mathrm{Rvol}}(J^e)\Big),\end{aligned} \tag{4.87}$$

with

$$\beta \stackrel{\text{def}}{=} \mathcal{L}^{-1}\left(\frac{\bar{\lambda}\lambda_b^{-1}}{\sqrt{n}}\right), \qquad \text{and} \qquad \beta_0 \stackrel{\text{def}}{=} \mathcal{L}^{-1}\left(\frac{\lambda_b^{-1}}{\sqrt{n}}\right). \tag{4.88}$$

Note that in (4.87) and (4.88) it is the modified stretch-measure $(\bar{\lambda}\lambda_b^{-1})$ which gives rise to changes in the entropy of the network.

Let

$$\varepsilon_{\mathrm{R}} = Nn\hat{\varepsilon}_b(\lambda_b) \tag{4.89}$$

denote the internal energy density of an elastomeric network due to bond stretching. Further, let λ_b^f denote a critical value of bond stretch when a Kuhn segment fails, and denote the corresponding value of the dissociation energy for a single Kuhn segment by

$$\varepsilon_b^f \stackrel{\text{def}}{=} \hat{\varepsilon}_b(\lambda_b^f). \tag{4.90}$$

Then, as a simple criterion for failure of a "material point" of an elastomeric network due to chain-scission, Mao et al. (2017b) proposed that failure occurs when $\varepsilon_{\mathrm{R}} = \varepsilon_{\mathrm{R}}^f$, where

$$\varepsilon_{\mathrm{R}}^f \stackrel{\text{def}}{=} Nn\varepsilon_b^f \tag{4.91}$$

represents the energy of per unit volume when all Kuhn segments in a network at a "material point" are broken.

Remark. This failure criterion of Mao et al. (2017b) essentially assumes that all Kuhn segments are uniformly stretched and that they all fail simultaneously. This is a significant assumption, because at the microscopic level the chains are subject to thermal fluctuations and one expects that such fluctuations will lead to failure of a single bond rather than all the bonds simultaneously. However, to construct a simple and tractable model of failure at the macroscopic level, we neglect such complications arising from thermal fluctuations, and adopt the failure criterion of Mao et al. (2017b); we argue for its plausibility on the grounds that the binding energy of backbone units of typical polymers is large in comparison to the average thermal energy at room temperature. □

Specialized form for the free energy accounting for bond stretch and damage

We account for damage by using the field $d \in [0,1]$ and modify the free-energy function (4.87) to read as,

$$\begin{aligned}\psi_{\mathrm{R}} = \mu_{\mathrm{R}}^0 c_{\mathrm{R}} + \frac{R\vartheta}{\Omega}\left[\frac{\phi_0}{\phi}\Big((1-\phi)\ln(1-\phi)+\chi\phi(1-\phi)\Big)\right] \\ + (Nk_B\vartheta)\,n\left[\left(\frac{\bar{\lambda}\lambda_b^{-1}}{\sqrt{n}}\right)\beta + \ln\left(\frac{\beta}{\sinh\beta}\right)\right] - (Nk_B\vartheta)\left(\frac{\sqrt{n}}{3\lambda_b}\beta_0\right)\ln J \\ + g(d)\underbrace{\Big(Nn\hat{\varepsilon}_b(\lambda_b) + \hat{\varepsilon}_{\mathrm{Rvol}}(J^e)\Big)}_{\equiv\hat{\varepsilon}_{\mathrm{R}}^0(\lambda_b,J^e)} + \hat{\varepsilon}_{\mathrm{R,nonloc}}(\nabla d).\end{aligned} \tag{4.92}$$

As particular forms for the functions $\hat{\varepsilon}_b(\lambda_b)$ and $\hat{\varepsilon}_{\mathrm{Rvol}}(J^e)$ we choose the simple energies,

$$\hat{\varepsilon}_b(\lambda_b) = \frac{1}{2}E_b(\lambda_b-1)^2, \qquad \hat{\varepsilon}_{\mathrm{Rvol}}(J^e) = \frac{K}{8}(J^e - J^{e-1})^2, \tag{4.93}$$

where $E_b > 0$ denote the stiffness of a Kuhn segment, $K > 0$ a bulk modulus for intermolecular interactions.

Remark. In our finite element simulations we encountered some convergence difficulties with the simple quadratic form,

$$\hat{\varepsilon}_{\mathrm{Rvol}}(J^e) = \frac{1}{2}K(J^e-1)^2,$$

of the volumetric internal energy at late stages of the damage. Accordingly, in our computations we have used the alternate form $(4.93)_2$ which reduces to a simple quadratic energy as $J^e \to 1$,

$$\hat{\varepsilon}_{\mathrm{Rvol}}(J^e) = \frac{K}{8}(J^e - J^{e-1})^2 = \frac{K}{8}(J^e-1)^2\left(1+\frac{1}{J^e}\right)^2 \approx \frac{1}{2}K(J^e-1)^2. \tag{4.94}$$

If for some numerical reason J^e becomes large during the iteration process, then the particular form $(4.93)_2$ leads to a softer response (see Schröder and Neff, 2003). The particular form of the volumetric internal energy is not crucial for elastomeric gels in which the volume changes due to elastic deformation are typically quite small relative to distortional deformations. □

Thus, denoting the undamaged part of the internal energy in (4.92) by $\hat{\varepsilon}_{\mathrm{R}}^0(\lambda_b, J^e)$, we have

$$\hat{\varepsilon}_{\mathrm{R}}^0(\lambda_b, J^e) = \frac{1}{2}\bar{E}_b(\lambda_b-1)^2 + \frac{K}{8}(J^e - J^{e-1})^2, \tag{4.95}$$

where we have introduced the notation,

$$\bar{E}_b \stackrel{\text{def}}{=} NnE_b, \tag{4.96}$$

for a macroscopic measure of bond-stiffness.

The function $g(d)$ describes the degradation of the internal energy storage capacity of the material, with the properties

$$g(0) = 1, \quad g(1) = 0, \quad \text{and} \quad g'(1) = 0. \tag{4.97}$$

A widely-used degradation function is

$$g(d) = (1-d)^2; \tag{4.98}$$

we adopt it here.

The term $\hat{\varepsilon}_{\text{R,nonloc}}(\nabla d)$ in the internal energy density is the nonlocal contribution

$$\hat{\varepsilon}_{\text{R,nonloc}}(\nabla d) = \frac{1}{2}\,\varepsilon_{\text{R}}^{f}\,\ell^2\,|\nabla d|^2\,, \tag{4.99}$$

with $\varepsilon_{\text{R}}^{f}$ the macroscopic bond failure energy defined in (5.32). Also the parameter ℓ represents an intrinsic material length scale in our gradient damage theory for elastomeric gels.

With these specializations, and writing

$$G_0 \stackrel{\text{def}}{=} Nk_B\vartheta, \tag{4.100}$$

for a ground-state shear modulus, the expression for the free energy may be written as

$$\begin{aligned}\psi_{\text{R}} = {}& \mu_{\text{R}}^0 c_{\text{R}} + \frac{R\vartheta}{\Omega}\left[\frac{\phi_0}{\phi}\Big((1-\phi)\ln(1-\phi) + \chi\phi(1-\phi)\Big)\right] \\ & + G_0\, n\left[\left(\frac{\bar{\lambda}\lambda_b^{-1}}{\sqrt{n}}\right)\beta + \ln\left(\frac{\beta}{\sinh\beta}\right) - \left(\frac{1}{3\lambda_b\sqrt{n}}\beta_0\right)\ln J\right] \\ & + (1-d)^2\underbrace{\left(\frac{1}{2}\bar{E}_b(\lambda_b-1)^2 + \tfrac{K}{8}(J^e - J^{e-1})^2\right)}_{\equiv\hat{\varepsilon}_{\text{R}}^0(\lambda_b, J^e)} + \frac{1}{2}\,\varepsilon_{\text{R}}^{f}\,\ell^2\,|\nabla d|^2\,,\end{aligned} \tag{4.101}$$

with

$$\beta \stackrel{\text{def}}{=} \mathcal{L}^{-1}\left(\frac{\bar{\lambda}\lambda_b^{-1}}{\sqrt{n}}\right), \qquad \text{and} \qquad \beta_0 \stackrel{\text{def}}{=} \mathcal{L}^{-1}\left(\frac{\lambda_b^{-1}}{\sqrt{n}}\right). \tag{4.102}$$

Remark. An important physical consideration in our specialization above is that the degradation function $g(d) = (1-d)^2$ only degrades the internal energy $\hat{\varepsilon}_{\text{R}}^0(\lambda_b, J^e)$ of the gel and not the entropic contributions. Thus, as $d \to 1$, the internal energy part $(1-d)^2\hat{\varepsilon}_{\text{R}}^0(\lambda_b, J^e)$

will become zero. Even though we do not directly degrade the entropic part of the free energy, as $d \to 1$, the entropic part also goes to zero since $\lambda_b \to \infty$. □

4.13.2 Specialized form for the Ginzburg-Landau evolution equation for the effective bond stretch λ_b

Recall (4.66), viz.

$$\hat{\kappa}_b(\mathbf{\Lambda})\,\dot{\lambda}_b = -\frac{\partial \hat{\psi}_{\mathrm{R}}(\mathbf{\Lambda})}{\partial \lambda_b}, \tag{4.103}$$

with $\kappa_b = \hat{\kappa}_b(\mathbf{\Lambda}) > 0$ a kinetic modulus.

As the damage variable $d \to 1$, the bond stretch λ_b also changes dramatically and eventually $\lambda_b \to \infty$. We use a specialized form of $\hat{\kappa}_b(\mathbf{\Lambda})$ to limit any dynamic effects of the breaking of bonds of the polymer chains. Since $\lambda_b \in [1, \infty)$, λ_b is not the suitable order parameter to characterize the phase transition associated with the bond-scission process. The simplest choice of an order parameter to describe this transition is the inverse of λ_b which lies in the bounded range $\lambda_b^{-1} \in [0, 1]$. A simple Ginzburg-Landau equation for the order parameter λ_b^{-1} is

$$\xi_b \dot{\overline{\lambda_b^{-1}}} = -\frac{\partial \hat{\psi}_{\mathrm{R}}(\mathbf{\Lambda})}{\partial \lambda_b^{-1}}, \tag{4.104}$$

with $\xi_b > 0$ a positive-valued kinetic modulus. Since $\dot{\overline{\lambda_b^{-1}}} = \lambda_b^{-2}\dot{\lambda}_b$ and $d\lambda_b^{-1} = \lambda_b^{-2} d\lambda_b$, (4.104) may be written as

$$\left(\xi_b \lambda_b^{-4}\right)\dot{\lambda}_b = -\frac{\partial \hat{\psi}_{\mathrm{R}}(\mathbf{\Lambda})}{\partial \lambda_b}, \tag{4.105}$$

which is of the general form (4.103), with

$$\kappa_b = \xi_b \lambda_b^{-4}. \tag{4.106}$$

4.13.3 Specialized form for ϖ_{diss}

Next we specialize the expression for the dissipative microforce ϖ_{diss} that expends power through $\dot{d}$.[3] The dissipative microforce is partitioned into a rate-independent part and a rate-dependent part through

$$\varpi_{\mathrm{diss}} = \underbrace{\hat{\alpha}(\mathbf{\Lambda})}_{\text{rate-independent}} + \underbrace{\hat{\zeta}(\mathbf{\Lambda})\dot{d}}_{\text{rate-dependent}} . \tag{4.107}$$

[3] Cf. eqs. (4.57) and $(9.215)_1$.

Based on physical model of Mao et al. (2017b), the rate-independent part of the dissipative microforce α is the sum of the contributions from each chain given by (5.32), and is given by

$$\alpha = \varepsilon_{\mathrm{R}}^{f}. \tag{4.108}$$

The rate-dependent contribution to the dissipative microforce is here taken to be simply described by a constant kinetic modulus $\zeta > 0$, with the rate-independent limit given by $\zeta \to 0$.

4.13.4 Specialized form for the evolution equation for d

Using the specialized free energy (4.101) and the specialization for ϖ_{diss} above, eq. (9.221), which gives the evolution of d, becomes

$$\zeta \dot{d} = 2(1-d)\hat{\varepsilon}_{\mathrm{R}}^{0}(\lambda_b, J^e) + \varepsilon_{\mathrm{R}}^{f}\ell^2\Delta d - \varepsilon_{\mathrm{R}}^{f}. \tag{4.109}$$

Remark. Consider the rate-independent limit ($\zeta = 0$) in the absence of any gradient in the damage field d. Then (5.39) reduces to

$$0 = 2(1-d)\hat{\varepsilon}_{\mathrm{R}}^{0}(\lambda_b, J^e) - \varepsilon_{\mathrm{R}}^{f}. \tag{4.110}$$

Using the fact that d lies in the range $d \in [0,1]$, (5.41) gives that

$$d = \begin{cases} 0, & \text{if } \hat{\varepsilon}_{\mathrm{R}}^{0}(\lambda_b, J^e) \leq \varepsilon_{\mathrm{R}}^{f}/2, \\ 1 - \dfrac{\varepsilon_{\mathrm{R}}^{f}/2}{\hat{\varepsilon}^{0}(\lambda_b, J^e)} & \text{if } \hat{\varepsilon}^{0}(\lambda_b, J^e) > \varepsilon_{\mathrm{R}}^{f}/2. \end{cases} \tag{4.111}$$

□

The evolution equation (5.39) can be rewritten to enforce the constraint $d \in [0,1]$ in a simple way. Add and subtract the term $\varepsilon_{\mathrm{R}}^{f} d$ to (5.39) to get,

$$\zeta \dot{d} = 2(1-d)\left(\hat{\varepsilon}^{0}(\lambda_b, J^e) - \varepsilon_{\mathrm{R}}^{f}/2\right) - \varepsilon_{\mathrm{R}}^{f}\left[d - \ell^2\Delta d\right].$$

Since $\hat{\varepsilon}_{\mathrm{R}}^{0}(\lambda_b, J^e)$ is the major driving energy for the evolution of d, the constraint $d \in [0,1]$ is satisfied if the equation above is modified to read as,

$$\zeta \dot{d} = 2(1-d)\left\langle \hat{\varepsilon}_{\mathrm{R}}^{0}(\lambda_b, J^e) - \varepsilon_{\mathrm{R}}^{f}/2 \right\rangle - \varepsilon_{\mathrm{R}}^{f}\left[d - \ell^2\Delta d\right], \tag{4.112}$$

where $\langle \bullet \rangle$ are Macauley brackets, i.e.,

$$\langle x \rangle = \begin{cases} 0, & x < 0, \\ x, & x \geq 0. \end{cases}$$

In this form, a threshold for the driving energy for damage is made explicit.

At this stage in the development of the model for the evolution of d, the irreversible nature of scission is not yet reflected in the model. To this end, we replace the term $\langle \hat{\varepsilon}^0_{\mathrm{R}}(\lambda_b, J^e) - \varepsilon^f_{\mathrm{R}}/2 \rangle$ in (4.112) with the monotonically increasing history function (cf., Miehe et al., 2010),

$$\mathcal{H}(t) \stackrel{\text{def}}{=} \max_{s\in[0,t]} \left\langle \hat{\varepsilon}^0_{\mathrm{R}}(\lambda_b(s), J^e(s)) - \varepsilon^f_{\mathrm{R}}/2 \right\rangle . \tag{4.113}$$

The Ginzburg-Landau evolution equation for d (9.221) may then be written in a form similar to that found in the numerous papers by Miehe and co-workers on phase-field fracture (cf., e.g., Miehe et al., 2010; Miehe and Schänzel, 2014; Raina and Miehe, 2016),[4]

$$\zeta \dot{d} = 2(1-d)\mathcal{H} - \varepsilon^f_{\mathrm{R}} \left[d - \ell^2 \Delta d \right] . \tag{4.114}$$

The free energy (4.101) gives the vector microstress as $\boldsymbol{\xi} = \varepsilon^f_{\mathrm{R}} \ell^2 \nabla d$, so that the boundary conditions conditions (5.14) for the partial differential equation (4.114) may be written as,

$$\dot{d} = 0 \quad \text{on } \mathcal{S}_d \times [0,T], \qquad \text{and} \qquad (\nabla d) \cdot \mathbf{n}_{\mathrm{R}} = 0 \quad \text{on } \partial \mathrm{B} \setminus \mathcal{S}_d \times [0,T]. \tag{4.115}$$

The latter boundary condition thus means that the gradient of phase field ∇d is taken to be perpendicular to the normal $\mathbf{n}_{\mathrm{R}}$ to the surface $\partial \mathrm{B} \setminus \mathcal{S}_d$, so that any "diffuse crack" intersects the boundary in a perpendicular fashion. Such a boundary condition is widely used in gradient damage theories in the literature (cf., e.g., Miehe et al., 2010).

4.13.5 Specialization of the referential fluid mobility tensor M

We note that with

$$c \stackrel{\text{def}}{=} J^{-1} c_{\mathrm{R}} \qquad \text{and} \qquad \mathbf{j} \stackrel{\text{def}}{=} J^{-1} \mathbf{F} \mathbf{j}_{\mathrm{R}}, \tag{4.116}$$

respectively, denoting the fluid content measured per unit volume of the deformed body, and the fluid flux measured per unit area of the deformed body per unit time, the referential balance law (4.15) may be expressed spatially as,

$$\dot{c} = -\mathrm{div} \mathbf{j}. \tag{4.117}$$

At present not much is known experimentally about the precise constitutive equation for the flux $\mathbf{j}$. Here we use a simple form to capture the essence of the diffusion of the fluid in the gel. Specifically, we assume that the spatial flux depends linearly on the spatial gradient of the chemical potential, with the mobility tensor spherical, so that

$$\mathbf{j} = -m \, \mathrm{grad} \, \mu, \tag{4.118}$$

[4]However, our derivation of (4.114) differs in substantial detail from that in the papers by Miehe et al.

with

$$m = \hat{m}(c, d, \vartheta) > 0 \tag{4.119}$$

a positive-valued mobility coefficient. The assumption that the spatial mobility tensor is spherical, $m\mathbf{1}$, implies that the fluid diffusion always remains isotropic and is not influenced by deformation or damage of the gel. We assume further that the spatial scalar mobility m at a given temperature ϑ is given by,

$$m = \frac{Dc}{R\vartheta} \qquad \text{with} \qquad D = \hat{D}(d) > 0, \tag{4.120}$$

where D represents a diffusion coefficient with units of m^2/s. Finally, using the transformations $(4.116)_2$ and $\operatorname{grad}\mu = \mathbf{F}^{-\mathsf{T}}\nabla\mu_{\mathrm{R}}$, the spatial relation (4.118) may be converted to its referential counterpart,

$$\mathbf{j}_{\mathrm{R}} = -\mathbf{M}\nabla\mu_{\mathrm{R}}, \tag{4.121}$$

with

$$\mathbf{M} = J\left(\frac{Dc}{R\vartheta}\right)\mathbf{C}^{-1} \qquad \text{with} \qquad D = \hat{D}(d) > 0, \tag{4.122}$$

a positive-semidefinite referential mobility tensor. The precise dependence of the damage on the diffusion coefficient is not known; we expect that as the damage d increases then so also does the diffusion coefficient D, but in our numerical calculations — for simplicity — we take D to be a constant.[5]

Actually, more precise expression for mobility can be obtained if we reconsider Equation (4.118). Generally for the case without damage, we pick the isotropic mobility tensor in spatial configuration, like

$$\mathbf{j} = -\mathbf{m}\operatorname{grad}\mu \tag{4.123}$$

here $\mathbf{m} = m_1\mathbf{1}$ with m_1 here is the mobility for undamaged material. For this case, we can use the following form(Duda et al., 2010; Chester and Anand, 2010)

$$m_1 = \frac{D_1}{R\vartheta}c^n \equiv \frac{D_1}{R\vartheta}(J^{-1}c_{\mathrm{R}})^n \tag{4.124}$$

with D_1 is the diffusivity of the solvent in the polymer network. As the material part be degraded, the material is supposed change from the polymer network with solvent to be another material, pretty much like air or solvent. For this fully damage part, the diffusivity becomes isotropic again, and the spatial flux is still given by (4.123) but $\mathbf{m} = m_2\mathbf{1}$ with m_2 is the mobility of the solvent within the air. Typically $m_2 \gg m_1$ and can be simply described by a constant

$$m_2 = \frac{D_2}{R\vartheta} \tag{4.125}$$

[5]This assumption is approximately valid in the numerical simulations that we report in the simulation chapter 6, since in these simulations the rupture happens very quickly, and any dependency of the mobility on damage may be neglected.

with D_2 is the diffusivity of the solvent in this fully degraded material. Then at first order of approximation, we can describe the dependency of mobility on damage as

$$\mathbf{m}(d) = m_1\kappa(d)\mathbf{1} + m_2(1-\kappa(d))\mathbf{1} \tag{4.126}$$

here $\kappa(d) \in [0,1]$ is the degrade function for mobility. As $d = 0$ $\kappa(d) = 1$, the material is undamaged and $\mathbf{m}(d) = m_1\mathbf{1}$; as $d = 1$ we have $\kappa(d) = 0$, then the material is fully damaged and $\mathbf{m}(d) = m_2\mathbf{1}$.

However, in the partially damaged material, the mobility is anisotropic. The physical observation is that the mobility along the spatial gradient of damage grad d is much smaller than the mobility along the directions perpendicular to grad d. In order including this effect, we modify (4.126) as following,

$$\mathbf{m} = m_1\kappa(d)\mathbf{1} + m_2(1-\kappa(d))(\mathbf{1} - \mathbf{s}_d \otimes \mathbf{s}_d) \tag{4.127}$$

with $\mathbf{s}_d = \text{grad } d/|\text{grad } d|$ is the unit normal direction along the gradient of damage.

We can easily exam whether this mobility tensor satisfies the above mentioned physical observation as following. For the direction perpendicular to the spatial gradient of damage, the mobility is given by $m_\perp = m_1\kappa(d) + m_2(1-\kappa(d))$ while for the direction along the spatial gradient of damage, the mobility is given by $m_\parallel = m_1\kappa(d)$. Generally $m_\perp$ increases as d changes from 0 to 1 and $m_\parallel$ decreases as d changes from 0 to 1. For simplicity, we pick $k(d) \equiv g(d) = (1-d)^2$ for now.

Finally, we need make $\mathbf{j}$ back to the referential flux $\mathbf{j}_{\text{R}}$. Recall the relation (4.116) we have

$$\begin{aligned} \mathbf{j}_{\text{R}} &= J\mathbf{F}^{-1}\mathbf{j} = J\mathbf{F}^{-1}(-\mathbf{m}\text{grad }\mu) \\ &= J\mathbf{F}^{-1}(-\mathbf{m}\mathbf{F}^{-\top}\nabla\mu) = -\mathbf{M}\nabla\mu \end{aligned} \tag{4.128}$$

with

$$\begin{aligned} \mathbf{M} &= J\mathbf{F}^{-1}\mathbf{m}\mathbf{F}^{-\top} \\ &= J[m_1\kappa(d) + m_2(1-\kappa(d))]\mathbf{C}^{-1} - Jm_2(1-\kappa(d))\frac{[\mathbf{C}^{-1}\nabla d]\otimes[\mathbf{C}^{-1}\nabla d]}{\mathbf{C}^{-1} : [\nabla d \otimes \nabla d]} \end{aligned} \tag{4.129}$$

Clearly this is semi-positive-definite.

This sophisticated mobility expression is very useful for the case that fracture propagation is very slow. In our following simulation, the two mobility expressions (4.129) and (4.122) provide similar results.

4.14 Summary of the governing equations for the specialized theory

1. **Balance of forces**: Neglecting body forces, balance of forces requires

$$\mathrm{Div}\,\mathbf{T}_{\mathrm{R}} = \mathbf{0}, \tag{4.130}$$

with $\mathbf{T}_{\mathrm{R}}$ given by

$$\mathbf{T}_{\mathrm{R}} = \bar{G}\mathbf{F} - \bar{G}_0\mathbf{F}^{-\mathsf{T}} + (1-d)^2\frac{1}{4}K(J^{e2} - J^{e-2})\mathbf{F}^{-\mathsf{T}}, \tag{4.131}$$

where

$$\bar{G} \overset{\text{def}}{=} G_0\left(\frac{\sqrt{n}}{3\bar{\lambda}\lambda_b}\right)\beta, \qquad G_0 = Nk_{\mathrm{B}}\vartheta, \qquad \beta = \mathcal{L}^{-1}\left(\frac{\bar{\lambda}\lambda_b^{-1}}{\sqrt{n}}\right), \tag{4.132}$$

and

$$\bar{G}_0 \overset{\text{def}}{=} G_0\left(\frac{\sqrt{n}}{3\lambda_b}\right)\beta_0, \qquad \beta_0 \overset{\text{def}}{=} \mathcal{L}^{-1}\left(\frac{\lambda_b^{-1}}{\sqrt{n}}\right), \tag{4.133}$$

and $\mathcal{L}^{-1}(\cdot)$ is the inverse of the Langevin function $\mathcal{L}(x) = \coth x - x^{-1}$.

The bond-stretch λ_b is solved by integrating the evolution equation

$$\left(\frac{\xi_b}{G_0 n}\lambda_b^{-3}\right)\dot{\lambda}_b = -(1-d)^2\frac{\bar{E}_b}{G_0 n}(\lambda_b - 1)\lambda_b + \frac{\bar{\lambda}\lambda_b^{-1}}{\sqrt{n}}\beta - \frac{\lambda_b^{-1}}{3\sqrt{n}}\left(\beta_0 + \frac{\partial\beta_0}{\partial r_0}r_0\right)\ln J, \tag{4.134}$$

in which

$$\bar{E}_b = N\,n\,E_b, \qquad \text{and} \qquad r_0 \overset{\text{def}}{=} \frac{1}{\sqrt{n}\,\lambda_b}.$$

2. **Balance of fluid concentration**:

$$\dot{c}_{\mathrm{R}} = -\mathrm{Div}\,\mathbf{j}_{\mathrm{R}}, \tag{4.135}$$

with $\mathbf{j}_{\mathrm{R}} = -\mathbf{M}\nabla\mu_{\mathrm{R}}$, with the mobility given by (4.122) and the chemical potential by

$$\mu_{\mathrm{R}} = \mu_{\mathrm{R}}^0 + R\vartheta[\ln(1-\phi) + \phi + \chi\phi^2] - (1-d)^2\,J^{s-1}\,\frac{1}{4}\,K(J^{e2} - J^{e-2})\Omega. \tag{4.136}$$

3. **Evolution equation for the damage variable** d:

$$\zeta\dot{d} = 2(1-d)\mathcal{H} - \varepsilon_{\mathrm{R}}^f\left[d - \ell^2\Delta d\right], \tag{4.137}$$

in which

$$\varepsilon_{\mathrm{R}}^{f} = N\, n\, \varepsilon_{b}^{f}, \tag{4.138}$$

is energy required to fail the Kuhn segments, ℓ is a material length scale, and $\mathcal{H}$ is a history functional defined by

$$\mathcal{H}(t) \stackrel{\text{def}}{=} \max_{s\in[0,t]} \left\langle \hat{\varepsilon}_{\mathrm{R}}^{0}(\lambda_b(s), J^e(s)) - \varepsilon_{\mathrm{R}}^{f}/2 \right\rangle, \tag{4.139}$$

where at each $s \in [0,t]$,

$$\hat{\varepsilon}_{\mathrm{R}}^{0}(\lambda_b(s), J^e(s)) = \frac{1}{2} N\, n\, E_b\, (\lambda_b(s) - 1)^2 + \frac{1}{8} K (J^e(s) - J^{e-1}(s))^2. \tag{4.140}$$

The theory involves the following material parameters:

$$N, \quad n, \quad E_b, \quad K, \quad \xi_b, \quad \mu_{\mathrm{R}}^{0}, \quad \Omega, \quad \chi, \quad D, \quad \varepsilon_{b}^{f}, \quad \ell, \quad \text{and} \quad \zeta. \tag{4.141}$$

Here, N is the number of chains per unit volume; n represents number of links in a chain; E_b represents a modulus related to stretching of the bonds (Kuhn segments) of the polymer molecules; K, represents the bulk modulus of the material; ξ_b is a kinetic modulus for the evolution of the bond stretch; μ_{R}^{0} is the reference chemical potential of the solvent; Ω is the molar volume of the diffusing fluid; χ is the Flory-Huggins interaction parameter between the polymer and solvent; D is the diffusivity of the fluid molecules; ε_{b}^{f}, a bond dissociation energy per unit volume; ℓ is a characteristic length scale of the gradient damage theory under consideration; and ζ is a kinetic modulus for the evolution of the damage.

In the numerical simulations to described in Section 4.15, instead of the parameter list (5.46), we use the parameter list,

$$\begin{aligned} \text{Network parameters}: \quad & G_0 = N k_B \vartheta, \quad n, \quad \bar{E}_b = N n E_b, \quad K, \\ & \xi_b, \quad \varepsilon_{\mathrm{R}}^{f} = N n \varepsilon_{b}^{f}, \quad \ell, \quad \text{and} \quad \zeta, \\ \text{Fluid diffusion parameters}: \quad & \mu_{\mathrm{R}}^{0}, \quad \Omega, \quad \chi, \quad \text{and} \quad D, \end{aligned} \tag{4.142}$$

where G_0 is the ground-state shear modulus for the polymer network, $\bar{E}_b$ is a bond-stiffness parameter for the network, and $\varepsilon_{\mathrm{R}}^{f}$ represents the energy per unit volume for the dissociation of all the Kuhn segments in a network.

The boundary conditions for these partial differential equations have been discussed previously in Section 5.3.1.

4.15 Numerical implementation

We have numerically implemented our theory in the open-source finite element code MOOSE (Gaston et al., 2009) by writing our own application to solve 3D, plane-strain, plane-stress,

axisymmetric problems. MOOSE uses a sophisticated nonlinear solver technology, and it may be massively parallelized. The details of numerical implementation of our theory is displayed in Appendix B. Using this new numerical capability, in next following chapters we report on two aspects of our theory.

- In Chapter 5, we first focus on simulations of coupled deformation-fracture of elastomeric materials. In this case, we suppress the diffusion in the system, and study the capability of our theory to describe the fracture in rubber. Moreover, following the same routine, we study the fracture of rubber by crosslink failure.

- In Chapter 6, we show some representative simulations of coupled diffusion-deformation-fracture of a polymeric gel.

All simulations are done in a linux cluster with $\sim$100 cores, and the visualization of the results was performed by using the open-source code ParaView (Ayachit, 2015).

Chapter 5

Progressive damage and rupture of elastomers

5.1 Introduction

In this chapter we focus on physics and numerical modelings of fracture in elastomeric materials. There are two typical failure micromechanisms in soft materials: chain scission and crosslink failure. If the cross-linking chemical bonds in an elastomeric network are strong covalent bonds, then fracture is expected to occur by scission of the chains between the crosslinks, while if the chemical crosslinks are weak then fracture is expected to occur because of the scission of the cross-linking bonds themselves; cf. Fig. 5-1.

The Lake-Thomas argument (Lake and Thomas, 1967) is the first molecular theory to understand the fracture of elastomers by chain scission. They proposed that when any of the main bonds in a polymer chain breaks, then the total energy of each bond of the stretched chain is irreversibly lost. Therefore, the energy necessary to break a chain is proportional to the length of that chain, i.e., proportional to the number of backbone bonds, n, comprising the chain.[1] In an important paper Akagi *et. al.* (Akagi et al., 2013) presented results from their investigations on the fracture behavior of tetra(polyethylene glycol) (Tetra-PEG) gels with precisely controlled network structures. These controlled network structures, with greatly suppressed heterogeneity, enabled Akagi et al. (2013) to validate the predictions of the Lake-Thomas model; also see Sakai (2013). From physics and modeling perspective, we show in Chapter 3 that our idea on stretchability of Kuhn segments within polymer chains is consistent with Lake-Thomas argument. This highlights that the theory that we developed in Chapter 4 should be useful to modeling the progressive damage and rupture in elastomers, if the failure mode in the specific elastomers is chain scission and the diffusion is suppressed.

[1] Actually proportional to $\sqrt{n}$; cf. Sakai (2013) and also the Remark on page 110.

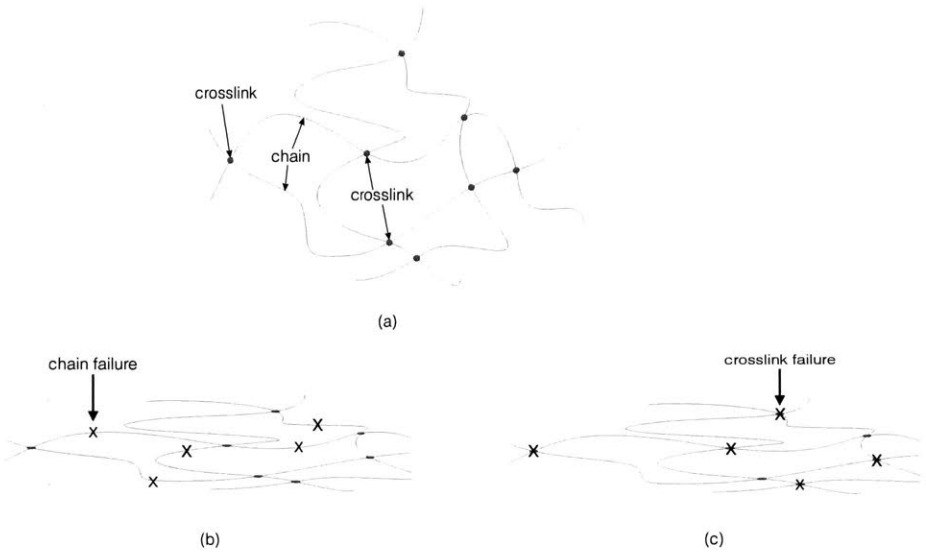

Figure 5-1: (a) Schematic of a crosslinked elastomeric network. (b) Schematic of failure by chain scission. (c) Schematic of failure by crosslink scission.

We will show numerically in section 5.2 that indeed our theory can pickup the essence of the fracture of elastomers by chain scission.

However, in many synthetic polymers the Kuhn segments are quite stiff and strong. Instead, it is the weak crosslinks in the network which are stretched and eventually lead to failure.[2] In this case, we need modify our theory to accounting for crosslink failure in the polymer network. Much of the continuum-level theory developed in previous chapter is unchanged, but what is changed is that here we introduce an *effective crosslink stretch* λ_c — rather than an *effective bond stretch* λ_b — as an internal variable of the theory. Also changed are the specialized constitutive equations for the internal energy and entropy of the network because the micromechanism of damage and failure is fundamentally different from what we had considered previously. The details of fracture of elastomers by crosslink failure are displayed in Section 5.3.

Because of the fundamentally different between these two micromechanism of damage and failure in elastomers, some important consequence will appear. For example, we show that for elastomeric materials in which fracture occurs by crosslink stretching and scission, the Lake-Thomas scaling Lake and Thomas (1967); Akagi et al. (2013); Sakai (2013); Creton (2017) — that is the toughness G_c is proportional to $1/\sqrt{G_0}$, with $G_0 = Nk_b\vartheta$ the ground-state shear modulus of the material — does not hold. A new scaling is proposed, and some important consequences of this scaling are remarked upon. More details of these consequences are displayed in section 5.4.

[2]For example the 4-arm polyethylene glycol network with reversible metal-ligand crosslinks Grindy et al. (2016).

5.2 Fracture of elastomers by chain scission

5.2.1 Application of the model to study flaw-sensitivity in elastomers

We demonstrate the behavior of the full nonlocal network model through an example. To this end, we apply the model to the problem of plane-stress Mode-I loading of a single-edge-notched specimen (see Fig. 5-2).

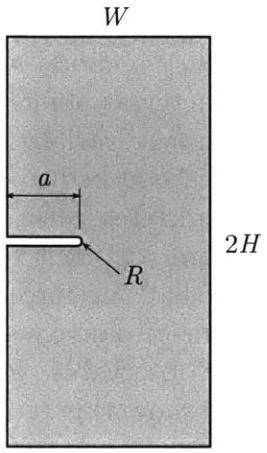

Figure 5-2: Geometric parameters defining a single-edge-notched specimen (not to scale). We take $W = 10a$ and $H = 20a$, and R is the root-radius of the notch.

The material properties used in our simulations are given in Table 6.1. The parameters G_0, n, and K approximate those of a well cross-linked engineering elastomer. The values of the parameters $\bar{E}_b$ and $\varepsilon_{\mathrm{R}}^f$ are in line with the estimates made in Mao et al. (2017b), and the length scale is set at $\ell = 1\mu$m. The kinetic modulus ζ was chosen through trial-and-error so that it has only a minor effect on the load-displacement curves in the simulations.

Table 5.1: Material properties for the single-edge-notch simulations.

$G_0 = Nk_B\vartheta$	n	$\bar{E}_b = NnE_b$	K	$\varepsilon_{\mathrm{R}}^f = Nn\varepsilon_b^f$	ℓ	ζ
0.25 MPa	4	500 MPa	625 MPa	25 MJ/m^3	1 μm	50 MPa·s

We consider a series of geometries of different size that are each pre-notched to 10% of the specimen width. Referring to Fig. 5-2, each specimen is defined by the in-plane width W, half-height H, notch-depth a, and notch-root-radius R. We examine the case of flaws that are small enough to allow the material to stiffen significantly due to chain straightening before rupture occurs. The notch lengths considered are,

$$a = \{0.5\mu\mathrm{m}, 1\mu\mathrm{m}, 5\mu\mathrm{m}, 10\mu\mathrm{m}\}, \tag{5.1}$$

which when normalized by the length scale $\ell = 1\mu$m are,

$$a/\ell = \{0.5,\ 1,\ 5,\ 10\}.$$

We set the notch-root radius to be $R = 1\mu$m for all geoemetries. For each notch-length a, we take $W = 10a$ and $2H = 40a$. The geometries thus range from 5 μm wide by 20μm high ($a/\ell = 0.5$) to 100 μm by 400 μm ($a/\ell = 10$). Note that there is not perfect similarity between the geometries, since the notch radius is kept fixed at 1μm in all cases. Each specimen is pulled in uniaxial tension at a nominal stretch rate of 1×10^{-2} s^{-1}.

Fig. 6-1 shows the result from our simulation for a notch with $a/\ell = 1$. The nominal stress, normalized by $G_0 = Nk_B\vartheta$, versus nominal stretch curve is shown in Fig. 6-1(i), and Fig. 6-1(ii) shows the deformed geometry at points (a) through (g) on the stress-stretch curve, together with contours of the damage variable d. The image (a) in Fig. 6-1(ii) is the initial configuration. As the sample is streched to point (b) the sharp crack is blunted, but no damage has initiated. Damage initiates when the sample is stretched further to a stretch level of ~ 3.5 (a point just before (c)), but the force is still increasing, and it is after additional macroscopic stretching that the force reaches a peak at point (d) in the stress-stretch curve, and from the contour of damage shown in Fig. 6-1(ii) (d), the damage zone ahead of the crack becomes clearly observable. Further stretching begins the rupture process, and Figs. 6-1(ii) (e) through (g) show this progressive rupturing, with (g) showing the final failed configuration.

Next, we examine the role of the bond stretching on the overall response. In Figs. 5-4 and 5-5, we plot contours of the bond stretch λ_b during the deformation process. Highly damaged elements ($d > 0.95$) are again hidden from view. The contours are plotted on the reference configuration to highlight the extent of crack propagation, relative to the initial specimen geometry.

Figure 5-4 shows the bond deformation for a small flaw, $a/\ell = 1$. The image in the first frame is taken when extension of the notch has proceeded a small amount, while that in the last frame is just before final rupture of the specimen. The contour levels of λ_b show that there is appreciable bond-stretch in the entire specimen. The overall response is strongly influenced by the mechanics of bond-stretching, and the stress-bearing capacity of the material is being used efficiently.

A contour plot for λ_b for a specimen with a large flaw, $a/\ell = 10$, is shown in Figure 5-5; the crack has propagated halfway through the specimen. In this case bond-stretching is limited to a small region in the vicinity of the crack tip; the majority of the specimen displays negligible bond-stretching, and that part of the specimen is thus well described by the Arruda-Boyce model without bond-stretching. This plot illustrates a case where the damage process zone at the crack-tip is small compared with the other in-plane dimensions of the specimen. For such circumstances a traditional top-down fracture mechanics approach based on the critical energy release rate may be applied, *but we do pursue such an approach here.*

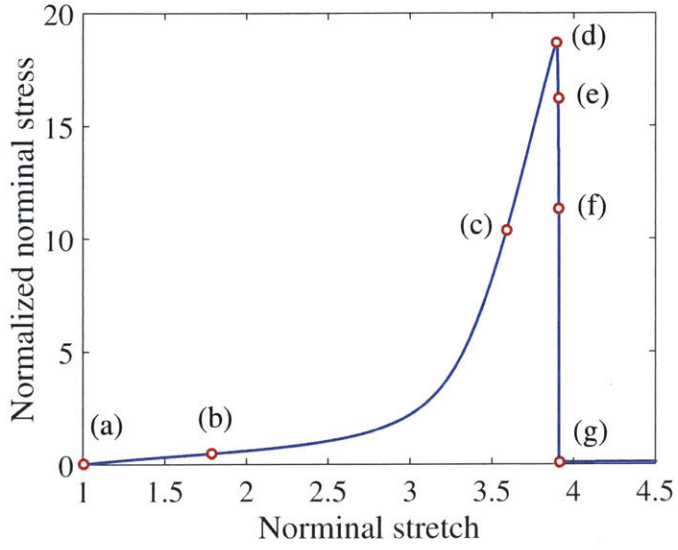

(i)

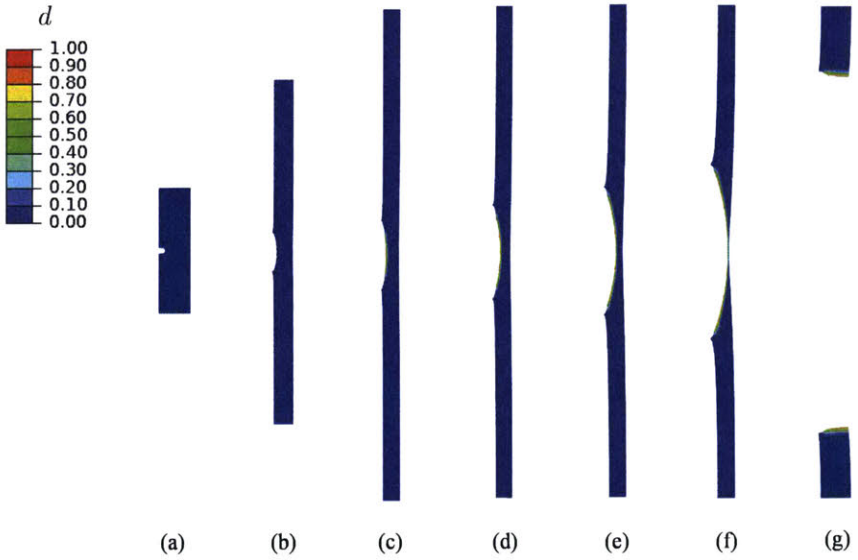

(ii)

Figure 5-3: Progressive damage and rupture for the case $a/\ell = 1$. (i) Computed nominal stress, normalized by $G_0 = Nk_B\vartheta$, versus nominal stretch curve. (ii) Deformed configurations of the specimen with contours of the damage variable d at points (a) through (g) in the stress-stretch curve. To aid visualization of the damage, elements with an average value of $d > 0.95$ are removed from the plots.

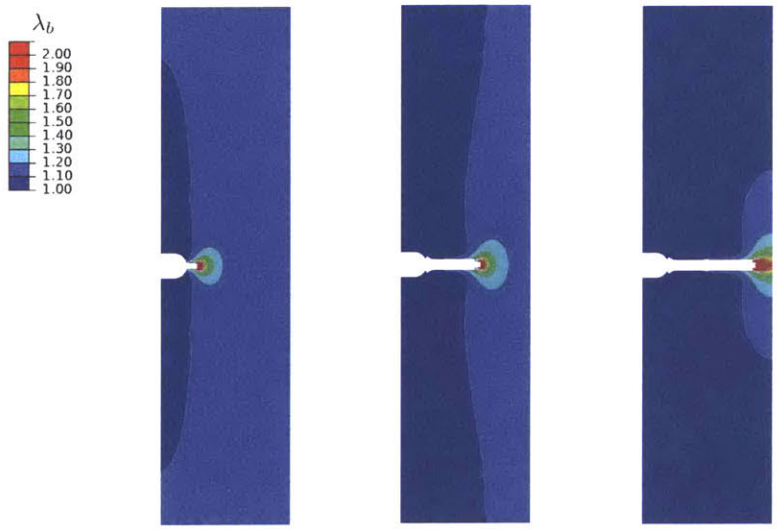

Figure 5-4: Contours of bond stretch λ_b during the fracture process for a notch with $a/\ell = 1$. Significant bond deformation occurs throughout the entire specimen. Snapshots are shown at three different stages of crack propagation. Contours are plotted on the reference configuration. Elements are removed from the figures when $d > 0.95$.

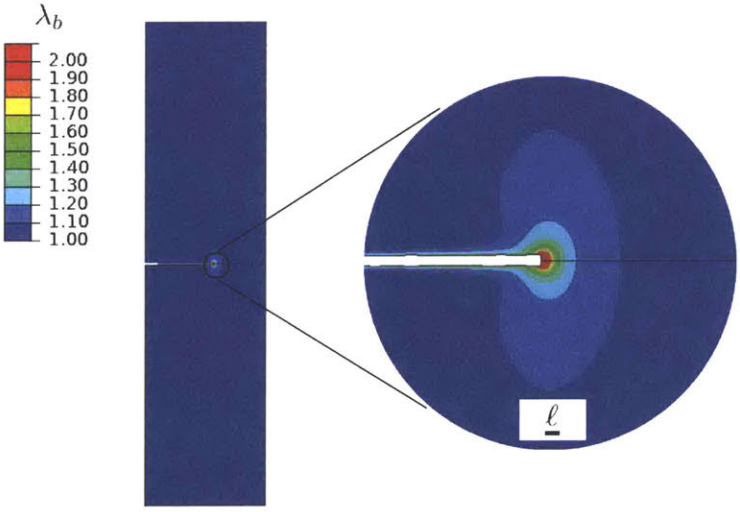

Figure 5-5: Contours of bond stretch λ_b during the fracture process for a notch with $a/\ell = 10$. The bond stretch is appreciable only in a small process zone near the crack tip. Contours are plotted on the reference configuration. Elements are removed from the figures when $d > 0.95$.

The normalized nominal stress versus nominal stretch response for all the geometries $a/\ell = \{0.5, 1, 5, 10\}$ is shown in Figure 5-6. For comparison, the ideal behavior of the material with no flaw is included on the plot as a dashed curve.[3] As the notch size decreases, the body approaches the strength of the local response. Note also that the gradual failure that occurs in the local response becomes a sudden event in the boundary value problem. This is indicative of the nonlocal behavior, with energy remote from the crack-tip being released to extend the crack.

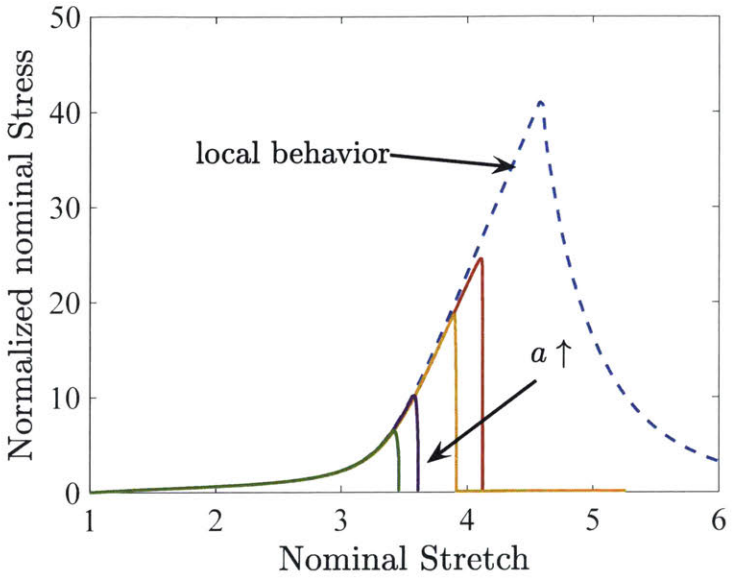

Figure 5-6: Nominal stress, normalized by $G_0 = Nk_B\vartheta$, versus nominal stretch for all single-edge-notched geometries, with $a/\ell = \{0.5, 1, 5, 10\}$ (solid lines). The dashed curve shows the local behavior of the model, representative of a homogeneous deformation state.

5.2.2 Double-edge-notched thin sheets in tension

In the previous section 5.2.1 we studied the capability of the model to describe flaw-size sensitivity in single-edge-notched specimens which are sub-millimeter in size, with micron-dimensioned cracks. In this section we show the capability of or theory and numerical simulation capability to model the experimental results of Hocine et al. (2002) on fracture of double-edge-notched specimens of a styrene-butadiene elastomer (SBR) — specimens which are tens of millimeters in size, with millimeter-dimensioned cracks.

Remark. In our gradient-damage theory the free energy has a contribution (5.31) in which $\varepsilon_{\mathrm{R}}^{f}$ represents the energy of crosslink scission per unit volume, and ℓ is a length scale to

[3] The ideal behavior is computed by applying a uniaxial, plane stress deformation to a single material point, neglecting the nonlocal ∇d term.

account for gradient effects in the damage field d. Theoretically, ℓ is an intrinsic material parameter of the theory. Actual values of ℓ in elastomeric materials are expected to be $\ell \lessapprox 1\mu$m. For such a value of ℓ, to numerically resolve regions of sharp gradients in the damage variable d, the finite element size h_e must be much smaller than ℓ — typically $h_e \lessapprox \ell/10$ — so that $h_e \lessapprox 100$nm, which is *exceedingly small.* Use of such a small element size in the damage zone is computationally tractable (on our computers) if the in-plane dimensions of a single-edge-notched specimen are less than 1mm, and an edge crack is a few microns is size. However, if one is interested in simulating the fracture of specimens which have a macroscopic in-plane dimensions of say 10mm or larger, then use of such a small value of ℓ and therefore a small value of h_e, will result in prohibitively expensive simulations. Under these circumstances, for pragmatic reasons, ℓ may be considered a regularization parameter for the gradient-damage theory. Corresponding to a small but computationally-tractable mesh size h_e selected for macroscopic-dimensioned specimens, a suitably large value of ℓ may be chosen, and the value of $\varepsilon^f_{\mathrm{R}}$ suitable reduced so that $\varepsilon^f_{\mathrm{R}} \times \ell \approx G_c$, where G_c is the value of experimentally-measured macroscopic critical energy release rate for a given material. *We take this pragmatic approach for the numerical simulations shown in this section.*

□

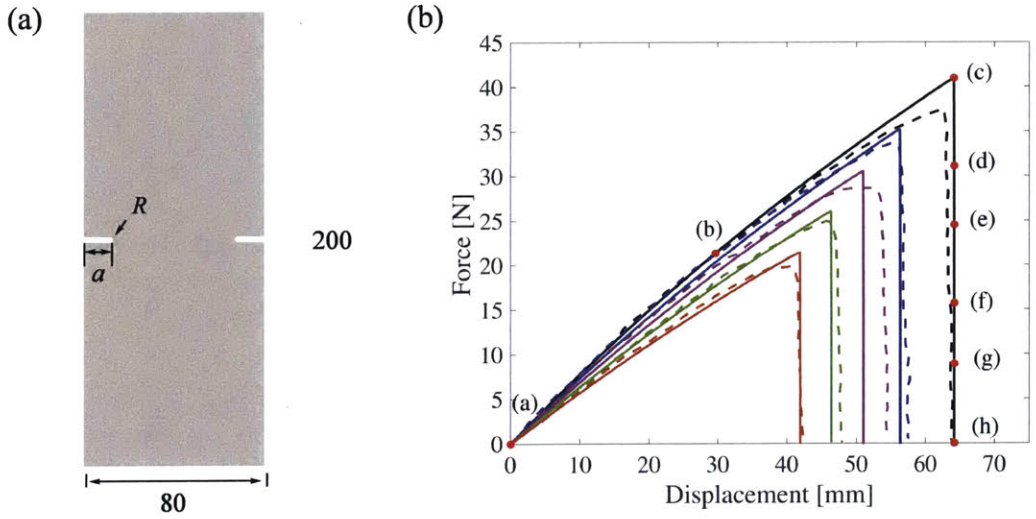

Figure 5-7: Double-edge-notched specimen in tension. (a) Geometry of the specimen in mm, with different initial notch lengths $a = \{12, 16, 20, 24, 28\}$ mm. The root-radius of the notch is fixed at $R = 1$ mm (b). Comparison of load-deflection curves from simulations (solid-lines) against the experimental results of Hocine et al. (2002) (dashed-lines).

Fig. 5-7 (a) shows a schematic of the specimen geometry in the experiments of Hocine et al. (2002). The overall size of a notched sheet sample is 80 mm × 200 mm in the plane, and the sheet is 3 mm thick. We consider specimens with notch lengths $a = 12$, 16, 20, 24, and 28 mm; the initial root-radius of the notch is fixed at $R = 1$ mm. The displacement of the bottom edge of the specimen is fixed, while the top-edge is prescribed a displacement at

a nominal stretch rate of 1×10^{-3}/s. The simulations are performed in plane-stress. The material parameters used in this set of simulations for the SBR elastomer of Hocine et al. (2002) are shown in Table 5.2. A large value of $n = 1000$ is chosen to represent the essentially neo-Hookean response of the SBR elastomer. Also, the rather large value of $\ell = 1$mm is chosen for the pragmatic reasons discussed in the Remark on page 83.[4]

Table 5.2: Material properties for the double-edge-notched specimens of Hocine et al. (2002).

$G_0 = Nk_B\vartheta$	n	$\bar{E}_b = NnE_b$	K	$\varepsilon_{\mathrm{R}}^f = Nn\varepsilon_b^f$	ℓ	ζ
0.268 MPa	1000	15 MPa	2.68 MPa	0.235 MJ/m^3	1 mm	10 kPa·s

Fig. 5-7(b) shows the calculated force-displacement curves as solid lines for notches with initial lengths of

$$a = 12,\ 16,\ 20,\ 24, \text{and } 28\,\text{mm}.$$

As expected, as the initial length of a notch increases, the overall force level becomes lower, and the displacement at which final fracture occurs, becomes smaller. This figure also shows a comparison of load-deflection curves from the simulations against the experimental results of Hocine et al. (2002) (dashed-lines); there is an acceptable match between the simulations and the experimentall-measured results.

Fig. 5-8 shows the deformed geometry at points (a) through (h) on the force-displacement curve in Fig. 5-7(b) for $a = 28$mm, together with contours of the damage variable d, which are barely visible. To aid visualization of the damage, elements with an average value of $d > 0.95$ are not plotted. Fig. 5-8(a) is the initial configuration. As the sample is streched to (b) the notch is blunted, but no damage has initiated. Damage initiates when the sample is stretched further to a displacement level of $\sim$ 60mm (a point just before (c)), but the force is still increasing, and it is after another $\sim$ 3 mm of extension that the force reaches a peak at point (c) in force-displacement curve, and from the contour of damage shown in Fig. 5-8(c), a small damage zone ahead of the notch becomes observable. Further stretching begins the rupture process, and Figs. 5-8(d) through (h) show this progressive rupturing, with (h) showing the final failed configuration.

5.3 Fracture of elastomers by crosslink failure

Next let us switch our focus to fracture of elastomers by crosslink failure. The plan of this section is as follows. In Subsection 5.3.1 we summarize the essence of our continuum-level model. Since the structure of the continuum-level model is essentially unchanged from our

[4]For large values of n, it is useful for numerical reasons to rewrite the implicit equation (5.36) for the bond-stretch as,

$$(1-d)^2\bar{E}_b\,(\lambda_{\mathrm{b}} - 1) - G_0\left(\frac{\sqrt{n}\bar{\lambda}}{\lambda_b^2}\right)\mathcal{L}^{-1}\left(\frac{\bar{\lambda}\lambda_b^{-1}}{\sqrt{n}}\right) = 0. \tag{5.2}$$

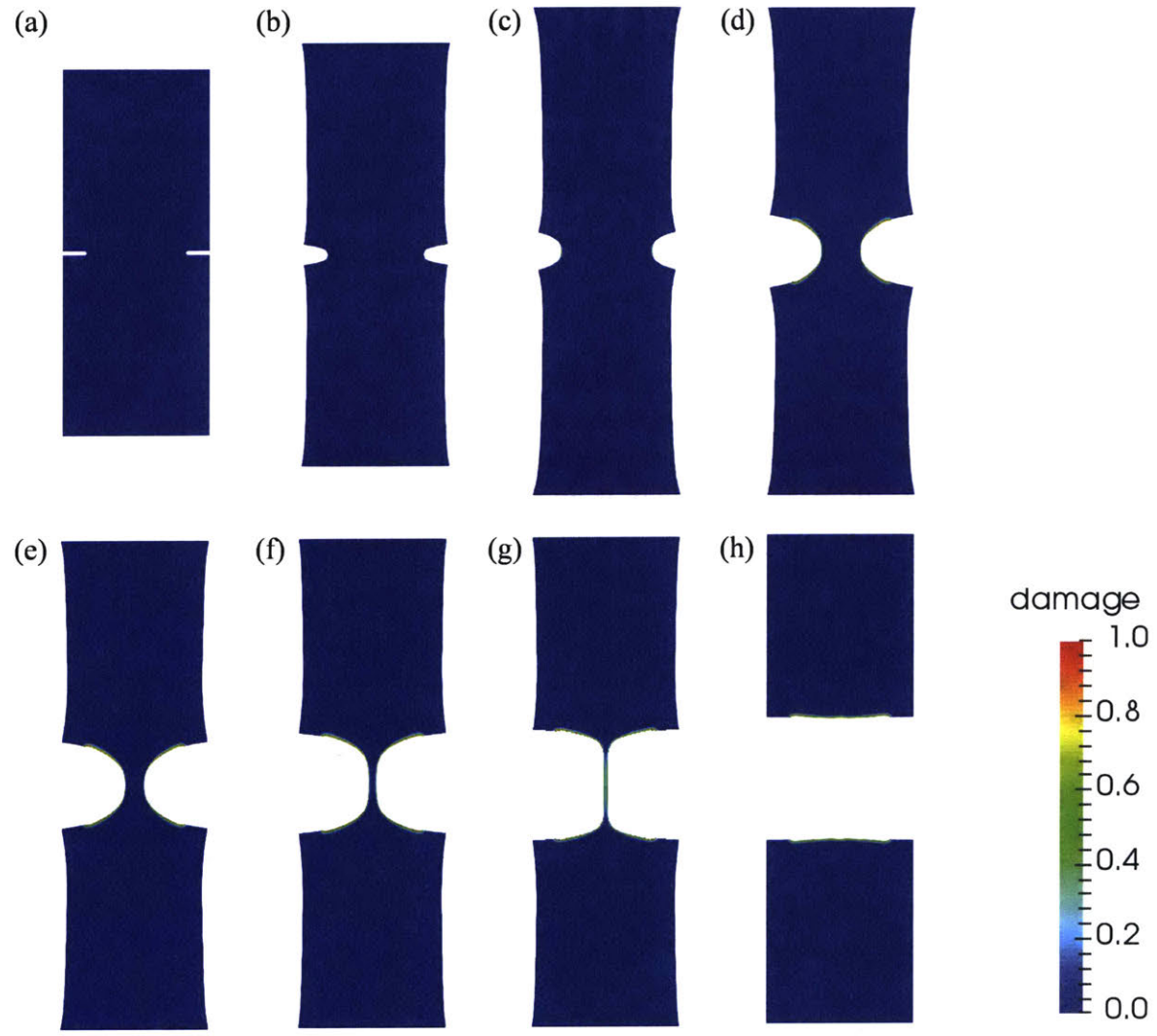

Figure 5-8: Images of the deformed geometry with contour plots of the damage variable d for a double-edge-notched specimen with $a = 28$mm. To aid visualization, elements with an average value of $d > 0.95$ have been removed from the plots.

previous section and our paper (Talamini et al., 2018), we simply reproduce the constitutive theory presented in Chapter 4 of Talamini et al. (2018) with the effective bond stretch λ_b replaced by an effective crosslink stretch λ_c. In Section 5.3.2 we give the specialized constitutive equations which allow for failure due to damage of crosslinks in the network.

In Section 5.3.3 we study the capability of our theory and its numerical implementation in a finite elememnt program to model *plane stress* fracture of (i) single-edge-notched specimens; (ii) an asymmetric double-edge-notched specimen; and (iii) fracture of a sheet specimen with multiple circular and elliptical holes.

5.3.1 Summary of the constitutive theory, governing partial differential equations, and boundary conditions

At the continuum-level our theory is essentially that developed in our previous paper Talamini et al. (2018), but here we allow for an *effective crosslink stretch* λ_c, rather than an *effective bond stretch* λ_b, as an internal variable of the theory. Our theory relates the following basic fields:

$\mathbf{x} = \boldsymbol{\chi}(\mathbf{X}, t)$,	motion;
$\mathbf{F} = \nabla\boldsymbol{\chi}, \quad J = \det\mathbf{F} > 0$,	deformation gradient;
$\bar{\mathbf{F}} = J^{-1/3}\mathbf{F}$,	distortional part of $\mathbf{F}$;
$\mathbf{C} = \mathbf{F}^{\mathsf{T}}\mathbf{F}$,	right Cauchy-Green tensor;
$\bar{\mathbf{C}} = \bar{\mathbf{F}}^{\mathsf{T}}\bar{\mathbf{F}} = J^{-2/3}\mathbf{C}$,	distortional part of $\mathbf{C}$;
$\mathbf{T}_{\mathrm{R}}$, $\mathbf{T}_{\mathrm{R}}\mathbf{F}^{\mathsf{T}} = \mathbf{F}\mathbf{T}_{\mathrm{R}}^{\mathsf{T}}$	Piola stress;
$\mathbf{T}_{\mathrm{RR}} = \mathbf{F}^{-1}\mathbf{T}_{\mathrm{R}}$,	second Piola stress;
ψ_{R},	free energy density per unit reference volume;
ε_{R},	internal energy density per unit reference volume;
$\lambda_c > 0$	effective crosslink stretch (an internal variable);
$d(\mathbf{X}, t) \in [0, 1]$,	damage variable or phase-field;
ϖ	scalar microstress conjugate to $\dot{d}$;
$\boldsymbol{\xi}$	vector microstress conjugate to $\nabla\dot{d}$.

Note that we use standard notation of modern continuum mechanics Gurtin et al. (2010). Specifically: ∇ and Div denote the gradient and divergence with respect to the material point $\mathbf{X}$ in the reference configuration, and $\Delta = \mathrm{Div}\nabla$ denotes the referential Laplace operator; grad, div, and div grad denote these operators with respect to the point $\mathbf{x} = \boldsymbol{\chi}(\mathbf{X}, t)$ in the deformed body; a superposed dot denotes the material time-derivative. Throughout, we write $\mathbf{F}^{e-1} = (\mathbf{F}^e)^{-1}$, $\mathbf{F}^{e-\mathsf{T}} = (\mathbf{F}^e)^{-\mathsf{T}}$, etc. We write $\mathrm{tr}\,\mathbf{A}$, $\mathrm{sym}\,\mathbf{A}$, $\mathrm{skw}\,\mathbf{A}$, $\mathbf{A}_0$, and $\mathrm{sym}_0\mathbf{A}$ respectively, for the trace, symmetric, skew, deviatoric, and symmetric-deviatoric parts of a tensor $\mathbf{A}$. Also, the inner product of tensors $\mathbf{A}$ and $\mathbf{B}$ is denoted by $\mathbf{A} : \mathbf{B}$, and the magnitude of $\mathbf{A}$ by $|\mathbf{A}| = \sqrt{\mathbf{A} : \mathbf{A}}$.

Constitutive equations

1. Free energy

This is given by

$$\psi_{\text{R}} = \hat{\psi}_{\text{R}}(\mathbf{\Lambda}), \tag{5.3}$$

with $\mathbf{\Lambda}$ the list

$$\mathbf{\Lambda} = \{\mathbf{C}, \lambda_c, d, \nabla d\}. \tag{5.4}$$

2. Second Piola stress. Piola stress

The second Piola stress is given by

$$\mathbf{T}_{\text{RR}} = 2\,\frac{\partial \hat{\psi}_{\text{R}}(\mathbf{\Lambda})}{\partial \mathbf{C}}, \tag{5.5}$$

and the Piola stress by

$$\mathbf{T}_{\text{R}} = \mathbf{F}\mathbf{T}_{\text{RR}}. \tag{5.6}$$

3. Implicit equation for the effective crosslink stretch

The thermodynamic requirement

$$\frac{\partial \hat{\psi}_{\text{R}}(\mathbf{\Lambda})}{\partial \lambda_c} = 0, \tag{5.7}$$

reflects the fact that the actual value of the effective crosslink stretch λ_c adopted by the material is the one that *minimizes* the free energy. This equation serves as an implicit equation to determine λ_c in terms of the other constitutive variables.[5]

4. Microstresses ϖ and $\boldsymbol{\xi}$

The scalar microstress ϖ conjugate to the rate of change of the damage variable $\dot{d}$ is given by,

$$\varpi = \underbrace{\frac{\partial \hat{\psi}_{\text{R}}(\mathbf{\Lambda})}{\partial d}}_{\varpi_{\text{en}}} + \underbrace{\alpha + \zeta \dot{d}}_{\varpi_{\text{dis}}}, \tag{5.8}$$

with $\alpha = \hat{\alpha}(\mathbf{\Lambda})$ and $\zeta = \hat{\zeta}(\mathbf{\Lambda})$ positive-valued scalar functions. Here ϖ_{en} and ϖ_{dis} denote the energetic and dissipative parts of ϖ.

The vector microstresses $\boldsymbol{\xi}$ conjugate to $\nabla \dot{d}$ is given by,

$$\boldsymbol{\xi} = \frac{\partial \hat{\psi}_{\text{R}}(\mathbf{\Lambda})}{\partial \nabla d}, \tag{5.9}$$

[5] To limit the dynamics of failure by crosslink stretch, eq. (5.7) may be modified by introducing a rate-dependent term of the form $\partial \hat{\psi}_{\text{R}}(\mathbf{\Lambda})/\partial \lambda_{\text{c}} = -\kappa_c(\lambda_c)\dot{\lambda}_c$, as we did in Mao and Anand (2018).

and is taken to be purely energetic with no dissipative contribution.

Governing partial differential equations

The governing partial differential equations consist of:

1. **Equation of motion**:

$$\mathrm{Div}\,\mathbf{T}_{\mathrm{R}} + \mathbf{b}_{0\mathrm{R}} = \rho_{\mathrm{R}}\ddot{\boldsymbol{\chi}}, \tag{5.10}$$

where $\mathbf{b}_{0\mathrm{R}}$ is a non-inertial body force, ρ_{R} is the referential mass density, $\ddot{\boldsymbol{\chi}}$ the acceleration, and the Piola stress $\mathbf{T}_{\mathrm{R}}$ is given by (5.6). In the numerical simulations presented later in the paper we neglect all inertial effects.

2. **Microforce balance**:

The microforces ϖ and $\boldsymbol{\xi}$ obey the balance

$$\mathrm{Div}\boldsymbol{\xi} - \varpi = 0. \tag{5.11}$$

This microforce balance, together with the thermodynamically consistent constitutive equations (5.8) and (5.9) for ϖ and $\boldsymbol{\xi}$ gives the following evolution equation for the damage variable d,[6]

$$\hat{\zeta}(\boldsymbol{\Lambda})\dot{d} = -\frac{\partial\hat{\psi}_{\mathrm{R}}(\boldsymbol{\Lambda})}{\partial d} + \mathrm{Div}\left(\frac{\partial\hat{\psi}_{\mathrm{R}}(\boldsymbol{\Lambda})}{\partial\nabla d}\right) - \hat{\alpha}(\boldsymbol{\Lambda}). \tag{5.12}$$

Since ζ is positive-valued, the right hand side of (5.12) must be positive for $\dot{d}$ to be positive and the damage to increase monotonically.

Boundary and initial conditions

We also need boundary and initial conditions to complete the theory.

1. **Boundary conditions for the pde governing the evolution of the motion $\boldsymbol{\chi}$**:

Let $\mathcal{S}_{\boldsymbol{\chi}}$ and $\mathcal{S}_{\mathbf{t}_{\mathrm{R}}}$ be complementary subsurfaces of the boundary ∂B of the body B. Then for a time interval $t \in [0, T]$ we consider a pair of boundary conditions in which the motion is specified on $\mathcal{S}_{\boldsymbol{\chi}}$ and the surface traction on $\mathcal{S}_{\mathbf{t}_{\mathrm{R}}}$:

$$\left.\begin{aligned} \boldsymbol{\chi} &= \breve{\boldsymbol{\chi}} \quad \text{on } \mathcal{S}_{\boldsymbol{\chi}} \times [0,T], \\ \mathbf{T}_{\mathrm{R}}\mathbf{n}_{\mathrm{R}} &= \breve{\mathbf{t}}_{\mathrm{R}} \quad \text{on } \mathcal{S}_{\mathbf{t}_{\mathrm{R}}} \times [0,T]. \end{aligned}\right\} \tag{5.13}$$

In the boundary conditions above $\breve{\boldsymbol{\chi}}$ and $\breve{\mathbf{t}}_{\mathrm{R}}$ are *prescribed* functions of $\mathbf{X}$ and t.

[6]We use the phrases "damage variable" and "phase-field" interchangeably to describe d.

2. **Boundary conditions for the pde governing the evolution of the damage variable** d:

   The presence of microscopic stresses $\boldsymbol{\xi}$ results in an expenditure of power

   $$\int_{\partial \mathrm{B}} (\boldsymbol{\xi} \cdot \mathbf{n}_{\mathrm{R}}) \dot{d} \, da_{\mathrm{R}}$$

   by the material in contact with the body, and this necessitates a consideration of boundary conditions on ∂B involving the microscopic tractions $\boldsymbol{\xi} \cdot \mathbf{n}_{\mathrm{R}}$ and the rate of change of the damage variable $\dot{d}$.

   - *We restrict attention to boundary conditions that result in a null expenditure of microscopic power in the sense that* $(\boldsymbol{\xi} \cdot \mathbf{n}_R)\dot{d} = 0$.

   A simple set of boundary conditions which satisfies this requirement is,

   $$\begin{aligned} \dot{d} &= 0 \quad \text{on } \mathcal{S}_d \times [0,T], \\ \boldsymbol{\xi} \cdot \mathbf{n}_{\mathrm{R}} &= 0 \quad \text{on } \partial \mathrm{B} \setminus \mathcal{S}_d \times [0,T], \end{aligned} \tag{5.14}$$

   with the microforce $\boldsymbol{\xi}$ given by (5.9).

The initial data is taken as

$$\boldsymbol{\chi}(\mathbf{X},0) = \mathbf{X}, \qquad \dot{\boldsymbol{\chi}}(\mathbf{X},0) = \mathbf{v}_0(\mathbf{X}), \quad \text{and} \quad d(\mathbf{X},0) = 0 \quad \text{in} \quad \mathrm{B}. \tag{5.15}$$

The coupled set of equations (5.10) and (5.12) together with (5.13), (5.14), and (5.15) yield an initial/boundary-value problem for the motion $\boldsymbol{\chi}(\mathbf{X},t)$, and the damage variable $d(\mathbf{X},t)$.

5.3.2 Specialization of the constitutive equations

To build a predictive model we wish to characterize the process of rupture in elastomeric materials with weak crosslinks in terms of the microscopic mechanics of molecular crosslink deformation and failure. However, traditional hyperelasticity models for elastomers neglect the energetics of crosslinks deformation. Accordingly we formulate a hyperelastic constitutive model that accounts for the energetics of crosslink stretch, as well as the well-known entropic effects of polymer elasticity. In what follows we begin by considering the process of deformation of a single chain, and then extend the single chain considerations to bulk polymer networks undergoing damage and eventual failure.

Deformation of a single chain

Consider a single chain with n *unstretchable* segments, each of initial length L_b. Let

- $r_0 = \sqrt{n}\, L_b$ denote the unstretched chain length determined from random-walk statistics, and
- let r denote the end-to-end distance of chain in a deformed configuration.

The classical freely jointed chain theory gives the free energy ψ of a single chain as Kuhn and Grün (1942); Doi (1996),

$$\psi = \hat{\psi}(r) = k_{\mathrm{B}}\vartheta n \left[\frac{r}{nL_b}\beta + \ln\left(\frac{\beta}{\sinh\beta}\right)\right] \qquad \text{with} \qquad \beta = \mathcal{L}^{-1}\left(\frac{r}{nL_b}\right), \tag{5.16}$$

where k_{B} is Boltzmann's constant, ϑ is the absolute temperature, and $\mathcal{L}^{-1}$ is the inverse of the Langevin function $\mathcal{L}(x) = \coth x - x^{-1}$.

In order to arrive to an expression for the free energy which accounts for cross-link deformation, we first consider the behavior of a single chain with a crosslink at each end, each of length L_c (see Figure 5-9).

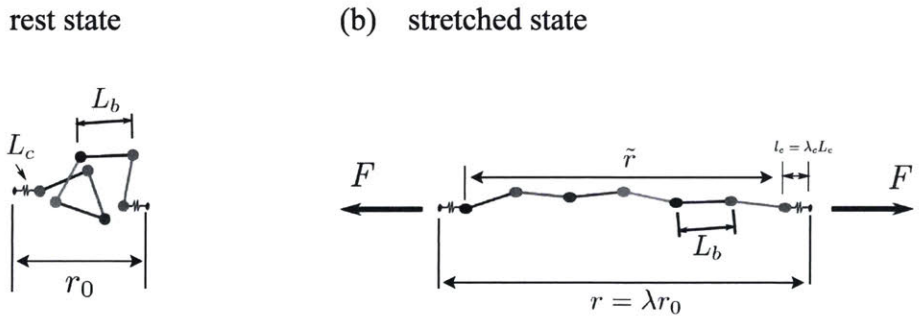

Figure 5-9: Schematic of a single chain with weak crosslinks at each end: (a) rest state and (b) stretched state. The Kuhn segments are assumed to be rigid while the crosslinks are assumed to be deformable.

Generally, the overall deformation of the single polymer chain under load is due to three sources:

(i) the alignment of the Kuhn segments;

(ii) stretching of the Kuhn segments; and

(iii) stretching of the molecular bonds associated with crosslinks at each end.

We make the constitutive assumption that

- the Kuhn segments in the chain are much stiffer than the molecular bonds associated with the two crosslinks at each end, so that the stretchability and the internal energy stored within the Kuhn segments is negligible.

To further simplify the physical picture we assume that the configurational entropy stored within the molecular bonds associated with crosslinks are negligible, and that both the crosslink bonds are aligned with and follow the direction of the stretching force (cf. Fig. 5-9(b)).

The stretchable bonds associated with crosslinks may extend such that their deformed length is

$$l_c = \lambda_c L_c, \tag{5.17}$$

where λ_c is a dimensionless stretch which we refer to as the *crosslink stretch.* Then, with $\hat{\varepsilon}_c(\lambda_c)$ denoting the internal energy associated with the stretching of the crosslinks, we take the free energy to be given by,

$$\begin{aligned} \psi = \hat{\psi}(\tilde{r}, \lambda_c) &= 2\hat{\varepsilon}_c(\lambda_c) + k_B \vartheta n \left(\frac{\tilde{r}}{nL_b}\beta + \ln\left(\frac{\beta}{\sinh\beta}\right)\right) \\ \text{with} \qquad \beta &= \mathcal{L}^{-1}\left(\frac{\tilde{r}}{nL_b}\right), \end{aligned} \tag{5.18}$$

and with

$$\tilde{r} = r - 2\lambda_c L_c \tag{5.19}$$

the net end-to-end distance of the part of the chain with rigid Kuhn segments. It is convenient to rewrite the free energy (5.18) in terms of the overall chain stretch

$$\lambda = \frac{r}{r_0}, \tag{5.20}$$

where r_0, the unstretched chain length, which is now given by

$$r_0 = \sqrt{n} L_b + 2L_c. \tag{5.21}$$

Typically the statistical segment length L_b is approximately 5 to 10 times the length of a backbone bond within the polymer chain ($\approx 0.15\,\text{nm}$), and the effective length L_c of a crosslink is of the same order as the length of a backbone bond. This gives $L_c \sim 0.1$ to $0.2L_b$, so that neglecting the term $2L_c$ relative to the first term $\sqrt{n}L_b$ in (A.21), we can simplify the rest length of chain with the two crosslinks as

$$r_0 \sim \sqrt{n} L_b. \tag{5.22}$$

Using (5.17), (5.19), (A.20), (A.21), and (5.22) in(5.18) yields the following expression for the free energy,

$$\begin{aligned} \psi = \hat{\psi}(\lambda, \lambda_c) &= 2\hat{\varepsilon}_c(\lambda_c) + k_B \vartheta n \left[\left(\frac{\lambda}{\sqrt{n}} - \frac{2L_c\lambda_c}{nL_b} \right) \beta + \ln \left(\frac{\beta}{\sinh \beta} \right) \right], \\ \text{with } \beta &= \mathcal{L}^{-1} \left(\frac{\lambda}{\sqrt{n}} - \frac{2L_c\lambda_c}{nL_b} \right). \end{aligned} \tag{5.23}$$

As it stands, the contribution from the change in entropy to the free energy in (5.23) does not reduce to the classical expression (5.16) in the limit $\lambda_c \to 1$. To achieve this we require that $\hat{\varepsilon}_c(1) = 0$ and modify (5.23) to read as,

$$\begin{aligned} \psi &= \hat{\psi}(\lambda, \lambda_c) \\ &= \underbrace{2\hat{\varepsilon}_c(\lambda_c)}_{\hat{\varepsilon}^0(\lambda_c)} + \underbrace{k_B \vartheta n \left[\left(\frac{\lambda}{\sqrt{n}} - \frac{2L_c(\lambda_c - 1)}{nL_b} \right) \beta + \ln \left(\frac{\beta}{\sinh \beta} \right) \right]}_{-\vartheta \hat{\eta}(\lambda, \lambda_c)}, \\ \text{with } \beta &= \mathcal{L}^{-1} \left(\frac{\lambda}{\sqrt{n}} - \frac{2L_c(\lambda_c - 1)}{nL_b} \right). \end{aligned} \tag{5.24}$$

Here, the first term denotes the internal energy associated with the stretching of the crosslinks, and the second term is for the configurational entropy associated with Kuhn segments.

At any *fixed* stretch λ, increasing λ_c increases the internal energy contribution to the free energy while decreasing the entropic part. This competition induces an optimal value of λ_c which will minimize the free energy and will be the actual state adopted by the system. Thus, setting $\partial\psi/\partial\lambda_c = 0$ provides an implicit equation for λ_c, which reads

$$\frac{\mathrm{d}\hat{\varepsilon}_c(\lambda_c)}{\mathrm{d}\lambda_c} - k_B \vartheta \frac{L_c}{L_b} \mathcal{L}^{-1} \left(\frac{\lambda}{\sqrt{n}} - \frac{2L_c(\lambda_c - 1)}{nL_b} \right) = 0. \tag{5.25}$$

Deformation, damage, and failure of a crosslinked network of polymer chains

We employ the widely-used eight-chain network representation of Arruda and Boyce (1993) to extend the single chain model to a continuum model for a polymer network.[7] The entropy and energy of the network can be obtained by summing the contributions from individual chains as given by the single chain model. To this end, we follow Anand (1996) and define the effective chain stretch

$$\bar{\lambda} \stackrel{\text{def}}{=} \sqrt{\operatorname{tr} \bar{\mathbf{C}}/3}, \tag{5.26}$$

[7] Note that in addition to the usual assumption of weak chain interactions, we must additionally assume that the damage in each chain is independent in order apply the Arruda-Boyce network model.

where $\mathrm{tr}(\cdot)$ represents the trace of a second order tensor, $\bar{\mathbf{C}} = \bar{\mathbf{F}}^{\top}\bar{\mathbf{F}}$ is the distortional right Cauchy-Green tensor, and $\bar{\mathbf{F}} = (\det \mathbf{F})^{-1/3}\mathbf{F}$ is the distortional part of the deformation gradient. Then, with

- N representing the number of chains per unit volume of the reference configuration,

the entropy density of the network is given by

$$\begin{aligned} \eta_{\mathrm{R}} = \hat{\eta}_{\mathrm{R}}(\bar{\lambda}, \lambda_c) &= -Nk_B n \left[\left(\frac{\bar{\lambda}}{\sqrt{n}} - \frac{2L_c(\lambda_c - 1)}{nL_b} \right) \beta + \ln \left(\frac{\beta}{\sinh \beta} \right) \right], \\ \beta &= \mathcal{L}^{-1} \left(\frac{\bar{\lambda}}{\sqrt{n}} - \frac{2L_c(\lambda_c - 1)}{nL_b} \right), \end{aligned} \tag{5.27}$$

where

- L_b is the *statistical segment length* of a rigid-link of the chain, and
- L_c is an effective length of a crosslink.

As mentioned previously, typically the statistical segment length L_b is about 5 to 10 times the length of a backbone bond within the polymer chain ($\approx 0.15\,\mathrm{nm}$), and the effective length L_c of a crosslink is of the same order as the length of a backbone bond.

Also, the internal energy density ε_{R} of the network is taken to depend on λ_c, a damage variable d and its gradient ∇d, and we also allow for internal energy contribution due to volume ratio J,

$$\varepsilon_{\mathrm{R}} = \hat{\varepsilon}_{\mathrm{R}}(\lambda_c, J, d, \nabla d) = g(d)\hat{\varepsilon}^0_{\mathrm{R}}(\lambda_c, J) + \hat{\varepsilon}_{\mathrm{R,nonloc}}(\nabla d). \tag{5.28}$$

We consider the following specializations for the different terms in the expression (5.28) for the internal energy per unit refrence volume:

(i) The term $\hat{\varepsilon}^0_{\mathrm{R}}(\lambda_c, J)$ represents an *undamaged* internal energy per unit reference volume for which we choose a simple constitutive relation of the form,

$$\hat{\varepsilon}^0_{\mathrm{R}}(\lambda_c, J) = \frac{1}{2} N_c\, E_c(\lambda_c - 1)^2 + \underbrace{\frac{1}{2} K(J-1)^2}_{\hat{\varepsilon}_{\mathrm{Rvol}}(J)}, \tag{5.29}$$

where,

- E_c represents a stiffness of the crosslinks;
- N_c is the number of crosslinks per unit reference volume, with $N_c \lessapprox N$; and
- K a bulk modulus for the network to account for intermolecular interactions and a slight compressibility of the material.[8]

[8] The particular form of the volumetric internal energy is not crucial for elastomers in which the volume changes due to intermolecular interactions are typically quite small relative to distortional deformations. In

(ii) The function $g(d)$ is a monotonically decreasing *degradation function* with values,

$$g(0) = 1, \qquad g(1) = 0, \qquad \text{and} \qquad g'(1) = 0.$$

A widely-used degradation function is

$$g(d) = (1-d)^2; \tag{5.30}$$

we adopt it here.

(iii) The term $\hat{\varepsilon}_{\mathrm{R,nonloc}}(\nabla d)$ in the internal energy density is a nonlocal contribution

$$\hat{\varepsilon}_{\mathrm{R,nonloc}}(\nabla d) = \frac{1}{2}\varepsilon_{\mathrm{R}}^{f}\,\ell^2\,|\nabla d|^2\,, \tag{5.31}$$

where ℓ represents an intrinsic length scale for the damage process, and

$$\varepsilon_{\mathrm{R}}^{f} \stackrel{\mathrm{def}}{=} N_c\varepsilon_c^f \tag{5.32}$$

represents the energy of crosslink scission per unit volume when all crosslinks are broken.[9]

With the constitutive relations (5.27)-(5.32) for ε_{R} and η_{R} in hand, the free energy $\psi_{\mathrm{R}} = \varepsilon_{\mathrm{R}} - \vartheta\eta_{\mathrm{R}}$ is given by

$$\begin{aligned}\psi_{\mathrm{R}} &= (1-d)^2\left(\frac{1}{2}\bar{E}_c(\lambda_c-1)^2 + \frac{1}{2}K(J-1)^2\right)\\ &\quad + G_0 n\left[\left(\frac{\bar{\lambda}}{\sqrt{n}} - \frac{2L_c(\lambda_c-1)}{nL_b}\right)\beta + \ln\left(\frac{\beta}{\sinh\beta}\right)\right],\\ &\quad + \frac{1}{2}\varepsilon_{\mathrm{R}}^{f}\,\ell^2\,|\nabla d|^2\,, \qquad \text{with} \qquad \beta = \mathcal{L}^{-1}\left(\frac{\bar{\lambda}}{\sqrt{n}} - \frac{2L_c(\lambda_c-1)}{nL_b}\right),\end{aligned} \tag{5.33}$$

our finite element simulations we encountered some convergence difficulties with the simple quadratic form $\hat{\varepsilon}_{\mathrm{Rvol}}(J) = 1/2K(J-1)^2$ of the volumetric internal energy at late stages of the damage. Accordingly, in our computations we have used the alternate form $\hat{\varepsilon}_{\mathrm{Rvol}}(J) = K/8(J-J^{-1})^2$ which reduces to a simple quadratic energy as $J \to 1$,

$$\hat{\varepsilon}_{\mathrm{Rvol}}(J) = \frac{K}{8}(J-J^{-1})^2 = \frac{K}{8}(J-1)^2\left(1+\frac{1}{J}\right)^2 \approx \frac{1}{2}K(J-1)^2.$$

If for some numerical reason J becomes large during the iteration process, then the alternate form leads to a softer response (see Schröder and Neff, 2003).

[9]In formulating a theory that accounts for the stretching and failure of the crosslinks we have assumed that all crosslinks in a continuum material point are uniformly stretched and that they fail simultaneously. This is clearly a major approximation since the actual failure process is expected to be stochastic in nature, with the weakest link failing first.

where we have introduced the notations

$$G_0 \stackrel{\text{def}}{=} N k_B \vartheta \qquad \text{and} \qquad \bar{E}_c \stackrel{\text{def}}{=} N_c E_c, \tag{5.34}$$

with G_0 representing the ground-state shear modulus for the polymer network, and $\bar{E}_c$ a crosslink stiffness parameter for the network.

Using this free energy (9.7), equations (5.5) and (5.6) give the Piola stress $\mathbf{T}_{\text{R}}$ as

$$\begin{aligned} &\mathbf{T}_{\text{R}} = \bar{G}\left(J^{-2/3}\mathbf{F} - \bar{\lambda}^2\mathbf{F}^{-\top}\right) + (1-d)^2 K(J-1)J\mathbf{F}^{-\top}, \qquad \text{where} \\ &\bar{G} \stackrel{\text{def}}{=} G_0\left(\frac{\sqrt{n}}{3\bar{\lambda}}\right)\mathcal{L}^{-1}\left(\frac{\bar{\lambda}}{\sqrt{n}} - \frac{2L_c(\lambda_c-1)}{nL_b}\right), \end{aligned} \tag{5.35}$$

is a generalized shear modulus. Also, (5.7) gives that the effective crosslink stretch λ_c is determined by solving the implicit equation

$$(1-d)^2\bar{E}_c\,(\lambda_c - 1) - 2G_0\frac{L_c}{L_b}\mathcal{L}^{-1}\left(\frac{\bar{\lambda}}{\sqrt{n}} - \frac{2L_c(\lambda_c-1)}{nL_b}\right) = 0. \tag{5.36}$$

Note that generalized shear modulus $\bar{G}$ is connected to the damage field d implicitly through equation (5.36) for λ_c.

To complete the specification of the constitutive relations, we specify the dissipative microforce ϖ_{diss} that expends power through $\dot{d}$.[10] The dissipative microforce is partitioned into a rate-independent part and a rate-dependent part through

$$\varpi_{\text{diss}} = \underbrace{\alpha}_{\text{rate-independent}} + \underbrace{\zeta\dot{d}}_{\text{rate-dependent}}. \tag{5.37}$$

The rate-independent part of the dissipative microforce α is the sum of the contributions from each crosslink and given by (5.32), thus

$$\alpha = \varepsilon^f_{\text{R}}. \tag{5.38}$$

The rate-dependent contribution to the dissipative microforce $\zeta\dot{d}$, is simply described by a constant kinetic modulus $\zeta > 0$, with the rate-independent limit of damage evolution given by $\zeta \to 0$.

Using the specializations above, the microforce balance (5.12), which gives the evolution of d, becomes

$$\zeta\dot{d} = 2(1-d)\hat{\varepsilon}^0_{\text{R}}(\lambda_c, J) + \varepsilon^f_{\text{R}}\ell^2\Delta d - \varepsilon^f_{\text{R}}. \tag{5.39}$$

[10] Cf. eq. (5.9).

The microforce balance (5.39) can be rewritten to enforce the constraint $d \in [0,1]$ in a simple way. Add and subtract the term $\varepsilon_{\mathrm{R}}^f d$ to get

$$\zeta \dot{d} = 2(1-d)\left(\hat{\varepsilon}_{\mathrm{R}}^0(\lambda_c, J) - \varepsilon_{\mathrm{R}}^f/2\right) - \varepsilon_{\mathrm{R}}^f d + \varepsilon_{\mathrm{R}}^f \ell^2 \Delta d. \tag{5.40}$$

The constraint $d \in [0,1]$ is automatically satisfied if the equation above is modified to read as,

$$\zeta \dot{d} = 2(1-d)\left\langle \hat{\varepsilon}_{\mathrm{R}}^0(\lambda_c, J) - \varepsilon_{\mathrm{R}}^f/2 \right\rangle - \varepsilon_{\mathrm{R}}^f \left(d - \ell^2 \Delta d\right). \tag{5.41}$$

where $\langle \bullet \rangle$ are Macauley brackets, i.e.,

$$\langle x \rangle = \begin{cases} 0, & x < 0, \\ x, & x \geq 0. \end{cases}$$

At this stage the irreversible nature of crosslink scission is not yet reflected in the model. To this end, we replace the term $\langle \hat{\varepsilon}_{\mathrm{R}}^0(\lambda_c, J) - \varepsilon_{\mathrm{R}}^f/2 \rangle$ in the microforce balance with the monotonically increasing history field function (cf., Miehe et al., 2010):

$$\mathcal{H}(t) \stackrel{\text{def}}{=} \max_{s \in [0,t]} \left\langle \hat{\varepsilon}_{\mathrm{R}}^0(\lambda_c(s), J(s)) - \varepsilon_{\mathrm{R}}^f/2 \right\rangle, \tag{5.42}$$

where at each $s \in [0,t]$,

$$\hat{\varepsilon}_{\mathrm{R}}^0(\lambda_c(s), J(s)) = \frac{1}{2}\bar{E}_c \left(\lambda_c(s) - 1\right)^2 + \frac{1}{2}K(J(s)-1)^2, \tag{5.43}$$

and

$$\varepsilon_{\mathrm{R}}^f = N_c \, \varepsilon_c^f, \tag{5.44}$$

is a fracture energy. With these modifications the evolution equation (5.12) for the damage variable d becomes,

$$\zeta \dot{d} = 2(1-d)\mathcal{H} - \varepsilon_{\mathrm{R}}^f (d - \ell^2 \Delta d), \tag{5.45}$$

which is of a form similar to that in the paper by Miehe and Schänzel (2014) on phase field modeling of fracture of rubbery polymers.

Material parameters in the theory: The theory involves the following material parameters:

$$L_b, \quad n, \quad N, \quad L_c, \quad N_c, \quad E_c, \quad K, \quad \varepsilon_c^f, \quad \ell, \quad \text{and} \quad \zeta. \tag{5.46}$$

Here, L_b is the statistical length of a rigid segment in a chain; n is the number of rigid segments in a chain; N is the number of chains per unit volume; L_c is the length of a crosslink; N_c is the number of crosslinks per unit volume; E_c represents the stiffness of the crosslinks; K represents the bulk modulus of the material; ε_c^f, a crosslink dissociation energy per unit volume; ℓ is a characteristic length scale of the gradient theory under consideration;

and ζ is a kinetic modulus for the evolution of the damage. All parameters are required to be positive.

In the numerical simulations to described in the next section, instead of the parameter list (5.46), we use the parameter list,

$$L_c = 0.2L_b, \quad G_0 = Nk_B\vartheta, \quad n, \quad \bar{E}_c = N_cE_c, \quad K, \quad \varepsilon_{\mathrm{R}}^f = N_c\varepsilon_c^f, \quad \ell, \quad \text{and} \quad \zeta, \tag{5.47}$$

where G_0 is the ground-state shear modulus for the polymer network, $\bar{E}_c$ is a crosslink-stiffness parameter for the network, and $\varepsilon_{\mathrm{R}}^f$ represents the energy per unit volume for the dissociation of the crosslinks in a network.

5.3.3 Application of the theory to study plane-stress fracture of elastomers

We have numerically implemented our theory in the open-source finite element code MOOSE Gaston et al. (2009) by writing our own application to solve 3D, plane strain, plane-stress, axisymmetric problems. MOOSE uses a sophisticated nonlinear solver technology, and it may be massively parallelized. Using this new numerical capability, in this section we report on some representative simulations of deformation and fracture of an elastomeric material. Specifically, we study the capability of the model to describe *plane stress* fracture of

(i) single-edge-notched specimens;

(ii) an asymmetric double-edge-notched specimen; and

(iii) fracture of a sheet specimen with multiple circular and elliptical holes.

All simulations were performed on a parallelized linux cluster. Visualization of the results was performed by using the open-source code ParaView Ayachit (2015).

Single-edge-notch Mode-I loading under plane-stress conditions with different notch lengths

We begin with a study of fracture in single-edge-notch specimens with different crack lengths, under plane-stress Mode-I loading conditions. Fig. 6-1(a) shows a schematic of the specimen geometry. The overall size of the notched sheet sample is 18 mm $\times$ 20 mm in the plane, and the sheet is 1 mm thick. We consider specimens with notch lengths c = 3, 6, and 9 mm; the initial root-radius of the notch is fixed at 0.1 mm. The material parameters used in our simulations are shown in Table 6.1. In our simulation, we utilize the symmetry, and the middle edge of the specimen is fixed, while the top edge is prescribed a displacement at a nominal stretch rate of 1×10^{-3}/s.

Some remarks concerning the choice of material parameters:

Table 5.3: Representative values of the material parameters used in the simulations.

$G_0 = Nk_B\vartheta$	n	$\bar{E}_c = N_c E_c$	K	$\varepsilon_{\mathrm{R}}^f = N_c \varepsilon_c^f$	ℓ	ζ
0.2 MPa	4	0.2 MPa	20 MPa	1 MPa	100μm	10 kPa·s

1. The kinetic modulus ζ, which has units of Pa-s, may be thought of as a viscous regularization parameter for an essentially rate-independent damage process, and ζ/G_0 therefore represents a time constant in the theory. For a given macroscopic stretch-rate $\dot{\lambda}$, our numerical experiments have shown that a value of ζ which is commensurate with $(\zeta\dot{\lambda}/G_0) \lessapprox 10^{-3}$ is small enough to give an almost rate-independent damage evolution. For the values of ζ and G_0 listed in Table 6.1 and a nominal stretch rate $\dot{\lambda} = 1 \times 10^{-3}$/s, we have $(\zeta\dot{\lambda}/G_0) = 5 \times 10^{-5}$ which well-approximates a rate-independent damage evolution response.

2. We have used a value of the bulk modulus K which is 100 times larger than the ground state shear modulus G_0; this corresponds to a ground-state Poisson's ratio of $\nu = 0.495$, which approximates an elastically incompressible material. We tried using larger values of K relative to that of G_0, but that slowed down our numerical procedures considerably. So in all the calculations reported in this paper we have used $K/G_0 = 100$.

3. We have intentionally chosen a small value $n = 4$ for the number of links in the chain to illustrate the features of our theory, so that failure of the chains in our simulations occurs at reasonable levels of macroscopic stretch.

Fig. 5-10(b) shows the calculated force-displacement curves for cracks with initial lengths of $c = 3$, 6, 9 mm. As expected, as the initial length of the crack increases the overall force level becomes lower, and the stretch at which final fracture occurs becomes smaller. Contour plots for the damage variable d at points (a) through (h) on the load displacement curve for a specimen with $c = 9$ mm are shown in Fig. 5-11.

Fig. 5-11 shows the deformed geometry at points (a) through (h) on the force-displacement curve in Fig. 5-10(b), together with contours of the damage variable d. To aid visualization of the damage, elements with an average value of $d > 0.99$ are not plotted. Since the length scale $\ell = 100\,\mu$m is very small when compared with the overall dimension of the specimen (~ 20 mm), the damage zone is barely visibly in this sequence of plots. Fig. 5-11(a) is the initial configuration. As the sample is stretched to (b) the notch is blunted, but no damage has initiated. Damage initiates when the sample is stretched further to a displacement level of ~ 5.5 mm (a point just before (c)), but the force is still increasing, and it is after another ~ 0.5 mm of extension that the force reaches a peak at point (c) in force-displacement curve, and from the contour of damage shown in Fig. 5-11(c), a small damage zone ahead of the crack becomes observable. Further stretching begins the rupture process, and Figs. 5-11(d)

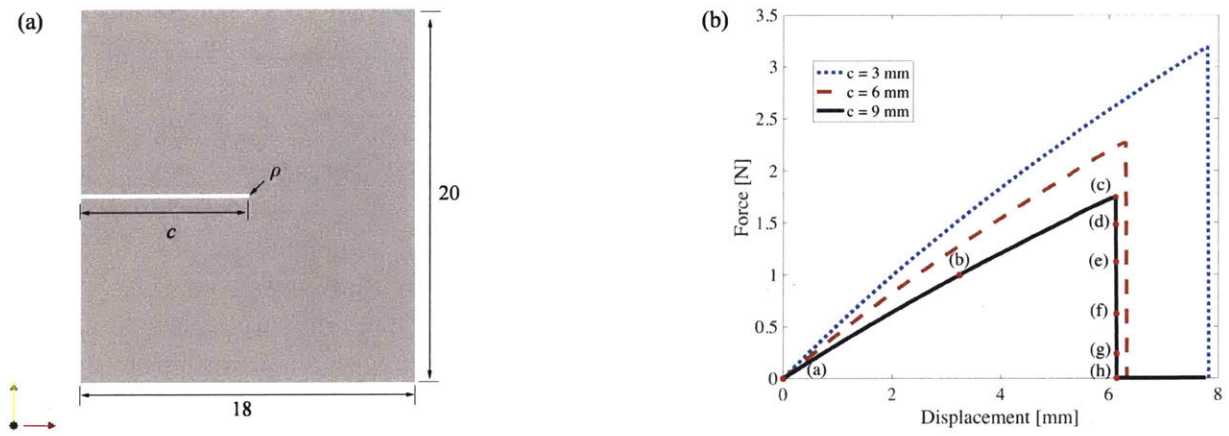

Figure 5-10: (a) Schematic of the single-edge-notch specimen geometry; all dimensions are in mm. The thickness of the sample is 1 mm; the notch length is denoted by c; and $\rho = 0.1$ mm is the notch-root radius. (b) Calculated force-displacement curves for $c = 3$, 6, 9 mm. Contour plots for the damage variable d at points (a) through (h) on the load displacement curve for a specimen with $c = 9$ mm are shown in Fig. 5-11.

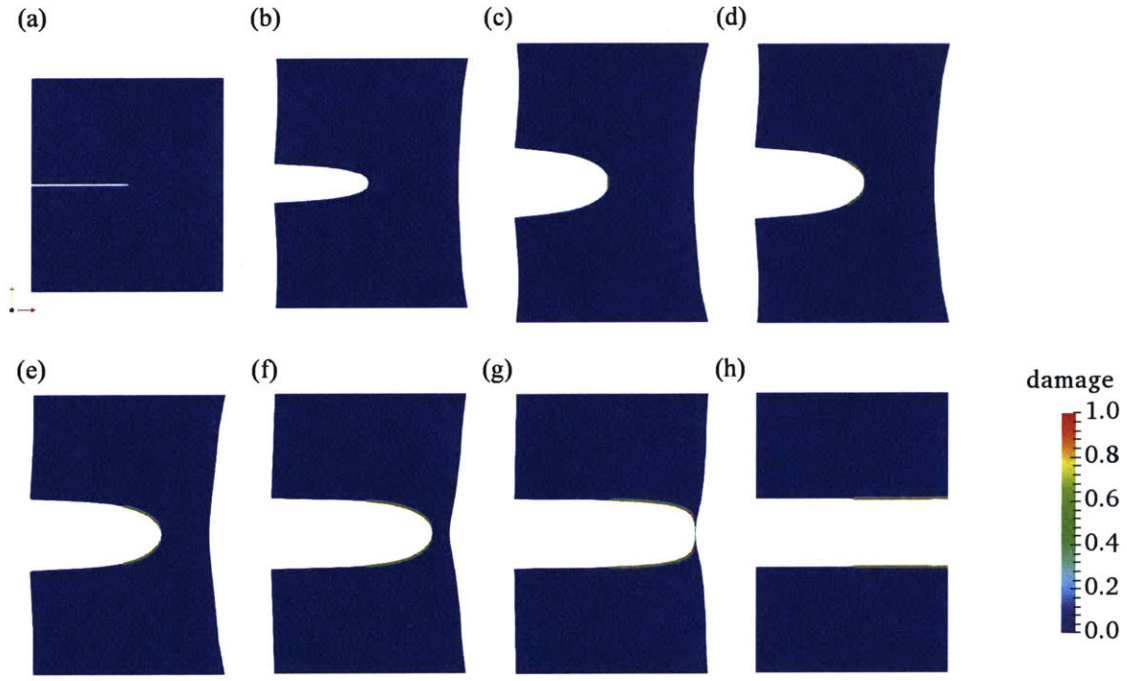

Figure 5-11: Images of the deformed geometry with contour plots of the damage variable d. To aid visualization of the damage, elements with an average value of $d > 0.99$ are removed from the plots. Since the length scale $\ell = 100\,\mu$m is very small when compared with the overall dimension of the specimen (~ 20 mm), the damage zone is barely visibly in this this sequence of contour plots for d.

through (h) show this progressive rupturing, with (h) showing the final failed configuration. Note from Fig. 5-10(b) that the force at stage (h) stage is essentially zero.

Figure 5-12 shows a contour plot of the crosslink stretch, λ_c, at a particular stage of the failure process for a specimen with an initial notch depth of $c = 9\,\text{mm}$. The crack has propagated almost halfway through the remaining ligament of the specimen. The contours are plotted on the reference configuration in order to highlight the extent of crack propagation relative to the initial specimen geometry. Also, the highly damaged elements ($d > 0.99$) are again hidden from view. When failure occurs for a large sample, the deformation localizes to a small region in the vicinity of the crack-tip. In this region, the effective stretch $\bar{\lambda}$ can be very large, and λ_c will increase to the level of $\bar{\lambda}\frac{\sqrt{n}L_b}{2L_c}$, which is also very large. Therefore, in order to visualize the contours of λ_c, we have set the maximum value of the contour in λ_c to 10. As is clear from Figures 5-12, the region of high crosslink stretch is limited to a small region in the vicinity of the crack tip, on a scale comparable to the length scale ℓ, while the majority of the specimen displays negligible crosslink stretching.

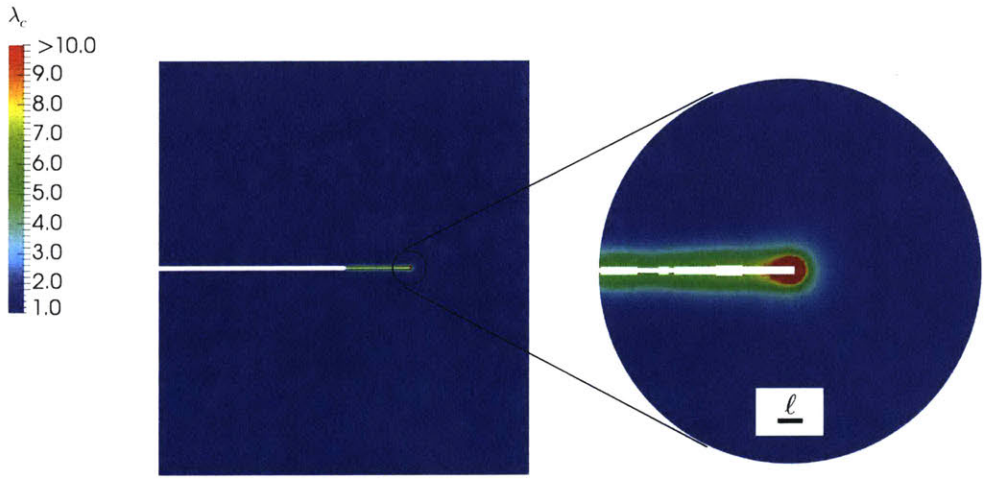

Figure 5-12: Contours of crosslink stretch λ_c during the fracture process in a specimen with $c = 9\,\text{mm}$. The crosslink stretch is appreciable only in a small zone near the crack tip. The contours are plotted on the reference configuration. Elements with $d > 0.99$ are removed from the visualization.

Fracture in an asymmetric-double-edge-notched sheet of an elastomeric sample under Mode-I plane-stress loading

In this section we study fracture of an asymmetric-double-notched sheet specimen of an elastomeric sample under Mode-I plane-stress loading. This example shows the powerful capability of our gradient-damage theory to model the merging of two growing cracks.

Fig. 5-13(a) shows a schematic of the specimen geometry. The overall size of the double-edge-notched sheet sample is $18\,\text{mm} \times 20\,\text{mm}$ in the plane, and the sheet is 1 mm thick. The two offset notches each have a of length $c = 3\,\text{mm}$; the initial root-radius of the notch is

0.1 mm. We use the same values of the material parameters as in Section 5.3.3. The bottom edge of the specimen is fixed, while the top-edge is prescribed a displacement at a nominal stretch rate of 1×10^{-3}/s. Fig. 5-13(b) shows the calculated force-displacement curve.

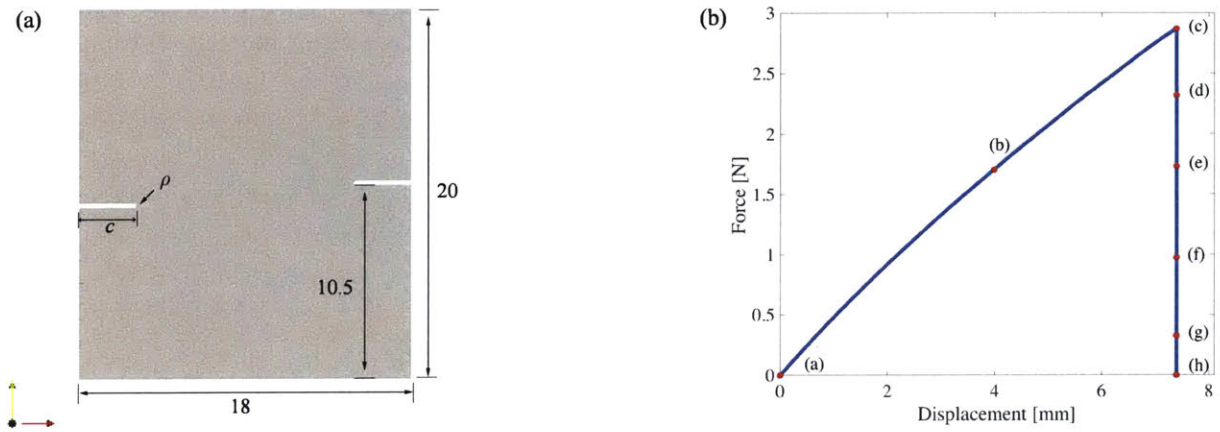

Figure 5-13: (a) Schematic of the asymmetric-double-edge-notch specimen geometry; all dimensions are in mm. The thickness of the sample is 1 mm; the notches are of length $c = 3$ mm; and $\rho = 0.1$ mm is the notch-root radius. (b) Calculated force-displacement curve. The contour plots for the damage variable d at points (a) through (j) on the load displacement curve are shown in Fig. 5-14.

The contour plots for the damage variable, d at points (a) through (h) on the load displacement curve in Fig. 6-6(b) are shown in in Fig. 6-7. To aid visualization of the damage, elements with an average value of $d > 0.99$ are removed from the plots. Since the length scale $\ell = 100\,\mu$m is very small compared with the overall dimension of the specimen (20 mm), the damage zone is barely visibly in this this sequence of plots. Fig. 6-7(a) is the initial configuration. As the sample is stretched to (b) both the notches get blunted, but no damage has initiated. Damage initiates when the sample is stretched further to a displacement of $\sim$ 6.4mm (just before state (c)), but the force is still increasing; it is only after another $\sim$ 1 mm of extension that the force reaches a peak at point (c) in the force-displacement curve Fig. 6-6(b), and from the contour of damage d shown in Fig. 6-7 (c), a small damaged zone ahead of the crack becomes observable. Figs. 6-7(d) through (h) shows the subsequent rupturing process on two cracks merging, with Fig. 6-7(g) shows a pinching off process, which leads to final fracture into two separate pieces, as shown in Fig. 6-7(h).

Fracture in a sample with several circular and elliptical holes under plane-stress tension

In this section we study fracture of a sample with several circular and elliptical holes under plane-stress tension. Sharp cracks are necessary for classical fracture mechanics analysis. However, sharp cracks are not necessary in our gradient-damage theory of fracture. This

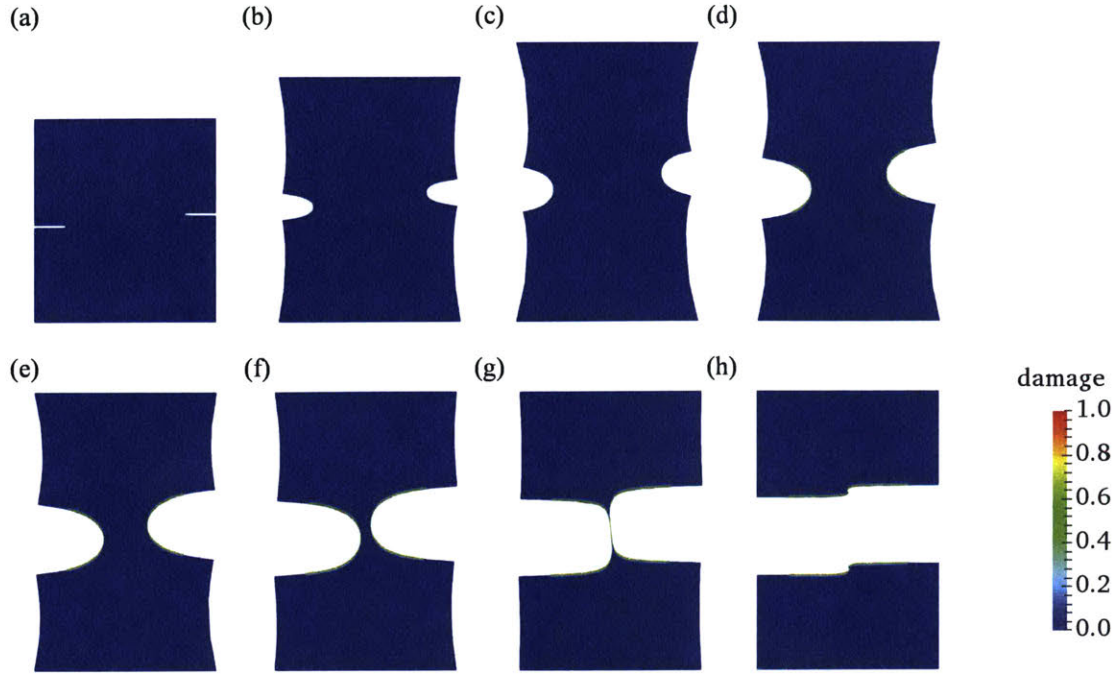

Figure 5-14: The deformed geometry with contour plots of the damage variable d. To aid visualization of the damage, elements with an average value of $d > 0.99$ are removed from the plots. Since the length scale $\ell = 100\,\mu$m is very small compared with the overall dimension of the specimen ($\sim 20\,$mm), the damage zone is barely visibly in this sequence of plots.

example shows the powerful capability of our gradient-damage theory to simulate the complicated fracture process of nucleation, propagation, branching and merging of cracks in arbitrary geometries — propagating cracks are tracked automatically by the evolution of the smooth damage-field d on a fixed mesh.

Fig. 5-15 shows a schematic of the specimen geometry. The overall size of the sample is $20\,\text{mm} \times 10\,\text{mm}$ in the plane, and the sheet is 1 mm thick. We use the same values of the material parameters as in Section 6.1. The bottom edge of the specimen is fixed, while the top-edge is prescribed a displacement at a nominal stretch rate of $1 \times 10^{-3}/\text{s}$.

Fig. 5-16(a) shows the calculated force-displacement curve. There are four different stages in the force-displacement curve:

(i) The blue line indicates the first stage. In this stage, as the specimen is stretched the force increases, and at the end of this stage the force reaches a peak and begins to drop.

(ii) The dashed-black line indicates the second stage, and represents the initial phase of the force drop.

(iii) The solid-yellow line indicates the third stage, and represents the next phase of the force drop.

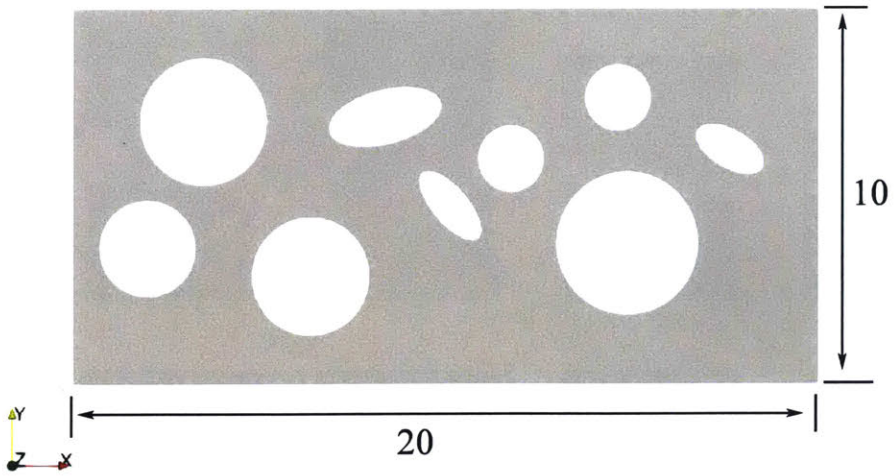

Figure 5-15: Schematic of the geometry of specimen with several circular and elliptical holes; all dimensions are in mm. The thickness of the sample is 1 mm.

(iv) And the dotted-pink line indicates the fourth stage, and represents the final phase of the force-displacement curve.

Fig. 5-16(b) through (d) show zoom-ins of the force decreasing portions in stages two, three, and four. Within each of these stages there are instances in which the force-displacement curve resembles the shape of the number "7". For example, as shown in Fig. 5-16(b), there are three "7"-shaped instances in the second stage. Each "7"-shaped instance corresponds to the failure of a ligament in the sample. Labels (b1)-(b4) through (h1)-(h4) marked on the force displacement curves in Fig. 5-16(b) through (d) are used to indicate important frames for the failure of a specific ligament.

Contour plots for the damage variable d at points (a) through (h) on the load displacement curve for a specimen are shown in Fig. 5-17 and Fig. 5-18. To aid visualization of the damage, elements with an average value of $d > 0.99$ are not plotted. A red arrow is used to indicate the ligament in which damage and rupture is occurring.

Fig. 5-17(a1) shows the initial configuration. As the sample is stretched to (a2) and (a3) the holes are deformed, but no damage has initiated. Damage initiates when the sample is stretched further to a displacement level of $\sim$ 9 mm, a point just before (a4), but the force is still increasing. It is after another $\sim$ 0.85 mm of extension that the force reaches a peak at point (a4) in force-displacement curve. From the contours of the damage shown in Fig. 5-17(a4), a small damage zone indicated by a red arrow becomes observable. The ligaments between the holes in the soft matrix become highly stretched by point (a4). Further stretching begins the progressive rupture process of these ligaments.

The second stage in the force-displacement curve corresponds to failure of three ligaments, as indicated in Fig. 5-16(b) and Fig. 5-17 (b) through (d). In these curves the marks (b1)-(b4), (c1)-(c4), and (d1)-(d4) are used to indicate important frames for the failure of a

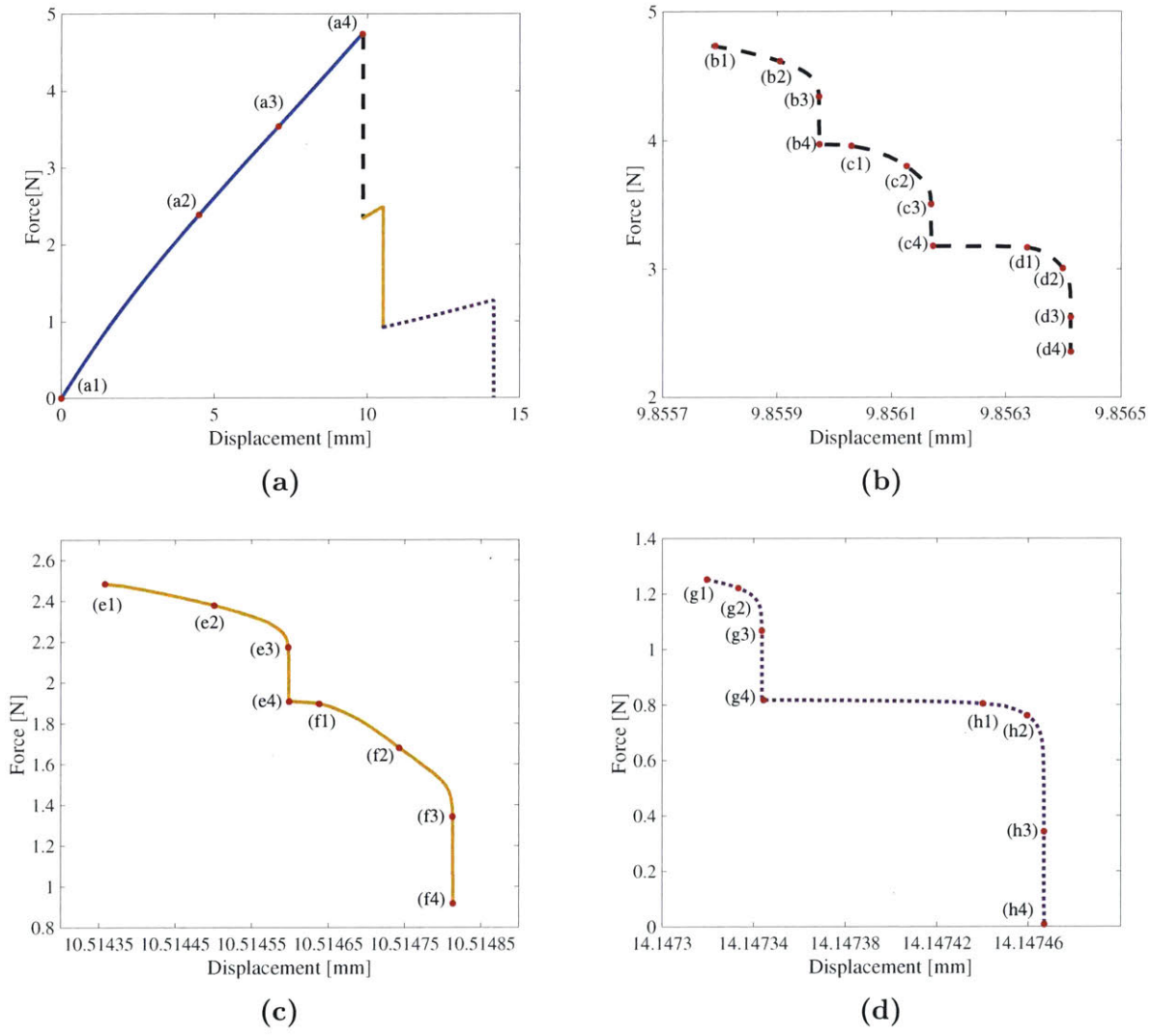

Figure 5-16: (a) Calculated force-displacement curve. There are four different stages within the curve: (i) The blue line indicates the first stage. (ii) The dashed-black line indicates the second stage. (iii) The solid-yellow line indicates the third stage. And (iv) the dotted-pink line indicates the fourth stage. (b) throuh (d) show zoom-in figures for the corresponding force drop stages. The contour plots for the damage variable d at points (a) through (h) on the load displacement curve are shown in Fig. 5-17 and Fig. 5-18.

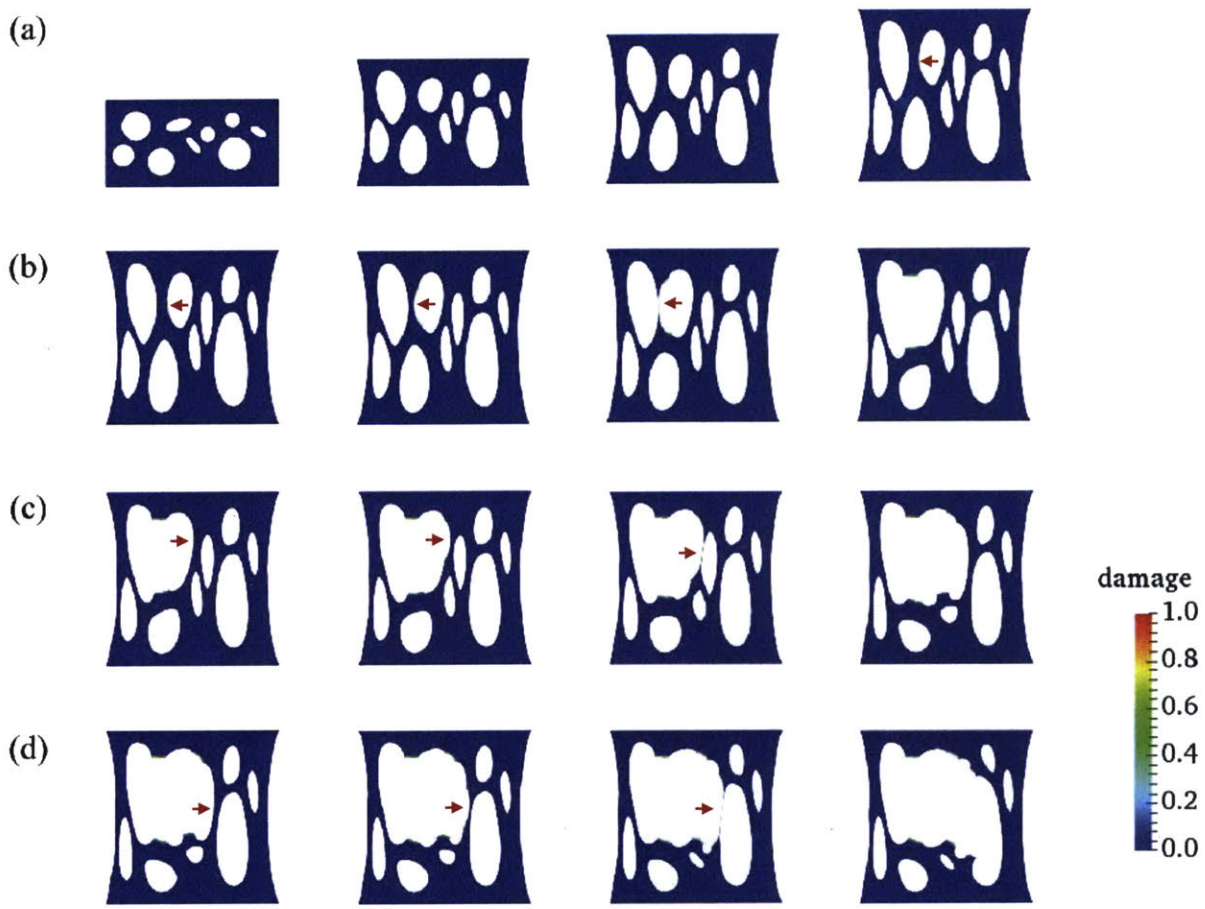

Figure 5-17: Images of the deformed geometry with contour plots of the damage variable d for first and second stages. To aid visualization of the damage, elements with an average value of $d > 0.99$ are removed from the plots. The red arrows indicate the ligaments in which damage and rupture occurs.

specific ligament. For example, in Fig. 5-17(b) the damage within a ligament indicated by the red arrow is initiated in (b1), and (b2) represents a state of progressive damage of the ligament, (b3) shows a pinching-off process, and (b4) shows the total failure of the specific ligament. As the three ligaments in Fig. 5-17 (b) through (d) fail progressively, the cavities within the sample start to merge, and form a big cavity, cf. Fig. 5-17(d4).

After the rupture of the first three ligaments described in the paragraph above, the total displacement of the top surface is 9.85 mm; cf. Fig. 5-16(b). At this point the energy stored in the remaining ligaments is not sufficient to drive further damage. To initiate further damage an additional macroscopic displacement of $\sim$ 1 mm needs to be imposed on the sample. As this extra displacement is imposed, the remaining ligaments are further stretched and the force increases again until the beginning of the third stage; cf. Fig. 5-16(a). Upon application of this additional displacement the stored energy within two of the remaining

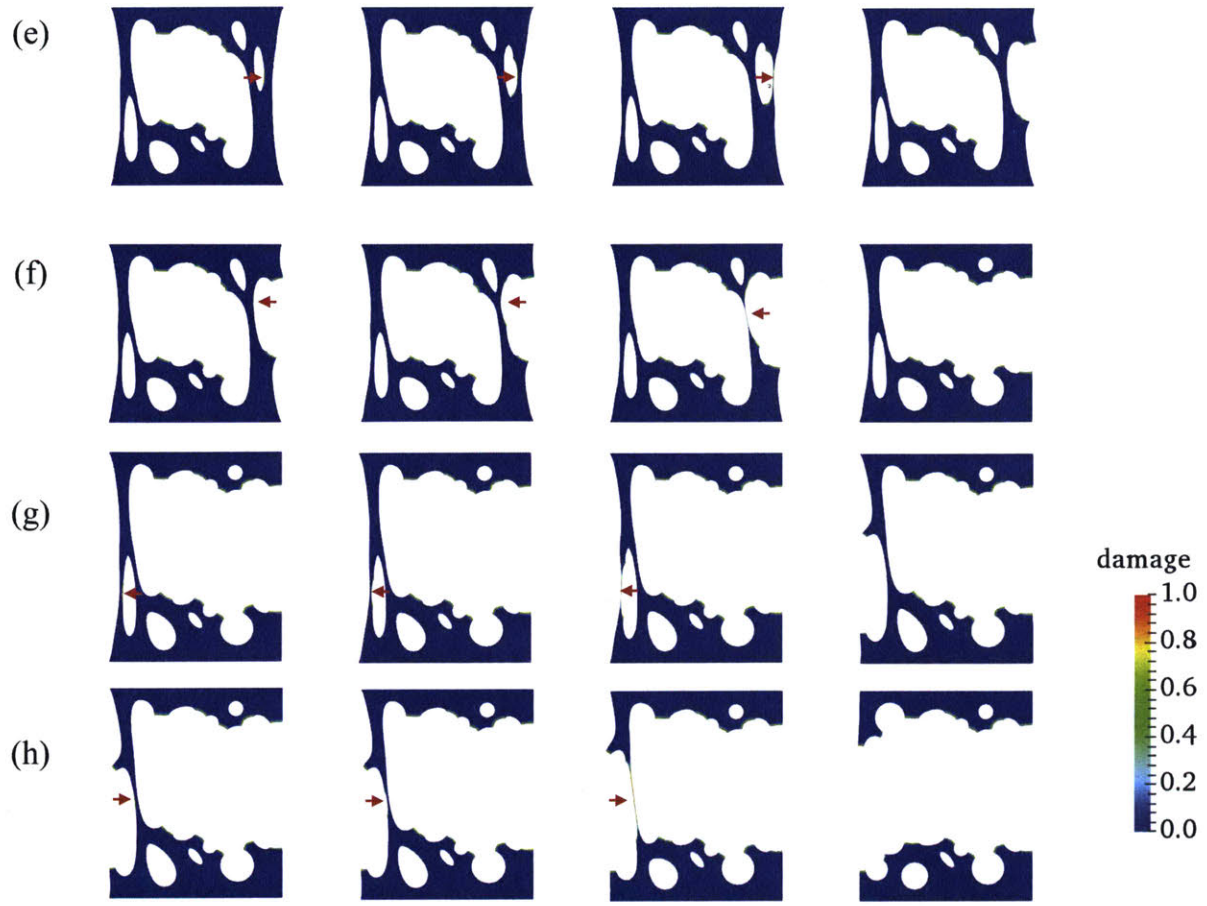

Figure 5-18: Images of the deformed geometry with contour plots of the damage variable d for third and forth stages. To aid visualization of the damage, elements with an average value of $d > 0.99$ are removed from the plots. The red arrows indicate the ligaments in which damage and rupture occurs.

ligaments attains and exceeds the critical value and damage and rupture restarts, as shown in Fig. 5-16(c) and Figs. 5-18(e) and (f).

After the rupture of the first five ligaments, the total displacement of the top surface is 10.514 mm; cf. Fig. 5-16(c). Again, at this point the energy stored in the remaining two ligaments is not sufficient to drive further damage. To initiate further damage an additional macroscopic displacement of ~ 3.7 mm needs to be imposed on the sample. As this extra displacement is imposed, the remaining two ligaments become highly stretched and the force again increases. The remaining ligaments accumulate energy during this additional stretching and eventually they start to damage and fail rapidly, as shown in Fig. 5-16(d) and Fig. 5-18(g) and (h). Fig. 5-18 (h4) shows the final failed configuration.

5.4 Remarks and Conclusion

5.4.1 Some Remarks

Remark. It is of interest to make a comparison between fracture resulting from the chain scission mode and that resulting from crosslink failure mode, and to identify the critical material parameters for these two competing mechanisms. To do this we suppress the damage field d and any discussion of the final damage process. From the discussion on fracture due to the chain scission mechanism (See section 5.2 or related papers Mao et al. (2017b); Talamini et al. (2018)), and the discussion on fracture due to crosslink failure (See section 5.3 or related paper Mao and Anand (submitted)), the free energy for a single chain *accounting for both bond stretch and crosslink stretch* may be expressed as,[11]

$$\begin{aligned}\psi =& n\hat{\varepsilon}_b(\lambda_b) + 2\hat{\varepsilon}_c(\lambda_c) \\ &+ nk_B\vartheta\left[\left(\frac{\lambda}{\sqrt{n}\lambda_b} - \frac{2L_c}{nL_b}\frac{\lambda_c - 1}{\lambda_b}\right)\beta + \ln\left(\frac{\beta}{\sinh\beta}\right)\right],\end{aligned} \tag{5.48}$$

with

$$\beta = \mathcal{L}^{-1}\left(\frac{\lambda}{\sqrt{n}\lambda_b} - \frac{2L_c}{nL_b}\frac{\lambda_c - 1}{\lambda_b}\right), \tag{5.49}$$

and

$$\hat{\varepsilon}_b(\lambda_b) = \frac{1}{2}E_b(\lambda_b - 1)^2, \qquad \hat{\varepsilon}_c(\lambda_c) = \frac{1}{2}E_c(\lambda_c - 1)^2. \tag{5.50}$$

In equation (5.48), the first term represents the internal energy due to Kuhn segments stretch, the second term for the internal energy due to crosslink stretch, and the third term is due to the configurational entropy change.

The equations which determine the bond stretch λ_b and the crosslink stretch λ_c, are again obtained by minimizing the free energy with respect to these two variables,

$$\frac{\partial\psi}{\partial\lambda_b} = 0, \qquad \text{and} \qquad \frac{\partial\psi}{\partial\lambda_c} = 0, \tag{5.51}$$

which using the free energy expression (5.48) give the following two equations to determine λ_b and λ_c,

$$\begin{aligned}E_b(\lambda_b - 1) &= k_B\vartheta\beta\lambda_b^{-1}\left(\frac{\lambda}{\sqrt{n}\lambda_b} - \frac{2L_c}{nL_b}\frac{\lambda_c - 1}{\lambda_b}\right), \qquad \text{and} \\ E_c(\lambda_c - 1) &= k_B\vartheta\beta\left(\frac{L_c}{L_b}\right)\lambda_b^{-1}.\end{aligned} \tag{5.52}$$

[11] Detailed derivations are displayed in Appendix A.

Next let us consider fracture of a single chain for which the Kuhn segments and the crosslinks are allowed to stretch. Physically, as the chain is stretched, the internal energy due to bond-stretch $\hat{\varepsilon}_b(\lambda_b)$ and that due to crosslink stretch $\hat{\varepsilon}_c(\lambda_c)$ will increase. The chain will fail by the chain scission mode or the crosslink failure mode depending on whether $\hat{\varepsilon}_b(\lambda_b)$ or $\hat{\varepsilon}_c(\lambda_c)$ first reach their respective dissociation energies ε_b^f and ε_c^f. To represent this competition we introduce a positive-valued dimensionless factor,

$$\gamma \stackrel{\text{def}}{=} \frac{\hat{\varepsilon}_c(\lambda_c)/\varepsilon_c^f}{\hat{\varepsilon}_b(\lambda_b)/\varepsilon_b^f}. \tag{5.53}$$

Thus, if $\gamma > 1$ then the energy stored in crosslink bonds will reach its critical value first, and the chain will fail by the crosslink failure mode. On the other hand, if $\gamma < 1$ then the energy stored in Kuhn segments will reach its critical value first, and the chain will fail by the chain scission mode.

By using (5.50), we may rewrite γ defined in (5.53) as,

$$\gamma = \frac{E_c(\lambda_c - 1)^2}{E_b(\lambda_b - 1)^2}\left(\frac{\varepsilon_b^f}{\varepsilon_c^f}\right) = \frac{E_c^2(\lambda_c - 1)^2}{E_b^2(\lambda_b - 1)^2}\left(\frac{E_b}{E_c}\right)\left(\frac{\varepsilon_b^f}{\varepsilon_c^f}\right). \tag{5.54}$$

Next, using (5.52) we write γ alternativley as,

$$\gamma = \left(\frac{\lambda}{\sqrt{n}\lambda_b} - \frac{2L_c}{nL_b}\frac{\lambda_c - 1}{\lambda_b}\right)^{-2}\left(\frac{L_c}{L_b}\right)^2\left(\frac{E_b}{E_c}\right)\left(\frac{\varepsilon_b^f}{\varepsilon_c^f}\right). \tag{5.55}$$

Physically when failure occurs, by either failure mode, the quantity $\left(\frac{\lambda}{\sqrt{n}\lambda_b} - \frac{2L_c}{nL_b}\frac{\lambda_c - 1}{\lambda_b}\right)$ in (5.55) is very close to unity, and hence

$$\gamma \approx \left(\frac{L_c}{L_b}\right)^2\left(\frac{E_b}{E_c}\right)\left(\frac{\varepsilon_b^f}{\varepsilon_c^f}\right). \tag{5.56}$$

Thus, by using straightforward scaling relations in going from a single chain to a polymer network (as we did in Section 5.2 and Section 5.3)

$$\gamma \approx \left(\frac{N_c L_c}{nNL_b}\right)^2\left(\frac{\bar{E}_b}{\bar{E}_c}\right)\left(\frac{\varepsilon_{\mathrm{R},b}^f}{\varepsilon_{\mathrm{R},c}^f}\right). \tag{5.57}$$

This expression for γ reveals the material parameters in a polymer network which control the competition between the crosslink failure mechanism and the chain scission failure mechanism. If one knows the values of the material parameters in (5.57) for a specific material, then one can determine the failure mode of the material:

- If $\gamma > 1$, then the network will fail by the crosslink failure mode.

- If $\gamma < 1$, then the network will fail by the chain scission failure mode.

□

Remark. The overall mechanical response of our model for fracture of polymers due to crosslink failure is similar to our model for failure of polymers due to chain scission. However, because of the intrinsic physical differences embedded in these two models, there is an important difference in the consequences from these two models regarding the scaling of G_c with microstructural parameters. Specifically:

- The internal energy in our previous model for fracture by chain scission reads as

$$\varepsilon_{\mathrm{R}}^f = Nn\varepsilon_b^f, \tag{5.58}$$

where ε_b^f is a bond dissociation energy. With ρ the mass density of the polymer and m the molecular mass of a Kuhn segment, the number of chains per unit reference volume is given by $N = \rho/(mn)$, so that

$$Nn = \frac{\rho}{m}. \tag{5.59}$$

Using

$$G_c \propto \varepsilon_{\mathrm{R}}^f \times \ell, \tag{5.60}$$

and an estimate for ℓ in terms of the rest length $r_0 = \sqrt{n}L_b$ of a chain,

$$\ell \propto \sqrt{n}L_b, \tag{5.61}$$

eq. (5.60) gives

$$G_c \propto \left(\frac{\varepsilon_b^f L_b \rho}{m}\right)\sqrt{n}. \tag{5.62}$$

In this scenario the Lake-Thomas scaling holds — the toughness G_c is proportional to $\sqrt{n}$.

As noted earlier, in their fracture experiments on Tetra-PEG gels, with precisely controlled network structures, Akagi et al. (2013) showed that

$$G_c \propto \sqrt{n},$$

which confirmed the Lake-Thomas scaling for these materials (cf., Sakai, 2013, Fig. 8).[12]

[12] Since for swollen gels $\rho = \phi_p \rho_{\mathrm{R}}$, where ρ_{R} is the mass density in an unswollen reference configuration and ϕ_p is the polymer volume fraction, they actually showed that

$$G_c \propto \phi_p \sqrt{n}.$$

Further, from (5.59) and the expression $G_0 = Nk_B\vartheta$ for the ground state shear modulus we have that

$$\sqrt{n} = \sqrt{\frac{\rho}{m}}\frac{1}{\sqrt{N}} = \sqrt{\frac{\rho\, k_B\vartheta}{m}}\frac{1}{\sqrt{G_0}}, \tag{5.63}$$

use of which in (5.62) gives that

$$G_c \propto \frac{1}{\sqrt{G_0}}. \tag{5.64}$$

Thus, for fixed crosslink elastomers which fail by chain scission there is a trade-off between toughness (fracture energy G_c) and stiffness (shear modulus G_0): by increasing the cross-linking density the initial stiffness $G_0 = Nk_B\vartheta$ increases proportionally to the increase in the number N of chains (elastically effective strands) per unit volume, while the toughness G_c decreases owing to the decrease in the number n of monomers in a chain. As reviewed recently by Creton (2017), such a trade-off between the stiffening and toughening in conventional fixed-crosslink elastomers and gels has been observed experimentally.

- However, the internal energy in the present model for fracture due to crosslink stretch and failure is

$$\varepsilon_{\mathrm{R}}^f = N_c\varepsilon_c^f, \tag{5.65}$$

where ε_c^f is a crosslink dissociation energy. In this case from (5.60), with an estimate (5.61) for ℓ in terms of the rest length $r_0 = \sqrt{n}L_b$ of a chain, and with the number of crosslinks per unit reference volume N_c proportional to the number of chains per unit reference volume N,

$$N_c \propto N = \frac{\rho}{mn}, \tag{5.66}$$

we obtain

$$G_c \propto \left(\frac{\varepsilon_c^f\, L_b\, \rho}{m}\right)\frac{1}{\sqrt{n}}. \tag{5.67}$$

In the crosslink failure based micromechanism of fracture the Lake-Thomas scaling *does not hold* — the toughness G_c is proportional to $1/\sqrt{n}$ and not $\sqrt{n}$.

Further, using (5.63), (5.67) implies that

$$G_c \propto \sqrt{G_0}. \tag{5.68}$$

Thus, for stretchable crosslink elastomers the toughness (fracture energy G_c) *increases* as the stiffness (shear modulus G_0) increases — a desirable outcome, indeed. However, as far as we know such a scaling has not been experimentally verified in the literature for any polymer, but would indeed be a means to experimentally determine whether failure of a polymer occurs by chain scission or by crosslink failure.

That is, swollen gels with the same number of links per chain, n, have a lower toughness than the dry elastomer.

In any event, our study suggests that introducing stretchable crosslinks and a crosslink failure mode in polymer networks is a potential solution to the problem of the trade-off between stiffness and toughness observed in conventional fixed-crosslink elastomers and gels.

□

5.4.2 Conclusions

We have formulated a theory for progressive damage and failure of elastomeric materials in which fracture occurs by chain scission and crosslink failure. Specifically, we have extended the freely jointed inverse-Langevin model for a single chain, and the corresponding 8-chain Arruda-Boyce model for a network, to account for changes in internal energy due to stretching of the crosslinks. Monomers within the backbone chain or crosslink damage and failure is postulated to occur upon the attainment of a critical value of the internal energy due to Kuhn segment stretching or crosslink stretching.

We have shown in this paper that the Lake-Thomas scaling (Lake and Thomas, 1967; Akagi et al., 2013; Sakai, 2013; Creton, 2017) — that the toughness G_c of an elastomeric material is proportional to $1/\sqrt{G_0}$, with $G_0 = Nk_b\vartheta$ the ground-state shear modulus of the material — does not hold for elastomeric materials in which fracture occurs by crosslink stretching and scission. According to our theory, for such materials the toughness is proportional to $\sqrt{G_0}$. That is, for stretchable crosslink elastomers the toughness increases as the stiffness increases — a desirable outcome, indeed. However, as far as we know such a scaling has not been experimentally verified in the literature for any polymer, but would indeed be a means to experimentally determine whether failure of a polymer occurs by chain scission or by crosslink failure. In any case, our theory clearly suggests that introducing stretchable crosslinks and the crosslink failure mode in polymer networks is a potential solution to the problem of the trade-off between stiffness and toughness observed in conventional fixed-crosslink elastomers and gels.

At the continuum-level our theory is a gradient-damage or phase-field theory of fracture of elastomeric materials. We have numerically implemented this theory in an open-source finite element code MOOSE (Gaston et al., 2009) by writing our own application. Using this simulation capability we have presented results from simulations of: (i) fracture of single-edge-notched specimens; (ii) fracture of an asymmetric double-edge-notched specimen; and (iii) fracture of a sheet specimen with multiple circular and elliptical holes, under our plane stress conditions. These examples show the powerful capability of our gradient-damage theory and its numerical implementation to simulate the complicated fracture process of nucleation, propagation, branching and merging of cracks in elastomeric materials in arbitrary geometries undergoing large deformations. We expect that our theory and numerical simulation capability will be useful in studying various interesting phenomena such as crazing and cavitation in soft materials.

In this chapter we have focused our attention on fracture of an "ideal" dry single-network elastomeric material in which fracture occurs by crosslink failure. It would be useful to extend these ideas to materials which exhibit additional microscopic dissipation mechanisms — e.g., viscoelasticity, Mullins effect, degradation of interpenetrating networks with sacrificial bonds, fluid diffusion — that accompany the rupture process in elastomeric materials and their gels (Zhao, 2014; Ducrot et al., 2014; Creton, 2017; Mao et al., 2017a; Mao and Anand, 2018).

Chapter 6

Coupled deformation-diffusion-fracture simulations of gels

In this chapter we focus on coupled deformation-diffusion-damage simulations of gels. Some interesting phenomena are numerically studied. Specifically,

- In section 6.1 the single-edge-notch Mode-I loading under plane-stress conditions with different notch lengths is displayed;
- In section 6.2, we show the results on single-edge-notch Mode-I loading under plane-stress conditions with different diffusivities;
- In section 6.3, fracture in an asymmetric-double-edge-notched sheet of a gel under Mode-I plane-stress loading is studied; and
- In section 6.4, delayed fracture in gels and the interaction between diffusion and damage is studied.

6.1 Single-edge-notch Mode-I loading under plane-stress conditions with different notch lengths

We begin with a study of fracture in single-edge-notch specimens with different notch lengths, under plane-stress Mode-I loading conditions. Fig. 6-1(a) shows a schematic of the specimen geometry. The overall size of the notched sheet sample is 20 mm $\times$ 18 mm in the plane, and the sheet is 1 mm thick. We consider specimens with notch lengths c = 3, 6, and 9 mm; the initial root-radius of the notch is fixed at 0.1 mm. The temperature is kept constant at

$\vartheta = 300$K, and the initial volume fraction of polymer is set at $\phi_0 = 0.5$. The displacement of the bottom edge of the specimen is fixed, while the top-edge is prescribed a displacement at a nominal stretch rate of 1×10^{-3}/s. We use a zero-fluid-flux boundary condition on all the boundaries of the specimen, so that no fluid goes into or out of the specimen — but the fluid is allowed to diffuse within the specimen.[1]

The material parameters used in our simulations are shown in Table 6.1. For simplicity, the reference chemical potential is set to $\mu_{\mathrm{R}}^0 = 0$. In order to study the effects of diffusion on deformation and fracture,

- we have purposely chosen a rather high value of the diffusivity D,

in order to represent fast diffusion within the notched-specimen relative to the time-scale at which it is being extended (a nominal stretch rate of 1×10^{-3}/s). For a systematic study of the effect of the fluid diffusivity on fracture, see the next section 6.2.[2]

Table 6.1: Representative values of the material parameters used in the simulations.

$G_0 = Nk_B\vartheta$	n	$\bar{E}_b = NnE_b$	K	$\varepsilon_{\mathrm{R}}^f = Nn\varepsilon_b^f$	ℓ	ξ_b and ζ
0.1 MPa	4	5 MPa	10 MPa	1 MPa	100μm	1 kPa·s
μ_{R}^0	Ω	χ	D			
0	1×10^{-4} m^3/mol	0.1	1×10^{-3}m^2/s			

Fig. 6-1(b) shows the calculated force-displacement curves for notches with initial lengths of $c = 3$, 6, 9 mm. As expected, as the initial length of the notch increases the overall force level becomes lower, and the stretch at which final fracture occurs becomes smaller. Contour plots for the damage variable d and the polymer volume fraction ϕ at points (a) through (h) on the load displacement curve for a specimen with $c = 9$ mm are shown in in Figs. 6-2 and 6-3, respectively.

Fig. 6-2 shows the deformed geometry at points (a) through (h) on the force-displacement curve in Fig. 6-1 (b), together with with contours of the damage variable d. To aid visualization of the damage, elements with an average value of $d > 0.99$ are not plotted. Since the length scale $\ell = 100\,\mu$m is very small when compared with the overall dimension of the specimen (~ 20 mm), the damage zone is barely visibly in this this sequence of plots. Fig.

[1] Our theory and numerical procedures allow for boundary conditions that allow for fluid influx or efflux on the boundary, but in this initial study we do not consider such boundary conditions as they complicate the situation by introducing another time-scale in the problem. We will show an example "evaporation-induced fracture" to highlight this type of boundary conditions.

[2] Also, in our numerical calculations we have used a value of the bulk modulus K which is 100 times larger than the ground state shear modulus G_0; this corresponds to a ground-state Poisson's ratio of $\nu = 0.495$, which approximates an elastically incompressible material. We tried using larger values of K relative to that of G_0, but that slowed down our numerical procedures considerably. So in all the calculations reported here we have used $K/G_0 = 100$.

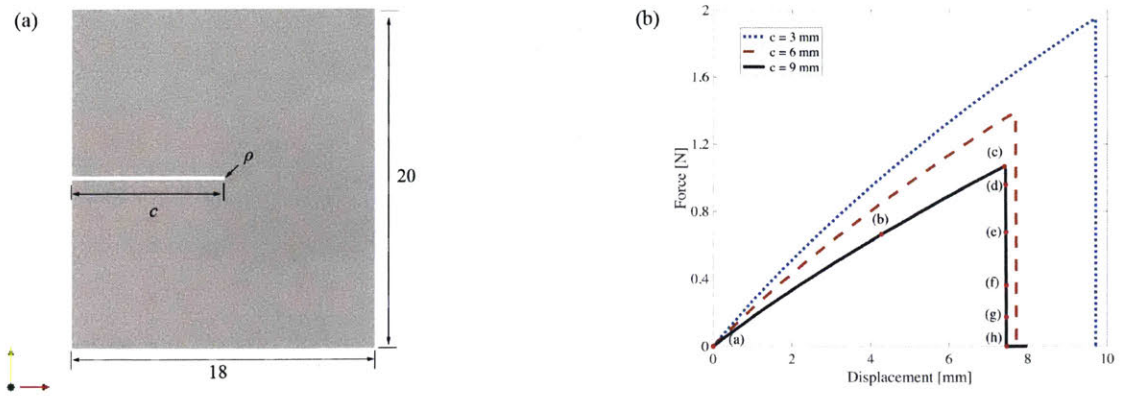

Figure 6-1: (a) Schematic of the single-edge-notch specimen geometry; all dimensions are in mm. The thickness of the sample is 1 mm; the notch length is denoted by c; and $\rho = 0.1$ mm is the notch-root radius. (b) Calculated force-displacement curves for $c = 3$, 6, 9 mm. Contour plots for the damage variable d and the polymer volume fraction ϕ at points (a) through (h) on the load displacement curve for a specimen with $c = 9$ mm are shown in Fig. 6-2 and Fig. 6-3.

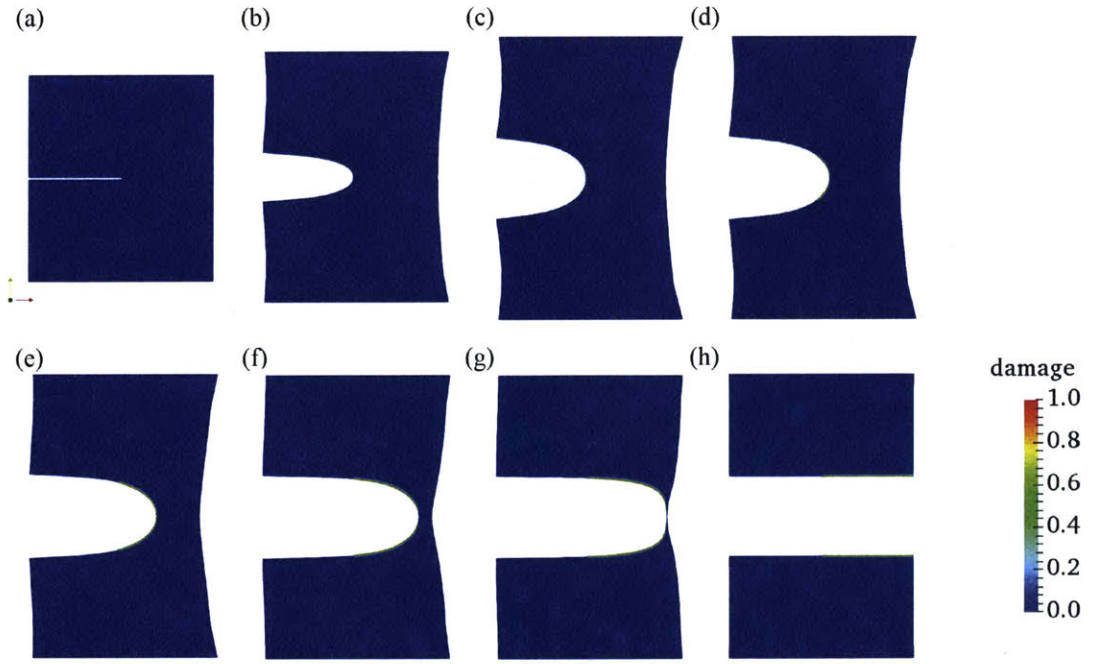

Figure 6-2: Images of the deformed geometry with contour plots of the damage variable d. To aid visualization of the damage, elements with an average value of $d > 0.99$ are removed from the plots. Since the length scale $\ell = 100\,\mu$m is very small when compared with the overall dimension of the specimen (~ 20 mm), the damage zone is barely visibly in this this sequence of contour plots for d.

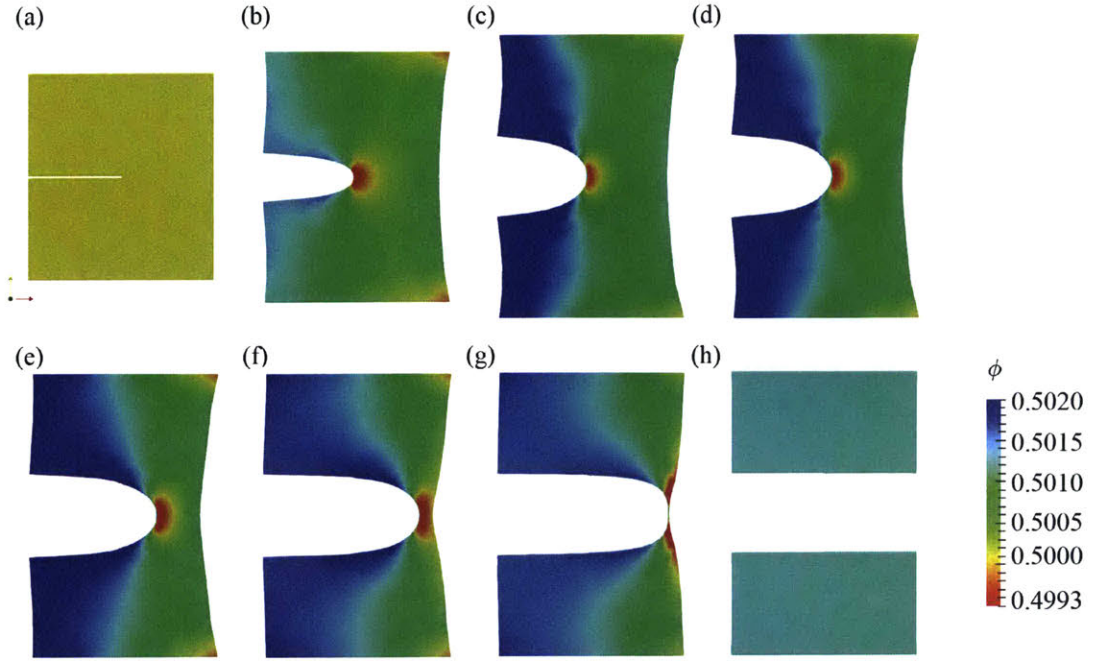

Figure 6-3: Images of the deformed geometry with contour plots of the volume fraction of polymer ϕ. To aid visualization of the damage, elements with an average value of $d > 0.99$ are removed from the plots.

6-2(a) is the initial configuration. As the sample is stretched to (b) the notch is blunted, but no damage has initiated. Damage initiates when the sample is stretched further to a displacement level of $\sim 7\,\text{mm}$ (a point just before (c)), but the force is still increasing, and it is after another $\sim 0.5\,\text{mm}$ of extension that the force reaches a peak at point (c) in the force-displacement curve, and from the contour of damage shown in Fig. 6-2 (c), a small damage zone ahead of the notch becomes observable. Further stretching begins the rupture process, and Figs. 6-2(d) through (h) show this progressive rupturing, with (h) showing the final failed configuration. Note from Fig. 6-1(b) that the force at stage (h) stage is essentially zero.

Fig. 6-3 shows the deformed geometry with contour plots of the volume fraction of polymer ϕ corresponding to the points (a) through (h) in Fig. 6-1(b). Again, to aid visualization of the damage, elements with an average value of $d > 0.99$ are removed from the plots. At the initial stage (a) the volume fraction of polymer ϕ has a constant value $\phi_0 = 0.5$. Fig. 6-3 shows that as the sample is stretched the volume fraction of polymer ahead of the notch-tip decreases, with a zone of low volume fraction of polymer moving with notch-tip. The region of lower polymer volume fraction — and therefore higher fluid concentration — increases the propensity to damage and failure because of the lower number of polymer chains in such regions which are also more highly stretched. After full rupture, the polymer concentration in the two halves of the specimen once again becomes almost uniform (except in the fully-damaged and deleted portion).

6.2 Single-edge-notch Mode-I loading under plane-stress conditions with different diffusivities

Next, we show results from simulations for a single-edge-notch specimen with a fixed notch length of $c = 9\,\text{mm}$, but with three different diffusivities,

$$D = 0, \quad 1 \times 10^{-6}, \quad \text{and} \quad 1 \quad \text{m}^2/\text{s}. \tag{6.1}$$

The case $D = 0$ corresponds to the fracture of a gel in which the diffusion is completely suppressed within the specimen, while $D = 1$ corresponds to very fast diffusion. As in the previous section, we prescribe no-flux boundary conditions on the boundaries of the specimen. The displacement of the bottom edge of the specimen is fixed, while the top-edge is prescribed a displacement at a nominal stretch rate of $1 \times 10^{-3}/\text{s}$.

Fig. 6-4(a) shows the resulting force-displacement curves for the three different diffusivities, and Fig. 6-4(b) shows a zoom in of the part of the force-displacement curves in the vicinity of load-drop. Fig. 6-4(a) shows that there are very small differences between the macroscopic load-displacement curves for the different diffusivities while the force-displacement curves are increasing, and Fig. 6-4(b) shows that the load-peak and its position differs for the three different diffusivities.

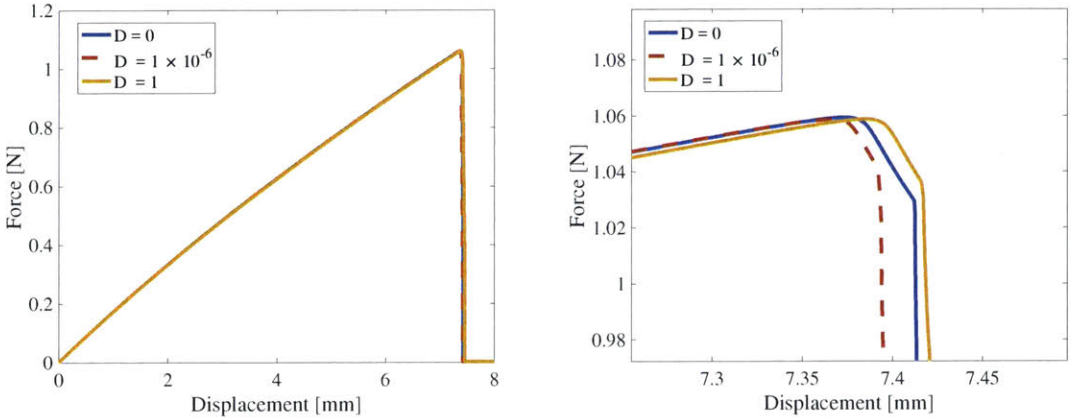

Figure 6-4: (a) The effect of diffusivity D on the force-displacement curve of a single-edge-notch specimen with notch length $c = 9\,\text{mm}$. The nominal stretch rate of the specimen is $1 \times 10^{-3}/\text{s}$ for all cases. (b) A zoom in of the region in the vicinity of load-drop.

Let

$$W_{\text{R}}^f \overset{\text{def}}{=} \text{External work done to completely rupture the specimen.} \tag{6.2}$$

Values of W_{R}^f are calculated by integrating the area under the load-displacement curves (such as those shown in in Fig. 6-4(a)) for the different values of the diffusivity within a wide range — $D = 0$ to $1\text{m}^2/\text{s}$. In Fig. 6-5 the value of W_{R}^f for the baseline case of $D = 10^{-16} \approx 0$ is

plotted as the most left point, and the results for the other values of W_{R}^f for the different diffusivities are shown as open blue circles.

As we have discussed earlier, diffusion of the fluid to the notch-tip region increases the propensity of the material to fracture in that region because of the smaller number of highly stretched polymer chains per unit volume, and this will cause a decrease in the value of W_{R}^f. However, migration of the solvent in the specimen is a dissipative process and this increases the overall energy that is dissipated in the process of rupturing of the gel, and causes an increase in W_{R}^f. It is these two competing mechanisms which cause the W_{R}^f versus D curve in Fig. 6-5 to first decrease and then to increase, as the diffusivity D increases.

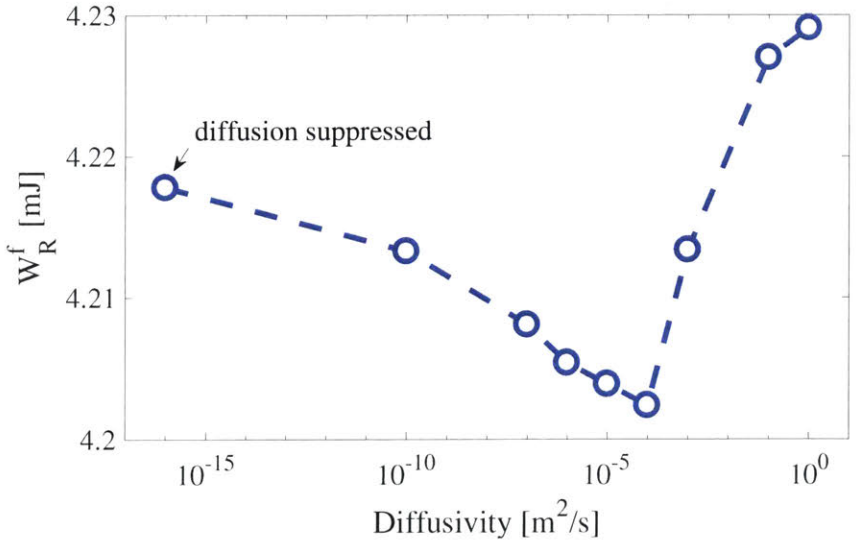

Figure 6-5: The effect of diffusivity, D, on the external work needed to rupture a sample, W_{R}^f, for a specimen with notch length $c = 9\,\mathrm{mm}$. The macroscopic stretch rate is $1 \times 10^{-3}/\mathrm{s}$ for all cases.

6.3 Fracture in an asymmetric-double-edge-notched sheet of a gel under Mode-I plane-stress loading

In this section we study fracture of an asymmetric-double-notched sheet specimen of a gel under Mode-I plane-stress loading. This example shows the powerful capability of our gradient-damage theory to model the merging of two growing notches.

Fig. 6-6(a) shows a schematic of the specimen geometry. The overall size of the double-edge-notched sheet sample is $20\,\mathrm{mm} \times 20\,\mathrm{mm}$ in the plane, and the sheet is 1 mm thick. The two offset notches each have a of length $c = 2.5\,\mathrm{mm}$; the initial root-radius of the notch is 0.1 mm. As in our single-edge notch simulations in Section 6.1, the temperature is kept constant at $\vartheta = 300\mathrm{K}$, the initial volume fraction of polymer is set to be $\phi_0 = 0.5$, and we use the same values of the material parameters as in Section 6.1. The bottom edge of

the specimen is fixed, while the top-edge is prescribed a displacement at a nominal stretch rate of 1×10^{-3}/s. We use a zero-fluid-flux boundary condition on all the boundaries of the specimen, so that no fluid goes into or out of the body, but the fluid is allowed to diffuse within the specimen. Fig. 6-6(b) shows the calculated force-displacement curve.

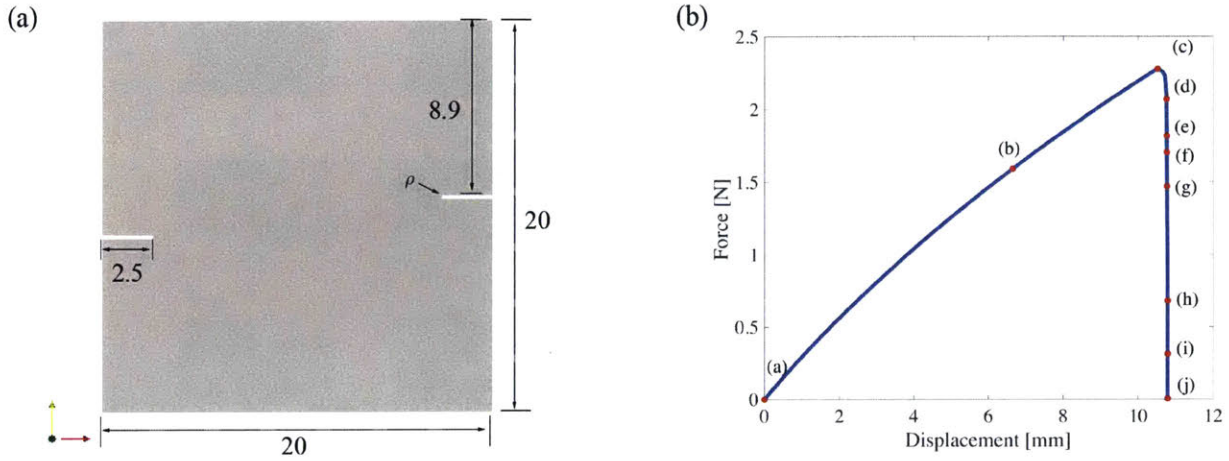

Figure 6-6: (a) Schematic of the asymmetric-double-edge-notch specimen geometry; all dimensions are in mm. The thickness of the sample is 1 mm; the notches are of length $c = 2.5$ mm; and $\rho = 0.1$ mm is the notch-root radius. (b) Calculated force-displacement curve. The contour plots for the damage variable d at points (a) through (j) on the load displacement curve are shown in Fig. 6-7.

The contour plots for the damage variable, d, and the polymer volume fraction ϕ at points (a) through (j) on the load displacement curve in Fig. 6-6(b) are shown in in Fig. 6-7. To aid visualization of the damage, elements with an average value of $d > 0.99$ are removed from the plots. Since the length scale $\ell = 100\,\mu$m is very small compared with the overall dimension of the specimen (20 mm), the damage zone is barely visibly in this this sequence of plots.

Fig. 6-7(a) is the initial configuration. As the sample is stretched to (b) both the notches get blunted, but no damage has initiated. Damage initiates when the sample is stretched further to a displacement of $\sim$ 11mm (just before state (c)), but the force is still increasing; it is only after another $\sim$ 1 mm of extension that the force reaches a peak at point (c) in the force-displacement curve Fig. 6-6(b), and from the contour of damage d shown in Fig. 6-7 (c), a small damaged zone ahead of the notch becomes observable. Figs. 6-7(d) through (j) shows the subsequent rupturing process, with (j) the final failed configuration.

Fig. 6-8 shows contours of the volume fraction of polymer, ϕ, corresponding to the points (a) through (j) in Fig. 6-6(b). Again, to aid visualization of the damage, elements with an average value of $d > 0.99$ are removed from the plots. At the initial stage (a) the volume fraction of polymer ϕ has a constant value $\phi_0 = 0.5$. As the sample is stretched, cf. (b) and (c), the volume fraction of polymer ahead of both notch-tips decreases. Upon further stretching the zones of low polymer volume fraction move with the notch-tips, and since

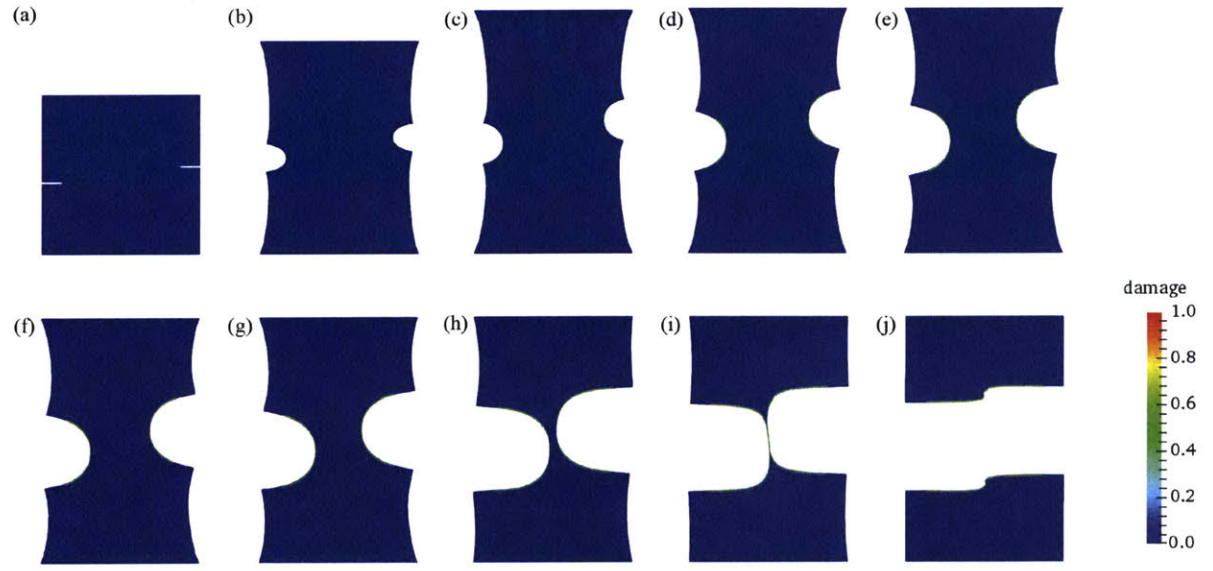

Figure 6-7: The deformed geometry with contour plots of the damage variable d. To aid visualization of the damage, elements with an average value of $d > 0.99$ are removed from the plots. Since the length scale $\ell = 100\,\mu\text{m}$ is very small compared with the overall dimension of the specimen ($\sim 20\,\text{mm}$), the damage zone is barely visibly in this sequence of plots.

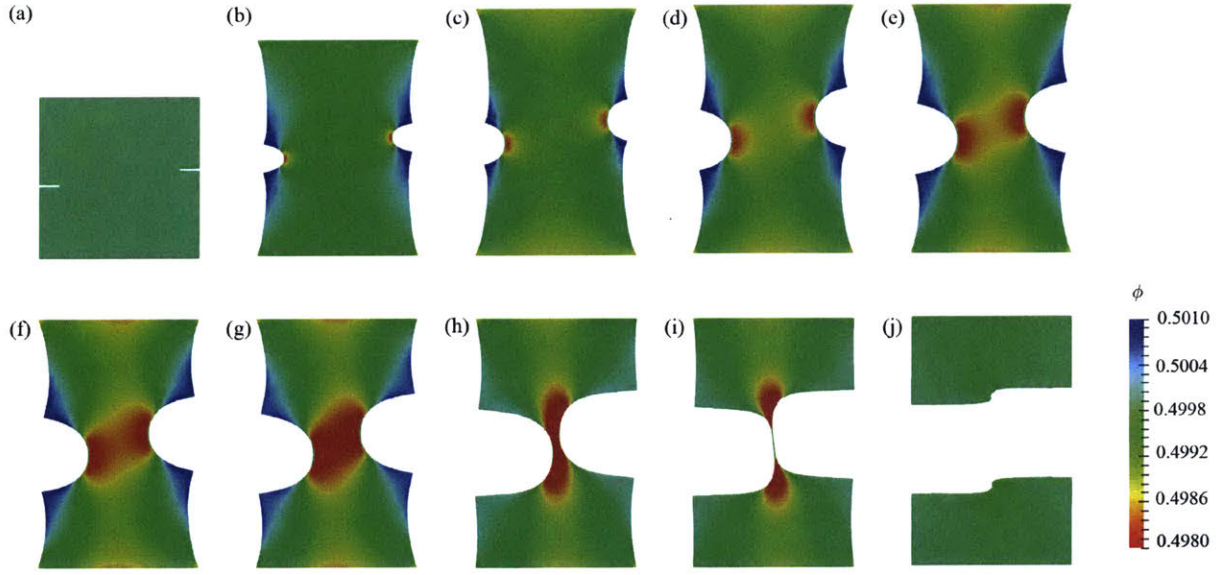

Figure 6-8: The deformed geometry with contour plots of the volume fraction of polymer ϕ. To aid visualization of the damage, elements with an average value of $d > 0.99$ are removed from the plots.

the size of these zone grows, the distance between the two zones decreases. The two zones eventually interact and merge with each other, as shown in (e) through (h). Figure (i) shows a pinching off process, which leads to final fracture into two separate pieces, as shown in (j). After final fracture the polymer volume fraction once again becomes almost uniform in the two halves of specimen (except in the fully-damaged and deleted portion).

6.4 Delayed fracture in gels: interaction between diffusion and damage

In the previous section we have shown that by changing the diffusivity but keeping the stretch-rate constant, that our model can capture the effect of diffusion on the deformation and damage processes of gels in a single-edge-notch specimen. However, for actual gels the diffusivity cannot be substantially changed, it is always about $D \approx 1 \times 10^{-9}$ to 1×10^{-8} m^2/s; but what one can be controlled is the macroscopic stretch rate of a notched specimen. The competition between the time-scale for the stretching and the time-scale for diffusion is vividly displayed in an experiment in which a notched-sample is first rapidly stretched to a level below which damage is initiated at the notch-tip, and the macroscopic displacement is thereafter held constant. Fracture is observed to occur after a substantial period of time, as the fluid migrates in the specimen to highly-stressed region near the notch-tip. We study this interesting phenomenon of "delayed-fracture" next.

We set $D = 1 \times 10^{-8}$ m^2/s, and with all other material parameters as before, a single-edge-notch specimen with initial notch length $c = 9\,mm$ (cf. Fig.6-1(a)) is loaded in two steps, as shown in Fig. 6-9(a): the applied stretch rate is 0.02/s in the first step (blue), and 0 in the second step (red). Examining Fig. 6-4 (b) we see that the case with different diffusivity, failure starts at a displacement of $\sim 7.38\,mm$. Guided by these results, in our simulation we choose the total displacement imposed to sample at the end of the first step to be 7.30 mm, and thereafter hold the displacement fixed at this value. Fig. 6-9(b) shows the resulting force versus time curve from our simulation. Three periods are identified from this force-time curve: loading, incubation, and quick rupture. Since the initial loading rate is relatively fast, the diffusion within this loading period is limited. To understand what is happening during the incubation period, we mark the start and the end of incubation by "S" and "E" in Fig. 6-9(b), and compare the contours of the polymer volume fraction and damage fields for these two configurations in Fig. 6-10.

Fig. 6-10(a) and Fig. 6-10(b) show contours of the volume fraction of polymer and damage at the start and end of the incubation time, respectively; to aid visualization, the contours of the damage and the volume fraction of polymer are displayed on the undeformed configuration. At the start of the incubation period a limited amount of damage appears at the notch-tip. While Fig. 6-9(b) shows the force versus time curve is essentially flat between the stages "S" and "E", Fig. 6-10 shows that that even though the change in the macroscopic force-time response of the sample is negligible, substantial changes in the fields ϕ and d occur during the incubation time, as the solvent diffuses to the highly-stressed

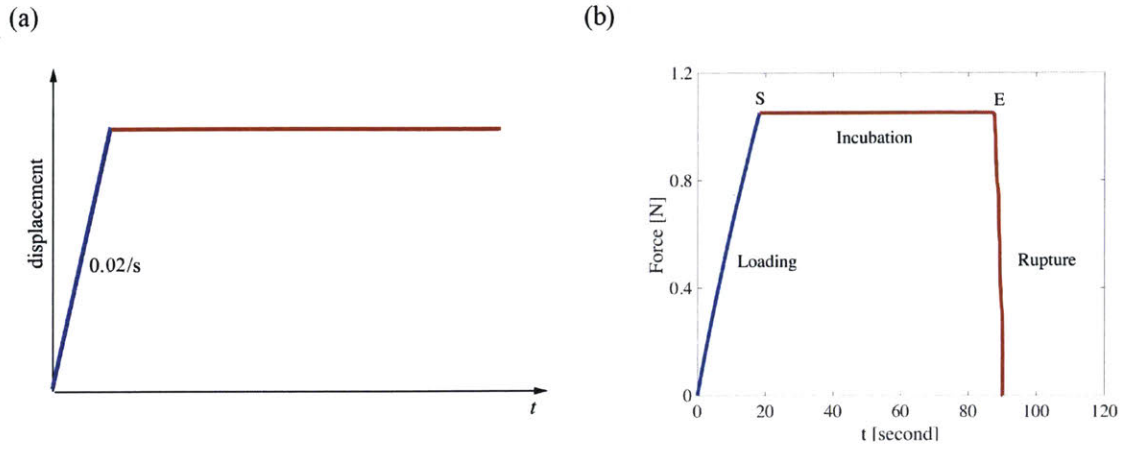

Figure 6-9: Delayed-fracture in a gel due to diffusion of the fluid. (a) The macroscopic applied stretch rate is 0.02/s in the first step (blue), and 0 in the second step (red). (b). The force-time curve obtained from simulation. The incubation period is ~70 seconds.

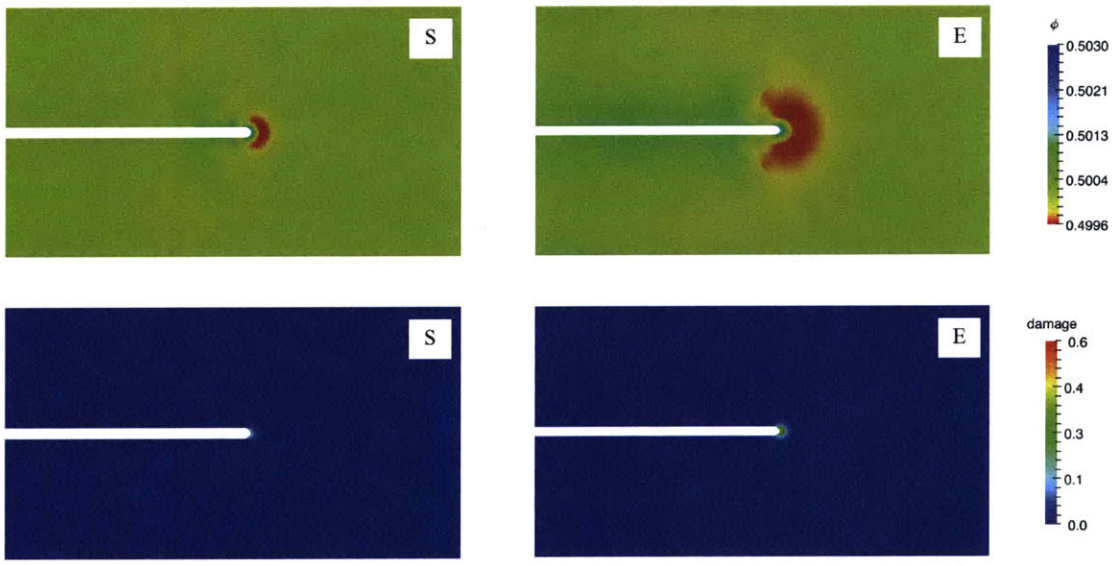

Figure 6-10: (a) Contours of polymer volume fraction ϕ at the start and end of incubation time, respectively. (b) Contours of damage d at the start and end of incubation time, respectively. To aid visualization, the contours of the damage and the volume fraction of polymer are displayed on the undeformed configuration.

notch-tip region from the rest of the specimen. As we have discussed earlier, diffusion of the fluid to the notch-tip region increases the propensity of the material to fracture in that region because of the smaller number of highly stretched polymer chains per unit volume, and this drives the damage process in the notch-tip zone. At the end of the incubation time enough damage has accumulated, and thereafter it starts to grow rapidly, the force starts to drop dramatically, and rupture occurs.

Chapter 7

Concluding remarks

In this part of the thesis, we first discuss several important theoretical aspects related with elastomeric materials.

- We first generally discuss the physics of fracture in elastomeric materials. As we repeatedly state in this thesis, the deformation and fracture aspects in elastomeric materials are not consistent in previous literature. One of the distinguishing features of elastomeric materials, which consist of a network of flexible polymeric chains, is that the deformation response is dominated by changes in entropy. Accordingly, most classical theories of rubber-like elasticity consider only the entropy and neglect any changes in internal energy. On the other hand, the fracture of strongly cross-linked elastomers is essentially energy dominated, as argued in the well-known Lake-Thomas model for the toughness of elastomers. The newly-introduced bond stretch field λ_b is the exactly the missing piece to resolve the inconsistency of deformation and fracture responses of elastomeric soft materials. We also show that both classical Arruda-Boyce model and the Lake-Thomas arguments can be recovered from our theory with the newly introduced Kuhn segment stretch field λ_b. Finally, we highlight that for the other important failure mode, i.e. crosslink failure mode, in elastomeric materials, we need introduce a new field called crosslink stretch field λ_c instead of bond stretch field λ_b. Many different scaling laws emerge from the fundamental different micromechanisms. For example, we show that for elastomeric materials in which fracture occurs by crosslink stretching and scission the Lake-Thomas Lake and Thomas (1967) scaling — that the toughness G_c of an elastomeric material is proportional to $1/\sqrt{G_0}$, with $G_0 = Nk_b\vartheta$ the ground-state shear modulus of the material — does not hold. A new scaling is proposed, and some important consequences of this scaling are remarked upon.

- Based on these new understandings of the fracture in elastomeric materials, we have formulated a theory for fracture of polymeric gels — a theory which accounts for the coupled effects of fluid diffusion, large deformations, damage, and also the gradient

effects of damage. The particular constitutive equations for fracture of a gel proposed in this thesis contain two essential new ingredients:

(i) Our constitutive equation for the change in free energy of a polymer network accounts for not only changes in the entropy, but also changes in the internal energy due the stretching of the Kuhn segments of the polymer chains in the network.

(ii) The damage and failure of the polymer network is taken to occur by chain-scission, a process which is driven by the changes in the internal energy of the stretched polymer chains in the network, and not directly by changes in the configurational entropy of the polymer chains.

With this coupled deformation-diffusion-damage theory for polymeric gels, we have numerically implemented it in an open-source finite element code MOOSE (Gaston et al., 2009) by writing our own application. Using this simulation capability we have presented several important results.

- In Chapter 5 we present results for our simulations of fracture of elastomers by suppressing the diffusion within the body. We also discuss the case when the elastomers failed by crosslink failure instead of Kuhn segments scission. For both cases, we study several interesting cases such as
  - Flaw sensitivity in soft materials;
  - Mode-I fracture in single-edge-notch under plane-stress conditions;
  - Asymmetric-double-edge-notch geometries under plane-stress conditions;
  - Fracture of a sheet specimen with multiple circular and elliptical holes.
- In Chapter 6 we present results of fracture of gels from our simulations. The cases that we studied are:
  - Single-edge-notch Mode-I loading under plane-stress conditions with different notch lengths;
  - Single-edge-notch Mode-I loading under plane-stress conditions with different diffusivities;
  - Fracture in an asymmetric-double-edge-notched sheet of a gel under Mode-I plane-stress loading;
  - Delayed fracture in gels and the interaction between diffusion and damage;

These examples show the powerful capability of our gradient-damage theory to simulate the complicated fracture process of nucleation, propagation, branching and merging of cracks in arbitrary geometries –propagating cracks are tracked automatically by the evolution of the smooth damage field.

In this part we have focused our attention on fracture of an "ideal" single-network polymeric gel with strong chemical crosslinks. It would be useful in the future to extend the theory presented in this paper to interpenetrating-multiple-network gels which incorporate additional non-trivial dissipation mechanisms to toughen polymeric gels (cf., e.g., Gong et al., 2003; Zhao, 2014; Mao et al., 2017a).

Part II

Fracture of steels due to hydrogen embrittlement

Chapter 8

Introduction

Atomic hydrogen readily dissolves in and permeates through most metals. The deleterious effects of hydrogen on the mechanical response of structural materials are well-known, and this in turn affects the integrity of many structural components used in industry; cf. Robertson et al. (2015) and Dadfarnia et al. (2015) for recent reviews of the vast literature on the subject.

The purpose of the second part of the thesis is to develop a continuum theory for modeling hydrogen embrittlement in metals. While our considerations are quite general, we shall focus on hydrogen embrittlement of *ferritic line pipe steels*, which is one of the main problems in hydrogen distribution through pipeline networks (Srinivasan and Neeraj, 2014). This topic is also receiving increasing attention because of its potential application to the development of the emerging technology of large-scale production, storage, and distribution of hydrogen in the "hydrogen economy" (cf., e.g., San Marchi et al., 2007; Dadfarnia et al., 2009, 2010).

Modeling hydrogen embrittlement is a challenging problem. There is a significant existing literature on the topic, with many claims on the dominant mechanism, but no wide-agreement on any one of the proposed mechanisms even for a given class of materials. The recent experimental study by Neeraj et al. (2012) on ferritic line pipe steels show the presence of nanoscale voids on fracture surfaces in the presence of hydrogen. A hydrogen embrittlement mechanism proposed by Li et al. (2015), in connection with these experiments, is that plastic deformation leads to production of vacancies due to dislocation multiplication interactions, which in the presence of hydrogen are stabilized as hydrogen-vacancy complexes which can agglomerate and grow in size to nucleate nanovoids, which in turn serve as precursors to final fracture. In addition to the nanoscale voids observed by Neeraj et al. (2012), the experimental studies of Martin et al. (2011b,a) show that the fracture surfaces in steels also show *quasi-cleavage* features. Such features are commonly found on hydrogen-induced fracture surfaces, they are cleavage-like but not along any known cleavage plane, or grain boundaries.

Based on these experimental observations, and guided by the hydrogen embrittlement mechanism proposed by Li et al. (2015), the purpose of this part of the thesis is to formulate a continuum theory for the diffusion of hydrogen coupled with the elastic-plastic response of metals, together with an accounting for microscopic effects due to the generation of hydrogen-vacancy complexes. We postulate that when such hydrogen-vacancy complexes reach a critical concentration there is a *change in mechanism* of plastic deformation from plastic flow by dislocation glide to plastic flow by *quasi-cleavage* — a change in mechanism which is reminiscent of a transition between "shear-yielding" and "crazing" in amorphous polymers. We have formulated a criterion for this change in mechanism together with an attendant dilatant craze-plasticity flow rule, and a corresponding gradient damage theory to model hydrogen embrittlement of ferritic line-pipe steels.

The plan of this part is follows. We begin in Section 8.1 by summarizing some experimental observations on hydrogen embrittlement in

(i) an ASME SA-106 medium strength carbon steel by Xu and Rana (2009);

(ii) an API X60 HIC grade line pipe steel summarized recently by Dadfarnia et al. (2015); and

(iii) in an X65 line pipe steel by Neeraj et al. (2012).

In Section 8.2 we argue that the process of hydrogen induced failure in ferritic steels in the presence of hydrogen is *qualitativley similar to the process of craze-failure in amorphous polymers.*

Based on our review of the recent experimental literature on hydrogen embrittlement of ferritic steels (Martin et al., 2011b,a; Robertson et al., 2015; Dadfarnia et al., 2015), the study by Neeraj et al. (2012) and Li et al. (2015), and our own previous work on hydrogen in metals (Anand, 2011; Di Leo and Anand, 2013), in Chapter 9 we summarize our theory for the diffusion of hydrogen coupled with the elastic-plastic response of metals, together with an accounting for microscopic effects due to the generation of hydrogen-vacancy complexes. Further, based on our previous study of crazing in amorphous polymers (Gearing and Anand, 2004), we also formulate a continuum-level *craze-intiation criterion*, a *craze-flow rule*, a corresponding *gradient damage theory* to model hydrogen embrittlement of ferritic line-pipe steels.

Our theory introduces an equivalent craze strain ϵ^c as a measure of the history of crazing in the material. An increase in the craze strain will result in the formation of localized dilational craze bands. Eventually when a chemoelastic free energy per unit reference volume ψ_{R}^0 exceeds a critical value, $\psi_{\mathrm{R}}^{\mathrm{crit}}$, the process of "break-down" of the crazed material will start. In order to model the final fracturing process we introduce an *order-parameter* $d(\mathbf{X}, t) \in [0, 1]$, which evolves ($\dot{d} > 0$) when ψ_{R}^0 exceeds $\psi_{\mathrm{R}}^{\mathrm{crit}}$. When $d = 1$ at some material point, then that point is fractured; values of d between zero and one correspond to partially-fractured material. With the aim of "regularizing" the strain-softening behavior during craze break-down, and to *avoid mesh-dependency related issues* during finite element simulations we follow recent phase-field theories of fracture in ductile materials (cf., e.g., Miehe et al., 2015,

2016; Borden et al., 2016) and develop a fracture theory which depends not only on d but also its gradient ∇d, which is considered to be a measure of the spatial inhomogeneity of the damage during the craze break-down fracture process.

We have numerically implemented a our theory in the commercial finite element program Dassault Systèmes (v. 6.14) by writing a user-element subroutine (UEL). Representative numerical examples which demonstrate the ability of the theory and its implementation to model failure due to hydrogen embrittlement is some technically relevant geometries are given in Chapter 10. We close in Chapter 11 with some final remarks.

8.1 A brief review some experimental observations

8.1.1 Experimental observations by Xu and Rana

Fig. 8-1, taken from Xu and Rana (2009), shows the effects of hydrogen embrittlement for a medium strength carbon steel (ASME SA-106). For different hydrogen pressures, Fig. 8-1(a) shows engineering stress-strain curves in tension; (b) shows ductility curves, both elongation and reduction of area; and (c) shows macrographs of the specimens, and micrographs of fracture surfaces obtained in a scanning electron microscope. The tension experiments were performed in an autoclave mounted in a servohydraulic testing machine at a low strain rate of 1.3×10^{-4}/s at room temperature; this low strain rate was chosen to allow for sufficient time for hydrogen to diffuse into the specimen, and hence to enhance the embrittlement effect.

The experiments of Xu and Rana (2009) show that:

- There is a negligible affect of hydrogen on the stress-strain curves prior to the sudden drop in the stress carrying capacity of their steel specimens at room temperature.
- The tensile ductility markedly decreases as the hydrogen pressure is increased to 6.9 MPa, but thereafter the rate of decrease in the ductility with an increase in hydrogen pressure is not very large.
- Hydrogen has a significant effect on the fracture mode of the specimens:
  - (i) The base-line specimen tested in air exhibited significant necking and an eventual cup-and-cone fracture, with a typical dimpled ductile fracture surface.
  - (ii) At 3.5 MPa H_2, a macroscopic manifestation of the effect of hydrogen is the *presence of numerous fissures* on the surface of the specimen, which appear perpendicular to the direction of extension. The specimen still exhibited some necking and considerable ductility. Also, the fracture surface was still dominated by ductile dimples, albeit with the presence of some quasi-cleavage features.
  - (iii) At 6.9 MPa H_2 there were fissures on the surface, there was no visible necking, and the ductility was significantly reduced. Presumably one of the fissures developed into a mature crack which propagated across the cross-section of the specimen

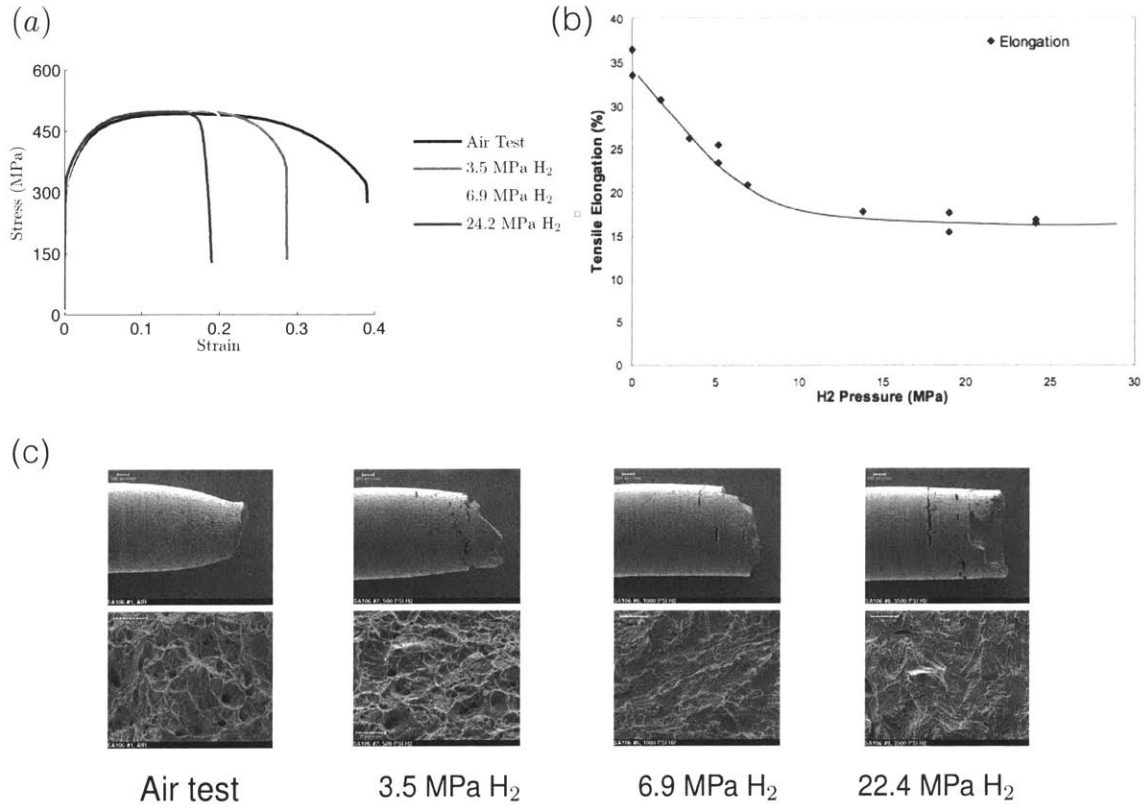

Figure 8-1: ASME SA-106 Steel: (a) Tensile stress-strain curves at different hydrogen pressures. (b) Dependence of tensile ductility, both elongation and reduction of area, as a function of hydrogen pressure. (c) Specimen surfaces and fracture surfaces of tensile specimens at four different hydrogen pressures. From Xu and Rana (2009).

perpendicular to the tension axis. The fracture surface was very flat and ductile dimples were not observed. The fracture mode was transgranular quasi-cleavage, with some tear-ridges.

(iv) At 24.2 MPa H_2 there were numerous fissure cracks on the surface of the specimen and there was no visible necking. The fracture surface was very similar to the one at 6.9 MPa H_2.

The fissures that are visible on the surface of the steel specimens when it is embrittled by the hydrogen, form predominantly *in a direction perpendicular to the maximum principal stress direction.* At high hydrogen pressures (greater than 6.9 MPa for this material) one of the fissures eventually develops into a mature crack which propagates across the cross-section to cause final fracture.

8.1.2 Experimental observations by Martin et al. (2011b,a)

Martin et al. (2011b,a) have reported on their studies of hydrogen embrittlement in a line-pipe steel (API X60 HIC grade). Their observations have been summarized by Robertson et al. (2015) and Dadfarnia et al. (2015) in their recent review papers. The results of Martin et al. (2011b,a) for the fracture toughness tests on compact tension tests in a high-pressure hydrogen gas environment showed that hydrogen causes a decrease in the fracture toughness. Fractographic studies on compact tension specimens tested at hydrogen gas pressure of 21MPa showed that hydrogen-induced fracture surface of line-pipe steels had distinct morphologies including microvoid coalescence, secondary cracks, as well as two distinct morphologies which they called (i) "quasi-cleavage",[1] and (ii) "flat" or featureless. We summarize below the remarks of Martin et al. (2011b,a), Robertson et al. (2015), and Dadfarnia et al. (2015) regarding these features.

"Quasi-cleavage" features on fracture surface:

The characteristic features of a "quasi-cleavage" fracture surface are shown in Fig. 8-2a and b. The low-magnification image (Fig. 8-2a) shows striations running approximately parallel to the crack propagation direction. The higher-magnification image (Fig. 8-2b) shows that these markings are in fact ridges, with thin electron transparent sawteeth at the tip of most ridges. Comparing these saw-teeth features with ligaments formed in TEM foils strained to failure, they concluded that the saw-teeth form due to extensive plasticity during the final separation process of ridges. A schematic, taken from Martin et al. (2011b), showing the relationship between the ridges on either side of the fracture surface and the formation of the saw-teeth ligaments is shown in Fig. 8-3.

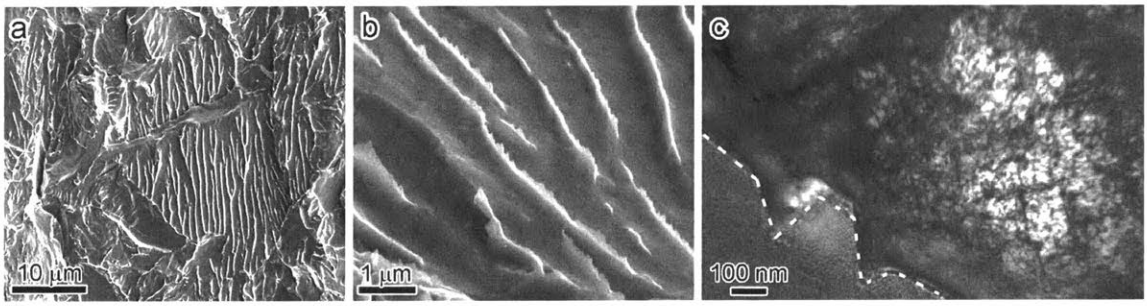

Figure 8-2: Hydrogen-induced "quasi-cleavage" of an API X60 line pipe steel. (a) SEM micrograph of the fracture surface; (b) higher magnification image; (c) TEM micrograph normal to the "quasi-cleavage" fracture surface showing the microstructure underneath the surface. The fracture surface is shown by the dashed lines. From Martin et al. (2011b), as shown in Dadfarnia et al. (2015).

[1]The term "quasi-cleavage" is a commonly used to describe of regions of hydrogen induced fracture surfaces, and refers to failure on *non-cleavage planes* with fine lines that run approximately parallel to the direction of crack advance.

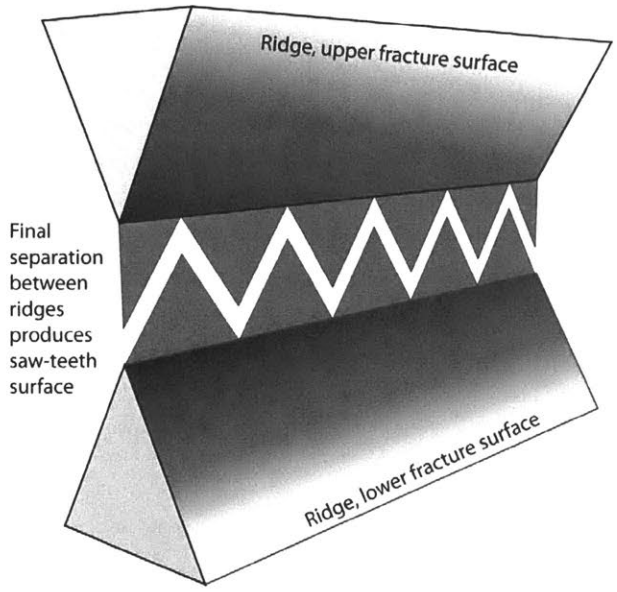

Figure 8-3: Schematic showing the relationship between the ridges on either side of the fracture surface and the formation of the saw-teeth ligaments. From Martin et al. (2011b).

Further, using a focused-ion-beam lift-out technique, Martin et al. (2011b) extracted TEM samples under the "quasi-cleavage" regions. Fig. 8-2c shows such a micrograph from a region normal to two closely spaced ridges on the fracture surface. There is enhanced dislocation activity under the fracture surface. Also, no carbides were observed to be associated with the ridges, which indicates that such second phase particle, which are invariably present in these steels, do not play a role in the formation of these "quasi-cleavage" fracture surfaces.

By studying the features on the "quasi-cleavage" surface and microstructure below such surfaces, Martin et al. (2011b) hypothesized that the fracture process involves the nucleation of nanoscale voids at slip band intersections. Then each void is expanded by dislocation processes until encountering another void, and that final failure took place along tops of ridges forming saw-teeth. They concluded that the "quasi-cleavage" fracture surfaces are formed by a hydrogen enhanced plasticity processes, and not by a cleavage-like decohesion mechanism. The role of hydrogen was concluded to be the creation of conditions for the development of dislocation structures which facilitate the initiation of nanovoids and their subsequent growth through dislocation-based processes.

"Flat" features on fracture surface:

A characteristic "flat" region on the fracture surface is shown in Fig. 8-4a and b. While these features were flat in plan-view at low magnification, an examination using high resolution SEM showed that what one sees as a flat surface at lower magnifications is actually covered with undulations and rounded mounds as shown in Fig. 8-4b. The roughness of the "flat"

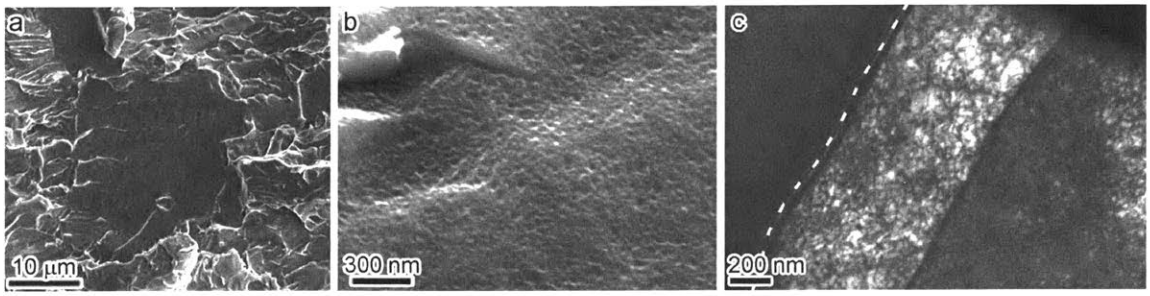

Figure 8-4: "Flat" features (or featureless region) in hydrogen-induced fracture of a line pipe steel. a) SEM micrograph of the fracture surface; b) high resolution SEM micrograph; c) TEM micrograph showing the microstructure immediately under the flat surface illustrated by the dashed line. From Martin et al. (2011a), as shown in Dadfarnia et al. (2015).

region was measured by atomic force microscopy, which revealed that the diameters of the mounds were about 50nm and their height differences were about 5 nm. Fig. 8-4c, which shows the microstructure beneath a "flat" feature, it exhibits a high density of dislocations which persisted over several microns beneath the fracture surface. As for the case of "quasi-cleavage" features, no carbide particles appear to have affected the crack path.

Martin et al. (2011a) proposed that the plasticity and underlying dislocation structure plays a major role in establishing the conditions for the formation of the flat surface morphology. They suggested that the difference between the conditions which produce the "quasi-cleavage" features discussed above, and the flat features is the orientation and constraints on the grains leading to the development of different dislocation structures.

8.1.3 Experimental observations by Neeraj et al.

Neeraj et al. (2012) reported on their studies of hydrogen embrittlement in several line pipe steels. Here, we briefly summarize their experimental observations and interpretation of fracture surface features and deformation microstructures underneath the fracture surface for their API X65 steel.

Fig. 8-5a shows an SEM micrograph of the fracture surface of a single-edge-notch-bend (SENB) specimen tested after hydrogen charging, quasi-brittle fracture features are observed.[2] At higher magnifications, Fig. 8-5b shows that the quasi-brittle fracture surfaces were covered with nanoscale dimples 5-20 nm wide and 1-5 nm deep. Based on analyses of conjugate fracture surfaces, (i) and (ii) in (b), they found that most of the nanodimples appear to be "valley-on-valley" type, rather than "mound-on-valley" type, indicating nanovoid nucleation and growth in the plastically flowing medium prior to ultimate failure.[3]

[2]The quasi-brittle fracture surface features observed by Neeraj et al. (2012) in the X65 steel are similar to the "flat" features observed by Martin et al. (2011a) in their X60 steel. Neeraj et al. (2012) do not report any "quasi-cleavage" features with "ridges" on their fracture surface similar to that reported by Martin et al. (2011b), Fig. 8-2a,b.

[3]Martin et al. (2011a) called similar features "mounds", cf. Fig. 8-4b.

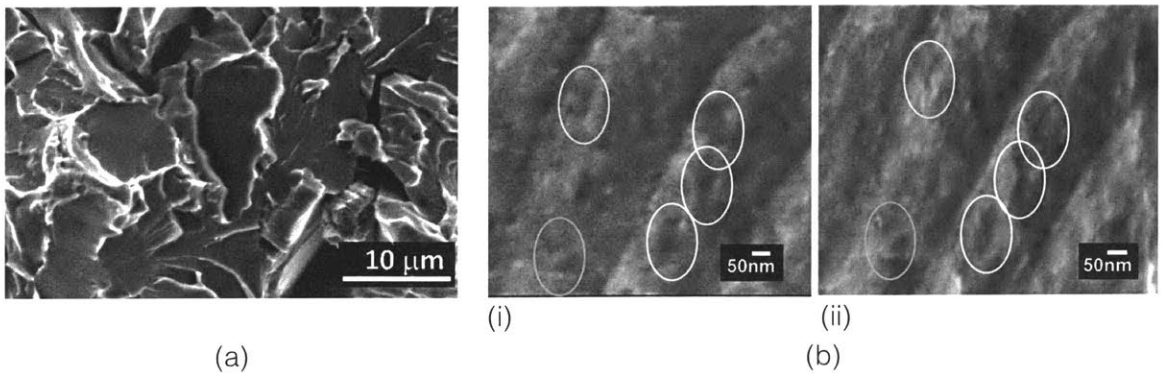

Figure 8-5: (a) SEM micrograph of the fracture surface shows quasi-brittle fracture features in X65 SENB specimens tested after hydrogen charging. (b) High resolution SEM images of conjugate surfaces, (i) and (ii), showing presence of 5-20 nm sized nanoscale "dimples," consistent with a "valley-on-valley" phenomenon; like-colored circles/ovals indicate mating features on conjugate surfaces. From Srinivasan and Neeraj (2014).

Neeraj et al. (2012) also studied the microstructure just beneath the fracture surfaces using transmission electron microscopy, Fig. 8-6. Significant dislocation plasticity was observed just beneath the fracture surfaces. The dislocation density just beneath the fracture surface observed in Fig. 8-6b was much greater than that observed in sample tested without hydrogen, Fig. 8-6a.

The experimental study by Neeraj et al. (2012), and a recent companion atomistic simulation study by Li et al. (2015) indicates that plastic deformation leads to production of vacancies due to dislocation multiplication interactions. In the absence of hydrogen such vacancies are usually quickly swept away by the moving dislocations. However in the presence of hydrogen the vacancies are stabilized as hydrogen-vacancy complexes which cannot be easily swept away by the moving dislocations. Hydrogen stabilizes vacancies in Fe by both lowering the vacancy formation energy and by reducing the mobility of vacancies. Based on their experimental and modeling studies Neeraj et al. (2012) and Li et al. (2015) have proposed that hydrogen-vacancy complexes can grow in size to nucleate nanovoids which in turn serve as precursors to fracture.

In his recent review paper, Robertson et al. (2015) has questioned the efficacy of such a vacancy-induced nanovoid nucleation and growth mechanism for fracture initiation, by raising the following points:

- While the production of vacancies or small vacancy clusters can occur during deformation, and the presence of hydrogen can decrease the formation energy of defects, it is necessary to consider how the agglomeration of the vacancies occurs to generate the fracture surface, why defects with similar dimensions to the surface features are not found elsewhere beneath the surface and how the vacancy agglomeration mechanism explains the "quasi-cleavage" regions that exist on the same fracture surface.

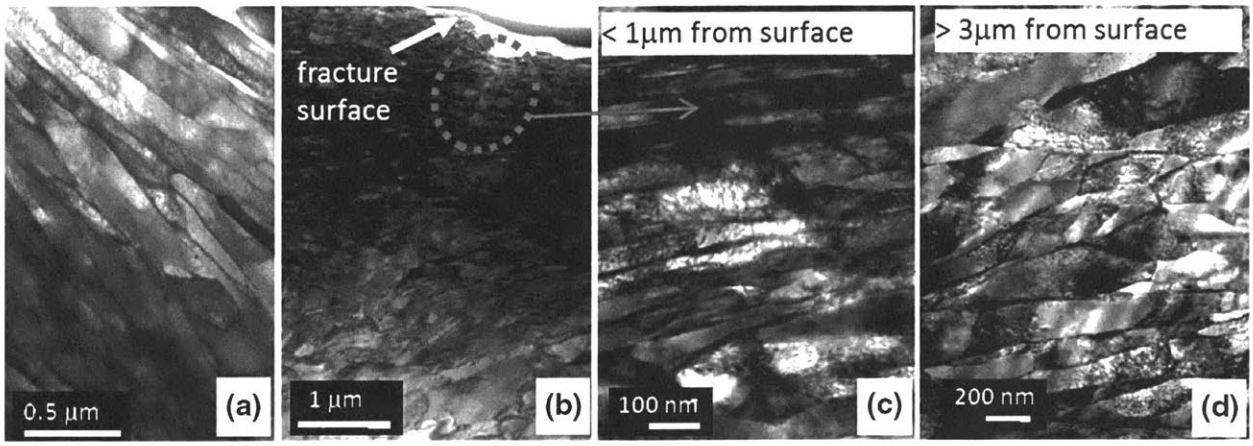

Figure 8-6: (a) Deformation substructure in uncharged, and (b) hydrogen-charged X65 steel. Greater subgrain refinement is observed in the hydrogen-charged X65, along with gradation in subgrain size. (c) Extremely fine subgrains are observed immediately near the fracture surface, while (d) slightly larger subgrains are observed a few micrometers beneath the fracture surface. From Neeraj et al. (2012) as reported in Srinivasan and Neeraj (2014).

- Assuming the surface features are representative of the failure mechanism, it is pertinent to consider if vacancy clusters along the fracture plane serve as the nucleation sites for the formation of the surface void features. If the nucleation sites are the vacancy clusters, they should persist throughout the lattice which would mean they should influence the deformation processes prior to failure. Having such a dense field of obstacles would influence the mobility of dislocations much in the same way that vacancy clusters produced by irradiation influence the behavior — here they result in a strengthening of the matrix and the deformation is restricted to channels in which the defect density is reduced by the passage of dislocations.

- Lastly, there is no experimental evidence which demonstrates how a nano-sized vacancy-produced "void" can grow to become micron-sized and coalescence with another void to produce fracture. Stresses needed to grow nano-sized voids are in the GPa range, whereas in mild steels embrittlement can occur in the MPa range.

Robertson et al. offer a possible alternative explanation for the formation of the nanodimple features on "flat" surfaces, they consider that the nanodimples could be generated in a manner similar to the saw-teeth observed atop the ridges, river markings, on the "quasi-cleavage" surface. These were attributed to the very final stages of separation and even if they were influenced by hydrogen, they are inconsequential in establishing the conditions that promote failure initiation.

In addition to the critique of Robertson et al. (2015), Tehranchi et al. (2016) have recently reported on their own atomistic simulations of the interactions between dislocations, hydrogen atoms, and vacancies to assess the viability of the mechanism proposed by Li et al. (2015) for the formation of nanoscale voids in steels in the presence of hydrogen. They

conclude that, "that neither dislocations nor hydrogen play any clearly positive role in the formation of vacancy clusters and, thus, that nanovoid formation by the processes envisioned in recent work is not operative."

In closing our brief review of the recent literature on hydrogen embrittlement of ferritic steels, it is fair to say that the microstructural level processes that eventually lead to the formation of the "nanodimple" features and "quasi-cleavage" features on fracture surfaces, still remain *murky. But what is clear is that such features are present on hydrogen-generated fracture surfaces and that they are the result of underlying plasticity processes.* We argue in the next section that the presence of these features suggests a *change in mechanism of inelastic deformation from dislocation glide based plastic flow to a dilatant quasi-cleavage like mechanism, which leads to eventual fracture.*

8.2 Failure process in ferritic steels in the presence of hydrogen is qualitativley similar to the process of craze-failure in amorphous polymers

The

- vacancy-induced "nanovoid nucleation and growth mechanism" proposed by Neeraj et al. (2012);
- the "quasi-cleavage" features observed on the fracture surfaces in the presence of hydrogen in the experiments of Martin et al. (2011b); and
- the macroscopic "fissures" perpendicular to the maximum principal stress direction which form as precursors to final fracture in the presence of hydrogen in smooth specimens, as in the experiments of Xu and Rana (2009),

all suggest that the process of hydrogen embrittlement in ferritic steels *bears a certain similarity* to the "crazing" process which eventually leads to fracture in certain amorphous polymeric materials. Fig. 8-7 shows a micrograph of distributed crazing in polymethylmethacrylate (PMMA), and a micrograph of the structure of a single craze in polystyrene.

In amorphous polymers which exhibit crazing, the crazes are

- *localized bands of plastic dilational deformation with nano-scale cavities and polymer fibrils which bridge the boundaries of the bands.*

Argon (2011), in his recent review paper on crazing states that "molecular level processes that govern craze initiation still remains murky." And as we have seen they are also still murky in hydrogen embrittlement of steels. Nevertheless,

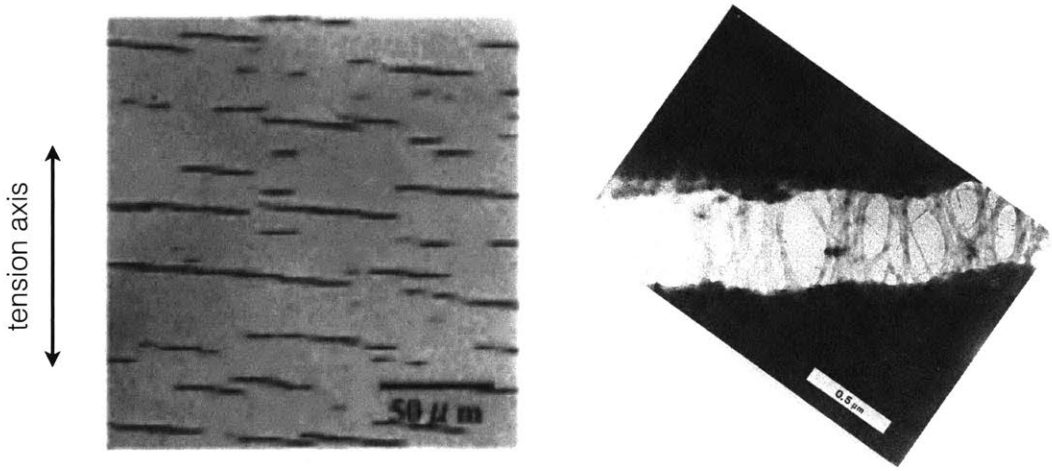

Figure 8-7: (a) Distributed crazing in PMMA prior to fracture, observed at low magnification; from Ishiyama et al. (2001). (b) Structure of a single craze in polystyrene showing polymer fibrils bridging the boundaries of a craze band, oberved at high magnification; from Argon and Hannoosh (1977).

- by analogy to crazes that are precursors to brittle fracture in amorphous polymers, we herefater call the surface fissures that appear due to the effects of hydrogen in steels, cf. Fig 8-2(a) and (b), **crazes**.

For the crazes observed due to the hydrogen embrittlement effects in steels, there are of course no fibrils bridging the boundaries of the crazes. However, the ridges and sawtooth caps on the "quasi-cleavage" features on fracture surfaces of the line pipe steel studied by Martin et al. (2011b) show that there is some similarity between the effects of hydrogen on the failure of ferritic steels and crazing of amorphous polymers.

Based on our review of the recent experimental literature on hydrogen embrittlement of ferritic steels (Martin et al., 2011b,a; Robertson et al., 2015; Dadfarnia et al., 2015), the study by Neeraj et al. (2012) and Li et al. (2015), and our own previous work on hydrogen in metals (Anand, 2011; Di Leo and Anand, 2013), in the next section we summarize our continuum-level theory for the diffusion of hydrogen coupled with the elastic-plastic response of metals. Further, based on the previous model of Gearing and Anand (2004) of crazing in amorphous polymers, we propose that there is a change in mechanism of inelastic deformation form standard dislocation glide based plasticity to a *craze-type* plasticity, and formulate a continuum-level *craze-intiation criterion*, a *craze-flow rule*, and a *phase-field theory* of fracture to model hydrogen embrittlement of steels.

Chapter 9

A phase field damage theory for hydrogen diffusion in steels coupled with large elastic-plastic deformations

9.1 Kinematics

Consider a macroscopically-homogeneous body B with the region of space it occupies in a fixed *reference configuration*, and denote by $\mathbf{X}$ an arbitrary material point of B. A *motion* of B is then a smooth one-to-one mapping $\mathbf{x} = \boldsymbol{\chi}(\mathbf{X}, t)$ with *deformation gradient*, *velocity*, and *velocity gradient* given by

$$\mathbf{F} = \nabla\boldsymbol{\chi}, \qquad \mathbf{v} = \dot{\boldsymbol{\chi}}, \qquad \mathbf{L} = \operatorname{grad}\mathbf{v} = \dot{\mathbf{F}}\mathbf{F}^{-1}. \tag{9.1}$$

We base our theory on the Kröner (1959)-Lee (1969) multiplicative decomposition of the deformation gradient,

$$\mathbf{F} = \mathbf{F}^e\mathbf{F}^i. \tag{9.2}$$

As is standard, we assume that

$$J \stackrel{\text{def}}{=} \det\mathbf{F} > 0, \tag{9.3}$$

and hence, using (9.2),

$$J = J^eJ^i, \qquad \text{where} \qquad J^e \stackrel{\text{def}}{=} \det\mathbf{F}^e > 0 \qquad \text{and} \qquad J^i \stackrel{\text{def}}{=} \det\mathbf{F}^i > 0, \tag{9.4}$$

so that $\mathbf{F}^e$ and $\mathbf{F}^i$ are invertible. Here, suppressing the argument t:

(i) $\mathbf{F}^i(\mathbf{X})$ represents the local deformation in an infinitesimal neighborhood of material at $\mathbf{X}$ due to two major micromechanisms for inelastic deformation under consideration:

plastic deformation due to motion of dislocations, or due to "craze"-type plasticity which results in *quasi-cleavage* failure.

(ii) $\mathbf{F}^e(\mathbf{X})$ represents the subsequent local deformation of material in an due to stretch and rotation of the microscopic structure.

We refer to $\mathbf{F}^i$ and $\mathbf{F}^e$ as the *inelastic and elastic distortions*, and we refer to the local space at $\mathbf{X}$ represented by the range of $\mathbf{F}^i(\mathbf{X})$, as a local *intermediate space* at $\mathbf{X}$.

The right polar decomposition of $\mathbf{F}^e$ is given by

$$\mathbf{F}^e = \mathbf{R}^e\mathbf{U}^e, \tag{9.5}$$

where $\mathbf{R}^e$ is a rotation, while $\mathbf{U}^e$ is a symmetric, positive-definite tensor with

$$\mathbf{U}^e = \sqrt{\mathbf{F}^{e\mathsf{T}}\mathbf{F}^e}. \tag{9.6}$$

As is standard, we define

$$\mathbf{C}^e = \mathbf{U}^{e2} = \mathbf{F}^{e\mathsf{T}}\mathbf{F}^e. \tag{9.7}$$

By $(9.1)_3$ and (9.2),

$$\mathbf{L} = \mathbf{L}^e + \mathbf{F}^e\mathbf{L}^i\mathbf{F}^{e-1}, \tag{9.8}$$

with

$$\mathbf{L}^e = \dot{\mathbf{F}}^e\mathbf{F}^{e-1}, \qquad \mathbf{L}^i = \dot{\mathbf{F}}^i\mathbf{F}^{i-1}. \tag{9.9}$$

As is standard, we define the elastic and inelastic stretching and spin tensors through

$$\left.\begin{aligned} \mathbf{D}^e &= \operatorname{sym}\mathbf{L}^e, \qquad \mathbf{W}^e = \operatorname{skw}\mathbf{L}^e, \\ \mathbf{D}^i &= \operatorname{sym}\mathbf{L}^i, \qquad \mathbf{W}^i = \operatorname{skw}\mathbf{L}^i, \end{aligned}\right\} \tag{9.10}$$

so that $\mathbf{L}^e = \mathbf{D}^e + \mathbf{W}^e$ and $\mathbf{L}^i = \mathbf{D}^i + \mathbf{W}^i$.

We make the following additional kinematical assumptions concerning inelastic flow:

(i) First, from the outset we constrain the theory by assuming that the inelastic flow is *irrotational*, in the sense that[1]

$$\mathbf{W}^i = \mathbf{0}. \tag{9.11}$$

Then, trivially, $\mathbf{L}^i \equiv \mathbf{D}^i$ and

$$\dot{\mathbf{F}}^i = \mathbf{D}^i\mathbf{F}^i. \tag{9.12}$$

(ii) Next, we assume that the inelastic stretching $\mathbf{D}^i$ is given by

$$\mathbf{D}^i = \mathbf{D}^p + \mathbf{D}^c, \qquad \text{with} \qquad \operatorname{tr}\mathbf{D}^p = 0, \tag{9.13}$$

where

[1]This assumption is adopted here solely on pragmatic grounds: when discussing finite deformations the theory without plastic spin is far simpler than one with plastic spin.

- $\mathbf{D}^p$ represents an inelastic stretching due to dislocation plasticity; and
- $\mathbf{D}^c$ represents an inelastic stretching resulting from a crazing mechanism.

Remark. For ease of presentation, at this stage in the development of the theory we conceptually allow both $\mathbf{D}^p$ and $\mathbf{D}^c$ to simultaneously be non-zero. However, later when we specialize the theory, we will consider a *transition* from dislocation-based non-dilatant plasticity to craze-type dilatant plasticity when certain conditions for a change in mechanism are satisfied.

□

On account of (9.13) and (9.11), the relation (9.8) reduces to

$$\mathbf{L} = \mathbf{L}^e + \mathbf{F}^e\mathbf{D}^p\mathbf{F}^{e-1} + \mathbf{F}^e\mathbf{D}^c\mathbf{F}^{e-1}. \tag{9.14}$$

For later use we introduce some new notation. Whenever $|\mathbf{D}^p| \neq 0$,

$$\mathbf{N}^p = \frac{\mathbf{D}^p}{|\mathbf{D}^p|}, \qquad \text{with} \qquad \operatorname{tr}\mathbf{N}^p = 0, \tag{9.15}$$

defines the *deviatoric plastic flow direction.* Further, letting

$$\dot{\gamma}^p \stackrel{\text{def}}{=} \sqrt{2}|\mathbf{D}^p| \geq 0, \tag{9.16}$$

denote an *equivalent plastic shear strain rate*, we may write the plastic stretching as

$$\mathbf{D}^p = \frac{\dot{\gamma}^p}{\sqrt{2}}\mathbf{N}^p. \tag{9.17}$$

We call

$$\gamma^p \stackrel{\text{def}}{=} \int_0^t \dot{\gamma}^p(s)ds. \tag{9.18}$$

the *equivalent plastic shear strain.*

Next, we assume that $\mathbf{D}^c$ has the form (Gearing and Anand, 2004)

$$\mathbf{D}^c = \dot{\epsilon}^c\mathbf{N}^c, \qquad \text{with} \qquad \mathbf{N}^c = \mathbf{m} \otimes \mathbf{m}, \tag{9.19}$$

where $\mathbf{m}$ is a unit vector (yet to be specified),

$$\dot{\epsilon}^c = |\mathbf{D}^c| \geq 0 \tag{9.20}$$

represents a *craze extension rate* in the direction $\mathbf{m}$. We call

$$\epsilon^c \stackrel{\text{def}}{=} \int_0^t \dot{\epsilon}^c(s)\, ds \tag{9.21}$$

the *craze-strain.* Thus, using (9.1), (9.2), (9.17) and (9.19) we may write (9.14), for future use, as

$$(\nabla\dot{\boldsymbol{\chi}})\mathbf{F}^{-1} = \dot{\mathbf{F}}^e\mathbf{F}^{e-1} + \sqrt{1/2}\dot{\gamma}^p\,\mathbf{F}^e\,\mathbf{N}^p\,\mathbf{F}^{e-1} + \dot{\epsilon}^c\,\mathbf{F}^e\,\mathbf{N}^c\,\mathbf{F}^{e-1}. \tag{9.22}$$

9.2 Phase-field

To describe fracture we introduce a *order-parameter* or *phase-field,*

$$d(\mathbf{X},t) \in [0,1]. \tag{9.23}$$

If $d = 0$ at a point then that point is intact, while if $d = 1$ at some point, then that point is fractured. Values of d between zero and one correspond to partially-fractured material. We assume that d grows montonically so that

$$\dot{d}(\mathbf{X},t) \geq 0, \tag{9.24}$$

which is a constraint that represents the usual assumption that microstructural changes leading to fracture are *irreversible.*

9.3 Development of the theory based on the principle of virtual power

Next, following the virtual-power method of Gurtin (2002) and Gurtin and Anand (2005, 2009), we assume that

- *the power expended by each independent "rate-like" kinematical descriptor* — $\dot{\boldsymbol{\chi}}$, $\dot{\mathbf{F}}^e$, $\dot{\gamma}^p$, $\dot{\epsilon}^c$, $\dot{d}$, *and* $\nabla\dot{d}$ — *be expressible in terms of an associated force systems consistent with their own balances,*

and determine these balances using the principle of virtual power. In exploiting the principle of virtual power we note that the rates ($\dot{\boldsymbol{\chi}}$, $\dot{\mathbf{F}}^e$, $\dot{\gamma}^p$, $\dot{\epsilon}^c$) are not independent — they are constrained by,

$$(\nabla\dot{\boldsymbol{\chi}})\mathbf{F}^{-1} = \dot{\mathbf{F}}^e\mathbf{F}^{e-1} + \sqrt{1/2}\dot{\gamma}^p\,\mathbf{F}^e\,\mathbf{N}^p\,\mathbf{F}^{e-1} + \dot{\epsilon}^c\,\mathbf{F}^e\,\mathbf{N}^c\,\mathbf{F}^{e-1}. \tag{9.25}$$

We denote by P an arbitrary part (subregion) of the reference body B with $\mathbf{n}_{\mathrm{R}}$ the outward unit normal on the boundary ∂P of P. With each evolution of the body we associate macroscopic and microscopic force systems. The macroscopic system is defined by:

(i) A traction $\mathbf{t}_{\mathrm{R}}(\mathbf{n}_{\mathrm{R}})$, for each unit vector $\mathbf{n}_{\mathrm{R}}$, that expends power over the velocity $\dot{\boldsymbol{\chi}}$, an external generalized body force $\mathbf{b}_{\mathrm{R}}$ — presumed to account for inertia — that also expends power over $\dot{\boldsymbol{\chi}}$. That is,

$$\mathbf{b}_{\mathrm{R}} = \mathbf{b}_{0\mathrm{R}} - \rho_{\mathrm{R}}\ddot{\boldsymbol{\chi}}, \tag{9.26}$$

where $\mathbf{b}_{0\mathrm{R}}$ represents the conventional body force per unit volume of the reference body, and $(-\rho_{\mathrm{R}}\ddot{\boldsymbol{\chi}})$ represents the inertial body force; ρ_{R} is the mass density of the referential body.

(ii) An elastic stress $\mathbf{S}^e$ that expends power over the elastic distortion rate $\dot{\mathbf{F}}^e$.

The microscopic system, which is nonstandard, is defined by:

(a) a positive-valued scalar microscopic stress π that expends power over the equivalent plastic shear strain rate $\dot{\gamma}^p$;

(b) a positive-valued scalar microscopic stress ω that expends power over the craze strain rate $\dot{\epsilon}^c$;

(c) a scalar microscopic stress ϖ that expends power over the rate $\dot{d}$ of the microvariable d;

(d) a vector microscopic stress $\boldsymbol{\xi}$ that expends power over the gradient $\nabla\dot{d}$;

(e) a scalar microscopic traction $\xi(\mathbf{n}_{\mathrm{R}})$ that expends power over $\dot{d}$ on the boundary of the part.

We characterize the force systems through the manner in which these forces expend power; that is, given any part P, through the specification of $\mathcal{W}_{\mathrm{ext}}(\mathrm{P})$, the power expended on P by material *external* to P, and $\mathcal{W}_{\mathrm{int}}(\mathrm{P})$, a concomitant expenditure of power *within* P. Specifically,[2]

$$\left.\begin{aligned}\mathcal{W}_{\mathrm{ext}}(\mathrm{P}) &= \int_{\partial\mathrm{P}} \mathbf{t}_{\mathrm{R}}(\mathbf{n}_{\mathrm{R}})\cdot\dot{\boldsymbol{\chi}}\,da_{\mathrm{R}} + \int_{\mathrm{P}} \mathbf{b}_{\mathrm{R}}\cdot\dot{\boldsymbol{\chi}}\,dv_{\mathrm{R}} + \int_{\partial\mathrm{P}} \xi(\mathbf{n}_{\mathrm{R}})\,\dot{d}\,da_{\mathrm{R}},\\ \mathcal{W}_{\mathrm{int}}(\mathrm{P}) &= \int_{\mathrm{P}} \left(\mathbf{S}^e:\dot{\mathbf{F}}^e + \pi\dot{\gamma}^p + \omega\dot{\epsilon}^c + \varpi\dot{d} + \boldsymbol{\xi}\cdot\nabla\dot{d}\right) dv_{\mathrm{R}},\end{aligned}\right\} \tag{9.27}$$

where, $\mathbf{S}^e$, π, ω, ϖ, and $\boldsymbol{\xi}$ are defined over the body for all time.

Principle of virtual power

Assume that, at some arbitrarily chosen but *fixed time*, the fields $\boldsymbol{\chi}$, $\mathbf{F}^e$ (and hence $\mathbf{F}$ and $\mathbf{F}^i$), $\mathbf{N}^p$, and $\mathbf{N}^c$ are known, and consider the fields $\dot{\boldsymbol{\chi}}$, $\dot{\mathbf{F}}^e$, $\dot{\gamma}^p$, and $\dot{\epsilon}^c$ as virtual velocities to be specified independently in a manner consistent with (9.25); that is, denoting the virtual fields by $\tilde{\boldsymbol{\chi}}$, $\tilde{\mathbf{F}}^e$, $\tilde{\gamma}^p$, and $\tilde{\epsilon}^c$ to differentiate them from fields associated with the actual evolution of the body, we require that

$$(\nabla\tilde{\boldsymbol{\chi}})\mathbf{F}^{-1} = \tilde{\mathbf{F}}^e\mathbf{F}^{e-1} + \sqrt{1/2}\,\tilde{\gamma}^p\mathbf{F}^e\,\mathbf{N}^p\,\mathbf{F}^{e-1} + \tilde{\epsilon}^c\mathbf{F}^e\,\mathbf{N}^c\,\mathbf{F}^{e-1}. \tag{9.28}$$

[2]In (9.27), da_{R} and dv_{R} denote elemental area and volume, respectively, and the symbol d in these quantities is not to be confused with the damage variable.

Further, also considering $\dot{d}$ to be a virtual velocity, and denoting its virtual counterpart by $\tilde{d}$, we define a generalized virtual velocity to be a list

$$\mathcal{V} = (\tilde{\boldsymbol{\chi}}, \tilde{\mathbf{F}}^e, \tilde{\gamma}^p, \tilde{\epsilon}^c, \tilde{d}),$$

consistent with (9.28).

We refer to a macroscopic virtual field $\mathcal{V}$ as *rigid* if it satisfies

$$(\nabla\tilde{\boldsymbol{\chi}}) = \tilde{\mathbf{F}} = \boldsymbol{\Omega}\mathbf{F}, \tag{9.29}$$

with $\boldsymbol{\Omega}$ a spatially constant skew tensor, together with

$$\tilde{\mathbf{F}}^e = \boldsymbol{\Omega}\mathbf{F}^e, \quad \tilde{\gamma}^p = 0, \quad \tilde{\epsilon}^c = 0, \quad \tilde{d} = 0. \tag{9.30}$$

Writing

$$\left.\begin{aligned} \mathcal{W}_{\text{ext}}(\mathrm{P}, \mathcal{V}) &= \int_{\partial \mathrm{P}} \mathbf{t}_{\mathrm{R}}(\mathbf{n}_{\mathrm{R}}) \cdot \tilde{\boldsymbol{\chi}}\, da_{\mathrm{R}} + \int_{\mathrm{P}} \mathbf{b}_{\mathrm{R}} \cdot \tilde{\boldsymbol{\chi}}\, dv_{\mathrm{R}} + \int_{\partial \mathrm{P}} \xi(\mathbf{n}_{\mathrm{R}})\, \tilde{d}\, da_{\mathrm{R}}, \\ \mathcal{W}_{\text{int}}(\mathrm{P}, \mathcal{V}) &= \int_{\mathrm{P}} \left(\mathbf{S}^e : \tilde{\mathbf{F}}^e + \pi\tilde{\gamma}^p + \omega\tilde{\epsilon}^c + \varpi\tilde{d} + \boldsymbol{\xi} \cdot \nabla\tilde{d} \right) dv_{\mathrm{R}}, \end{aligned}\right\} \tag{9.31}$$

respectively, for the external and internal expenditures of virtual power, the *principle of virtual power* consists of two basic requirements:

(V1) Given any part P,

$$\mathcal{W}_{\text{ext}}(\mathrm{P}, \mathcal{V}) = \mathcal{W}_{\text{int}}(\mathrm{P}, \mathcal{V}) \quad \text{for all generalized virtual velocities } \mathcal{V}. \tag{9.32}$$

(V2) Given any part P and a *rigid* virtual velocity $\mathcal{V}$,

$$\mathcal{W}_{\text{int}}(\mathrm{P}, \mathcal{V}) = 0 \quad \text{whenever } \mathcal{V} \text{ is a rigid macroscopic virtual velocity.} \tag{9.33}$$

To deduce the consequences of the principle of virtual power, assume that (9.32) and (9.33) are satisfied. Note that in applying the virtual balance we are at liberty to choose any $\mathcal{V}$ consistent with the constraint (9.28).

9.3.1 Macroscopic force and moment balances

Consider a generalized virtual velocity with $\tilde{\gamma}^p \equiv 0$, $\tilde{\epsilon}^c \equiv 0$, $\tilde{d} \equiv 0$ so that $(\nabla\tilde{\boldsymbol{\chi}})\mathbf{F}^{i-1} = \tilde{\mathbf{F}}^e$. For this choice of $\mathcal{V}$, (9.32) yields

$$\int_{\partial \mathrm{P}} \mathbf{t}_{\mathrm{R}}(\mathbf{n}_{\mathrm{R}}) \cdot \tilde{\boldsymbol{\chi}}\, da_{\mathrm{R}} + \int_{\mathrm{P}} \mathbf{b}_{\mathrm{R}} \cdot \tilde{\boldsymbol{\chi}}\, dv_{\mathrm{R}} = \int_{\mathrm{P}} \mathbf{S}^e : \tilde{\mathbf{F}}^e\, dv_{\mathrm{R}} = \int_{\mathrm{P}} (\mathbf{S}^e\mathbf{F}^{i-\mathsf{T}}) : \nabla\, \tilde{\boldsymbol{\chi}}\, dv_{\mathrm{R}}, \tag{9.34}$$

which, by defining

$$\mathbf{T}_{\mathrm{R}} \stackrel{\mathrm{def}}{=} \mathbf{S}^{e}\mathbf{F}^{i-\top}, \tag{9.35}$$

may be rewritten as

$$\int_{\partial \mathrm{P}} \mathbf{t}_{\mathrm{R}}(\mathbf{n}_{\mathrm{R}}) \cdot \tilde{\boldsymbol{\chi}}\, da_{\mathrm{R}} = \int_{\mathrm{P}} \left(\mathbf{T}_{\mathrm{R}} : \nabla \tilde{\boldsymbol{\chi}} - \mathbf{b}_{\mathrm{R}} \cdot \tilde{\boldsymbol{\chi}} \right) dv_{\mathrm{R}}, \tag{9.36}$$

and using the divergence theorem we may conclude that

$$\int_{\partial \mathrm{P}} \left(\mathbf{t}_{\mathrm{R}}(\mathbf{n}_{\mathrm{R}}) - \mathbf{T}_{\mathrm{R}}\mathbf{n}_{\mathrm{R}} \right) \cdot \tilde{\boldsymbol{\chi}}\, da_{\mathrm{R}} + \int_{\mathrm{P}} (\mathrm{Div}\, \mathbf{T}_{\mathrm{R}} + \mathbf{b}_{\mathrm{R}}) \cdot \tilde{\boldsymbol{\chi}}\, dv_{\mathrm{R}} = 0.$$

Since this relation must hold for all P and all $\tilde{\boldsymbol{\chi}}$, standard variational arguments yield the traction condition

$$\mathbf{t}_{\mathrm{R}}(\mathbf{n}_{\mathrm{R}}) = \mathbf{T}_{\mathrm{R}}\mathbf{n}_{\mathrm{R}}\,, \tag{9.37}$$

and the local macroscopic force balance

$$\mathrm{Div}\, \mathbf{T}_{\mathrm{R}} + \mathbf{b}_{0\,\mathrm{R}} = \rho_{\mathrm{R}} \ddot{\boldsymbol{\chi}}, \tag{9.38}$$

respectively, where in writing (9.38) we have used (9.26).

Next, we deduce the consequences of requirement (V2) of the principle of virtual power. Using (9.30) and $(9.31)_2$, requirement (V2) of the principle of virtual power leads to the requirement that

$$\int_{\mathrm{P}} (\mathbf{S}^{e}\mathbf{F}^{e\top}) : \boldsymbol{\Omega}\, dv_{\mathrm{R}} = 0. \tag{9.39}$$

Since P is arbitrary, we obtain that $(\mathbf{S}^{e}\mathbf{F}^{e\top}) : \boldsymbol{\Omega} = 0$ for all skew tensors $\boldsymbol{\Omega}$, which implies that $\mathbf{S}^{e}\mathbf{F}^{e\top}$ is *symmetric*:

$$\mathbf{S}^{e}\mathbf{F}^{e\top} = \mathbf{F}^{e}\mathbf{S}^{e\top}\,. \tag{9.40}$$

Moreover, (9.40) and (9.35) imply that

$$\mathbf{T}_{\mathrm{R}}\mathbf{F}^{\top} = \mathbf{F}\mathbf{T}_{\mathrm{R}}^{\top}. \tag{9.41}$$

- *In view of* (9.38) *and* (9.41) *the stress* $\mathbf{T}_{R}$ *represents the classical Piola stress, with* (9.38) *and* (9.41) *representing the local macroscopic force and moment balances in the reference body.*

As is standard, the Piola stress $\mathbf{T}_{\mathrm{R}}$ is related to the symmetric Cauchy stress $\mathbf{T}$ in the deformed body by

$$\mathbf{T}_{\mathrm{R}} = J\,\mathbf{T}\,\mathbf{F}^{-\top}, \tag{9.42}$$

so that

$$\mathbf{T} = J^{-1}\mathbf{T}_{\mathrm{R}}\mathbf{F}^{\top}. \tag{9.43}$$

It is convenient to introduce two new stress measures:

- The elastic second Piola stress,

$$\mathbf{T}^e \stackrel{\text{def}}{=} J^e \mathbf{F}^{e-1} \mathbf{T} \mathbf{F}^{e-\mathsf{T}}, \tag{9.44}$$

which is *symmetric* on account of the symmetry of the Cauchy stress $\mathbf{T}$.

- The Mandel stress,

$$\mathbf{M}^e \stackrel{\text{def}}{=} \mathbf{C}^e \mathbf{T}^e = J^e \mathbf{F}^{e\mathsf{T}} \mathbf{T} \mathbf{F}^{e-\mathsf{T}}. \tag{9.45}$$

which in general is *not symmetric.*

Using (9.35) and (9.42) we find that

$$\mathbf{S}^e = J \mathbf{T} \mathbf{F}^{e-\mathsf{T}}. \tag{9.46}$$

Thus, using the definitions (9.44) and (9.45) we find that

$$\mathbf{F}^{e-1} \mathbf{S}^e = \mathbf{T}^e \quad \text{and} \quad \mathbf{F}^{e\mathsf{T}} \mathbf{S}^e = \mathbf{M}^e. \tag{9.47}$$

9.3.2 Microscopic force balances

First microforce balance:

To discuss the microscopic counterparts of macroscopic force balance, consider first a generalized virtual velocity with $\tilde{\boldsymbol{\chi}} \equiv \mathbf{0}$, $\tilde{\epsilon}^c \equiv 0$, and $\tilde{d} = 0$, choose the virtual field $\tilde{\gamma}^p$ arbitrarily, and let

$$\tilde{\mathbf{F}}^e = -\sqrt{1/2}\, \tilde{\gamma}^p \mathbf{F}^e \mathbf{N}^p,$$

so that

$$\mathbf{S}^e : \tilde{\mathbf{F}}^e = -\tilde{\gamma}^p \left(\sqrt{1/2}\, (\mathbf{F}^{e\mathsf{T}} \mathbf{S}^e) : \mathbf{N}^p \right). \tag{9.48}$$

Next, using $(9.47)_2$ we introduce an *equivalent shear stress* $\bar{\tau}$ by the relation

$$\bar{\tau} \stackrel{\text{def}}{=} \sqrt{1/2}\, \mathbf{M}_0^e : \mathbf{N}^p, \tag{9.49}$$

where in writing the last relation we have used the fact that $\mathbf{N}^p$ is deviatoric. Then the power balance (9.32) yields the *microscopic virtual-power relation*

$$0 = \int_{\mathrm{P}} (\pi - \bar{\tau}) \tilde{\gamma}^p \, dv_{\mathrm{R}} \tag{9.50}$$

to be satisfied for all $\tilde{\gamma}^p$ and all P. This yields the first microscopic force balance,

$$\bar{\tau} = \pi. \tag{9.51}$$

Second microforce balance:

Next, consider a generalized virtual velocity with $\tilde{\boldsymbol{\chi}} \equiv \mathbf{0}$, $\tilde{\gamma}^p \equiv 0$, and $\tilde{d} = 0$, choose the virtual field $\tilde{\epsilon}^c$ arbitrarily, and let

$$\tilde{\mathbf{F}}^e = -\,\tilde{\epsilon}^c \mathbf{F}^e \mathbf{N}^c,$$

so that

$$\mathbf{S}^e : \tilde{\mathbf{F}}^e = -\,\tilde{\epsilon}^c (\mathbf{F}^{e\top} \mathbf{S}^e) : \mathbf{N}^c. \tag{9.52}$$

Next, using $(9.47)_2$ and introduce an *resolved tensile stress* σ by the relation

$$\sigma \overset{\text{def}}{=} \mathbf{M}^e : \mathbf{N}^c\,. \tag{9.53}$$

Then the power balance (9.32) yields the *microscopic virtual-power relation*

$$0 = \int_{\mathrm{P}} (\omega - \sigma) \tilde{\epsilon}^c dv_{\mathrm{R}} \tag{9.54}$$

to be satisfied for all $\tilde{\epsilon}^c$ and all P. This yields the second microscopic force balance,

$$\sigma = \omega. \tag{9.55}$$

Third microforce balance: Next, consider a generalized virtual velocity with $\tilde{\boldsymbol{\chi}} \equiv \mathbf{0}$, $\tilde{\gamma}^p \equiv 0$, and $\tilde{\epsilon}^c = 0$. Choose the virtual field $\tilde{d}$ arbitrarily, the power balance (9.32) yields the second microscopic virtual-power relation

$$\int_{\partial \mathrm{P}} \xi(\mathbf{n}_{\mathrm{R}}) \tilde{d}\, da_{\mathrm{R}} = \int_{\mathrm{P}} \left(\varpi\, \tilde{d} + \boldsymbol{\xi} \cdot \nabla \tilde{d} \right) dv_{\mathrm{R}} \tag{9.56}$$

to be satisfied for all $\tilde{d}$ and all P. Equivalently, using the divergence theorem,

$$\int_{\partial \mathrm{P}} \big(\xi(\mathbf{n}_{\mathrm{R}}) - \boldsymbol{\xi} \cdot \mathbf{n}_{\mathrm{R}} \big) \tilde{d}\, da_{\mathrm{R}} + \int_{\mathrm{P}} \big(\mathrm{Div}\, \boldsymbol{\xi} - \varpi \big) \tilde{d}\, dv_{\mathrm{R}} = 0,$$

and a standard argument yields the microscopic traction condition

$$\xi(\mathbf{n}_{\mathrm{R}}) = \boldsymbol{\xi} \cdot \mathbf{n}_{\mathrm{R}}, \tag{9.57}$$

and the third microscopic force balance

$$\mathrm{Div} \boldsymbol{\xi} - \varpi = 0. \tag{9.58}$$

9.3.3 Actual external and internal expenditures of power

Finally, using the traction conditions (9.37), and (9.57) the actual external expenditure of power (9.27) may be written as

$$\mathcal{W}_{\text{ext}}(\mathrm{P}) = \int_{\partial \mathrm{P}} (\mathbf{T}_{\mathrm{R}}\mathbf{n}_{\mathrm{R}}) \cdot \dot{\boldsymbol{\chi}}\, da_{\mathrm{R}} + \int_{\mathrm{P}} \mathbf{b}_{\mathrm{R}} \cdot \dot{\boldsymbol{\chi}}\, dv_{\mathrm{R}} + \int_{\partial \mathrm{P}} (\boldsymbol{\xi} \cdot \mathbf{n}_{\mathrm{R}})\, \dot{d}\, da_{\mathrm{R}}. \tag{9.59}$$

Also, using $(9.47)_1$ and (9.7), the stress power $\mathbf{S}^e : \dot{\mathbf{F}}^e$ may be alternatively written as

$$\mathbf{S}^e : \dot{\mathbf{F}}^e = \mathbf{T}^e : (\mathbf{F}^{e\mathsf{T}}\dot{\mathbf{F}}^e) = \frac{1}{2}\mathbf{T}^e : \dot{\mathbf{C}}^e. \tag{9.60}$$

Thus, the corresponding actual internal expenditure of power $(9.27)_1$ may be written as

$$\mathcal{W}_{\text{int}}(\mathrm{P}) = \int_{\mathrm{P}} \left(\frac{1}{2}\mathbf{T}^e : \dot{\mathbf{C}}^e + \pi\dot{\gamma}^p + \omega\dot{\epsilon}^c + \varkappa\dot{d} + \boldsymbol{\xi} \cdot \nabla\dot{d} \right) dv_{\mathrm{R}}. \tag{9.61}$$

9.3.4 Summary of consequences of the virtual power principle

To summarize, the consequences of the virtual power principle are:

(a) The stress $\mathbf{T}_{\mathrm{R}} \overset{\text{def}}{=} \mathbf{S}^e\mathbf{F}^{i-\mathsf{T}}$ satisfies $\mathbf{T}_{\mathrm{R}}\mathbf{F}^{\mathsf{T}} = \mathbf{F}\mathbf{T}_{\mathrm{R}}^{\mathsf{T}}$ and represents the classical Piola stress which is consistent with the macroscopic force balance

$$\operatorname{Div} \mathbf{T}_{\mathrm{R}} + \mathbf{b}_{0\,\mathrm{R}} = \rho_{\mathrm{R}}\ddot{\boldsymbol{\chi}}, \tag{9.62}$$

and the macroscopic traction condition,

$$\mathbf{t}_{\mathrm{R}}(\mathbf{n}_{\mathrm{R}}) = \mathbf{T}_{\mathrm{R}}\mathbf{n}_{\mathrm{R}}. \tag{9.63}$$

(b) With $\mathbf{M}^e \overset{\text{def}}{=} \mathbf{F}^{e\mathsf{T}}\mathbf{S}^e$ defining a Mandel stress, and

$$\bar{\tau} \overset{\text{def}}{=} \sqrt{1/2}\,\mathbf{M}^e : \mathbf{N}^p, \tag{9.64}$$

defining a resolved shear stress, with $\mathbf{N}^p$ a symmetric deviatoric tensor defining the "direction" of plastic flow (cf. eq.(9.15)), the microstress π satisfies the microforce balance

$$\bar{\tau} = \pi. \tag{9.65}$$

(c) With

$$\sigma \overset{\text{def}}{=} \mathbf{M}^e : \mathbf{N}^c, \tag{9.66}$$

defining a resolved tensile stress, with $\mathbf{N}^c$ a symmetric tensor defining the "direction" of craze flow (cf. eq.(9.19)), the microstress ω satisfies the microforce balance

$$\sigma = \omega. \tag{9.67}$$

(d) The microscopic stresses ϖ and $\boldsymbol{\xi}$ are consistent with the microscopic force balance

$$\mathrm{Div}\boldsymbol{\xi} - \varpi = 0, \tag{9.68}$$

and the microtraction condition

$$\xi(\mathbf{n}_{\mathrm{R}}) = \boldsymbol{\xi} \cdot \mathbf{n}_{\mathrm{R}}. \tag{9.69}$$

These macro- and microforce balances, when supplemented with a set of thermodynamically consistent constitutive equations, provide the governing mechanical equations for the theory.

9.4 Balance law for the diffusion of hydrogen

Let C(**X**,t) denote the *total number of moles of hydrogen atoms per unit reference volume.* Hydrogen is absorbed into the metal into *normal interstitial lattice sites* (NILS), and into *trapping sites* associated with internal microstructural defects such as vacancies and dislocation cores. We allow for m different sorts of traps, and accordingly assume that

$$C(\mathbf{X},t) = C_{\mathrm{L}}(\mathbf{X},t) + \sum_k C_{\mathrm{Tk}}(\mathbf{X},t). \tag{9.70}$$

where we have used the shorthand

$$\sum_k \stackrel{\mathrm{def}}{=} \sum_{k=1}^{m}.$$

Next, we introduce some definitions:

(i) **Number of moles of lattice sites per unit reference volume, N_{L}:** This is a property of the host metal given by

$$N_{\mathrm{L}} \stackrel{\mathrm{def}}{=} \varphi \frac{\rho_M}{\mathcal{M}_M} \quad (\mathrm{mol/m^3}), \tag{9.71}$$

with d the number of interstitial lattice sites per metal atom, ρ_M the mass density of the host metal ($\mathrm{kg/m^3}$) and $\mathcal{M}_M$ the molar mass of the host metal (kg/mol). In bcc and fcc metals, hydrogen can occupy either tetrahedral or octahedral sites. For α-iron, indirect evidence indicates tetrahedral site occupancy of hydrogen at room temperature 293 K, in which case $\varphi = 6$. The mass density of iron is $\rho_M = 7.87 \times 10^3\,\mathrm{kg/m^3}$; the molar mass is $\mathcal{M}_M = 55.8 \times 10^{-3}\,\mathrm{kg/mol}$. In this case $N_{\mathrm{L}} = 8.46 \times 10^5\,\mathrm{mol/m^3}$ (Krom and Bakker, 2000).

(ii) **Number of moles of trap sites per unit reference volume, N_{Tk} $(k = 1, \ldots, m)$:** For each different trap-type k, denote by N_{Tk} the number of moles of trap sites per unit reference volume,

$$N_{\mathrm{Tk}} \qquad (\mathrm{mol/m^3}) \qquad k = 1, \ldots, m. \tag{9.72}$$

Each number of trap sites N_{Tk} is *not a characteristic of the matrix* and is very difficult to estimate. However, various experimental investigations indicate that the trap density depends on the history of the prior plastic deformation. Accordingly, it is commonly assumed that

$$N_{\mathrm{Tk}} = \tilde{N}_{\mathrm{Tk}}(\gamma^p) \quad (\mathrm{mol/m^3}) \qquad k = 1, \ldots, m. \tag{9.73}$$

(iii) **Occupancy fraction θ_{L} and θ_{T}:** Let

$$\theta_{\mathrm{L}} \stackrel{\mathrm{def}}{=} \frac{C_{\mathrm{L}}}{N_{\mathrm{L}}}, \quad 0 \leq \theta_{\mathrm{L}} \leq 1, \tag{9.74}$$

denote the occupancy fraction of the lattice sites, and

$$\theta_{\mathrm{Tk}} \stackrel{\mathrm{def}}{=} \frac{C_{\mathrm{Tk}}}{N_{\mathrm{Tk}}}, \quad 0 \leq \theta_{\mathrm{Tk}} \leq 1, \tag{9.75}$$

denote the occupancy fraction of the trap sites.

Finally, changes in C_{L} in a part P are brought about by diffusion of C_{L} across the boundary ∂P of P, and by the transformation rate between lattice and trapped hydrogen. That is, the rates of change of lattice a hydrogen in P is given by

$$\dot{C}_{\mathrm{L}} = -\mathrm{Div}\mathbf{j}_{\mathrm{L}} - \sum_k \dot{C}_{\mathrm{Tk}}, \tag{9.76}$$

where $\mathbf{j}_{\mathrm{L}}(\mathbf{X}, t)$ is the *flux* of lattice hydrogen measured as the number of moles of hydrogen atoms per unit area per unit time, and $\dot{C}_{\mathrm{Tk}}$ is the *transformation rate* from lattice to trapped hydrogen measured as the number of moles of hydrogen atoms per unit volume per unit time. A specification of $\dot{C}_{\mathrm{Tk}}$ is deferred to a later section.

9.5 Balance of energy. Entropy imbalance. Free-energy imbalance

Our discussion of thermodynamics follows Gurtin et al. (2010, Section 64), and involves the following fields

ε_{R} the internal energy density per unit reference volume,
η_{R} the entropy density per unit reference volume,
$\mathbf{q}_{\mathrm{R}}$ the heat flux per unit reference area,
q_{R} the external heat supply per unit reference volume,
$\vartheta > 0$ the absolute temperature,
μ_{L} the chemical potential for the lattice hydrogen.

The balance of energy is given by

$$\overline{\int_{\mathrm{P}} \varepsilon_{\mathrm{R}}\, dv_{\mathrm{R}}}^{\cdot} = \mathcal{W}_{\mathrm{ext}}(\mathrm{P}) - \int_{\partial \mathrm{P}} \mathbf{q}_{\mathrm{R}} \cdot \mathbf{n}_{\mathrm{R}}\, da_{\mathrm{R}} + \int_{\mathrm{P}} q_{\mathrm{R}}\, dv_{\mathrm{R}} - \int_{\partial \mathrm{P}} \mu_{\mathrm{L}} \mathbf{j}_{\mathrm{L}} \cdot \mathbf{n}_{\mathrm{R}}\, da_{\mathrm{R}}, \tag{9.77}$$

where the last term in (9.77) represent the energy contribution into P by the lattice hydrogen. Applying the divergence theorem to the terms in (9.77) involving integrals over the boundary $\partial \mathrm{P}$ of P, and since $\mathcal{W}_{\mathrm{ext}}(\mathrm{P}) = \mathcal{W}_{\mathrm{int}}(\mathrm{P})$, using (9.61) we obtain

$$\int_{\mathrm{P}} \left(\dot{\varepsilon}_{\mathrm{R}} - \left(\frac{1}{2}\mathbf{T}^e : \dot{\mathbf{C}}^e + \pi \dot{\gamma}^p + \omega \dot{\epsilon}^c + \varpi \dot{d} + \boldsymbol{\xi} \cdot \nabla \dot{d} \right) + \mu_{\mathrm{L}} \mathrm{Div}\, \mathbf{j}_{\mathrm{L}} + \mathbf{j}_{\mathrm{L}} \cdot \nabla \mu_{\mathrm{L}} + \mathrm{Div}\, \mathbf{q}_{\mathrm{R}} - q_{\mathrm{R}} \right) dv_{\mathrm{R}} = 0, \tag{9.78}$$

which upon use of the concentration balance law (9.76), and using the fact that (9.78) must hold for all parts P, gives the local form of the energy balance as

$$\dot{\varepsilon}_{\mathrm{R}} = \left(\frac{1}{2}\mathbf{T}^e : \dot{\mathbf{C}}^e + \pi \dot{\gamma}^p + \omega \dot{\epsilon}^c + \varpi \dot{d} + \boldsymbol{\xi} \cdot \nabla \dot{d} \right) + \mu_{\mathrm{L}} \left(\dot{C}_{\mathrm{L}} + \sum_k \dot{C}_{\mathrm{Tk}} \right) - \mathbf{j}_{\mathrm{L}} \cdot \nabla \mu_{\mathrm{L}} - \mathrm{Div}\, \mathbf{q}_{\mathrm{R}} + q_{\mathrm{R}}\,. \tag{9.79}$$

Also, the second law takes the form of an entropy imbalance

$$\overline{\int_{\mathrm{P}} \eta_{\mathrm{R}}\, dv_{\mathrm{R}}}^{\cdot} \geq - \int_{\partial \mathrm{P}} \frac{\mathbf{q}_{\mathrm{R}} \cdot \mathbf{n}_{\mathrm{R}}}{\vartheta}\, da_{\mathrm{R}} + \int_{\mathrm{P}} \frac{q_{\mathrm{R}}}{\vartheta}\, dv_{\mathrm{R}}, \tag{9.80}$$

and the local entropy imbalance has the form of

$$\dot{\eta}_{\mathrm{R}} \geq -\mathrm{Div} \left(\frac{\mathbf{q}_{\mathrm{R}}}{\vartheta} \right) + \frac{q_{\mathrm{R}}}{\vartheta}. \tag{9.81}$$

Henceforth we restrict our attention to *isothermal conditions* at a fixed tempearture ϑ. In this case (9.81) reduces to

$$\vartheta \dot{\eta}_{\mathrm{R}} \geq -\mathrm{Div}\, \mathbf{q}_{\mathrm{R}} + q_{\mathrm{R}}, \tag{9.82}$$

and this with the local energy balance (9.79) implies that

$$\begin{aligned}(\dot{\varepsilon}_{\mathrm{R}} - \vartheta\dot{\eta}_{\mathrm{R}}) - \Big(\frac{1}{2}\mathbf{T}^e : \dot{\mathbf{C}}^e + \pi\dot{\gamma}^p + \omega\dot{\epsilon}^c + \varpi\dot{d} + \boldsymbol{\xi}\cdot\nabla\dot{d}\Big) \\ - \mu_{\mathrm{L}}\Big(\dot{C}_{\mathrm{L}} + \sum_k \dot{C}_{\mathrm{Tk}}\Big) + \mathbf{j}_{\mathrm{L}}\cdot\nabla\mu_{\mathrm{L}} \leq 0\,.\end{aligned} \tag{9.83}$$

Introducing the Helmholtz free energy

$$\psi_{\mathrm{R}} = \varepsilon_{\mathrm{R}} - \vartheta\eta_{\mathrm{R}}, \tag{9.84}$$

(9.83) yields the following local *free-energy imbalance under isothermal conditions*,

$$\begin{aligned}\dot{\psi}_{\mathrm{R}} - \frac{1}{2}\mathbf{T}^e : \dot{\mathbf{C}}^e - \pi\dot{\gamma}^p - \omega\dot{\epsilon}^c - \varpi\dot{d} - \boldsymbol{\xi}\cdot\nabla\dot{d} \\ - \mu_{\mathrm{L}}\Big(\dot{C}_{\mathrm{L}} + \sum_k \dot{C}_{\mathrm{Tk}}\Big) + \mathbf{j}_{\mathrm{L}}\cdot\nabla\mu_{\mathrm{L}} \leq 0\,.\end{aligned} \tag{9.85}$$

Remark. For brevity we have not discussed invariance properties of the various fields appearing in our theory. However, such considerations are straight-forward and extensively elaborated upon in the context of a similar diffusion-deformation theory by Anand (2011) and Di Leo and Anand (2013). Here, we simply note that all quantities in the free energy imbalance (9.85) are invariant under a change in frame. □

9.6 Constitutive theory

By (9.16) the equivalent tensile plastic strain satisfies

$$\gamma^p(\mathbf{X}, 0) = 0, \qquad \dot{\gamma}^p(\mathbf{X}, t) \geq 0, \tag{9.86}$$

and by (9.20) the craze plastic strain satisfies

$$\epsilon^c(\mathbf{X}, 0) = 0, \qquad \dot{\epsilon}^c(\mathbf{X}, t) \geq 0, \tag{9.87}$$

and hence both γ^p and ϵ^c increase with time in any "inelastic process". We view γ^p and ϵ^c as measures of the past history of inelastic strain in the material. Recall that we have also introduced an additional phase-field variable d. Here we consider a theory which allows for

- an energetic and dissipative effects associated with temporal changes in d, and the gradient

$$\mathbf{g}^d \stackrel{\text{def}}{=} \nabla d. \tag{9.88}$$

We consider the gradients $\mathbf{g}^d$ as a measure of the inhomogeneity of the microscale damage.

Let $\mathbf{\Lambda}$ denote the list

$$\mathbf{\Lambda} = (\mathbf{C}^e, C_{\mathrm{L}}, \vec{C}_{\mathrm{Tk}}, \epsilon^c, d, \mathbf{g}^d). \tag{9.89}$$

Guided by the free-energy imbalance (9.85), we first consider the following set of constitutive equations for the free energy ψ_{R}, the stress $\mathbf{T}^e$, the chemical potential μ_{L} of the lattice hydrogen, and $\vec{\mu}_{\mathrm{Tk}}$ the chemical potentials of the trapped hydrogen:

$$\psi_{\mathrm{R}} = \hat{\psi}_{\mathrm{R}}(\mathbf{\Lambda}), \qquad \mathbf{T}^e = \hat{\mathbf{T}}^e(\mathbf{\Lambda}), \qquad \mu_{\mathrm{L}} = \hat{\mu}_{\mathrm{L}}(\mathbf{\Lambda}), \qquad \mu_{\mathrm{Tk}} = \hat{\mu}_{\mathrm{Tk}}(\mathbf{\Lambda}). \tag{9.90}$$

Substituting the constitutive equations (9.90) into the free-energy imbalance (9.85), we find that it may be written as

$$\begin{aligned}\left(\frac{\partial\hat{\psi}_{\mathrm{R}}(\mathbf{\Lambda})}{\partial\mathbf{C}^e} - \frac{1}{2}\mathbf{T}^e\right) : \dot{\mathbf{C}}^e + \left(\frac{\partial\hat{\psi}_{\mathrm{R}}(\mathbf{\Lambda})}{\partial C_{\mathrm{L}}} - \mu_{\mathrm{L}}\right)\dot{C}_{\mathrm{L}} - \left(\omega - \frac{\partial\hat{\psi}_{\mathrm{R}}(\mathbf{\Lambda})}{\partial\epsilon^c}\right)\dot{\epsilon}^c \\ - \left(\varpi - \frac{\partial\hat{\psi}_{\mathrm{R}}(\mathbf{\Lambda})}{\partial d}\right)\dot{d} - \left(\boldsymbol{\xi} - \frac{\partial\hat{\psi}_{\mathrm{R}}(\mathbf{\Lambda})}{\partial\mathbf{g}^d}\right)\cdot\dot{\mathbf{g}}^d \\ - \pi\dot{\gamma}^p - \sum_k\left(\mu_{\mathrm{L}} - \frac{\partial\hat{\psi}_{\mathrm{R}}(\mathbf{\Lambda})}{\partial C_{\mathrm{Tk}}}\right)\dot{C}_{\mathrm{Tk}} + \mathbf{j}_{\mathrm{L}}\cdot\nabla\mu_{\mathrm{L}} \le 0.\end{aligned} \tag{9.91}$$

We assume that the free energy function $\hat{\psi}_{\mathrm{R}}(\mathbf{\Lambda})$ delivers the stress $\mathbf{T}^e$ and the chemical potentials μ_{L} and μ_{Tk} through the state relations

$$\mathbf{T}^e = 2\frac{\partial\hat{\psi}_{\mathrm{R}}(\mathbf{\Lambda})}{\partial\mathbf{C}^e}, \qquad \mu_{\mathrm{L}} = \frac{\partial\hat{\psi}_{\mathrm{R}}(\mathbf{\Lambda})}{\partial C_{\mathrm{L}}}, \qquad \mu_{\mathrm{Tk}} = \frac{\partial\hat{\psi}_{\mathrm{R}}(\mathbf{\Lambda})}{\partial C_{\mathrm{Tk}}}. \tag{9.92}$$

Further, introducing energetic microstresses (ω_{en},$\varkappa_{\mathrm{en}}$, $\boldsymbol{\xi}_{\mathrm{en}}$) through the relations

$$\omega_{\mathrm{en}} = \frac{\partial\hat{\psi}_{\mathrm{R}}(\mathbf{\Lambda})}{\partial\epsilon^c}, \qquad \varpi_{\mathrm{en}} = \frac{\partial\hat{\psi}_{\mathrm{R}}(\mathbf{\Lambda})}{\partial d}, \qquad \boldsymbol{\xi}_{\mathrm{en}} = \frac{\partial\hat{\psi}_{\mathrm{R}}(\mathbf{\Lambda})}{\partial\mathbf{g}^d}, \tag{9.93}$$

and dissipative microstresses ($\varkappa_{\mathrm{dis}}$, $\boldsymbol{\xi}_{\mathrm{dis}}$) through the relations

$$\omega_{\mathrm{dis}} = \omega - \omega_{\mathrm{en}}, \qquad \varpi_{\mathrm{dis}} = \varpi - \varpi_{\mathrm{en}}, \qquad \boldsymbol{\xi}_{\mathrm{dis}} = \boldsymbol{\xi} - \boldsymbol{\xi}_{\mathrm{en}}, \tag{9.94}$$

respectively, we are left with the following reduced dissipation inequality

$$\mathcal{D} = \pi\dot{\gamma}^p + \omega_{\mathrm{dis}}\dot{\epsilon}^c + \varpi_{\mathrm{dis}}\dot{d} + \boldsymbol{\xi}_{\mathrm{dis}}\cdot\dot{\mathbf{g}}^d + \sum_k\left(\mu_{\mathrm{L}} - \frac{\partial\hat{\psi}_{\mathrm{R}}(\mathbf{\Lambda})}{\partial C_{\mathrm{Tk}}}\right)\dot{C}_{\mathrm{Tk}} - \mathbf{j}_{\mathrm{L}}\cdot\nabla\mu_{\mathrm{L}} \ge 0. \tag{9.95}$$

To the constitutive equation (9.90), we append a Fick-type relation for the flux of the diffusing species,

$$\mathbf{j}_{\mathrm{R}} = -\mathbf{M}(\tilde{\mathbf{\Lambda}})\,\nabla\mu, \tag{9.96}$$

where $\mathbf{M}$ is a *mobility tensor*, and $\tilde{\mathbf{\Lambda}}$ is the list

$$\tilde{\mathbf{\Lambda}} = (\mathbf{C}^e, C_{\mathrm{L}}). \tag{9.97}$$

Using (9.96), the dissipation inequality (9.95) may be written as

$$\begin{aligned}\mathcal{D} =& \pi\dot{\gamma}^p + \omega_{\mathrm{dis}}\dot{\epsilon}^c + \varpi_{\mathrm{dis}}\dot{d} + \boldsymbol{\xi}_{\mathrm{dis}}\cdot\dot{\mathbf{g}}^d \\ &+ \sum_k \left(\mu_{\mathrm{L}} - \frac{\partial\hat{\psi}_{\mathrm{R}}(\mathbf{\Lambda})}{\partial C_{\mathrm{Tk}}}\right)\dot{C}_{\mathrm{Tk}} + \nabla\mu_{\mathrm{L}}\cdot\mathbf{M}\,\nabla\mu \geq 0.\end{aligned} \tag{9.98}$$

We assume that the terms in (9.98) individually satisfy the dissipation inequalities

$$\begin{aligned}&\pi\dot{\gamma}^p \geq 0, \quad \omega_{\mathrm{dis}}\dot{\epsilon}^c \geq 0, \quad \varpi_{\mathrm{dis}}\dot{d} \geq 0, \\ &\boldsymbol{\xi}_{\mathrm{dis}}\cdot\dot{\mathbf{g}}^d \geq 0, \quad (\mu_{\mathrm{L}} - \mu_{\mathrm{Tk}})\dot{C}_{\mathrm{Tk}} \geq 0, \quad \nabla\mu_{\mathrm{L}}\cdot\mathbf{M}\,\nabla\mu \geq 0.\end{aligned} \tag{9.99}$$

Thus, note that the mobility tensor $\mathbf{M}$ is positive-semidefinite.

The theory presented thus far is still quite general. In the following sections we introduce special constitutive equations which should be useful in applications.

9.7 Free energy

Henceforth we restrict our attention to materials for which the response function $\hat{\psi}_{\mathrm{R}}(\mathbf{\Lambda})$ is taken to depend on $\mathbf{C}^e$ ony through its principal invariants

$$\mathcal{I}_{\mathbf{C}^e} = (I_1(\mathbf{C}^e), I_2(\mathbf{C}^e), I_3(\mathbf{C}^e)), \tag{9.100}$$

so that the free energy function $(9.90)_1$ becomes

$$\psi_{\mathrm{R}} = \hat{\psi}_{\mathrm{R}}(\mathcal{I}_{\mathbf{C}^e}, C_{\mathrm{L}}, \vec{C}_{\mathrm{Tk}}, \epsilon^c, d, \mathbf{g}^d). \tag{9.101}$$

Thus, from (9.92), it follows that the constitutive equation for $\mathbf{T}^e$, μ_{L}, and μ_{T} are,

$$\mathbf{T}^e = 2\frac{\partial\,\hat{\psi}_{\mathrm{R}}(\mathcal{I}_{\mathbf{C}^e}, C_{\mathrm{L}}, \vec{C}_{\mathrm{Tk}}, \epsilon^c, d, \mathbf{g}^d)}{\partial\mathbf{C}^e}, \tag{9.102}$$

$$\mu_{\mathrm{L}} = \frac{\partial\hat{\psi}_{\mathrm{R}}(\mathcal{I}_{\mathbf{C}^e}, C_{\mathrm{L}}, \vec{C}_{\mathrm{Tk}}, \epsilon^c, d, \mathbf{g}^d)}{\partial C_{\mathrm{L}}}, \tag{9.103}$$

$$\mu_{\mathrm{Tk}} = \frac{\partial \hat{\psi}_{\mathrm{R}}(\mathcal{I}_{\mathbf{C}^e}, C_{\mathrm{L}}, \vec{C}_{\mathrm{Tk}}, \epsilon^c, d, \mathbf{g}^d)}{\partial C_{\mathrm{Tk}}}, \tag{9.104}$$

and that the constitutive equation for $\mathbf{T}^e$ is an *isotropic function* of $\mathbf{C}^e$. Then since the Mandel stress is defined by (cf. (9.45))

$$\mathbf{M}^e = \mathbf{C}^e\mathbf{T}^e, \tag{9.105}$$

we find that $\mathbf{T}^e$ and $\mathbf{C}^e$ commute,

$$\mathbf{C}^e\mathbf{T}^e = \mathbf{T}^e\mathbf{C}^e, \tag{9.106}$$

and hence that *the Mandel stress is symmetric.*

Now, the spectral representation of $\mathbf{C}^e$ is

$$\mathbf{C}^e = \sum_{i=1}^{3} (\lambda_i^e)^2 \mathbf{r}_i^e \otimes \mathbf{r}_i^e, \tag{9.107}$$

where $(\mathbf{r}_1^e, \mathbf{r}_2^e, \mathbf{r}_3^e)$ are the orthonormal eigenvectors of $\mathbf{C}^e$ and $\mathbf{U}^e$, and $(\lambda_1^e, \lambda_2^e, \lambda_3^e)$ are the positive eigenvalues of $\mathbf{U}^e$. Instead of using the invariants $\mathcal{I}_{\mathbf{C}^e}$, the free energy $\psi_{\mathrm{R}}^{(1)}$ may be alternatively expressed in terms of the principal stretches as,

$$\psi_{\mathrm{R}} = \breve{\psi}_{\mathrm{R}}(\lambda_1^e, \lambda_2^e, \lambda_3^e, C_{\mathrm{L}}, \vec{C}_{\mathrm{Tk}}, \epsilon^c, d, \mathbf{g}^d). \tag{9.108}$$

Let

$$\mathbf{E}^e \stackrel{\mathrm{def}}{=} \ln \mathbf{U}^e = \sum_{i=1}^{3} E_i^e \mathbf{r}_i^e \otimes \mathbf{r}_i^e, \tag{9.109}$$

denote the logarithmic elastic strain with principal values

$$E_i^e \stackrel{\mathrm{def}}{=} \ln \lambda_i^e, \tag{9.110}$$

and consider a free energy function of the form

$$\breve{\psi}_{\mathrm{R}}(\lambda_1^e, \lambda_2^e, \lambda_3^e, C_{\mathrm{L}}, \vec{C}_{\mathrm{Tk}}, \epsilon^c, d, \mathbf{g}^d) = \breve{\psi}_{\mathrm{R}}(E_1^e, E_2^e, E_3^e, C_{\mathrm{L}}, \vec{C}_{\mathrm{Tk}}, \epsilon^c, d, \mathbf{g}^d). \tag{9.111}$$

Then, the Mandel stress is given by

$$\mathbf{M}^e = \sum_{i=1}^{3} \frac{\partial \breve{\psi}_{\mathrm{R}}(E_1^e, E_2^e, E_3^e, C_{\mathrm{L}}, \vec{C}_{\mathrm{Tk}}, \epsilon^c, d, \mathbf{g}^d)}{\partial E_i^e} \mathbf{r}_i^e \otimes \mathbf{r}_i^e. \tag{9.112}$$

With the logarithmic strain defined by (9.109), and bearing in mind (9.111) and (9.112), we henceforth consider a free energy of the form

$$\psi_{\mathrm{R}} = \tilde{\psi}_{\mathrm{R}}(\mathcal{I}_{\mathbf{E}^e}, C_{\mathrm{L}}, \vec{C}_{\mathrm{Tk}}, \epsilon^c, d, \mathbf{g}^d), \tag{9.113}$$

with $\mathcal{I}_{\mathbf{E}^e}$ a list of principal invariants of $\mathbf{E}^e$, or equivalently a list of principal values of $\mathbf{E}^e$. The Mandel stress is then given by

$$\mathbf{M}^e = \frac{\partial \tilde{\psi}_{\mathrm{R}}(\mathcal{I}_{\mathbf{E}^e}, C_{\mathrm{L}}, \vec{C}_{\mathrm{Tk}}, \epsilon^c, d, \mathbf{g}^d)}{\partial \mathbf{E}^e}, \tag{9.114}$$

and the corresponding Cauchy stress is

$$\mathbf{T} = J^{e-1}\mathbf{R}^e\mathbf{M}^e\mathbf{R}^{e\mathsf{T}}. \tag{9.115}$$

Further, the chemical potentials μ_{L} and μ_{T} are given by

$$\mu_{\mathrm{L}} = \frac{\partial \tilde{\psi}_{\mathrm{R}}(\mathcal{I}_{\mathbf{E}^e}, C_{\mathrm{L}}, \vec{C}_{\mathrm{Tk}}, \epsilon^c, d, \mathbf{g}^d)}{\partial C_{\mathrm{L}}}, \tag{9.116}$$

and

$$\mu_{\mathrm{Tk}} = \frac{\partial \tilde{\psi}_{\mathrm{R}}(\mathcal{I}_{\mathbf{E}^e}, C_{\mathrm{L}}, \vec{C}_{\mathrm{Tk}}, \epsilon^c, d, \mathbf{g}^d)}{\partial C_{\mathrm{Tk}}}, \tag{9.117}$$

respectively.

As a further specialization we consider

$$\begin{aligned}\tilde{\psi}_{\mathrm{R}}(\mathcal{I}_{\mathbf{E}^e}, C_{\mathrm{L}}, \vec{C}_{\mathrm{Tk}}, \epsilon^c, d, \mathbf{g}^d) =& g(d)\tilde{\psi}^e_{\mathrm{R}}(\mathcal{I}_{\mathbf{E}^e}, C_{\mathrm{L}}, \vec{C}_{\mathrm{Tk}}) + \tilde{\psi}^{\mathrm{mix}}_{\mathrm{R}}(C_{\mathrm{L}}, \vec{C}_{\mathrm{Tk}}) \\ &+ g(d)\tilde{\psi}^c_{\mathrm{R}}(\epsilon^c) + \psi^{\mathrm{crit}}_{\mathrm{R}}\ell^2\,|\nabla d|^2.\end{aligned} \tag{9.118}$$

Here:

(i) ψ^e_{R} is a chemo-elastic energy given by

$$\begin{aligned}\tilde{\psi}^e_{\mathrm{R}}(\mathcal{I}_{\mathbf{E}^e}, C_{\mathrm{L}}, \vec{C}_{\mathrm{Tk}}) = G|\mathbf{E}^e|^2 + \frac{1}{2}\left(K - \frac{2}{3}G\right)(\mathrm{tr}\,\mathbf{E}^e)^2 \\ - (K\Omega_{\mathrm{H}})(C_{\mathrm{L}} - C^0_{\mathrm{L}})(\mathrm{tr}\,\mathbf{E}^e) - \sum_k (K\Omega_{\mathrm{Tk}})(C_{\mathrm{Tk}} - C^0_{\mathrm{Tk}})(\mathrm{tr}\,\mathbf{E}^e),\end{aligned} \tag{9.119}$$

which is a simple generalization of the classical strain energy function of infinitesimal isotropic elasticity combined with a thermal entropic contribution, and contributions due to the presence of lattice and trapped hydrogen in the material. Here G is the shear modulus, K the bulk modulus, C^0_{L} and C^0_{Tk} are reference lattice and trapped hydrogen

concentrations, and Ω_{H} and Ω_{Tk} are molar volumes of hydrogen in lattice and trapped sites, respectively. There is insufficient information from either physical experiments or detailed micromechanical models to distinguish between Ω_{H} and Ω_{Tk}. For simplicity, we assume henceforth that that the amount of chemical expansion caused by the trapped hydrogen is the same as that caused by the lattice hydrogen, so that

$$\Omega_{\mathrm{H}} = \Omega_{\mathrm{Tk}}. \tag{9.120}$$

(ii) $\psi_{\mathrm{R}}^{\mathrm{mix}}$ is a chemical free energy related to the mixing of hydrogen in the host metal, given by

$$\tilde{\psi}_{\mathrm{R}}^{\mathrm{mix}}(C_{\mathrm{L}}, \vec{C}_{\mathrm{Tk}}) = \tilde{\psi}_{\mathrm{R}}^{\mathrm{mix,latt}}(C_{\mathrm{L}}) + \tilde{\psi}_{\mathrm{R}}^{\mathrm{mix,trap}}(\vec{C}_{\mathrm{Tk}}), \tag{9.121}$$

where $\psi^{\mathrm{mix,latt}}$ and $\psi^{\mathrm{mix,trap}}$ are chemical free energies related to the mixing of lattice and trapped hydrogen in the host metal. As a simple continuum approximation to mixing, we take these to be given by the entropic contributions in a regular solution model (cf., e.g., DeHoff, 2006):

$$\tilde{\psi}_{\mathrm{R}}^{\mathrm{mix,latt}}(C_{\mathrm{L}}) = \mu_{\mathrm{L}}^{0} C_{\mathrm{L}} + R\vartheta N_{\mathrm{L}}(\theta_{\mathrm{L}} \ln \theta_{\mathrm{L}} + (1-\theta_{\mathrm{L}}) \ln(1-\theta_{\mathrm{L}})), \tag{9.122}$$

$$\tilde{\psi}_{\mathrm{R}}^{\mathrm{mix,trap}}(\vec{C}_{\mathrm{Tk}}) = \sum_{k} \left[\mu_{\mathrm{Tk}}^{0} C_{\mathrm{Tk}} + R\vartheta N_{\mathrm{Tk}}(\theta_{\mathrm{Tk}} \ln \theta_{\mathrm{Tk}} + (1-\theta_{\mathrm{Tk}}) \ln(1-\theta_{\mathrm{Tk}}))\right], \tag{9.123}$$

where μ_{L}^{0} and μ_{Tk}^{0} are reference chemical potentials, and R is the gas constant. a reference chemical potential, R the gas constant, and ϑ the constant temperature under consideration.

(iii) The function $g(d)$ is a monotonically decreasing *degradation function* of d, which satisfies

$$g(0) = 1, \quad g(1) = 0, \quad g'(d) \leq 0, \quad \text{and} \quad g'(1) = 0. \tag{9.124}$$

A widely-used degradation function is

$$g(d) = (1-d)^2; \tag{9.125}$$

we adopt it here.[3]

(iv) We assume that the crazing process gives rise to local disordering which stores energy according to,

$$\tilde{\psi}_{\mathrm{R}}^{c}(\epsilon^{c}) = (1-\varkappa)\, S^{c} \epsilon^{c}, \tag{9.127}$$

[3]In numerical calculations $g(d)$ is modified as

$$g(d) = (1-d)^2 + k, \tag{9.126}$$

where $k \approx 0$ is a small positive-valued constant which is introduced to prevent ill-conditioning of the model when $d = 1$.

with $S^c > 0$ a constant modulus with units of stress representing the craze flow resistance, and $\varkappa$ is positive-valued fraction, such that $\varkappa S^c \dot{\epsilon}^c$ represents the dissipation due to craze flow, and that the fraction $(1-\varkappa)\, S^c \epsilon^c$ is stored in the material.

(v) In order to account for gradient effects for the damage we have included a quadratic term dependent the gradient ∇d,

$$\psi_{\mathrm{R}}^{\mathrm{crit}} \ell^2 \, |\nabla d|^2, \tag{9.128}$$

where $\psi_{\mathrm{R}}^{\mathrm{crit}} > 0$ is coeficient with units of energy, and $\ell > 0$ is an internal length scale for the width of zones across which the damage varies rapidly.

Thus, combining (9.118), (9.119) and (9.122), the free energy is given by

$$\begin{aligned}
\psi_{\mathrm{R}} = g(d) & \underbrace{\left[G|\mathbf{E}^e|^2 + \frac{1}{2}\left(K - \frac{2}{3}G\right)(\mathrm{tr}\,\mathbf{E}^e)^2 - (K\Omega_{\mathrm{H}})(C - C^0)(\mathrm{tr}\,\mathbf{E}^e) \right]}_{\tilde{\psi}_{\mathrm{R}}^e(\mathcal{I}_{\mathbf{E}^e}, C)} \\
& + g(d) \underbrace{\left[(1-\varkappa)\, S^c \epsilon^c \right]}_{\tilde{\psi}_{\mathrm{R}}^c(\epsilon^c)} + \psi_{\mathrm{R}}^{\mathrm{crit}} \ell^2 \, |\nabla d|^2 \\
& + \mu_{\mathrm{L}}^0 C_{\mathrm{L}} + R\vartheta N_{\mathrm{L}}(\theta_{\mathrm{L}} \ln \theta_{\mathrm{L}} + (1-\theta_{\mathrm{L}}) \ln(1-\theta_{\mathrm{L}})) \\
& + \sum_k \left[\mu_{\mathrm{Tk}}^0 C_{\mathrm{Tk}} + R\vartheta N_{\mathrm{Tk}}(\theta_{\mathrm{Tk}} \ln \theta_{\mathrm{Tk}} + (1-\theta_{\mathrm{Tk}}) \ln(1-\theta_{\mathrm{Tk}})) \right].
\end{aligned} \tag{9.129}$$

Then, by (9.92) the Mandel stress, and the chemical potentials are given by

$$\begin{aligned}
\mathbf{M}^e &= g(d) \left[2G\mathbf{E}_0^e + K(\mathrm{tr}\,\mathbf{E}^e)\mathbf{1} - K\Omega_{\mathrm{H}}(C - C^0)\mathbf{1} \right], \\
\mu_{\mathrm{L}} &= \mu_{\mathrm{L}}^0 + R\vartheta \ln\left(\frac{\theta_{\mathrm{L}}}{1-\theta_{\mathrm{L}}}\right) - g(d) K\Omega_{\mathrm{H}}(\mathrm{tr}\,\mathbf{E}^e), \\
\mu_{\mathrm{Tk}} &= \mu_{\mathrm{Tk}}^0 + R\vartheta \ln\left(\frac{\theta_{\mathrm{Tk}}}{1-\theta_{\mathrm{Tk}}}\right) - g(d) K\Omega_{\mathrm{H}}(\mathrm{tr}\,\mathbf{E}^e),
\end{aligned} \tag{9.130}$$

where we have used

$$C \overset{\mathrm{def}}{=} C_{\mathrm{L}} + \sum_k C_{\mathrm{Tk}} \quad \text{and} \quad C^0 \overset{\mathrm{def}}{=} C_{\mathrm{L}}^0 + \sum_k C_{\mathrm{Tk}}^0. \tag{9.131}$$

Further, from (9.129) and (9.93)

$$\begin{aligned}
\omega_{\text{en}} &= g(d)\,(1-\varkappa)S^c,\\
\varpi_{\text{en}} &= g'(d)\,\left[\tilde{\psi}^e(\mathcal{I}_{\mathbf{E}^e}, C) + \tilde{\psi}^c_{\text{R}}(\epsilon^c)\right],\\
\boldsymbol{\xi}_{\text{en}} &= 2\psi^{\text{crit}}_{\text{R}}\ell^2\nabla d.
\end{aligned} \tag{9.132}$$

9.8 Hydrogen trapping

Recall that in the species balance law for hydrogen,

$$\dot{C}_{\text{L}} = -\text{Div}\mathbf{j}_{\text{L}} - \sum_k \dot{C}_{\text{Tk}}, \tag{9.133}$$

we need to get an estimate for the rate of change of hydrogen in trapped sites, $\dot{C}_{\text{Tk}}$. Also recall from the dissipation inequality $(9.99)_4$ that each $\dot{C}_{\text{Tk}}$ must satisfy a dissipation inequality of the form:

$$(\mu_{\text{L}} - \mu_{\text{Tk}})\dot{C}_{\text{Tk}} \geq 0. \tag{9.134}$$

The term

$$\mathcal{F}_k \overset{\text{def}}{=} (\mu_{\text{L}} - \mu_{\text{Tk}}), \tag{9.135}$$

represents a thermodynamic force conjugate to the time rate of change of hydrogen trapping at the kth trap type, From $(9.130)_{3,4}$ the thermodynamic force $\mathcal{F}_k$ is given by

$$\mathcal{F}_k = \mu^0_{\text{L}} - \mu^0_{\text{Tk}} + R\vartheta\left[\ln\left(\frac{\theta_{\text{L}}}{1-\theta_{\text{L}}}\right) - \ln\left(\frac{\theta_{\text{Tk}}}{1-\theta_{\text{Tk}}}\right)\right]. \tag{9.136}$$

Remark. Following (?), in the literature on trapping of hydrogen it is often assumed that the chemical potentials of the lattice and trapped hydrogen species at each different trap-type satisfy

$$\mu_{\text{L}} = \mu_{\text{Tk}} \quad \longrightarrow \quad \mathcal{F}_k = 0, \tag{9.137}$$

so that the mobile lattice hydrogen and the trapped hydrogen are always in **local equilibrium**. According to (9.137), $(9.130)_{3,4}$ give

$$\mu^0_{\text{L}} + R\vartheta\ln\left(\frac{\theta_{\text{L}}}{1-\theta_{\text{L}}}\right) = \mu^0_{\text{Tk}} + R\vartheta\ln\left(\frac{\theta_{\text{Tk}}}{1-\theta_{\text{Tk}}}\right), \tag{9.138}$$

which can be simplified to read

$$\frac{\theta_{\text{Tk}}}{1-\theta_{\text{Tk}}} = \frac{\theta_{\text{L}}}{1-\theta_{\text{L}}}K_{\text{Tk}}, \tag{9.139}$$

where K_{Tk} is an equilibrium factor given by

$$K_{\mathrm{Tk}} = \exp\left(-\frac{E_{Bk}}{R\vartheta}\right), \quad \text{with} \quad E_{Bk} = (\mu^0_{\mathrm{Tk}} - \mu^0_{\mathrm{L}}) = \text{constant}. \tag{9.140}$$

Here $E_{Bk} < 0$ represents a *binding energy* for the trap-type.

- Oriani's assumption of local equilibrium imples that once we know the lattice concentration C_{L} and the trap binding energy, we can calculate the occupancy fraction θ_{Tk} for the trap sites. Indeed for $\theta_{\mathrm{L}} \ll 1$, eq. (9.139) reduces to

$$\frac{\theta_{\mathrm{Tk}}}{1 - \theta_{\mathrm{Tk}}} = K_{\mathrm{Tk}}\,\theta_{\mathrm{L}}. \tag{9.141}$$

It is not always necessary to model hydrogen trapping through the assumption of equilibrium between lattice and trapped hydrogen using (9.137). Guided by (9.134) one may envision a constitutive equation for $\dot{C}_{\mathrm{T}}$ of the form

$$\dot{C}_{\mathrm{Tk}} = \tilde{\dot{C}}_{\mathrm{Tk}}(\mathcal{F}_k, \text{plus other factors}) \quad \text{with} \quad \mathcal{F}_k \stackrel{\text{def}}{=} \mu_{\mathrm{L}} - \mu_{\mathrm{Tk}}, \tag{9.142}$$

where the time rate of change of trapped hydrogen is a function of the difference in the chemical potentials and other factors affecting the trapping rate. □

In this paper we consider dislocation cores and vacancies as the major sites which trap hydrogen, and take

$$C_{\mathrm{T}} = C_{\mathrm{TD}} + C_{\mathrm{TV}}, \tag{9.143}$$

where C_{TD} and C_{TV} are concentrations of hydrogen trapped at dislocation cores and vacancies, respectively. We next provide estimates for $\dot{C}_{\mathrm{TV}}$ and $\dot{C}_{\mathrm{TD}}$, and based on the dissipation inequalities (9.134) require that

$$\mathcal{F}_{\mathrm{D}}\dot{C}_{\mathrm{TD}} \geq 0 \qquad \text{and} \qquad \mathcal{F}_{\mathrm{D}} = (\mu_{\mathrm{L}} - \mu_{\mathrm{TD}}). \tag{9.144}$$

and

$$\mathcal{F}_{\mathrm{V}}\dot{C}_{\mathrm{TV}} \geq 0 \qquad \text{and} \qquad \mathcal{F}_{\mathrm{V}} = (\mu_{\mathrm{L}} - \mu_{\mathrm{TV}}). \tag{9.145}$$

9.8.1 Hydrogen trapping by dislocation cores

For trapping at dislocation cores,

- we adopt the classical and widely-used Oriani's postulate of "local equilibrium" between lattice hydrogen and and hydrogen trapped at dislocation cores (?),

in which case (9.141) for $\theta_{\mathrm{L}} \ll 1$ gives

$$\frac{\theta_{\mathrm{TD}}}{1 - \theta_{\mathrm{TD}}} = K_{\mathrm{TD}}\theta_{\mathrm{L}}, \tag{9.146}$$

where K_{TD} is an equilibrium factor given by

$$K_{\text{TD}} = \exp\left(\frac{-E_{\text{BD}}}{R\vartheta}\right), \tag{9.147}$$

with $E_{\text{BD}} < 0$ a binding energy for the hydrogen and dislocation cores.

The time rate of change of trapped hydrogen $\dot{C}_{\text{TD}}$ can now be determined through the equilibrium equation (9.146). In what follows we essentially summarize the arguments of Sofronis and McMeeking (1989) and Krom et al. (1999). Since N_{L} and K_{TD} are constant, using (9.146) the trapped hydrogen concentration C_{TD} may be expressed as a function of C_{L} and N_{TD},

$$C_{\text{TD}} = \hat{C}_{\text{TD}}(C_{\text{L}}, N_{\text{TD}}) = \frac{N_{\text{TD}}}{1 + \dfrac{N_{\text{L}}}{K_{\text{TD}} C_{\text{L}}}}. \tag{9.148}$$

Thus the evolution of C_{T} is given by

$$\dot{C}_{\text{TD}} = \frac{\partial C_{\text{TD}}}{\partial C_{\text{L}}}\dot{C}_{\text{L}} + \frac{\partial C_{\text{TD}}}{\partial N_{\text{TD}}}\dot{N}_{\text{TD}}. \tag{9.149}$$

Next from (9.146)

$$\frac{\partial C_{\text{TD}}}{\partial C_{\text{L}}} = \frac{C_{\text{TD}}(1 - \theta_{\text{TD}})}{C_{\text{L}}}. \tag{9.150}$$

Let

$$N_{\text{TD}} = \hat{N}_{\text{TD}}(\gamma^p) \tag{9.151}$$

denote the number of moles per unit volume of dislocation-core trap sites, and

$$H_{\text{TD}} \overset{\text{def}}{=} \frac{d\hat{N}_{\text{TD}}(\gamma^p)}{d\gamma^p} \geq 0 \tag{9.152}$$

denote the rate of change of N_{TD} with plastic flow. Then

$$\frac{\partial C_{\text{TD}}}{\partial N_T}\dot{N}_{\text{TD}} = \theta_{\text{TD}}\, H_{\text{TD}}\, \dot{\gamma}^p. \tag{9.153}$$

Then, use of (9.150) and (9.153) in (9.149) gives the following important estimate for the time rate of change of C_{T}:

$$\dot{C}_{\text{TD}} = \frac{C_{\text{TD}}(1 - \theta_{\text{TD}})}{C_{\text{L}}}\dot{C}_{\text{L}} + \theta_{\text{TD}}\, H_{\text{TD}}\, \dot{\gamma}^p. \tag{9.154}$$

9.8.2 Hydrogen trapping by vacancies

As remarked earlier, it is not always necessary to model hydrogen trapping through the assumption of equilibrium between lattice and trapped hydrogen. Here we propose constitutive

equation for $\dot{C}_{\text{TV}}$ of the form

$$\dot{C}_{\text{TV}} = \begin{cases} A\dot{\gamma}^p > 0 & \text{if } \mu_{\text{L}} > \mu_{\text{TV}} \text{ and } \dot{\gamma}^p > 0, \\ 0 & \text{otherwise.} \end{cases} \tag{9.155}$$

This evolution equation (9.155) for C_{TV} is intended to hold during active plastic deformation $\dot{\gamma}^p > 0$, and not intended to allow for static recovery effects ($\dot{C}_{\text{TV}} < 0$) when there is no plastic flow ($\dot{\gamma}^p = 0$). In (9.155),

$$A = \hat{A}\left(C_{\text{L}}, \frac{\sigma_{\text{M}}}{\bar{\tau}}\right) \geq 0 \tag{9.156}$$

represents an *accumulation modulus* for the hydrogen-vacancy complexes during plastic flow, which we take to depend on the current values of C_{L}, and the Mandel stress $\mathbf{M}^e$ through the

$$\text{stress triaxility} \stackrel{\text{def}}{=} \frac{\sigma_{\text{M}}}{\bar{\tau}},$$

defined in terms of two of its invariants,[4]

$$\bar{\tau} \stackrel{\text{def}}{=} \frac{1}{\sqrt{2}} |\mathbf{M}^e_0| \quad \text{and} \quad \sigma_{\text{M}} \stackrel{\text{def}}{=} \frac{1}{3} \operatorname{tr} \mathbf{M}^e. \tag{9.157}$$

We expect that the accumulation modulus will increase as C_{L} increases, and it will also increase as the level of stress triaxiality increases, a stress state which we expect to favor an increase in the rate of hydrogen-vacancy complexes. The introduction of a dependence of the accumulation modulus on the stress triaxiality is motivated by the use of such a dependence in models for ductile fracture of steels.

To summarize an estimate of the rate of change of trapped hydrogen is given by

$$\begin{aligned} &\dot{C}_{\text{T}} = \dot{C}_{\text{TV}} + \dot{C}_{\text{TD}}, \qquad \text{with} \\ &\dot{C}_{\text{TD}} = \frac{C_{\text{TD}}(1-\theta_{\text{TD}})}{C_{\text{L}}} \dot{C}_{\text{L}} + \theta_{\text{TD}} H_{\text{TD}} \dot{\gamma}^p, \qquad \theta_{\text{TD}} = \frac{C_{\text{TD}}}{N_{\text{TD}}}, \qquad H_{\text{TD}} = \frac{d\hat{N}_{\text{TD}}(\gamma^p)}{d\gamma^p}, \\ &\dot{C}_{\text{TV}} = A\dot{\gamma}^p, \qquad A = \hat{A}\left(C_{\text{L}}, \frac{\sigma_{\text{M}}}{\bar{\tau}}\right) \geq 0. \end{aligned} \tag{9.158}$$

Remark. In the following chapter we show that the particular form,

$$A = A_0 \exp\left(\alpha \frac{\sigma_{\text{M}}}{\bar{\tau}}\right) \frac{1}{\left(1 + A_1 \exp\left(-\left(\frac{C_{\text{L}}}{C_{\text{ref}}}\right)^2\right)\right)}, \tag{9.159}$$

[4]We neglect a dependence on the third invariant $\det \mathbf{M}^e$.

for the accumulation modulus A, with material parameters $\{\alpha, A_0, A_1, C_{\text{ref}}\}$, is of use in modeling the trapping of hydrogen by vacancies. □

Remark. Modeling of hydrogen trapping is a difficult subject. We have not departed from the literature in our model for the evolution for C_{TD}. But evolution equation for C_{TV} proposed above is a new suggestion which will need to be refined as more information from atomistic modeling about trapping of hydrogen in the form of hydrogen-vacancy complex becomes available. □

Remark. In writing (9.148) we have assumed that $\theta_{\text{L}} \ll 1$, under this approximation the lattice chemical potential $(9.130)_3$ reduces to

$$\mu_{\text{L}} = \mu_{\text{L}}^0 + R\vartheta \ln\left(\frac{C_{\text{L}}}{N_{\text{L}}}\right) - g(d)K\Omega_{\text{H}}(\text{tr}\,\mathbf{E}^e). \tag{9.160}$$

□

9.9 Hydrogen flux

We take the hydrogen mobility tensor to have the representation

$$\mathbf{M} = m_{\text{L}}\mathbf{1} \quad \text{with} \quad m_{\text{L}} = \hat{m}_{\text{L}}(C_{\text{L}}) > 0 \tag{9.161}$$

the scalar species mobility. Using (9.161) we have that the hydrogen flux $\mathbf{j}_{\text{L}}$ is given by

$$\mathbf{j}_{\text{L}} = -m_{\text{L}}\nabla\mu_{\text{L}}. \tag{9.162}$$

We take the hydrogen mobilit m_{L} to be and given by

$$m_{\text{L}} = \frac{D_{\text{L}}C_{\text{L}}}{R\vartheta}. \tag{9.163}$$

9.10 Balance of chemical potential μ_{L}

We may write the local balance equation for the concentration of lattice hydrogen as a local balance equation for the lattice chemical potential. First, the local balance equation for the concentration of hydrogen atoms, reiterated from (9.76), is

$$\dot{C}_{\text{L}} + \dot{C}_T = -\text{Div}\,\mathbf{j}_{\text{L}} \tag{9.164}$$

Further, with $\dot{C}_T$ estimated in (9.158) and $\mathbf{j}_{\mathrm{L}} = -m_{\mathrm{L}}\nabla\mu_{\mathrm{L}}$, we obtain the following partial differential equation for $\dot{C}_{\mathrm{L}}$

$$\left(1 + \frac{C_{\mathrm{TD}}(1-\theta_{\mathrm{TD}})}{C_{\mathrm{L}}}\right)\dot{C}_{\mathrm{L}} = \mathrm{Div}\,(m_{\mathrm{L}}\nabla\mu_{\mathrm{L}}) - \theta_{\mathrm{TD}}\,H_{\mathrm{TD}}\,\dot{\gamma}^p - A\dot{\gamma}^p. \tag{9.165}$$

Taking the time rate of change of the constitutive equation for the lattice chemical potential (9.160) yields

$$\dot{\mu}_{\mathrm{L}} = \frac{R\vartheta}{C_{\mathrm{L}}}\dot{C}_{\mathrm{L}} - g(d)K\Omega_{\mathrm{H}}\,\mathrm{tr}\,\dot{\mathbf{E}}^e - g'(d)\dot{d}K\Omega_{\mathrm{H}}\,\mathrm{tr}\,\mathbf{E}^e. \tag{9.166}$$

Finally, eliminating $\dot{C}_{\mathrm{L}}$ by combining (9.165) and (9.166) yields the following local balance equation for the lattice chemical potential

$$\begin{aligned} D^*\frac{C_{\mathrm{L}}}{R\vartheta}\dot{\mu}_{\mathrm{L}} &= \mathrm{Div}\,(m_{\mathrm{L}}\nabla\mu_{\mathrm{L}}) - D^*\frac{C_{\mathrm{L}}}{R\vartheta}g(d)\,K\Omega_{\mathrm{H}}\,\mathrm{tr}\,\dot{\mathbf{E}}^e - D^*\frac{C_{\mathrm{L}}}{R\vartheta}\frac{dg(d)}{dd}\dot{d}K\Omega_{\mathrm{H}}\,\mathrm{tr}\,\mathbf{E}^e \\ &\quad - \theta_{\mathrm{TD}}\,H_{\mathrm{TD}}\dot{\gamma}^p - A\dot{\gamma}^p, \qquad \text{with} \\ D^* &= 1 + \frac{C_{\mathrm{TD}}(1-\theta_{\mathrm{TD}})}{C_{\mathrm{L}}}, \quad \text{and} \quad m_{\mathrm{L}} = \frac{D_{\mathrm{L}}C_{\mathrm{L}}}{R\vartheta}. \end{aligned} \tag{9.167}$$

with

$$D^* = 1 + \frac{C_{\mathrm{TD}}(1-\theta_{\mathrm{TD}})}{C_{\mathrm{L}}}, \quad \text{and} \quad m_{\mathrm{L}} = \frac{D_{\mathrm{L}}C_{\mathrm{L}}}{R\vartheta}. \tag{9.168}$$

9.11 Plastic flow rule

Next we consider a constitutive equation for the microforce π which is conjugate to $\dot{\gamma}^p$. To model the resistance to plastic flow offered by the underlying microstructructural state of the material we introduce a list

$$\vec{\xi} = \{\xi_1, \ldots, \xi_m\}$$

of m scalar internal variables, and presume that the microforce π is given by a constitutive equation

$$\pi = \mathcal{S}^p(\vec{\xi}, C_{\mathrm{L}}, \vec{C}_{\mathrm{Tk}}, \dot{\gamma}^p; \vartheta), \tag{9.169}$$

and in order to satisfy the dissipation inequality $(9.99)_1$, we require that

$$\mathcal{S}^p(\vec{\xi}, C_{\mathrm{L}}, \vec{C}_{\mathrm{Tk}}, \dot{\gamma}^p; \vartheta) > 0. \tag{9.170}$$

Here ϑ is the constant tempearture of the isothermal theory under consideration.

The microforce balance (9.65), viz.

$$\bar{\tau} = \pi, \tag{9.171}$$

and the thermodynamically consistent constitutive equation (9.177) give the **strength relation for plastic flow**,

$$\bar{\tau} = \mathcal{S}^p(\vec{\xi}, C_{\rm L}, \vec{C}_{\rm Tk}, \dot{\gamma}^p; \vartheta) \quad \text{when} \quad \dot{\gamma}^p > 0. \tag{9.172}$$

Recalling the definition (9.49) for the resolved shear stress, we find that (9.181) and $(9.99)_1$ require that

$$\left(\frac{1}{\sqrt{2}}\mathbf{M}_0^e : \mathbf{N}^p\right) = \mathcal{S}^p(\vec{\xi}, C_{\rm L}, \vec{C}_{\rm Tk}, \dot{\gamma}^p; \vartheta) \quad \text{when} \quad \dot{\gamma}^p > 0. \tag{9.173}$$

We assume that

- *the deviatoric plastic flow direction* $\mathbf{N}^p$ *is parallel to and points in the same direction as the direction of the deviatoric stress* $\mathbf{M}_0^e$:

$$\mathbf{N}^p = \frac{\mathbf{M}_0^e}{|\mathbf{M}_0^e|} \qquad \text{whenever} \qquad \mathbf{M}_0^e \neq \mathbf{0}. \tag{9.174}$$

We call this the **codirectionality hypothesis** (cf., Gurtin et al., 2010). In this case the *resolved shear stress* in given by

$$\bar{\tau} \stackrel{\text{def}}{=} \frac{1}{\sqrt{2}}|\mathbf{M}_0^e|. \tag{9.175}$$

Using (9.188) and (9.189) the plastic stretching $\mathbf{D}^p$ in (9.13) may be written as

$$\mathbf{D}^p = \dot{\gamma}^p \frac{\mathbf{M}_0^e}{2\bar{\tau}}. \tag{9.176}$$

The strength relation (9.182) serves to determine $\dot{\gamma}^p$ when it is non-zero.

9.11.1 Specialization of the strength relation for plastic flow

The rate-controlling process for plastic flow in crystalline metals is the thermally-activated motion of dislocations past *obstacles* on the slip planes. Obstacles to dislocation glide can be divided into two major types. In particular, one can distinguish between barriers that can be overcome with the aid of thermal activation and those that cannot — *thermally activatable* and *athermal* barriers, repectively (cf., e.g., Kocks et al., 1975). Accordingly, as a specialzation for the list of internal variables $\vec{\xi}$, we introduce two parameters

$$S_* \geq 0 \qquad \text{and} \qquad S_{\rm a} \geq 0,$$

and presume that they have *dimensions of stress.* The resistance S_* represents a resistance due to short-range thermally-activatable barriers, and $S_{\rm a}$ represents a resistance due to

long-range athermal barriers to plastic flow by dislocation glide. We call S_* the *thermally-activatable resistance* and S_a the *athermal resistance* to plastic flow.[5]

- **Short-range thermally-activatable obstacles**: Typical examples of short-range thermally-activatable obstacles include the lattice (or Peierls) resistance, vacancies, interstitials, solute atoms, and forest dislocations. Glide dislocations can overcome such obstacles with the aid of thermal-fluctuations. In pure bcc materials, S_* is primarily controlled by the interactions of the glide dislocations with the lattice resistance.
- **Long-range athermal barriers**: Typical examples of long-range athermal barriers include the elastic stress field due to dislocations clusters. Such barriers, whose resistance is represented by S_a, cannot be overcome with the aid of thermal fluctuations. The resistance S_a is usually taken to represent the strain-hardening characteristics due to dislocation accumulation.

Next we consider a constitutive equation for the microforce π which is conjugate to $\dot{\gamma}^p$, of the form

$$\pi = \mathcal{S}^p(S_a, S_*, \dot{\gamma}^p; \vartheta), \tag{9.177}$$

and in order to satisfy the dissipation inequality $(9.99)_1$, we require that

$$\mathcal{S}^p(S_a, S_*, \dot{\gamma}^p; \vartheta) > 0. \tag{9.178}$$

Here ϑ is the constant temperature of the isothermal theory under consideration. Adopting the thermally-activated theory of plastic flow by dislocation glide (Kocks et al., 1975), as a particular form for $\mathcal{S}^p(S_a, S_*, \dot{\gamma}^p; \vartheta)$ we consider

$$\mathcal{S}^p(S_a, S_*, \dot{\gamma}^p; \vartheta) = S_a + S_* R \quad \text{with} \quad R = \left[1 - \left\{\frac{k_B \vartheta}{\Delta F} \ln\left(\frac{\dot{\gamma}_0}{\dot{\gamma}^p}\right)\right\}^{\frac{1}{q}}\right]^{\frac{1}{p}}, \tag{9.179}$$

where the strain rate dependent function R has values $R \in [0, 1]$. Here $\dot{\gamma}_0$ is a reference shear rate, ΔF is an activation energy, and p and q are "barrier shape parameters" that lie in the ranges

$$0 \leq p \leq 1, \quad \text{and} \quad 1 \leq q \leq 2. \tag{9.180}$$

The microforce balance (9.65), viz.

$$\bar{\tau} = \pi, \tag{9.181}$$

and the thermodynamically consistent constitutive equations (9.177) and (9.179) give the **strength relation for plastic flow**,

$$\bar{\tau} = S_a + S_* R \quad \text{when} \quad \dot{\gamma}^p > 0. \tag{9.182}$$

[5]The thermally activatable resistance S_* is often denoted by $\hat{\tau}(0)$ and called the *mechanical threshold stress* in the literature (cf. e.g., Kocks et al., 1975).

Equation (9.182) implies that a necessary condition for $\dot{\gamma}^p > 0$ is that

$$(\bar{\tau} - S_{\mathrm{a}}) > 0; \tag{9.183}$$

we assume here that this condition is also sufficient for $\dot{\gamma}^p > 0$. This means that plastic flow occurs only when (9.183) holds. Equivalently $\dot{\gamma}^p = 0$, and no plastic fow occurs when

$$(\bar{\tau} - S_{\mathrm{a}}) < 0. \tag{9.184}$$

Thus, introducing

$$\bar{\tau}_{\mathrm{eff}} \stackrel{\mathrm{def}}{=} \bar{\tau} - S_{\mathrm{a}}, \tag{9.185}$$

as an *overstress*, the relation (9.182) may be inverted to give

$$\dot{\gamma}^p = \begin{cases} 0 & \text{if } \bar{\tau}_{\mathrm{eff}} \leq 0, \\ \dot{\gamma}_0 \exp\left[-\left(\dfrac{\Delta F}{k_{\mathrm{B}}\,\vartheta}\right)\left[1 - \left(\dfrac{\bar{\tau}_{\mathrm{eff}}}{S_*}\right)^p\right]^q\right] & \text{if } \bar{\tau}_{\mathrm{eff}} > 0. \end{cases} \tag{9.186}$$

Recalling the definition (9.49) for the equivalent shear stress, we find that (9.182) requires that

$$\left(\frac{1}{\sqrt{2}}\mathbf{M}_0^e : \mathbf{N}^p\right) = S_{\mathrm{a}} + S_*\,R \quad \text{when} \quad \dot{\gamma}^p > 0. \tag{9.187}$$

We assume that

- *the deviatoric plastic flow direction* $\mathbf{N}^p$ *is parallel to and points in the same direction as the direction of the deviatoric stress* $\mathbf{M}_0^e$:

$$\mathbf{N}^p = \frac{\mathbf{M}_0^e}{|\mathbf{M}_0^e|} \quad \text{whenever} \quad \mathbf{M}_0^e \neq \mathbf{0}. \tag{9.188}$$

We call this the **codirectionality hypothesis** (cf., Gurtin et al., 2010). In this case the *equivalent shear stress* in given by

$$\bar{\tau} \stackrel{\mathrm{def}}{=} \frac{1}{\sqrt{2}}|\mathbf{M}_0^e|. \tag{9.189}$$

The thermally activatable resistance S_* for bcc materials is primarily controlled by the Peierls lattice resistance, and for such materials it is reasonable to assume that

$$S_* \approx \text{constant}. \tag{9.190}$$

The athermal resistance S_{a}, is taken to represent a resistance to dislocation motion offered by the statistically stored dislocations. For the evolution equation for S_{a} we assume that

$$\dot{S}_{\mathrm{a}} = \left[H_0\left|\left(1 - \frac{S_{\mathrm{a}}}{S_{\mathrm{as}}}\right)\right|^r\right]\dot{\gamma}^p, \qquad S_{\mathrm{a}}|_{t=0} = S_{\mathrm{a0}} \tag{9.191}$$

where $H_0 > 0$ and $S_{as} \geq S_{a0}$, and r are material parameters.

9.11.2 Initiation condition for crazing and craze flow rule

Craze initiation condition

The spectral decomposition of the Mandel stress $\mathbf{M}^e$ is

$$\mathbf{M}^e = \sum_{i=1}^{3} \sigma_i \, \hat{\mathbf{e}}_i \otimes \hat{\mathbf{e}}_i \tag{9.192}$$

where $\{\sigma_i | i = 1, 2, 3\}$ are the principal values and and $\{\hat{\mathbf{e}}_i | i = 1, 2, 3\}$ are the principal directions of $\mathbf{M}^e$. We take that the principal stresses to be strictly ordered such that

$$\sigma_1 \geq \sigma_2 \geq \sigma_3.$$

We postulate that crazing in a material neighborhood will occur when the following two conditions are met:

(C1) With C_{TV} representing a concentration of hydrogen trapped as hydrogen-vacancy complexes, and $C_{\text{TV cr}}$ denoting a critical value of C_{TV} at which craze flow initiates, the first condition requires that

$$C_{\text{TV}} = C_{\text{TV cr}}. \tag{9.193}$$

(C2) This second condition requires that maximum principal stress and the mean normal stress be positive,

$$\sigma_1 > 0, \qquad \sigma_{\text{M}} = \frac{1}{3}(\sigma_1 + \sigma_2 + \sigma_3) > 0. \tag{9.194}$$

We will represent the transition from standard plastic-flow by dislocation glide to dilatant craze-flow by a *change in the flow rule* by using a switching parameter χ with values,

$$\chi = \begin{cases} 1 & \text{if conditions C1 and C2 are met,} \\ 0 & \text{otherwise,} \end{cases}$$

Craze flow rule

Not much is known about the details for craze flow. So on pragmatic grounds we assume that the dissipative microforce ω_{dis} is given by a simple constitutive equation

$$\omega_{\text{dis}} = g(d) \varkappa S^c \qquad \text{when} \qquad \dot{\epsilon}^c > 0. \tag{9.195}$$

We presume that

$$S^c > 0, \tag{9.196}$$

is a constant modulus with units of stress representing the craze flow resistance, and $\varpi > 0$ is positive-valued fraction, such that $\varpi S^c \dot{\epsilon}^c$ represents the dissipation due to craze flow, and so that the dissipation inequality $(9.99)_2$ is satisfied.

Next, from the microforce balance (9.67) and the constitutive equations $(9.132)_1$ and (9.195) we obtain the following *strength relation for craze flow*,

$$\sigma = g(d) S^c \quad \text{when} \quad \dot{\epsilon}^c > 0. \tag{9.197}$$

Recalling the definition (9.53) for the resolved tensile stress, we find that (9.197) requires that

$$\mathbf{M}^e : \mathbf{N}^c = g(d)\, S^c \quad \text{when} \quad \dot{\epsilon}^c > 0. \tag{9.198}$$

Let t^* denote the instant of time in a deformation history when crazing initiates. We assume that the direction $\mathbf{m}$ for craze extension coincides with the maximum principle stress direction $\hat{\mathbf{e}}_1$ at this time t^*,

$$\mathbf{m} \equiv \hat{\mathbf{e}}_1(t^*), \tag{9.199}$$

and thereafter remains *fixed*. That is, we assume that

- *the craze flow direction* $\mathbf{N}^c$ *is parallel to and points in the same direction as the direction of the eigen projection-tensor* $\hat{\mathbf{e}}_1(t^*) \otimes \hat{\mathbf{e}}_1(t^*)$ *corresponding to the maximum principal value* σ_1 *of* $\mathbf{M}^e$ *at time* t^*:

$$\mathbf{N}^c = \hat{\mathbf{e}}_1(t^*) \otimes \hat{\mathbf{e}}_1(t^*). \tag{9.200}$$

In this case the *resolved tensile stress* $\sigma = \mathbf{M}^e : \mathbf{N}^c$ is equal to the maximum principal value of $\mathbf{M}^e$,

$$\sigma \equiv \sigma_1. \tag{9.201}$$

Thus the strength relation (9.197) becomes,

$$\sigma_1 = g(d)\, S^c \quad \text{when} \quad \dot{\epsilon}^c > 0. \tag{9.202}$$

Recall that we have required that $\sigma_1 > 0$ when $\dot{\epsilon}^c > 0$.

We may rewrite (9.202) as

$$f = 0 \quad \text{when} \quad \dot{\epsilon}^c > 0, \tag{9.203}$$

where

$$f \stackrel{\text{def}}{=} \sigma_1 - g(d)\, S^c, \tag{9.204}$$

represents a *yield function* for craze flow. Equation (9.203) implies that a necessary condition for $\dot{\epsilon}^c > 0$ is that

$$f = 0; \tag{9.205}$$

we assume here that this condition is also sufficient for $\dot{\epsilon}^c > 0$. This means that craze flow occurs only when (9.205) holds. Equivalently $\dot{\epsilon}^c = 0$, and no craze flow occurs when

$$f < 0. \tag{9.206}$$

Thus, in our rate-independent theory for craze flow we have

$$\dot{\epsilon}^c \geq 0, \qquad f \leq 0, \qquad \dot{\epsilon}^c f = 0, \tag{9.207}$$

which are the Kuhn-Tucker conditions associated with rate-independent craze flow. It may be shown that in the rate-independent limit, $\dot{\epsilon}^c > 0$ if and only if the *consistency condition*

$$\dot{f} = 0 \qquad \text{when} \qquad f = 0 \tag{9.208}$$

is satisfied. The consistency condition may be used to determine the value of $\dot{\epsilon}^c$ when it is non-zero.

Using (9.200) and (9.19) the craze stretching $\mathbf{D}^c$ may be written as

$$\mathbf{D}^c = \dot{\epsilon}^c \, \hat{\mathbf{e}}_1 \otimes \hat{\mathbf{e}}_1. \tag{9.209}$$

The consistency condition (9.208) serves to determine $\dot{\epsilon}^c$ when it is non-zero.

9.11.3 Switching condition for the inelastic flow rule

In our continuum model we will represent the transition from shear plastic-flow to dilatant craze-flow by a *change in the flow rule.* To do this we introduce a switching parameter χ, which we specify as

$$\chi = \begin{cases} 1 & \text{if conditions C1 and C2 are met,} \\ 0 & \text{otherwise,} \end{cases} \tag{9.210}$$

and take the evolution equation for $\mathbf{F}^i$ as

$$\dot{\mathbf{F}}^p = \mathbf{D}^i \mathbf{F}^i, \qquad \text{with}$$

$$\mathbf{D}^i = \begin{cases} \dot{\gamma}^p \left(\dfrac{\mathbf{M}_0^e}{2\bar{\tau}} \right) & \text{if} \quad \chi = 0, \\ \dot{\epsilon}^c \hat{\mathbf{e}}_1 \otimes \hat{\mathbf{e}}_1 & \text{if} \quad \chi = 1. \end{cases} \tag{9.211}$$

Once the craze initiation conditions have been met, the craze-flow will be taken to continue as long as the maximum principal stress is positive.

Remark.

Let a quantity $(\cdot)^\dagger$ with a superscript $\dagger$ denote the value of the quantity at the instant that $\chi = 1$ and plastic flow transitions from shear flow to craze flow. Then in order to ensure

continuity of flow resistance the value of the craze resistance is taken as

$$S^{c\dagger} = \sqrt{3}\left[S^{\dagger} + S_{*}\left[1 - \left(\frac{k_{\mathrm{B}}\vartheta}{\Delta F}\ln\left(\frac{\dot{\gamma}_0}{\dot{\gamma}^p}\right)\right)^{\frac{1}{q}}\right]^{\frac{1}{p}}\right]. \tag{9.212}$$

The factor of $\sqrt{3}$ is introduced because the resistances for plastic flow are in shear, while that for craze flow is in tension.

□

9.12 Evolution equation for the phase-field/damage variable d

Recall the reduced dissipation inequalities $(9.99)_{3,4}$

$$\varpi_{\mathrm{dis}}\,\dot{d} \geq 0, \qquad \boldsymbol{\xi}_{\mathrm{dis}} \cdot \nabla\dot{d} \geq 0\,. \tag{9.213}$$

As special constitutive equations for $\boldsymbol{\xi}_{\mathrm{dis}}$ and $\varkappa_{\mathrm{dis}}$ we assume that the vector microstress $\boldsymbol{\xi}$ is *purely energetic* so that

$$\boldsymbol{\xi}_{\mathrm{dis}} = \mathbf{0}, \tag{9.214}$$

while ϖ_{dis} is taken to be given by

$$\varpi_{\mathrm{dis}} = a + \zeta\,\dot{d}, \qquad \text{with} \qquad a > 0, \quad \text{and} \quad \zeta > 0, \tag{9.215}$$

so that the dissipation inequality (9.213) is satisfied, that is

$$\mathcal{D} = \left(a + \zeta\,\dot{d}\right)\dot{d} > 0 \quad \text{whenever} \quad \dot{d} > 0. \tag{9.216}$$

Next, as a specialization for α we take take it to be given by

$$a = 2\psi_{\mathrm{R}}^{\mathrm{crit}}, \tag{9.217}$$

where $\psi_{\mathrm{R}}^{\mathrm{crit}} > 0$ is a material parameter. Note from (9.216) that in the rate-independent limit ($\zeta = 0$), the energy dissipated per unit volume as d increases from 0 to 1 is equal to

$$2\psi_{\mathrm{R}}^{\mathrm{crit}}. \tag{9.218}$$

Thus $2\psi_{\mathrm{R}}^{\mathrm{crit}}$ represents an energy per unit volume dissipated during fracturing. There is of course an additional "viscous" energy dissipation due to the contribution from the term involving ζ.

Next, recall from (9.94) the microstresses ϖ and $\boldsymbol{\xi}$ may be decomposed into energetic and dissipative parts as

$$\varpi = \varpi_{\text{en}} + \varpi_{\text{dis}}, \qquad \boldsymbol{\xi} = \boldsymbol{\xi}_{\text{en}} + \boldsymbol{\xi}_{\text{dis}}. \tag{9.219}$$

From (9.94), (9.132), (9.214), and (9.215) the scalar microstress $\varkappa$ and the vector microstress $\boldsymbol{\xi}$ are given by the thermodynamically consistent constitutive equations

$$\begin{aligned} \varpi &= \underbrace{-2(1-d)\left[\tilde{\psi}^e_{\text{R}}(\mathcal{I}_{\mathbf{E}^e}, C) + \tilde{\psi}^c_{\text{R}}(\epsilon^c)\right]}_{\text{energetic}} + \underbrace{2\psi^{\text{crit}}_{\text{R}} + \zeta\,\dot{d}}_{\text{dissipative}}, \\ \boldsymbol{\xi} &= \underbrace{2\psi^{\text{crit}}_{\text{R}}\ell^2 \nabla d}_{\text{energetic}}. \end{aligned} \tag{9.220}$$

These constitutive relations and the microforce balance (9.58), viz.

$$\text{Div}\,\boldsymbol{\xi} - \varpi = 0,$$

yield the following evolution equation for d,

$$\zeta \dot{d} = F, \tag{9.221}$$

with

$$F \overset{\text{def}}{=} 2(1-d)\,\psi^0_{\text{R}} - 2\psi^{\text{crit}}_{\text{R}} + 2\psi^{\text{crit}}_{\text{R}}\ell^2\,\Delta d, \tag{9.222}$$

where

$$\psi^0_{\text{R}} \overset{\text{def}}{=} \tilde{\psi}^e_{\text{R}}(\mathcal{I}_{\mathbf{E}^e}, C) + \tilde{\psi}^c_{\text{R}}(\epsilon^c) \qquad \text{and} \qquad \psi^{\text{crit}}_{\text{R}}, \tag{9.223}$$

represent an undamaged free energy, and a critical value of energy for damage, respectively.

Consider the rate independent limit ($\zeta = 0$) in the absence of the gradient energy. Then the microforce balance during the damaging process $\dot{d} > 0$ requires that

$$F = 2(1-d)\,\psi^0_{\text{R}} - 2\psi^{\text{crit}}_{\text{R}} = 0, \tag{9.224}$$

which gives

$$d = 1 - \frac{\psi^{\text{crit}}_{\text{R}}}{\psi^0_{\text{R}}},$$

when $\dot{d} > 0$. Next, using the fact that d lies in the range $d \in [0, 1]$, we must have that

$$\dot{d} = \begin{cases} 0, & \text{if } \psi^0_{\text{R}} \le \psi^{\text{crit}}_{\text{R}}, \\ > 0 & \text{possible if } \psi^0_{\text{R}} > \psi^{\text{crit}}_{\text{R}}. \end{cases} \tag{9.225}$$

To enforce this constraint in the rate-dependent evolution equation (9.221), in the expression (9.222) for F, we add and subtract the term $2d\psi_{\mathrm{R}}^{\mathrm{crit}}$ to obtain

$$F \stackrel{\mathrm{def}}{=} 2(1-d)\left[\psi_{\mathrm{R}}^{0}-\psi_{\mathrm{R}}^{\mathrm{crit}}\right]-2\psi_{\mathrm{R}}^{\mathrm{crit}}\left[d-\ell^{2}\Delta d\right]. \tag{9.226}$$

Then the constraint (9.225) is satisfied if eq. (9.226) is modified to include a Macauley bracket as follows,

$$F = 2(1-d)\left\langle\psi_{\mathrm{R}}^{0}-\psi_{\mathrm{R}}^{\mathrm{crit}}\right\rangle-2\psi_{\mathrm{R}}^{\mathrm{crit}}\left[d-\ell^{2}\Delta d\right]. \tag{9.227}$$

where $\langle\bullet\rangle$ is the Macauley bracket, i.e.,

$$\langle x\rangle = \begin{cases} 0, & x<0, \\ x, & x\geq 0. \end{cases}$$

We have not accounted for loading-and-unloading and only considered histories in which the undamaged free energy ψ_{R}^{0} increases monotonically. To account for loading-and-unloading we introduce a history field function $\mathcal{H}$ defined by (cf., Miehe et al., 2015, 2016)

$$\mathcal{H} \stackrel{\mathrm{def}}{=} \max_{s\in[0,t]}\left[\left\langle\psi_{\mathrm{R}}^{0}(s)-\psi_{\mathrm{R}}^{\mathrm{crit}}\right\rangle\right]. \tag{9.228}$$

Thus, if for some reason ψ_{R}^{0} is less than the maximum value attained in the past history, then there is no increase in damage.

Summarizing, the evolution of d is governed by an Allen-Cahn type phase-field partial differential equation,

$$\begin{aligned}
&\zeta\,\dot{d} = 2(1-d)\,\mathcal{H}-2\psi_{\mathrm{R}}^{\mathrm{crit}}(d-\ell^{2}\Delta d), \quad \text{with}\\
&\mathcal{H} \stackrel{\mathrm{def}}{=} \max_{s\in[0,t]}\left[\left\langle\psi_{\mathrm{R}}^{0}(s)-\psi_{\mathrm{R}}^{\mathrm{crit}}\right\rangle\right], \quad \text{where}\\
&\psi_{\mathrm{R}}^{0} \stackrel{\mathrm{def}}{=} \left[G|\mathbf{E}^{e}|^{2}+\frac{1}{2}\left(K-\frac{2}{3}G\right)(\mathrm{tr}\,\mathbf{E}^{e})^{2}-(K\Omega_{\mathrm{H}})(C-C^{0})(\mathrm{tr}\,\mathbf{E}^{e})\right]+(1-\varkappa)\,S^{c}\epsilon^{c}.
\end{aligned} \tag{9.229}$$

9.13 Numerical Implementation of the theory

We have implemented our theory in the finite element software Abaqus/Standard, 2016 by writing a user element subroutine (UEL) for four-noded isoparameteric quadrilateral plane-strain (UPE4) and axisymmetric (UAX4) elements which couple mechanical deformation, hydrogen diffusion, and damage. In our numerical implementation we neglect body forces. For the implementation of hydrogen diffusion we have chosen the lattice chemical potential as our solution variable.

Chapter 10

Coupled deformation-diffusion-fracture simulations of hydrogen embrittlement of a steel

In this chapter we focus on coupled deformation-diffusion-damage simulations of hydrogen embrittlement of a steel. Some interesting phenomena are numerically studied. Specifically,

- In section 10.1 we estimate the material parameters for a ferritic steel;
- In section 10.2, we show the results on uniaxial tension of round bars;
- In section 10.3, fracture in plane strain bending of U-notched specimens is studied; and
- Finally in section 10.4, Plane strain tension of an asymmetrically notched specimen is studied.

10.1 Estimation of material parameters for a ferritic steel

The several material parameters/functions that appear in the theory, need to be calibrated from experimental data. Unfortunately there is no complete set of experiments for any one given material in the literature, from which we may estimate all the material parameters in our theory. In this section we *estimate* the material parameters for the SA 106 ferritic steel studied experimentally by Xu and Rana (2009), and several other material parameters are taken directly from the published literature.

10.1.1 Material parameters which characterize the elastic-viscoplastic response of the steel in the absence of hydrogen

For the SA 106 steel we take the Young's modulus E and the Poisson's ratio ν to have values, $E = 204$GPa and $\nu = 0.254$, which using standard relations of isotropic linear elasticity may be converted a shear modulus G and a bulk modulus K, with values given in Table 10.1.

The data shown in Fig. 8-1 for the engineering stress-strain curve for the test done in air was used to estimate the viscoplasticity stress-strain response of the SA 106 steel. First, since we only have data at one strain rate, the flow parameters $\{\dot{\gamma}_0, \Delta F, p, q\}$ in (9.186) are estimated based on data for other bcc materials including steels available in the literature (cf., e.g., Kothari and Anand, 1998). These are given in Table 10.2.[1]

Next, the strain-hardening parameters $\{S_*, S_0, H_0, S_s, r\}$ listed in (9.190) and (9.191) were estimated by fitting the engineering stress-strain curve shown in Fig. 8-1 for the test done in air. To obtain a fit beyond the onset of necking in such a test required a finite element simulation of the tension test, and adjusting the material parameters shown in Table 10.2 to obtain the fit shown in Fig. 10-1. The red dotted curve is the experimental data, and the solid black line is the fit to this data. The fit is quite good. Our theory does not include a model for ductile fracture in air due to the classical mechanism of nucleation, growth, and coalescence of cavities, so the final drop off in load is *not* captured by our model, but until that point the engineering stress-strain curve for the SA 106 is well-captured by our model and the material parameters listed in this section.

Table 10.1: Elasticity parameters

G, GPa	K, GPa
81.34	138.21

Table 10.2: Viscoplastic flow parameters

$\dot{\gamma}_0$, s^{-1}	ΔF, J	p	q
1.73×10^6	1.38×10^{-19}	1	1

Table 10.3: Strain-hardening parameters

S_*, MPa	S_0, MPa	H_0, MPa	S_s, MPa	r
291.98	80.96	1920	262.12	1.2

[1] We have succesfully used these values of the viscoplastic flow parameters to model the strain-rate sensitive response of API X65 steel reported by El-Danaf et al. (2013). For brevity, we do not show the results for that steel here.

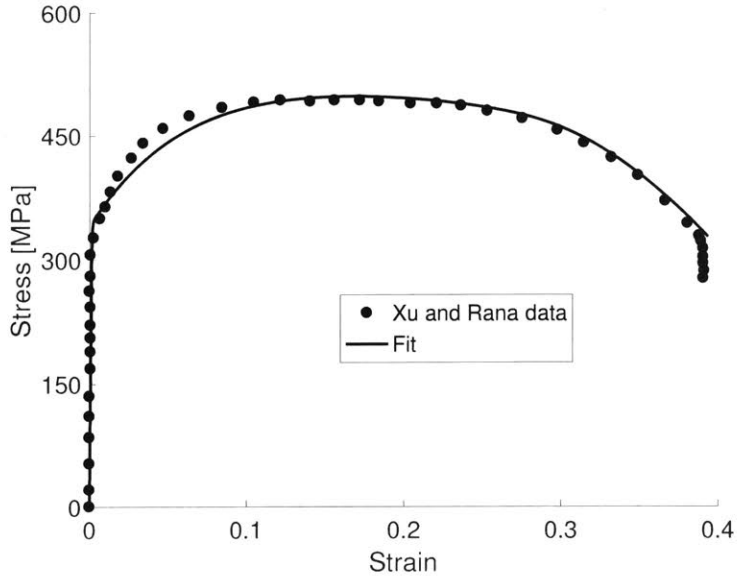

Figure 10-1: Fit of the engineering stress-strain curve for the SA 106 steel tested at a strain rate of $1.3 \times 10^{-4}\text{s}^{-1}$ in air by Xu and Rana (2009). The red dotted curve is the experimental data and the solid black line is the fit to this data.

10.1.2 Material parameters which characterize the solubility of hydrogen in the steel

In order to model the experimentally relevant boundary condition of a host metal exposed to — *and in equilibrium with* — a hydrogen atmosphere at a given partial pressure p_{H_2} and temperature ϑ, we must consider the equilibrium between the atomic hydrogen in the metal and hydrogen molecules in the gas (cf. e.g. San Marchi et al., 2007 and Krom et al., 1997). At equilibrium, the chemical potential of dissolved hydrogen in the solid must equal the chemical potential of the gas, that is $\mu_{\underline{\text{H}}} = \frac{1}{2}\mu_{\text{H}_2}$, where $\underline{\text{H}}$ denotes the atomic hydrogen dissolved in the solid. For an ideal gas, a simple analysis shows that the hydrogen concentration C_{L} dissolved in the lattice is given by Sieverts' law (San Marchi et al., 2007; Di Leo and Anand, 2013),

$$C_{\text{L}} = K\sqrt{p_{\text{H}_2}}, \qquad \text{with} \qquad K = K_0 \exp\left(\frac{-\Delta H}{R\vartheta}\right), \tag{10.1}$$

The solubility K in (10.1) is typically obtained from experiments under conditions in which the lattice is unstrained. The experimental data is fit to an Arrhenius relation of the form shown in $(10.1)_2$, from where the pre-exponential coefficient K_0 and the energetic term ΔH are determined. The solubility parameters used here, taken from San Marchi et al. (2007), are listed in Table 10.4. For a constant temperature of $\vartheta = 300\text{K}$, substituting these values

in Sievert's law (10.1) gives

$$C_{\mathrm{L}} = 0.0086\,\sqrt{p_{\mathrm{H_2}}}. \tag{10.2}$$

Table 10.4: Solubility of hydrogen in the steel

K_0, mol/(m$^3\sqrt{\text{MPa}}$)	ΔH, kJ/mol
820	28.6

10.1.3 Material parameters which characterize the diffusion of hydrogen in the steel

Values for the number of moles of lattice sites per unit reference volume, N_L (a property of the host metal), the partial molar volume of hydrogen Ω_{H}, and the the lattice diffusion coefficient D_L of hydrogen at room temperature of 300 K for iron are taken from the literature (Krom et al., 1999) and listed in Table 10.5.

Table 10.5: Diffusion of hydrogen in the steel

N_L, mol/m^3	Ω_{H}, mol/m^3	D_L, m^2/s
8.46×10^5	2×10^{-6}	$D_L = 1.27 \times 10^{-8}$

10.1.4 Material parameters which characterize the trapping of hydrogen at dislocations

In accordance with Kumnick and Johnson (1980), Sofronis and McMeeking (1989), and Krom et al. (1999), the number of trap sites N_T is assumed to increase with an increase in the equivalent plastic shear strain γ^p. This relation, and the trap binding energy E_{BD} are given in Table 10.6.

Table 10.6: Trapping of hydrogen at dislocations

N_{TD}, mol/m^3	E_{BD}, kJ/mol
$N_{TD} = 10^{(23.26-2.33\exp(-3.1754\,\gamma^p))}$	-60

10.1.5 Material parameters which characterize the trapping of hydrogen at vacancies, craze initiation, as well as damage initiation and evolution

Recall $(9.158)_3$ which gives the the rate of change of hydrogen trapped by vacancies, viz.

$$\dot{C}_{\mathrm{TV}} = A\dot{\gamma}^p, \qquad A = \hat{A}\left(C_{\mathrm{L}}, \frac{\sigma_{\mathrm{M}}}{\bar{\tau}}\right) \geq 0. \tag{10.3}$$

Here we specialize the expression for the accumulation modulus A, and estimate the material parameters appearing in this special from. First, we assume that the accumulation modulus may be expressed in the separable form

$$A = A_0 \exp\left(\alpha \frac{\sigma_{\rm M}}{\bar{\tau}}\right) f(C_{\rm L}) \geq 0, \tag{10.4}$$

where α is a a stress-triaxiality parameter, and $f(C_{\rm L})$ is a positive-valued function of $C_{\rm L}$.

First, using Sievert's law (10.2), we convert the data for elongation to failure versus hydrogen pressure data from Xu and Rana (2009) shown in Fig. 8-1(b), to elongation to failure versus lattice concentration of hydrogen; this is shown in Fig. 10-2.

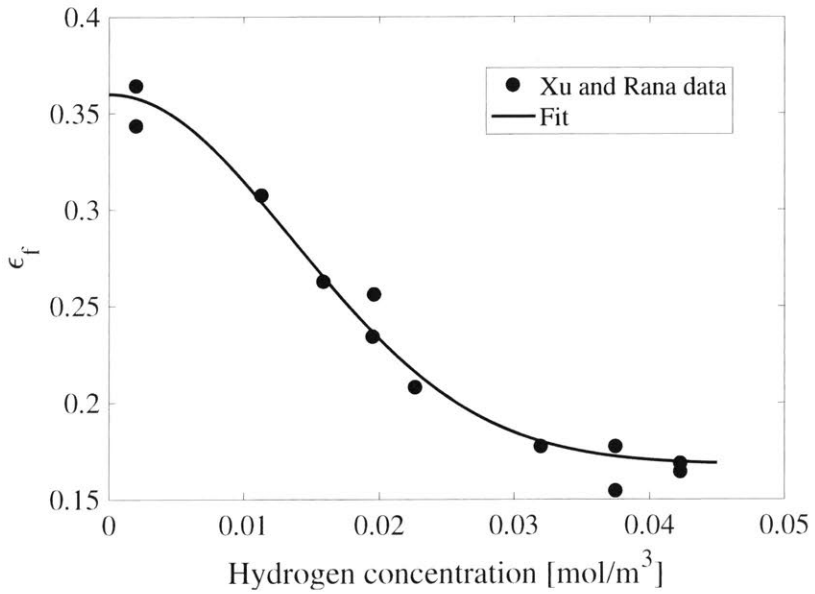

Figure 10-2: Elongation to failure ϵ_f versus initial lattice hydrogen concentration $C_{\rm L0}$, for the SA 106 steel tested at a strain rate of $1.3 \times 10^{-4}{\rm s}^{-1}$ in air by Xu and Rana (2009). The solid blue dots are the experimental data and the black line is the fit to this data, discussed below.

In simple tension under monotonic straining, and in the absence of hydrogen diffusion eq.$(10.3)_1$ may be integrated to give,

$$C_{\rm TV} = A\gamma^p = A\sqrt{3}\epsilon^p, \tag{10.5}$$

where $\epsilon^p = \gamma^p/\sqrt{3}$ is the equivalent tensile plastic strain. Recall from (9.193) that we require $C_{\rm TV}$ to reach a critical value $C_{\rm TV\,cr}$ for crazing to initiate. From (10.5) and (10.4) $C_{\rm TV\,cr}$ is given by,

$$C_{\rm TV\,cr} = \left[\sqrt{3}\, A_0 \exp\left(\alpha \frac{\sigma_{\rm M}}{\bar{\tau}}\right)\right] f(C_{\rm L})\, \epsilon^p{}_{\rm crit}, \tag{10.6}$$

which upon rearranging and writing $g(C_{\rm L}) = 1/f(C_{\rm L})$ gives,

$$\epsilon^{p}{}_{\rm crit} = \frac{C_{\rm TV\,cr}}{\sqrt{3}\,A_0 \exp\left(\alpha\frac{\sigma_{\rm M}}{\bar{\tau}}\right)}\, g(C_{\rm L}). \tag{10.7}$$

For hydrogen concentrations in which crazing initiates before necking, but sufficiently after the onset of yield so that the elastic strains are negligible relative to the plastic strains, we assume that $\epsilon^{p}{}_{\rm crit} \approx \epsilon_f$, where ϵ_f is the elongation to failure. Then (10.7) gives

$$\epsilon_f \approx \frac{C_{\rm TV\,cr}}{\sqrt{3}\,A_0 \exp\left(\alpha\frac{\sigma_{\rm M}}{\bar{\tau}}\right)}\, g(C_{\rm L}). \tag{10.8}$$

Fig. 10-2 gives the experimentally-measured dependence of ϵ_f on the lattice hydrogen concentration $C_{\rm L}$. We have fit that data to estimate the function $g(C_{\rm L})$ in (10.8) — dashed red line in Fig. 10-2, and the result is

$$\epsilon_f \approx \underbrace{\frac{C_{\rm TV\,cr}}{\sqrt{3}\,A_0 \exp\left(\alpha\frac{\sigma_{\rm M}}{\bar{\tau}}\right)}}_{=0.168} \underbrace{\left(1 + A_1 \exp\left(-\left(\frac{C_{\rm L}}{C_{\rm ref}}\right)^2\right)\right)}_{g(C_{\rm L})}, \qquad \text{with} \tag{10.9}$$

$$A_1 = 1.143, \qquad \text{and} \qquad C_{\rm ref} = 0.0192 \text{mol/m}^3.$$

We emphasize that this is a curve-fit valid only for lattice hydrogen concentrations in the range $0.005 \lesssim C_{\rm L} \lesssim 0.05$.

Consider the term

$$\frac{C_{\rm TV\,cr}}{\sqrt{3}\,A_0 \exp\left(\alpha\frac{\sigma_{\rm M}}{\bar{\tau}}\right)} = 0.168, \tag{10.10}$$

in eq. (10.9). Since we only have data from a simple tension test at a fixed triaxiality of $\sigma_{\rm M}/\bar{\tau} = 1/\sqrt{3}$, we set $\alpha = 1$, and for simple tension (10.10) reduces to $C_{\rm TV\,cr}/A_0 = 0.5183$. Since, only the ratio $C_{\rm TV\,cr}/A_0$ is known, and not the individual values $C_{\rm TV\,cr}$ and A_0, here we assume that $C_{\rm TV\,cr}$ is a small plausible number, $C_{\rm TV\,cr} = 0.001$,[2] in which case $A_0 = 0.00193$. Thus, the evolution equation for $C_{\rm TV}$ has the form

$$\dot{C}_{\rm TV} = A\dot{\gamma}^p, \qquad A = A_0 \exp\left(\alpha\frac{\sigma_{\rm M}}{\bar{\tau}}\right) \frac{1}{\left(1 + A_1 \exp\left(-\left(\frac{C_{\rm L}}{C_{\rm ref}}\right)^2\right)\right)} \geq 0, \tag{10.11}$$

and our first estimate of the material parameters appearing in this equation are listed in Table 10.7.

[2]Note from Fig. 10-4 that when $C_{\rm L} < 0.001$ then the material does not embrittle due to the prescnce of hydrogen.

Table 10.7: Preliminary set of parameters for trapping of hydrogen at vacancies

Parameter	Value
α	1.0
A_0	0.00193 mol/m^3
A_1	1.143
C_{ref}	0.0192 mol/m^3
$C_{\text{TV cr}}$	0.001 mol/m^3

Crazing initiates when $C_{\text{TV}} = C_{\text{TV cr}}$, and subsequently the crazes grow rapidly, and then damage initiates and also evolves quite rapidly towards final fracture. The material parameters which control the evolution of damage in eq. (9.229) are $\{\varkappa, \psi_{\text{R}}^{\text{crit}}, \ell, \zeta, k\}$. The parameter $\varkappa$ is the fraction inelastic power dissipated during crazing (cf. eq. (9.196)); we take its value to be $\varkappa \approx 0.8$. The parameter $\psi_{\text{R}}^{\text{crit}}$ is what controls the initiation of damage evolution, and an estimate for which we take to be given by

$$\psi_{\text{R}}^{\text{crit}} = S^c \times \epsilon_{\text{crit}}^c + \frac{S^{c\,2}}{2E}. \tag{10.12}$$

Here S^c is the value of the resistance to craze flow (cf. eq. (9.196)), which is approximately equal to the saturation value of the athermal resistance to plastic flow S_s, the parameter E is the Young's modulus of the material, and $\epsilon_{\text{crit}}^c \approx 10\%$ is a critical value of the craze strain. Physically (10.12) represents an estimate of the energy barrier that needs to be overcome for damage to initiate. The parameter ℓ is a damage regularization length scale which controls the spread of the diffuse damage; its value is chosen to be larger the about five times the size of the finite elements used to numerically model the diffuse damage zone. The parameter ζ is viscous regularization parameter for the evolution of damage, and the parameter k is a small number which we have introduced to prevent ill-conditioning of the numerical solution as the damage d tends to unity. The values for $\{\varkappa, \psi_{\text{R}}^{\text{crit}}, \ell, \zeta, k\}$ that we have used in our simulations are listed in Table 10.8.

Table 10.8: Material parameters for damage initiation and evolution

Parameter	Value
$\varkappa$	0.8
$\psi_{\text{R}}^{\text{crit}}$	21.14 MJ/m^3
ℓ	200 μm
ζ	10.0 MPa·s
k	1.0×10^{-4}

Using the parameters for damage initiation and evolution in Table 10.8, and with the parameters listed in Table 10.7 as guidelines, we conducted full finite element simulations of tension tests at different initial lattice hydrogen pressures (concentrations) and adjusted the parameters in Table 10.7 to those listed in Table 10.9 to obtain the fits to the stress-strain

curves and the elongation to failure as a function of the hydrogen concentration shown in Fig. 10-4. The adjusted parameters are list in Table 10.9.

Table 10.9: Refined set of parameters for trapping of hydrogen at vacancies

Parameter	Value
α	1.0
A_0	0.00195 mol/m^3
A_1	3.369
C_{ref}	0.0147 mol/m^3
$C_{\text{TV cr}}$	0.001 mol/m^3

In summary, the list of representative material parameters is shown in Table 10.10. All simulations done in this chapter are using this set of parameters.

10.2 Uniaxial tension of round bars

We first focus on simple tension tests of round bars in air and hydrogen environment that conducted by Xu and Rana (2009). To model these experiments we used an axisymmetric idealization of the round-bar tension tests conducted by these authors. The mesh that we used in our simulations is shown in Fig. 10-3; only one half of the axisymmetric specimen is meshed, and symmetry boundary conditions about midplane radial direction are imposed. We applied chemical potential boundary conditions on the exterior surface of the specimen corresponding to the pressure of the hydrogen gas in the environment in the experiments of Xu and Rana (2009). Thus, we allow for diffusion within the specimen, and also allow for hydrogen to permeate into the specimen through its boundaries. Also, as in the experiments of Xu and Rana the specimen was elongated at a rate of 1.3×10^{-4}/s.

Fig. 10-4(a) shows the fit of tensile stress-strain curves at different hydrogen pressures using the material parameters in Table 10.10. The experimental data for the stress-strain curves is given as dotted lines, while the numerically-calculated curves are shown as dashed lines. Fig. 10-4(b) shows the corresponding fit of the elongation to failure. The experimental data for the elongation as function of hydrogen concentration is given as filled black circles, while the numerically results are shown as open circles. The fit over a wide range of lattice hydrogen concentrations is quite good.

To study the process of hydrogen embrittlement and failure in slightly greater detail, we mark four instances (a) through (d) with red diamonds on the numerically calculated stress-strain curve for a hydrogen pressure of 22.4 MPa in Fig. 10-4(a), and show the corresponding contours of the equivalent tensile plastic strain $\bar{\epsilon}^p = \gamma^p/\sqrt{3}$, equivalent tensile plastic strain rate $\dot{\bar{\epsilon}}^p = \dot{\gamma}^p/\sqrt{3}$, concentration of hydrogen trapped in vacancies C_{TV}, and the craze strain ϵ^c, in Fig. 10-5.

In Fig. 10-4(a), the marked point (a) is at the peak of the stress-strain curve, and we can see from Fig. 10-5(a) that the accumulated plastic strain and plastic strain rate at this

Table 10.10: Representative material parameters for a ferritic steel

Elasticity parameters	G	GPa	81.34
	K	GPa	138.21
Viscoplasticity parameters	$\dot{\gamma}_0$	s^{-1}	1.73×10^6
	ΔF	J	1.38×10^{-19}
	p	-	1
	q	-	1
Strain-hardening parameters	S_*	MPa	291.8
	S_0	MPa	80.96
	H_0	MPa	1920
	S_s	MPa	262.12
	r	-	1.2
Solubility parameters	K_0	$\text{mol}/(\text{m}^3\sqrt{\text{MPa}})$	820
	ΔH	kJ/mol	28.6
Diffusion parameters	N_L	mol/m^3	8.46×10^5
	Ω_{H}	m^3/mol	2.0×10^{-6}
	μ_L^0	kJ/mol	28.6
	D_L	m^2/sec	1.27×10^{-8}
Trapping at dislocations	N_{TD}	mol/m^3	$N_{\text{TD}} = 10^{(23.26-2.33\exp(-3.1754\gamma^p)}$
	E_{BD}	kJ/mol	-60
Trapping at vacancies	α	-	1
	A_0	mol/m^3	0.00195
	A_1	-	3.369
	C_{ref}	mol/m^3	0.0147
	$C_{\text{TV cr}}$	mol/m^3	0.001
Damage initiation and evolution	$\varkappa$	-	0.8
	$\psi_{\text{R}}^{\text{crit}}$	MJ/m^3	21.14
	ℓ	μm	200
	ζ	MPa-s	10.0
	k	μm	1×10^{-4}

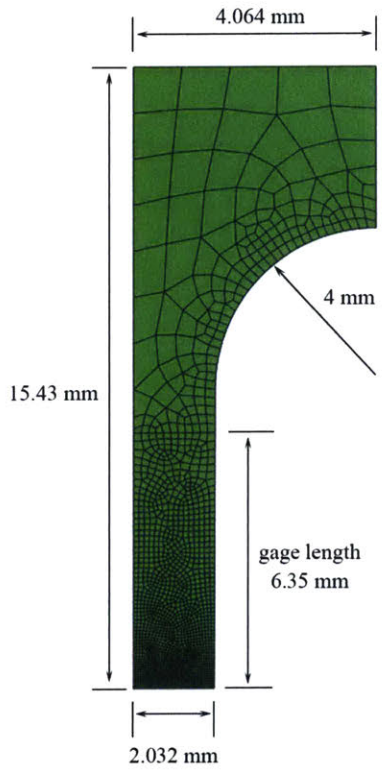

Figure 10-3: Axisymmetric finite element mesh corresponding to the tension specimens of Xu and Rana (2009).

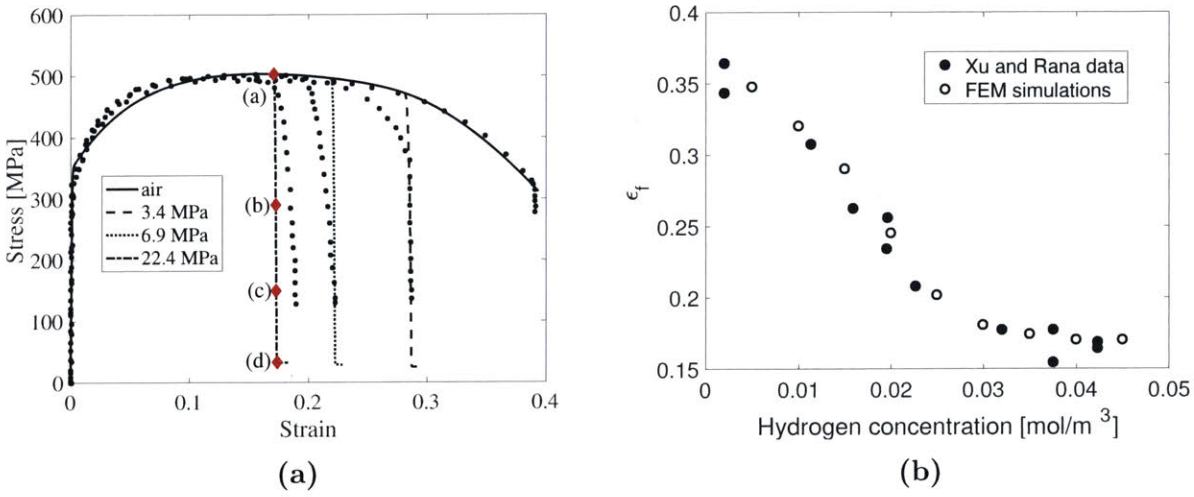

Figure 10-4: (a) Fit of tensile stress-strain curves at different hydrogen pressures using the material parameters in Table 10.10. The experimental data is given as dotted lines, while the numerically-simulated curves are shown as dashed lines. (b) Dependence of tensile elongation as a function of hydrogen concentration. The experimental data is given as filled circles, while the numerically results are shown as open circles. Experimental data from Xu and Rana (2009)

stage are almost uniform across the whole gage section — our specimen geometry was such that it was initially slightly tapered towards its midplane, and hence the contours of the equivalent plastic strain rate are slightly higher in that region. Further, at this stage $C_{\rm TV}$ has just reached its critical value of 0.001, and the craze straining ϵ^c is about to be triggered.

Fig. 10-5(b) shows that at stage (b) craze strain has accumulated at the middle plane, and indeed a small crack has nucleated and propagated from the surface towards the interior of the specimen. For brevity we do not show contour plots of the damage variable d, but to show crack formation and propagation, elements with a value of the damage variable $d > 0.95$ are removed from the plots. Together with the evolution of the crack, the overall stress has dropped to the point (b) point marked in Fig. 10-4(a). Even though the $\bar{\epsilon}^p$ contours are almost the same with that in Fig. 10-5(a), the $\dot{\bar{\epsilon}}^p$ contours have changed dramatically from those shown in Fig. 10-5(a). The plastic strain rate drops to almost zero, except for some elements ahead of the crack tip (which are not really visible in the plots shown here). This dramatic change in the contour of the equivalent tensile plastic strain rate indicates that regular shear plasticity has ceased to be operative in the majority of the specimen, and that the deformation has essentially localized in the form of a narrow band of dilational craze plasticity in the midplane region of the specimen.

Further stretching accumulates more craze strain and damage in the midplane region of the specimen, which causes the crack to propagate as shown in Fig. 10-5(c), and this eventually leads to the fracture of the specimen as shown in Fig. 10-5(d).[3] Correspondingly, the stress drops progressively, as indicated by point (c) and (d) in Fig. 10-4(a). At point (d) the sample is fully fractured.[4]

As mentioned previously there is no complete set of experiments for any one given material in the literature from which we may estimate all the material parameters in our theory. What Fig. 10-4 shows is that we are able to obtain reasonable estimates for the the material parameters for the SA106 steel studied experimentally by Xu and Rana (2009). *Much experimental work needs to be done to get more information to estimate the material parameters of the theory.* Of particular importance is the need for:

(i) Suitable experiments in which the stress-triaxiality is systematically varied so as to determine the value of the stress-triaxiality parameter α in eq. (9.159).

(ii) Suitable experiments which may be used to test the predictive capability of the theory and its numerical implementation.

As guidance of the type of experiments that one might conduct in the future to advance the theory and its applications, in the next section we numerically simulate:

[3] As mentioned above, to show crack propagation elements with a value of the damage variable $d > 0.95$ have been removed from the plots. We will use this scheme in all other plots in the paper to show the progression of failure.

[4] The stress at point (d) in Fig. 10-4(a) is $\sim$ 30 MPa and not zero because of the residual stiffness $k = 1 \times 10^{-4}$, cf. eq. (9.126), that we have chosen to prevent ill-conditioning of our numerical simulation as $d \to 1$, and final fracture occurs.

(i) Plane strain bending of U-notched specimens with different root radii to study the effects of stress-triaxiality on hydrogen embrittlement.

(ii) Plane strain tension of an asymmetrically notched specimen to validate the predictions of the theory and its numerical implementation.

Of course several other validation experiments may be envisaged, but we content ourselves in this paper with these two demonstrations of our numerical simulation capability.

10.3 Plane strain bending of U-notched specimens

The geometry of the plane strain of U-notched bend specimens is shown in Fig. 10-6. To study the effects of stress-triaxiality on hydrogen embrittlement we conducted simulations with notch-root radii of $\rho = 0.4, 1.2,$ and 2.4, with the notch depth fixed at 2 mm. We used the following boundary conditions:

- Mechanical boundary conditions: The top rollers are held fixed, while the the bottom roller is moved upward at a constant rate 1 μm/s.
- Chemical boundary conditions: All external surfaces are subjected to a constant chemical potential boundary condition corresponding to various values of C_{L0}.

The resulting force versus displacement curves for three-point bending of a U-notched specimen with root-radius of $\rho = 0.4$ mm, tested at different intial hydrogen concentration $C_{L0} \in [0.005, 0.045]$, are shown in Fig. 10-7.[5] In Fig. 10-7 we have also marked instances (a), (b), (c), and (d) on the curve for $C_{L0} = 0.015\text{mol/m}^3$, with point (a) corresponding to a peak in the force-dispalcement curve. In Fig. 10-8 we show the corresponding contours of the equivalent tensile plastic strain $\bar{\epsilon}^p = \gamma^p/\sqrt{3}$, equivalent tensile plastic strain rate $\dot{\bar{\epsilon}}^p = \dot{\gamma}^p/\sqrt{3}$, concentration of hydrogen trapped in vacancies C_{TV}, and the craze strain ϵ^c at these selected four instances. In these figures we have concentrated our attention on the middle portion of the bend specimen with the notch. Fig. 10-8(a) shows that at the point (a) the craze strain has accumulated to a sufficiently high level and that a crack is about to nucleate. Fig. 10-8(b)-(d) show the progressive nucleation and propagation of the crack during the bend test.

According to our model, the physical picture of crack initiation and propagation in ferritic as follows. If there is a notch in the specimen, then plasticity is most severe at the notch tip and the hydrogen trapped in vacancies will first reach its critical value at the notch tip, as compared to other parts of the sample. When a critical value of hydrogen trapped by the vacancies is reached, then the regular mechanism of shear plasticity gives way to craze plasticity. As the craze strain accumulates the portion of the free energy stored due to

[5] Although not shown here, the force-displacement curves shown in Fig. 10-7 are *mesh-objective*, in the sense that they are independent of the finite element mesh size, as long as the size of the finite elements is less than about 20% of the parameter $\ell = 200\mu$m in our gradient damage model.

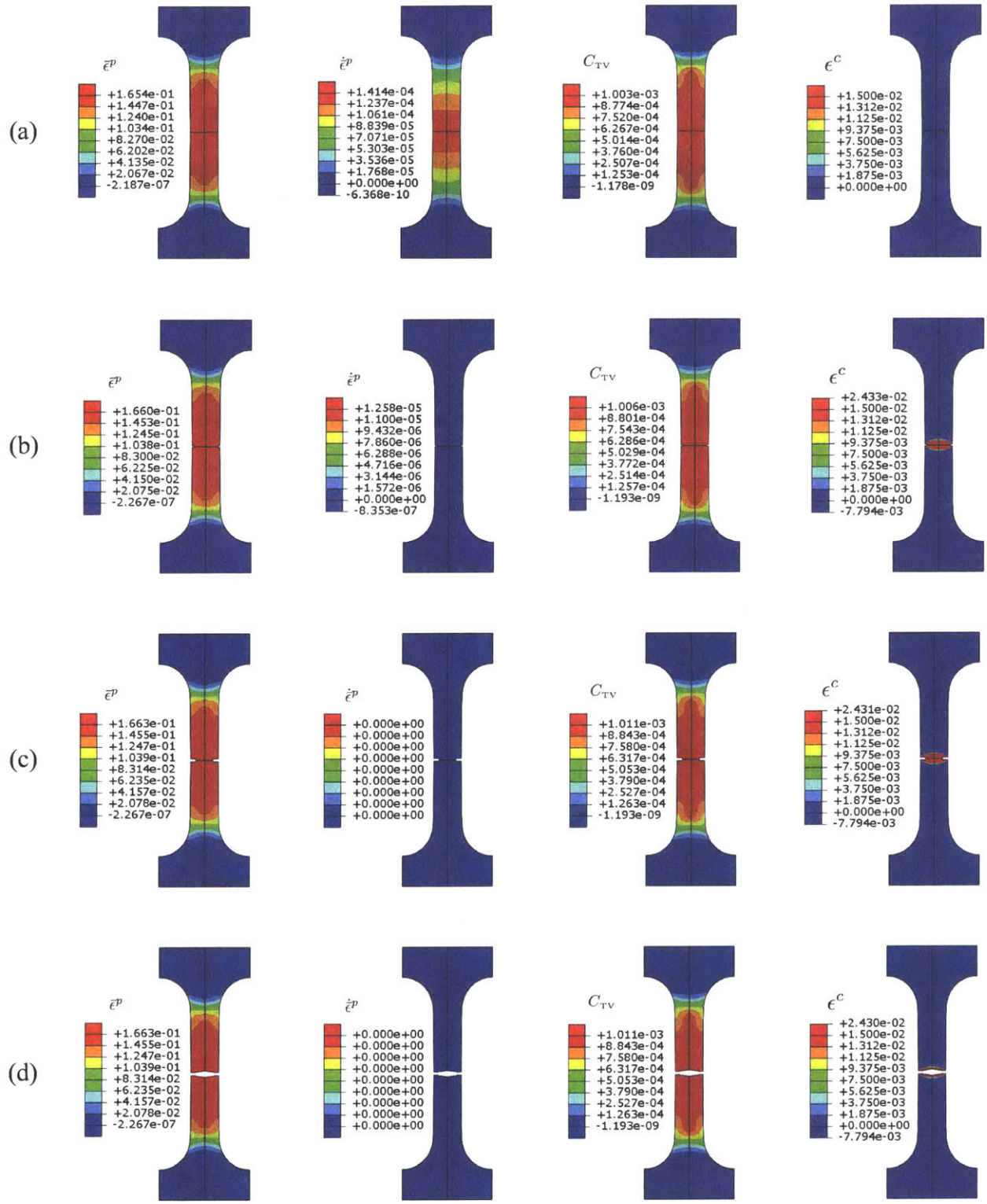

Figure 10-5: Contour plots of the equivalent tensile plastic strain $\bar{\epsilon}^p = \gamma^p/\sqrt{3}$, equivalent tensile plastic strain rate $\dot{\bar{\epsilon}}^p = \dot{\gamma}^p/\sqrt{3}$, concentration of hydrogen trapped in vacancies C_{TV}, and craze strain ϵ^c, at the instances (a), (b), (c), and (d) marked with red diamonds in Fig. 10-4(a).

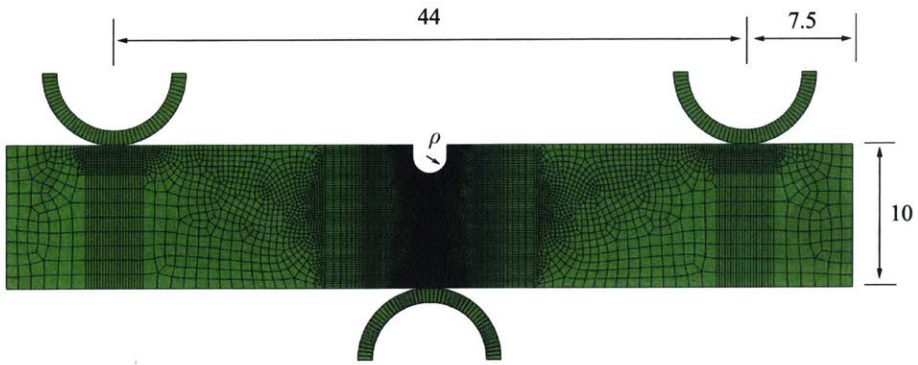

Figure 10-6: Geometry of the plane strain U-notched bend specimens. Simulations were conducted with notch-root radii of $\rho = 0.4, 1.2,$ and 2.4, with the notch depth fixed at 2 mm.

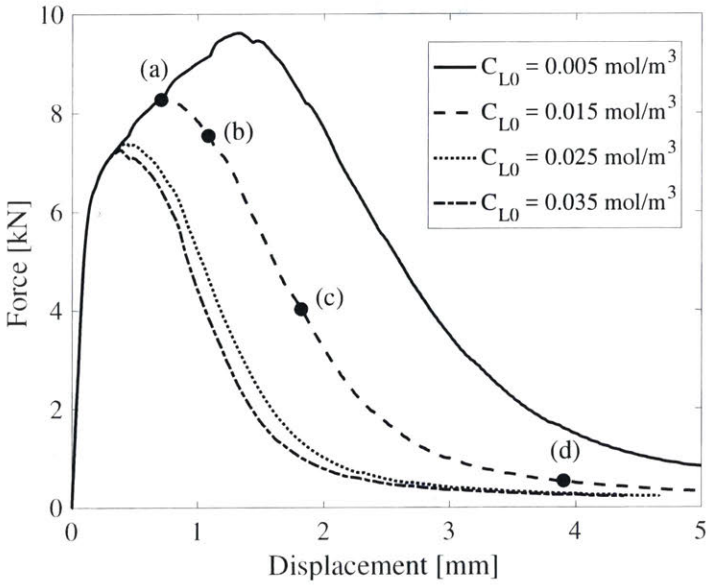

Figure 10-7: Force versus displacement curves for specimen with root-radius of $\rho = 0.4$ mm, tested in air as well as different initial hydrogen concentration $C_{L0} \in [0.005, 0.035]$.

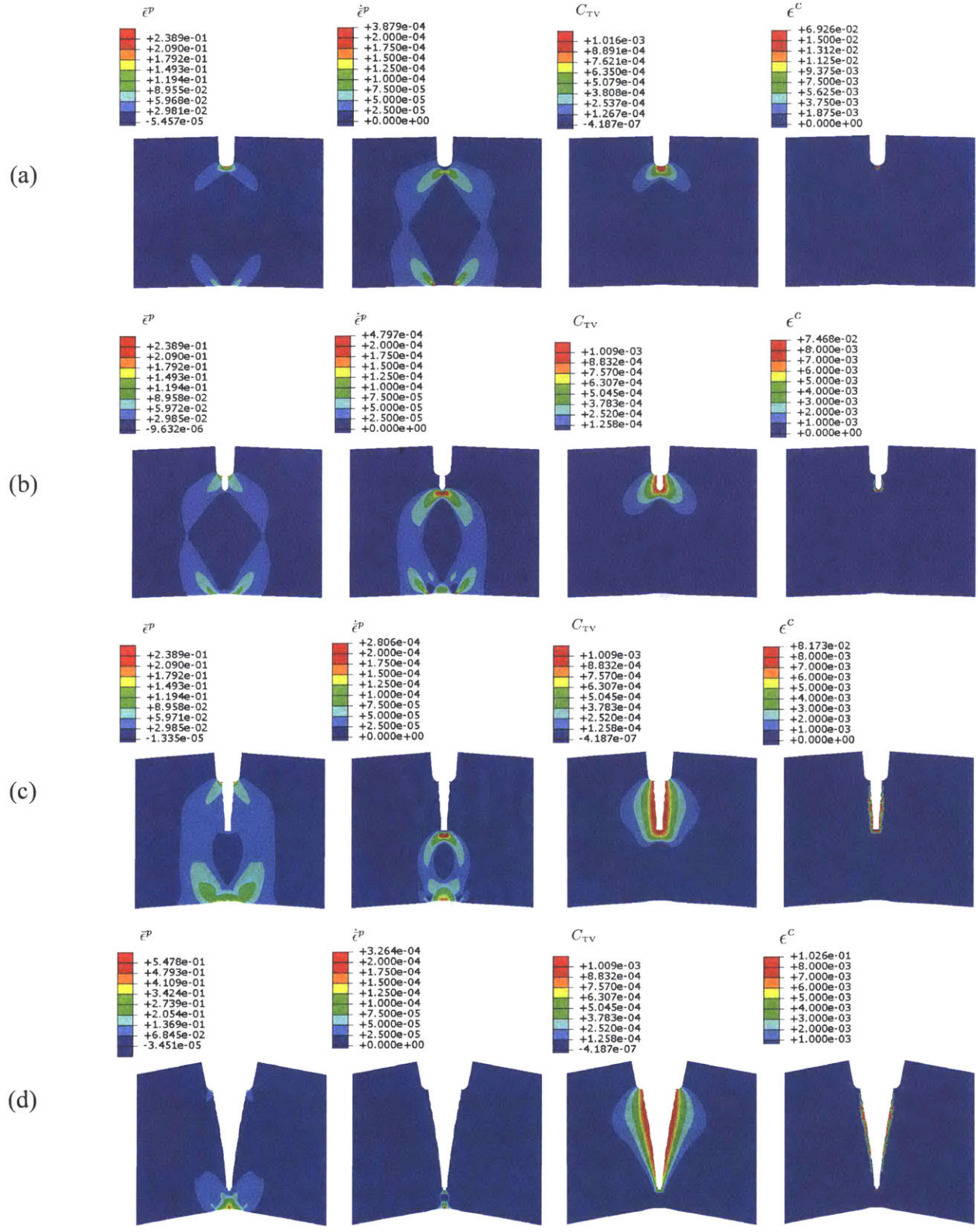

Figure 10-8: Contour plots of the equivalent tensile plastic strain $\bar{\epsilon}^p = \gamma^p/\sqrt{3}$, equivalent tensile plastic strain rate $\dot{\bar{\epsilon}}^p = \dot{\gamma}^p/\sqrt{3}$, concentration of hydrogen trapped in vacancies C_{TV}, and craze strain ϵ^c, at the instances (a), (b), (c), and (d) marked in Fig. 10-7.

crazing, together with the attendant elastic energy, reaches a critical value to trigger the evolution of the damage variable. Finally, as the damage accumulates and reaches unity, a crack nucleates and propagates. That is,

- an inhomogeneous deformation process which leads to regions of concentrated plastic strain also leads to a higher concentration of C_{TV} in these regions, which in turn leads to a field ϵ^c of the craze strain, and
- as the craze strain accumulates the conditions leading to growth of damage d are met, and when $d = 1$ the condition for fracture is met.

This physical picture is clearly evidenced in our numerical simulations of bending of a U-notched sample. In Fig. 10-8, we can see that the contours of non-zero ϵ^c are contained in regions of high C_{TV}, and the contours of ϵ^c always lead the nucleation and propagation of a crack.[6]

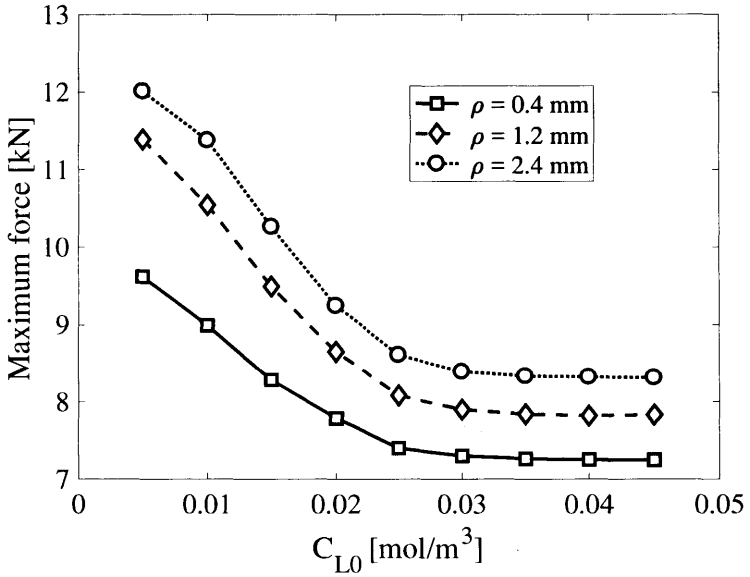

Figure 10-9: Maximum force in bending of U-notched specimens tested at different initial hydrogen concentrations in the range $C_{L0} \in [0.005, 0.045]$, for specimens with root-radii of $\rho = 0.4, 1.2,$ and $2.4\,\text{mm}$.

By conducting additional similar simulations we have collected the data for the maximum force in bending of specimens tested at different intial hydrogen concentrations in the range $C_{L0} \in [0.005, 0.045]$, for specimens with root radii of $\rho = 0.4, 1.2,$ and 2.4. The results are shown in Fig. 10-9. These simulation results are based on the material parameters in

[6]Recall that to show crack propagation elements with a value of the damage variable $d > 0.95$ have been removed from the plots.

Table 10.10. Because of lack of available experimental data of the type shown in Fig. 10-9, we had set the stress-triaxiality parameter α in (9.159) at $\alpha = 1$.

We suggest that in addition to simple tension tests at different hydrogen pressures (concentrations), as conducted by Xu and Rana (2009), in the future experiments of the type simulated in this section in which the stress triaxiality is varied systematically, should be part of any experimental program which aims to determine the effects of hydrogen on the embrittlement of steels. Data of the type shown in Fig. 10-7 and Fig. 10-9 would be very helpful in constructing calibrated models which have a wider range of applicability.[7]

10.4 Plane strain tension of an asymmetrically notched specimen

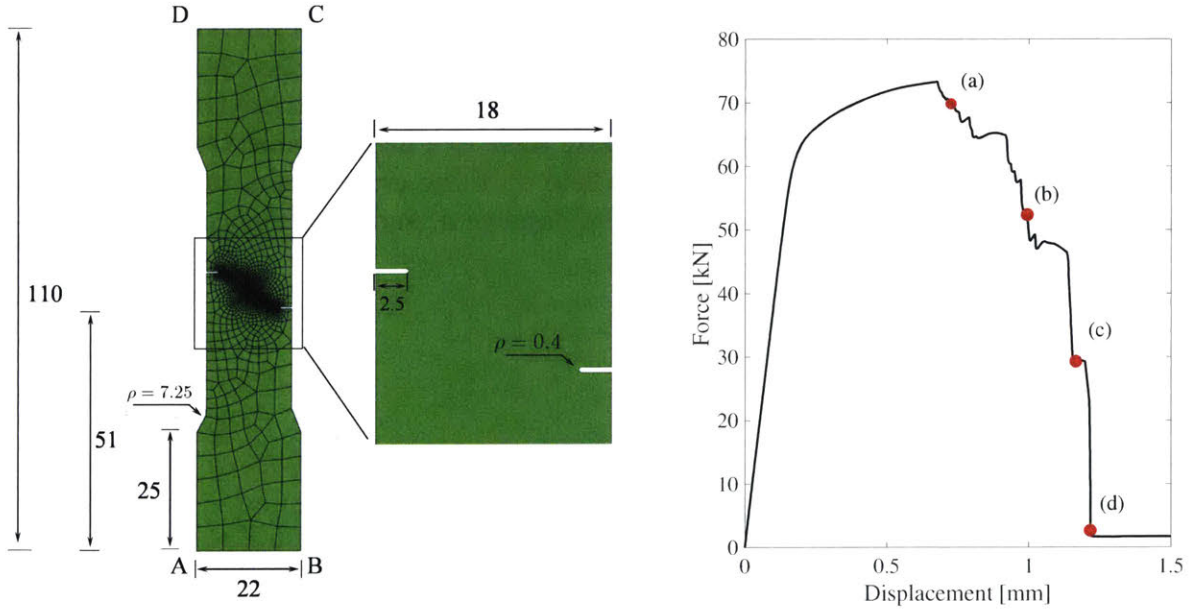

Figure 10-10: (a) Geometry and finite element mesh for an asymmetrical-notched tension specimen. Dimensions are in mm, with a plate thickness of 10mm. (b) Force versus displacement curve for the asymmetrical-notched tension specimen.

In this section we report on a simulation of plane strain tension of an *asymmetric* double-notched specimen, schematically shown in Fig. 10-10(a). We used the following boundary conditions:

[7]The experiments need not be U-notched bend tests, they could also be round bar U-notched tension test with different notch acuities.

- Mechanical boundary conditions: The bottom edge AB of the specimen is held fixed, while the top-edge CD is extended at a nominal strain rate of $1 \times 10^{-4}/\text{s}$.
- Chemical boundary conditions: Zero-flux boundary conditions are imposed on the bottom and top edges AB and CD of the specimen, while the lateral edges AD and BC are subjected to a constant chemical potential boundary condition corresponding to $C_{L0} = 0.015\text{mol}/\text{m}^3$.

The resulting force versus displacement curve form the simulation is shown in Fig. 10-10(b).

In Fig. 10-10(b) we have marked instances (a), (b), (c), and (d) on the force-displacement curve, and in Fig. 10-11 we focus our attention on a portion of the specimen which contains the two notches, and show contour plots of the equivalent tensile plastic strain $\bar{\epsilon}^p = \gamma^p/\sqrt{3}$, equivalent tensile plastic strain rate $\dot{\bar{\epsilon}}^p = \dot{\gamma}^p/\sqrt{3}$, concentration of hydrogen trapped in vacancies C_{TV}, and craze strain ϵ^c, at these selected instances. We see that at stage (a) the two offset notches have accumulated some craze strain and that a crack is about to nucleate in the vicinity of these notches. By stage (b) sufficient damage has accumulated and cracks have formed which are beginning to turn and propagate towards each other. Stage (c) shows that the two cracks are close to merging with each other, and final fracture into two separate pieces is observed at stage (d). The results from this simulation also clearly exhibit the physical picture embedded in the our model: an inhomogeneous deformation process which leads to regions of concentrated plastic strain, also leads to a higher concentration of the field C_{TV} in these regions, which in turn leads to a field ϵ^c of the craze strain, and accumulation of craze strain subsequently leads to evolution of damage d, and fracture occurs when $d = 1$.

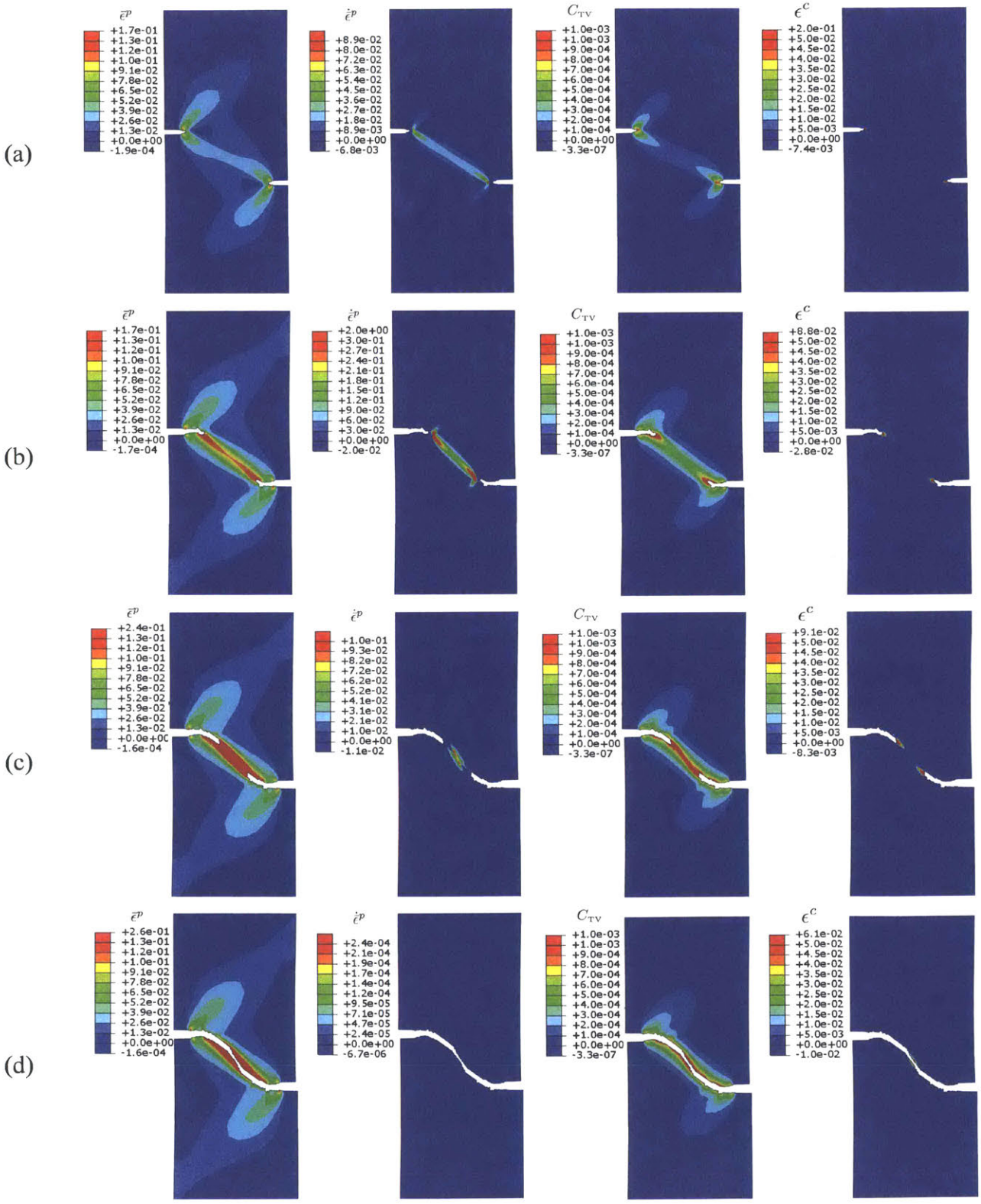

Figure 10-11: Contour plots of the equivalent tensile plastic strain $\bar{\epsilon}^p = \gamma^p/\sqrt{3}$, equivalent tensile plastic strain rate $\dot{\bar{\epsilon}}^p = \dot{\gamma}^p/\sqrt{3}$, concentration of hydrogen trapped in vacancies C_{TV}, and craze strain ϵ^c at the instances (a), (b), (c), and (d) marked in in Fig. 10-10.

Chapter 11

Concluding remarks

Guided by the recent experimental observations on hydrogen embrittlement of medium yield strength ferritic steels (Martin et al., 2011b,a; Neeraj et al., 2012; Robertson et al., 2015; Dadfarnia et al., 2015), and guided by the hydrogen embrittlement mechanism proposed by Li et al. (2015) for these materials, we have formulated a continuum theory for the diffusion of hydrogen coupled with the elastic-viscoplastic response of metals, together with an accounting for microscopic effects due to trapping of hydrogen in hydrogen-vacancy complexes. We have proposed that when the hydrogen which is trapped in hydrogen-vacancy complexes reach a critical concentration, then there is a change in mechanism of inelastic deformation from standard plastic flow by dislocation glide to plastic flow by a *quasi-cleavage* type mechanism — a change in mechanism which is reminiscent of a transition between "shear-yielding" and "crazing" in amorphous polymers. We have formulated a criterion for such a change in mechanism together with an attendant dilatant craze-plasticity flow rule, and a corresponding gradient damage theory to model fracture of ferritic steels due to hydrogen embrittlement. All these ingredients for modeling fracture due to hydrogen embrittlement are new.

We have numerically implemented our coupled diffusion-deformation-damage theory in Dassault Systèmes (v. 6.14) as a user-element (UEL) for plane strain, axisymmetric, and three-dimensional elements.

Unfortunately there is no complete set of data from experiments for any one given material from which we may estimate all the material parameters in our theory. However, we have shown in Section 10.1 of Chapter 10 that we are able to obtain reasonable estimates for the material parameters for the SA 106 steel studied experimentally by Xu and Rana (2009). Much experimental work needs to be done to get data to estimate the material parameters in our theory for a material of interest. As guidance of the type of experiments that one might conduct in the future to advance the theory and its applications, in Section 10.3 of Chapter 10 we have numerically simulated plane strain bending of U-notched specimens with different root radii to study the effects of stress-triaxiality on hydrogen embrittlement. We

suggest that in addition to simple tension tests at different hydrogen pressures (concentrations), as conducted by Xu and Rana (2009), in the future experiments of the type simulated in our paper in which the stress triaxiality is varied systematically, should also be part of any experimental program which aims to determine the effects of hydrogen on the embrittlement of steels. Experimental data of the type shown in Fig. 10-7, and Fig. 10-9 would be very helpful in constructing calibrated models which have a wider range of applicability.

In Section 10.4 of Chapter 10 we have shown a simulation of plane strain tension of an asymmetric double-notched specimen. This example shows the powerful capability of our gradient-damage theory and its numerical implementation to model the nucleation and merging of cracks emanating from two notches. Data from experiments of this type would be of substantial use in validating the predictions from any theory of fracture due to hydrogen embrittlement.

Part III

Conclusions and outlook

Chapter 12

Conclusion

12.1 Summary

Solids with deformation-diffusion coupling are ubiquitous in engineering applications. Understanding and modeling the fracture in such solids is vitally important. In this thesis, we have focus on studying the coupled deformation-diffusion-damage behaviors of two different classes of materials: (i) elastomeric gels and (ii) hydrogen embrittled steels. To conclude, we briefly summarize the main contributions of each part of this thesis:

- The first contribution of this thesis is introducing a new field related with stretch of Kuhn segments, to bridging the deformation of polymers and the fracture of polymers consistently. One of the distinguishing features of elastomeric materials, which consist of a network of flexible polymeric chains, is that the deformation response is dominated by changes in entropy. Accordingly, most classical theories of rubber-like elasticity consider only the entropy and neglect any changes in internal energy. On the other hand, the fracture of strongly cross-linked elastomers is essentially energy dominated, as argued in the well-known Lake-Thomas model for the toughness of elastomers. However, a single model unifying these two phenomena is still lacking. We provide a rational yet simple model for deformation and fracture of cross-linked polymers, based on two ingredients: (i) a non-Gaussian statistical mechanics model of polymer chains that accounts for the increase in energy due to the deformation of molecular bonds; (ii) a chain scission criterion based on the bond deformation energy attaining a critical value. Using this model, we can estimate the rupture stretch of elastomeric materials from fundamental quantities describing the polymer network. We use this model to relate the flaw sensitivity of elastomers to an intrinsic material length scale related to the network structure.

- The second contribution of this thesis is to build a thermodynamically-consistent theory for fracture of polymeric gels. — a theory which accounts for the coupled effects of fluid

diffusion, large deformations, damage, and also the gradient effects of damage. The particular constitutive equations for fracture of a gel proposed in our paper, contain two essential new ingredients: (i) Our constitutive equation for the change in free energy of a polymer network accounts for not only changes in the entropy, but also changes in the internal energy due the stretching of the Kuhn segments of the polymer chains in the network. (ii) The damage and failure of the polymer network is taken to occur by chain-scission, a process which is driven by the changes in the internal energy of the stretched polymer chains in the network, and not directly by changes in the configurational entropy of the polymer chains. The theory developed in this paper is numerically implemented in an open-source finite element code MOOSE, by writing our own application. Using this simulation capability we

  - study the fracture of elastomers by crosslink failure and chain scission, and
  - report on our study of the fracture of a polymeric gel, and some interesting phenomena which show the importance of the diffusion of the fluid on fracture response of the gel are highlighted.

- The third contribution of the thesis is formulating a experimental-based continuum theory for the diffusion of hydrogen coupled with the elastic-viscoplastic response of metals, together with an accounting for microscopic effects due to trapping of hydrogen in hydrogen-vacancy complexes, culminating in eventual fracture. We have numerically implemented our coupled diffusion-deformation-failure theory in a finite element program Abaqus by writing a user element subroutines (UEL), and we present representative numerical examples which show the ability of the simulation capability to qualitatively replicate the failure due to hydrogen embrittlement in some technically relevant geometries.

12.2 Outlook

While much has been accomplished, more remains to be done. Some outstanding issues are discussed below.

- Fracture in elastomeric materials:
  - In this thesis, we apply our idea on stretchable segment and crosslinks to modify Kuhn-Grun model (at single chain level) and Arruda-Boyce model (at continuum level). However, the idea itself can be applied to other models, like worm-like chain model, to understand and modeling *the deformation and the fracture* of soft materials described by these models.
  - The theory and numerical development presented in this thesis are based on sound physical and mathematical principles, however experimental characterization of an actual gel is lacking. In order the flesh-out the theory substantial experimental

work is required. In order to distinguish our theory and other phenomenological theories, tests at very small samples (at order of 1 micro) are needed. Bulk sample tests are not sufficient to verify the physical foundations of our theory.

- Our theory has been formulated for non-ionic elastomeric gels. An important extension of this work will be to develop a constitutive theory for gels that interact with external redox potential and thermal, chemical, optical, electric, and magnetic fields.
- The theory presented here is for elastomeric gels. It would be useful in the future to extend the theory presented in this thesis to interpenetrating-multiple-network gels which incorporate additional non-trivial dissipation mechanisms to toughen polymeric gels. Moreover, study on the failure mechanics of soft materials with entanglements, viscoelasticity, reactive diffusive solvents, transient networks, and self-healing are highly interesting.
- Apply the theory presented in this thesis to study other phenomena in soft materials, like the interplay between failure and various kinds of instability such as fringe and fingering (Biggins et al., 2013; Lin et al., 2016, 2017, 2018), will be a very fruitful direction. Moreover, using the theory developed in the thesis to study the fracture in soft materials with other phase transitions, such as polymeric multiferroics and liquid crystal elastomeric and gels, will be important.

- Fracture in hydrogen embrittled steels:
  - Even though the theory and numerical development presented in this thesis are based on sound physical and mathematical principles, completed experimental characterization of an actual material is lacking. In order the flesh-out the theory substantial experimental work is required. Of particular importance is the need for:
    (i) Suitable experiments in which the stress-triaxiality is systematically varied so as to determine the value of the stress-triaxiality parameter α in eq. (9.159).
    (ii) Suitable experiments which may be used to test the predictive capability of the theory and its numerical implementation.
  - To improve the theory and its predictive ability, more microscopic features in the materials shall be considered and included in the model. Moreover, more tests against the long-time atomistic simulations are also necessary.

Bibliography

Akagi, Y., Sakurai, H., Gong, J. P., Chung, U., Sakai, T., 2013. Fracture energy of polymer gels with controlled network structures. The Journal of Chemical Physics 139 (14), 144905.

Anand, L., 1996. A constitutive model for compressible elastomeric solids. Computational Mechanics 18 (5), 339–355.

Anand, L., 2011. A thermo-mechanically-coupled theory accounting for hydrogen diffusion and large elastic–viscoplastic deformations of metals. International journal of solids and structures 48 (6), 962–971.

Anand, L., 2012. A cahn-hilliard-type theory for species diffusion coupled with large elastic-plastic deformations. Journal of the Mechanics and Physics of Solids 60, 1983–2002.

Argon, A., 2011. Craze initiation in glassy polymers–revisited. Polymer 52 (10), 2319–2327.

Argon, A. S., Hannoosh, J. G., 1977. Initiation of crazes in polystyrene. Philosophical Magazine 36 (5), 1195–1216.

Arruda, E. M., Boyce, M. C., 1993. A three-dimensional constitutive model for the large stretch behavior of rubber elastic materials. Journal of the Mechanics and Physics of Solids 41 (2), 389–412.

Ayachit, U., 2015. The paraview guide: a parallel visualization application.

Beachem, C., 1972. A new model for hydrogen-assisted cracking (hydrogen embrittlement). Metallurgical transactions 3 (2), 441–455.

Biggins, J. S., Saintyves, B., Wei, Z., Bouchaud, E., Mahadevan, L., 2013. Digital instability of a confined elastic meniscus. Proceedings of the National Academy of Sciences 110 (31), 12545–12548.

Birnbaum, H. K., Sofronis, P., 1994. Hydrogen-enhanced localized plasticitya mechanism for hydrogen-related fracture. Materials Science and Engineering: A 176 (1-2), 191–202.

Bonn, D., Kellay, H., Prochnow, M., Ben-Djemiaa, K., Meunier, J., 1998. Delayed fracture of an inhomogeneous soft solid. Science 280 (5361), 265–267.

Borden, M. J., Hughes, T. J., Landis, C. M., Anvari, A., Lee, I. J., 2016. A phase-field formulation for fracture in ductile materials: Finite deformation balance law derivation, plastic degradation, and stress triaxiality effects. Computer Methods in Applied Mechanics and Engineering 312, 130–166.

Bouklas, N., Landis, C., Huang, R., 2015. Effect of solvent diffusion on crack-tip fields and driving force for fracture of hydrogels. Journal of Applied Mechanics 82, 081007.

Bourdin, B., Francfort, G. A., Marigo, J.-J., 2000. Numerical experiments in revisited brittle fracture. Journal of the Mechanics and Physics of Solids 48 (4), 797–826.

Bourdin, B., Francfort, G. A., Marigo, J.-J., 2008. The variational approach to fracture. Journal of elasticity 91 (1-3), 5–148.

Broger, L., Keip, M., Miehe, C., 2017b. Minimization and saddle-point principles for the phase-field modeling of fracture in hydrogels. Computational Materials Science 138, 47–485.

Broger, L., Nateghi, A., Miehe, C., 2017a. A minimization principle for deformation diffusion processes in polymeric hydrogels: constitutive modeling and fe implementation. International Journal of Solids and Structures 121, 257–274.

Brown, H., 2007. A model of the fracture of double network gels. Macromolecules 40 (10), 3815–3818.

Buehler, M. J., Abraham, F. F., Gao, H., 2003. Hyperelasticity governs dynamic fracture at a critical length scale. Nature 426 (6963), 141–146.

Chen, C., Wang, Z., Suo, Z., 2016. Flaw sensitivity of highly stretchable materials. Extreme Mechanics LettersHttp://dx.doi.org/10.1016/j.eml.2016.10.002.

Chester, S. A., Anand, L., 2010. A coupled theory of fluid permeation and large deformations for elastomeric materials. Journal of the Mechanics and Physics of Solids 58 (11), 1879–1906.

Chester, S. A., Anand, L., 2011. A thermo-mechanically coupled theory for fluid permeation in elastomeric materials: Application to thermally responsive gels. Journal of the Mechanics and Physics of Solids 59 (10), 1978–2006.

Chester, S. A., Di Leo, C., Anand, L., 2015. A finite element implementation of a coupled diffusion-deformation theory for elastomeric gels. JInternational Journal of solids and Structures 52, 1–18.

Creton, C., 2017. 50th anniversary perspective: Networks and gels: Soft but dynamic and tough. Macromolecules 50, 8297–8316.

Dadfarnia, M., Nagao, A., Wang, S., Martin, M. L., Somerday, B. P., Sofronis, P., 2015. Recent advances on hydrogen embrittlement of structural materials. International Journal of Fracture 196 (1-2), 223–243.

Dadfarnia, M., Novak, P., Ahn, D., Liu, J., Sofronis, P., Johnson, D., Robertson, I., 2010. Recent advances in the study of structural materials compatibility with hydrogen. Advanced Materials 22 (10), 1128–1135.

Dadfarnia, M., Somerday, B. P., Sofronis, P., Robertson, I. M., Stalheim, D., 2009. Interaction of hydrogen transport and material elastoplasticity in pipeline steels. Journal of Pressure Vessel Technology 131 (4), 041404.

Dassault Systèmes, v. 6.14. Abaqus FEA. Computer software.

deB. Darwent, B., 1970. Bond dissociation energies in simple molecules. NSRDS-NBS 31. U.S. Dept. of Commerce, National Bureau of Standards, Washington, D.C.

DeHoff, R., 2006. Thermodynamics in materials science. CRC Press.

Di Leo, C. V., Anand, L., 2013. Hydrogen in metals: A coupled theory for species diffusion and large elastic–plastic deformations. International Journal of Plasticity 43, 42–69.

Doi, M., 1996. Introduction to polymer physics. Oxford university press.

Doi, M., 2009. Gel dynamics. Journal of the Physical Society of Japan 78, 052001.

Ducrot, E., Chen, Y., Bulters, M., Sijbesma, R. P., Creton, C., 2014. Toughening elastomers with sacrificial bonds and watching them break. Science 344 (6180), 186–189.

Duda, F. P., Souza, A. C., Fried, E., 2010. A theory for species migration in a finitely strained solid with application to polymer network swelling. Journal of the Mechanics and Physics of Solids 58 (4), 515–529.

El-Danaf, E., Baig, M., Almajid, A., Alshalfan, W., Al-Mojil, M., Al-Shahrani, S., 2013. Mechanical, microstructure and texture characterization of api x65 steel. Materials & Design 47, 529–538.

Flory, P. J., 1942. Thermodynamics of high polymer solutions. The Journal of chemical physics 10 (1), 51–61.

Flory, P. J., Rehner, J., 1943. Statistical mechanics of cross-linked polymer networks ii. The Journal of chemical physics 11 (11), 521–526.

Francfort, G. A., Marigo, J.-J., 1998. Revisiting brittle fracture as an energy minimization problem. Journal of the Mechanics and Physics of Solids 46 (8), 1319–1342.

Gaston, D., Newman, C., Hansen, G., Lebrun-Grandie, D., 2009. Moose: A parallel computational framework for coupled systems of nonlinear equations. Nuclear Engineering and Design 239 (10), 1768–1778.

Gearing, B., Anand, L., 2004. On modeling the deformation and fracture response of glassy polymers due to shear-yielding and crazing. International Journal of Solids and Structures 41 (11-12), 3125–3150.

Gent, A. N., 1996. A new constitutive relation for rubber. Rubber chemistry and technology 69 (1), 59–61.

Ghatak, A., Vorvolakos, K., She, H., Malotky, D. L., Chaudhury, M. K., 2000. Interfacial rate processes in adhesion and friction. The Journal of Physical Chemistry B 104 (17), 4018–4030.

Gong, J., Katsuyama, Y., Kurokawa, T., Osada, Y., 2003. Double-network hydrogels with extremely high mechanical strength. Advanced Materials 15, 11155–1158.

Griffith, A. A., 1921. The phenomena of rupture and flow in solids. Philosophical transactions of the royal society of london. Series A, containing papers of a mathematical or physical character 221, 163–198.

Grindy, S. C., Lenz, M., Holten-Andersen, N., 2016. Engineering elasticity and relaxation time in metal-coordinate cross-linked hydrogels. Macromolecules 49 (21), 8306–8312.

Gurtin, M. E., 1996. Generalized ginzburg-landau and cahn-hilliard equations based on a microforce balance. Physica D: Nonlinear Phenomena 92 (3-4), 178–192.

Gurtin, M. E., 2002. A gradient theory of single-crystal viscoplasticity that accounts for geometrically necessary dislocations. Journal of the Mechanics and Physics of Solids 50 (1), 5–32.

Gurtin, M. E., Anand, L., 2005. A theory of strain-gradient plasticity for isotropic, plastically irrotational materials. part i: Small deformations. Journal of the Mechanics and Physics of Solids 53 (7), 1624–1649.

Gurtin, M. E., Anand, L., 2009. Thermodynamics applied to gradient theories involving the accumulated plastic strain: the theories of aifantis and fleck and hutchinson and their generalization. Journal of the Mechanics and Physics of Solids 57 (3), 405–421.

Gurtin, M. E., Fried, E., Anand, L., 2010. The mechanics and thermodynamics of continua. Cambridge University Press.

Hirth, J. P., 1980. Effects of hydrogen on the properties of iron and steel. Metallurgical Transactions A 11 (6), 861–890.

Hocine, N. A., Abdelaziz, M. N., Imad, A., 2002. Fracture problems of rubbers: J-integral estimation based upon η factors and an investigation on the strain energy density distribution as a local criterion. International Journal of Fracture 117 (1), 1–23.

Hong, W., Zhao, X., Zhou, J., Suo, Z., 2008. A theory of coupled diffusion and large deformation in polymeric gels. Journal of the Mechanics and Physics of Solids 56 (5), 1779–1793.

Huggins, M. L., 1942. Some properties of solutions of long-chain compounds. The Journal of Physical Chemistry 46 (1), 151–158.

Huheey, J. E., Keiter, E. A., Keiter, R. L., 1993. Inorganic chemistry :principles of structure and reactivity, 4th Edition. HarperCollins College Publishers, New York.

Hui, C., Long, R., Ning, J., 2013. Stress relaxation near the tip of a stationary modei crack in a poroelastic solid. Journal of Applied Mechanics 80, 021014.

Hutchinson, J., 1968. Singular behaviour at the end of a tensile crack in a hardening material. Journal of the Mechanics and Physics of Solids 16 (1), 13–31.

Hutchinson, J. W., Suo, Z., 1991. Mixed mode cracking in layered materials. Advances in applied mechanics 29, 63–191.

Ishiyama, C., Asai, T., Kobayashi, M., Shimojo, M., Higo, Y., 2001. Fatigue crack propagation mechanisms in poly (methyl methacrylate) by in situ observation with a scanning laser microscope. Journal of Polymer Science Part B: Polymer Physics 39 (24), 3103–3113.

Karma, A., Kessler, D. A., Levine, H., 2001. Phase-field model of mode iii dynamic fracture. Physical Review Letters 87 (4), 045501.

Kienzler, R., Herrmann, G., 2012. Mechanics in material space: with applications to defect and fracture mechanics. Springer Science & Business Media.

Kocks, U., Argon, A., Ashby, M., 1975. Thermodynamics and kinetics of slip, volume 19 in progress in materials science, b. chalmers, jw christian and tb massalsk, eds.

Kothari, M., Anand, L., 1998. Elasto-viscoplastic constitutive equations for polycrystalline metals: application to tantalum. Journal of the Mechanics and Physics of Solids 46 (1), 51–83.

Kresse, G., Furthmüller, J., 1996a. Efficiency of ab-initio total energy calculations for metals and semiconductors using a plane-wave basis set. Computational Materials Science 6 (1), 15–50.

Kresse, G., Furthmüller, J., 1996b. Efficient iterative schemes for ab initio total-energy calculations using a plane-wave basis set. Physical review B 54 (16), 11169.

Krom, A., Bakker, A., Koers, R., 1997. Modelling hydrogen-induced cracking in steel using a coupled diffusion stress finite element analysis. International Journal of Pressure Vessels and Piping 72 (2), 139–147.

Krom, A., Koers, R., Bakker, A., 1999. Hydrogen transport near a blunting crack tip. Journal of the Mechanics and Physics of Solids 47 (4), 971–992.

Krom, A. H., Bakker, A., 2000. Hydrogen trapping models in steel. Metallurgical and materials transactions B 31 (6), 1475–1482.

Kröner, E., 1959. Allgemeine kontinuumstheorie der versetzungen und eigenspannungen. Archive for Rational Mechanics and Analysis 4 (1), 273.

Kuhn, W., Grün, F., 1942. Beziehungen zwischen elastischen konstanten und dehnungsdoppelbrechung hochelastischer stoffe. Kolloid-Zeitschrift 101 (248).

Kumnick, A., Johnson, H., 1980. Deep trapping states for hydrogen in deformed iron. Acta Metallurgica 28 (1), 33–39.

Lake, G. J., Thomas, A. G., 1967. The strength of highly elastic materials. Proceedings of the Royal Society of London A: Mathematical, Physical and Engineering Sciences 300 (1460), 108–119.

Lawn, B., 1993. Fracture of brittle solids. Cambridge university press.

Lee, E. H., 1969. Elastic-plastic deformation at finite strains. Journal of applied mechanics 36 (1), 1–6.

Li, H., Liu, B., Zhang, X., Gao, C., Shen, J., Zou, G., 1999. Single-molecule force spectroscopy on poly (acrylic acid) by afm. Langmuir 15 (6), 2120–2124.

Li, S., Li, Y., Lo, Y.-C., Neeraj, T., Srinivasan, R., Ding, X., Sun, J., Qi, L., Gumbsch, P., Li, J., 2015. The interaction of dislocations and hydrogen-vacancy complexes and its importance for deformation-induced proto nano-voids formation in α-fe. International Journal of Plasticity 74, 175–191.

Lin, S., Cohen, T., Zhang, T., Yuk, H., Abeyaratne, R., Zhao, X., 2016. Fringe instability in constrained soft elastic layers. Soft matter 12 (43), 8899–8906.

Lin, S., Mao, Y., Radovitzky, R., Zhao, X., 2017. Instabilities in confined elastic layers under tension: Fringe, fingering and cavitation. Journal of the Mechanics and Physics of Solids 106, 229–256.

Lin, S., Mao, Y., Yuk, H., Zhao, X., 2018. Material-stiffening suppresses elastic fingering and fringe instabilities. International Journal of Solids and Structures.

Liu, F., Ming, P., Li, J., Aug 2007. Ab initio calculation of ideal strength and phonon instability of graphene under tension. Physical Review B 76, 064120.
URL http://link.aps.org/doi/10.1103/PhysRevB.76.064120

Lucantonio, A., Nardinocchi, P., Teresi, L., 2013. Transient analysis of swelling-induced large deformations in polymer gels. Journal of the Mechanics and Physics of Solids 61, 205–218.

Mao, Y., Anand, L., 2018. A theory for fracture of polymeric gels. Journal of Physics and Mechanics of Solids 115, 3053.

Mao, Y., Anand, L., submitted. Fracture of elastomeric materials by crosslink failure. Journal of Applied Mechanics.

Mao, Y., Lin, S., Zhao, X., Anand, L., 2017a. A large deformation viscoelastic model for double-network hydrogels. Journal of the Mechanics and Physics of Solids 100, 103–130.

Mao, Y., Talamini, B., Anand, L., 2017b. Rupture of polymers by chain scission. Extreme Mechanics Letters.

Mark, J. E., Erman, B., 2007. Rubberlike elasticity: a molecular primer. Cambridge University Press.

Martin, M., Robertson, I., Sofronis, P., 2011a. Interpreting hydrogen-induced fracture surfaces in terms of deformation processes: a new approach. Acta Materialia 59 (9), 3680–3687.

Martin, M. L., Fenske, J. A., Liu, G. S., Sofronis, P., Robertson, I. M., 2011b. On the formation and nature of quasi-cleavage fracture surfaces in hydrogen embrittled steels. Acta Materialia 59 (4), 1601–1606.

McMeeking, R., Parks, D., 1979. On criteria for j-dominance of crack-tip fields in large-scale yielding. In: Elastic-plastic fracture. ASTM International.

McMeeking, R. M., 1977. Finite deformation analysis of crack-tip opening in elastic-plastic materials and implications for fracture. Journal of the Mechanics and Physics of Solids 25 (5), 357–381.

Miehe, C., Aldakheel, F., Raina, A., 2016. Phase field modeling of ductile fracture at finite strains: A variational gradient-extended plasticity-damage theory. International Journal of Plasticity 84, 1–32.

Miehe, C., Hofacker, M., Schänzel, L.-M., Aldakheel, F., 2015. Phase field modeling of fracture in multi-physics problems. part ii. coupled brittle-to-ductile failure criteria and crack propagation in thermo-elastic–plastic solids. Computer Methods in Applied Mechanics and Engineering 294, 486–522.

Miehe, C., Schänzel, L.-M., 2014. Phase field modeling of fracture in rubbery polymers. part i: Finite elasticity coupled with brittle failure. Journal of the Mechanics and Physics of Solids 65, 93–113.

Miehe, C., Welschinger, F., Hofacker, M., 2010. Thermodynamically consistent phase-field models of fracture: Variational principles and multi-field fe implementations. International Journal for Numerical Methods in Engineering 83 (10), 1273–1311.

Nagumo, M., 2004. Hydrogen related failure of steels–a new aspect. Materials Science and Technology 20 (8), 940–950.

Nagumo, M., Ishikawa, T., Endoh, T., Inoue, Y., 2003. Amorphization associated with crack propagation in hydrogen-charged steel. Scripta materialia 49 (9), 837–842.

Neeraj, T., Srinivasan, R., Li, J., 2012. Hydrogen embrittlement of ferritic steels: observations on deformation microstructure, nanoscale dimples and failure by nanovoiding. Acta Materialia 60 (13-14), 5160–5171.

Noselli, G., Lucantonio, A., R., M., DeSimone, A., 2016. Poroelastic toughening in polymer gels: A theoretical and numerical study. Journal of of the Mechanics and Physics of Solids 94, 33–46.

Oriani, R., 1972. A mechanistic theory of hydrogen embrittlement of steels. Berichte der Bunsengesellschaft für physikalische Chemie 76 (8), 848–857.

Parks, D. M., 1977. The virtual crack extension method for nonlinear material behavior. Computer Methods in Applied Mechanics and Engineering 12 (3), 353–364.

Raina, A., Miehe, C., 2016. A phase-field model for fracture in biological tissues. Biomechanics and modeling in mechanobiology 15 (3), 479–496.

Rice, J., Rosengren, G. F., 1968. Plane strain deformation near a crack tip in a power-law hardening material. Journal of the Mechanics and Physics of Solids 16 (1), 1–12.

Rice, J. R., 1968. A path independent integral and the approximate analysis of strain concentration by notches and cracks. Journal of Applied Mechanics 35 (2), 379–386.

Rivlin, R., Thomas, A. G., 1997. Rupture of rubber. i. characteristic energy for tearing. In: Collected Papers of RS Rivlin. Springer, pp. 2615–2642.

Rivlin, R. S., Thomas, A. G., 1952. Rupture of rubber. i. characteristic energy for tearing. Journal of Polymer Science X (3), 291–318.

Robertson, I. M., Sofronis, P., Nagao, A., Martin, M., Wang, S., Gross, D., Nygren, K., 2015. Hydrogen embrittlement understood. Metallurgical and Materials Transactions A 46 (6), 2323–2341.

Sakai, T., 2013. Gelation mechanism and mechanical properties of tetra-peg gel. Reactive & Functional Polymers 73 (7), 898–903.

San Marchi, C., Somerday, B., Robinson, S., 2007. Permeability, solubility and diffusivity of hydrogen isotopes in stainless steels at high gas pressures. International Journal of Hydrogen Energy 32 (1), 100–116.

Schapery, R., 1984. Correspondence principles and a generalizedj integral for large deformation and fracture analysis of viscoelastic media. International Journal of Fracture 25 (3), 195–223.

Schröder, J., Neff, P., 2003. Invariant formulation of hyperelastic transverse isotropy based on polyconvex free energy functions. International Journal of Solids and Structures 40, 401–445.

Sih, G. C., 2012. Mechanics of fracture initiation and propagation: surface and volume energy density applied as failure criterion. Vol. 11. Springer Science & Business Media.

Sih, G. C., Provan, J., 2013. Probabilistic fracture mechanics and reliability. Vol. 6. Springer Science & Business Media.

Slepyan, L. I., 2012. Models and phenomena in fracture mechanics. Springer Science & Business Media.

Smith, S. B., Cui, Y., Bustamente, C., 1996. Overstretching b-dna: the elastic response of individual double-stranded and single-stranded dna molecules. Science 271 (5250), 795.

Sofronis, P., McMeeking, R., 1989. Numerical analysis of hydrogen transport near a blunting crack tip. Journal of the Mechanics and Physics of Solids 37 (3), 317–350.

Song, J., Curtin, W., 2014. Mechanisms of hydrogen-enhanced localized plasticity: an atomistic study using α-fe as a model system. Acta Materialia 68, 61–69.

Srinivasan, R., Neeraj, T., 2014. Hydrogen embrittlement of ferritic steels: deformation and failure mechanisms and challenges in the oil and gas industry. JOM 66 (8), 1377–1382.

Talamini, B., Mao, Y., Anand, L., 2018. Progressive damage and rupture in polymers. Journal of the Mechanics and Physics of Solids 111, 434–457.

Tanaka, Y., 2007. A local damage model for anomalous high toughness of double-network gels. EPL (Europhysics Letters) 78 (5), 56005.

Tang, J., Li, J., Vlassak, J. J., Suo, Z., 2017. Fatigue fracture of hydrogels. Extreme Mechanics Letters 10, 24–31.

Taylor, D., 2010. The theory of critical distances: a new perspective in fracture mechanics. Elsevier.

Tehranchi, A., Zhang, X., Lu, G., Curtin, W., 2016. Hydrogen–vacancy–dislocation interactions in α-fe. Modelling and Simulation in Materials Science and Engineering 25 (2), 025001.

Thomas, A. G., 1955. Rupture of rubber. II. the strain concentration at an incision. Journal of Polymer science 18 (88), 177–188.

Tracey, D., 1976. Finite element solutions for crack-tip behavior in small-scale yielding. Journal of Engineering Materials and Technology 98 (2), 146–151.

Treloar, L. R. G., 1975. The physics of rubber elasticity. Oxford University Press, USA.

Troiano, A. R., 1960. The role of hydrogen and other interstitials in the mechanical behavior of metals. trans. ASM 52 (1), 54–80.

Wang, X., Hong, W., 2012. Delayed fracture in gels. Soft Matter 8, 8171.

Wang, Y., Li, J., 2010. Phase field modeling of defects and deformation. Acta Materialia 58 (4), 1212–1235.

Watson, S., 2015. Experimental characterization of a coupled deformation-diffusion theory for elastomeric materials. http://hdl.handle.net/1721.1/98753.

Xu, K., Rana, M., 2009. Tensile and fracture properties of carbon and low alloy steels in high pressure hydrogen. In: Proceedings of the 2008 International Hydrogen Conference. pp. 349–356.

Yamakawa, H., 1971. Modern theory of polymer solutions. Harper & Row.

Zhang, T., Lin, S., Yuk, H., Zhao, X., 2015. Predicting fracture energies and crack-tip fields of soft tough materials. Extreme Mechanics Letters 4, 1–8.

Zhao, X., 2014. Multi-scale multi-mechanism design of tough hydrogels: building dissipation into stretchy networks. Soft Matter 10 (5), 672–687.

Appendix A

Detailed derivation of the model for single polymer chain with stretchable Kuhn segments and crosslinks

We make the kinematic assumption that the overall deformation of the polymer chain under load is due to three sources,

(i) the alignment of the Kuhn segments in the chain under load,

(ii) stretching of the segments due to deformation of the constituent molecular bonds, and

(iii) stretching of the molecular bonds associated with ending crosslinks.

Figure A-1 illustrate the idea.

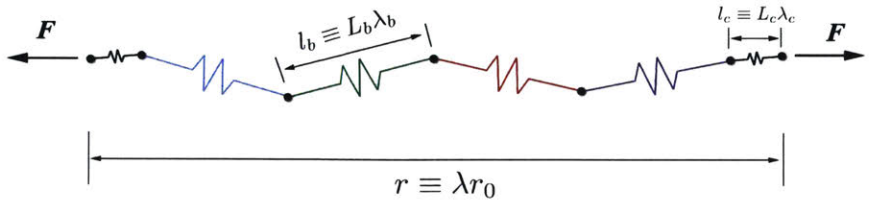

Figure A-1: Schematic for single chain with two ending cross-links. Overall, the length of the single chain is r and through the initial length r_0 we defined the stretch $\lambda \equiv r/r_0$. The Kuhn segments are assumed deformable due to deformation of the constituent bonds. The initial length of Kuhn segment is L_b while the deformed length is l_b, and the stretch is defined as $\lambda_b \equiv l_b/L_b$. Meanwhile, the two ending cross-links are assumed deformable. The initial length of cross-link bond is L_c while the deformed length is l_c, and the stretch is defined as $\lambda_c \equiv l_c/L_c$.

Consider a single chain with n Kuhn segments, each of initial length L_b. The current segment length l_b is related to the rest length L_b through $l_b = L_b\lambda_b$, where λ_b is a dimensionless stretch which we refer to as the *bond deformation stretch.* At the end of the single chain there are two ending crosslinks, with initial length L_c. The current segment length l_c is related to the rest length L_c through $l_c = L_c\lambda_c$, where λ_c is a dimensionless stretch which we refer to as the *deformation stretch of crosslinks.*

For simplification, we adopt the idea of freely-jointed chain, and neglect

(i) any possible interaction between segments and cross-links such as bond angle rotation, van der Waals interactions, etc., and

(ii) any kinetic effects such as the velocity dependent terms in Hamiltonian.

Using these simplifications, the Hamiltonian of the polymer chain with two ending cross-links simplify reads

$$\mathcal{H} = \sum_{i=1}^{n} \varepsilon_b^{(i)}(\lambda_b^{(i)}) + \sum_{i=1}^{2} \varepsilon_c^{(i)}(\lambda_c^{(i)}) \tag{A.1}$$

with

- n is the number of Kuhn segment.
- $\varepsilon_b^{(i)}(\cdot)$ is the potential for i^{th} Kuhn segment, and $\lambda_b^{(i)}$ is the stretch of i^{th} Kuhn segment.
- $\varepsilon_c^{(i)}(\cdot)$ is the potential for i^{th} cross-links, and $\lambda_c^{(i)}$ is the stretch of i^{th} cross-links.

At a certain time the force acts on two ends of polymer chain is $\mathbf{F}$, and the end-to-end vector reads $\mathbf{r}$. In the following derivation, we pick $\mathbf{F}$ as thermodynamics variable, and thus the partition function of the polymer chain is given by

$$Z(\mathbf{F}) = \sum_{\text{all states}} \exp\left(-(\mathcal{H} - \mathbf{F}\cdot\mathbf{r})/k_B\vartheta\right) \tag{A.2}$$

with ϑ is the absolute temperature. For simplicity and without lose the generality, we pick $\mathbf{F}$ along z-direction, and thus $\mathbf{F}\cdot\mathbf{r} = Fr_z$ with r_z is the separation of end-to-end in polymer chain in z-direction. Explicitly

$$r_z = \sum_{i=1}^{n} \mathbf{r}_b^{(i)}\cdot\mathbf{e}_z + \sum_{j=1}^{2} \mathbf{r}_c^{(j)}\cdot\mathbf{e}_z \tag{A.3}$$

Here $\mathbf{r}_b^{(i)}$ and $\mathbf{r}_c^{(i)}$ is the vector of Kuhn segment and cross-link bond, respectively. And $\mathbf{e}_z$ is the unit vector along z-direction. Since typically only one bond linked with one ending cross-link for each polymer chain, we can reasonably assume the projected length of bond linked with cross-link on z-direction is a constant, and marked it as L_c. Then

$$
\begin{aligned}
R_z &= \sum_i |\mathbf{r}^{(i)}| \cos\theta_i + \sum_{j=1}^{2} L_c^{(j)} \lambda_c^{(j)} \\
&= \sum_i L_b^{(i)} \lambda_b^{(i)} \cos\theta_i + \sum_{j=1}^{2} L_c^{(j)} \lambda_c^{(j)}
\end{aligned}
\tag{A.4}
$$

with

- θ_i is the angle between $\mathbf{r}^{(i)}$ and z-direction.
- $l_b^{(i)} = L_b^{(i)} \lambda_b^{(i)}$ is the length of i^{th} Kuhn segment after stretch and $L_b^{(i)}$ is the rest length of i^{th} Kuhn segment.
- $l_c^{(j)} = L_c^{(j)} \lambda_c^{(j)}$ is the length of j^{th} crosslinking bond after stretch and $L_c^{(j)}$ is the rest length of j^{th} crosslinking bond.

In the real materials, the typical value of $|L_b^{(i)}|$ is at the order of $\sim 10\text{Å}$ and $|L_c^{(j)}|$ is at the order of 1Å.

The summation for all states is the integration element $\prod_i 2\pi \sin\theta_i \mathrm{d}\lambda_b^{(i)} \mathrm{d}\theta_i \mathrm{d}\varphi_i$. By neglecting the constant pre-factor $\prod_i (4\pi^2)$ which only contributes a constant term to free energy (or partition function), then we have

$$
\begin{aligned}
Z &= \prod_{i=1}^{n} \int \mathrm{d}\lambda_b^{(i)} \sin\theta_i \mathrm{d}\theta_i \exp\left(-\frac{\varepsilon_b^{(i)}(\lambda_b^{(i)})}{k_B\vartheta} + \frac{F L_b^{(i)}}{k_B\vartheta} \lambda_b^{(i)} \cos\theta_i \right) \\
&\qquad \times \prod_{j=1}^{2} \int \mathrm{d}\lambda_c^{(j)} \exp\left(-\frac{\varepsilon_c^{(j)}(\lambda_c^{(j)})}{k_B\vartheta} + \frac{F L_c^{(j)}}{k_B\vartheta} \lambda_c^{(j)} \right) \\
&= \prod_i \int \mathrm{d}\lambda_b^{(i)} \exp\left(-\frac{\varepsilon_b^{(i)}(\lambda_b^{(i)})}{k_B\vartheta} + \ln\left[\frac{\sinh(F L_b^{(i)} \lambda_b^{(i)} / k_B\vartheta)}{F L_b^{(i)} \lambda_b^{(i)} / k_B\vartheta} \right] \right) \\
&\qquad \times \prod_{j=1}^{2} \int \mathrm{d}\lambda_c^{(j)} \exp\left(-\frac{\varepsilon_c^{(j)}(\lambda_c^{(j)})}{k_B\vartheta} + \frac{F L_c^{(j)}}{k_B\vartheta} \lambda_c^{(j)} \right)
\end{aligned}
\tag{A.5}
$$

In most of case, the expressions of $\varepsilon_b^{(i)}(\cdot)$ and $\varepsilon_c^{(j)}(\cdot)$ can be very complicated. Because of the possible complexity of these expressions, obtaining the closed and fully-analytic expression of this partition function is very hard. To obtained an approximated and closed form, we next construct the mean-field theory by considering the saddle point approximation. We

finally have

$$Z \approx \prod_i \sqrt{\frac{2\pi k_B\vartheta}{\varepsilon_b^{(i)\prime\prime}(\lambda_b^{(i)})}} \exp\left(-\frac{\varepsilon_b^{(i)}(\lambda_b^{(i)})}{k_B\vartheta} + \ln\left[\frac{\sinh(FL_b^{(i)}\lambda_b^{(i)}/k_B\vartheta)}{FL_b^{(i)}\lambda_b^{(i)}/k_B\vartheta}\right]\right) \times \prod_{j=1}^{2} \sqrt{\frac{2\pi k_B\vartheta}{\varepsilon_c^{(j)\prime\prime}(\lambda_c^{(j)})}} \exp\left(-\frac{\varepsilon_c^{(j)}(\lambda_c^{(j)})}{k_B\vartheta} + \frac{FL_c^{(j)}}{k_B\vartheta}\lambda_c^{(j)}\right). \tag{A.6}$$

Here $\varepsilon_b''(\lambda_b) = \frac{\mathrm{d}^2\varepsilon_b}{\mathrm{d}\lambda_b^2}$ and $\varepsilon_c''(\lambda_c) = \frac{\mathrm{d}^2\varepsilon_c}{\mathrm{d}\lambda_c^2}$. Physically, terms $\sqrt{\frac{2\pi k_B\vartheta}{\varepsilon_b^{(i)\prime\prime}(\lambda_b^{(i)})}}$ and $\sqrt{\frac{2\pi k_B\vartheta}{\varepsilon_c^{(j)\prime\prime}(\lambda_c^{(j)})}}$ come from the saddle point expansion. In expression (A.6) the $\lambda_b^{(i)}$ and $\lambda_c^{(j)}$ are stretches which optimize the probability. Both of them are determined by saddle point approximation. The equations to determine these stretches are

$$\varepsilon_b^{(i)\prime}(\lambda_b^{(i)}) - \left(\coth\left(\frac{FL_b^{(i)}\lambda_b^{(i)}}{k_B\vartheta}\right) - \frac{k_B\vartheta}{FL_b^{(i)}\lambda_b^{(i)}}\right) FL_b^{(i)} = 0 \tag{A.7}$$

and

$$\varepsilon_c^{(i)\prime}(\lambda_c^{(i)}) - FL_c^{(j)} = 0 \tag{A.8}$$

with $\varepsilon_b'(\lambda_b) = \frac{\mathrm{d}\varepsilon_b}{\mathrm{d}\lambda_b}$ and $\varepsilon_c'(\lambda_c) = \frac{\mathrm{d}\varepsilon_c}{\mathrm{d}\lambda_c}$.

With this approximated partition function, the total Gibbs-type free energy of the polymer chain with two ending cross-links reads

$$\begin{aligned} G(F) &= -k_B\vartheta \ln Z \\ &= \sum_{i=1}^{n}\left(\varepsilon_b^{(i)}(\lambda_b^{(i)}) + k_B\vartheta \ln\left[\frac{FL_b^{(i)}\lambda_b^{(i)}/k_B\vartheta}{\sinh(FL_b^{(i)}\lambda_b^{(i)}/k_B\vartheta)}\right] - k_B\vartheta \ln\sqrt{\frac{2\pi k_B\vartheta}{\varepsilon_b^{(i)\prime\prime}(\lambda_b^{(i)})}}\right) \\ &\quad + \sum_{j=1}^{2}\left(\varepsilon_c^{(j)}(\lambda_c^{(j)}) - FL_c^{(j)}\lambda_c^{(j)} - k_B\vartheta \ln\sqrt{\frac{2\pi k_B\vartheta}{\varepsilon_c^{(i)\prime\prime}(\lambda_c^{(i)})}}\right) \end{aligned} \tag{A.9}$$

and the end-to-end distance is

$$\begin{aligned} r = \langle r_z\rangle &= -\frac{\partial G}{\partial F} \\ &= \sum_{j=1}^{2} L_c^{(j)}\lambda_c^{(j)} + \sum_{i=1}^{n} L_b^{(i)}\lambda_b^{(i)}\left[\coth\left(\frac{FL_b^{(i)}\lambda_b^{(i)}}{k_B\vartheta}\right) - \frac{k_B\vartheta}{FL_b^{(i)}\lambda_b^{(i)}}\right] \end{aligned} \tag{A.10}$$

This physical explain for this expression of end-to-end distance is straightforward. The first term represents for the total length of crosslink bonds, and the second is the total length

of the Kuhn segments within the polymer chain. The second term also accounts for the contribution from rearrangeable configurations of Kuhn segments.

For most of cases, we can simplify the expression by assuming that

- Kuhn segments within the polymer chain are the same with each other (same rest length L_b and same stretch λ_b), and
- two crosslink bonds are the same with each other (same rest length L_c and same stretch λ_c).

These assumptions lead to simple form of Gibbs free energy,

$$\begin{aligned} G(F) = n\varepsilon_b(\lambda_b) + nk_B\vartheta \ln\left[\frac{FL_b\lambda_b/k_B\vartheta}{\sinh(FL_b\lambda_b/k_B\vartheta)}\right] - nk_B\vartheta \ln\sqrt{\frac{2\pi k_B\vartheta}{\varepsilon_b''(\lambda_b^\star)}} \\ + 2\varepsilon_c(\lambda_c) - 2FL_c\lambda_c - 2k_B\vartheta \ln\sqrt{\frac{2\pi k_B\vartheta}{\varepsilon_c''(\lambda_c)}}, \end{aligned} \tag{A.11}$$

and end-to-end distance,

$$r = 2L_c\lambda_c + nL_b\lambda_b\left[\coth\left(\frac{FL_b\lambda_b}{k_B\vartheta}\right) - \frac{k_B\vartheta}{FL_b\lambda_b}\right] \tag{A.12}$$

We can translate this Gibbs free energy to the corresponding Helmholtz free energy by changing the ensemble, and the Helmholtz free energy $\psi(r)$ reads,

$$\psi(r) = G(\mathbf{F}) + \mathbf{F}\cdot\mathbf{r} = G(F) + Fr, \tag{A.13}$$

and by using (A.11) and (A.12),[1] we finally have

$$\begin{aligned} \psi(r) = n\varepsilon_b(\lambda_b) + 2\varepsilon_c(\lambda_c) + nk_B\vartheta\left[\ln\left(\frac{\beta}{\sinh\beta}\right) + \beta\frac{r-2L_c\lambda_c}{nL_b\lambda_b}\right] \\ - 2k_B\vartheta\ln\sqrt{\frac{2\pi k_B\vartheta}{\varepsilon_c''(\lambda_c)}} - nk_B\vartheta\ln\sqrt{\frac{2\pi k_B\vartheta}{\varepsilon_b''(\lambda_b)}}, \end{aligned} \tag{A.14}$$

with

$$\beta = \mathcal{L}^{-1}\left(\frac{r-2L_c\lambda_c}{nL_b\lambda_b}\right), \tag{A.15}$$

[1] We also need to use the reversed version of equation (A.12), which gives

$$\frac{FL_b\lambda_b}{k_B\vartheta} = \mathcal{L}^{-1}\left(\frac{r-2L_c\lambda_c}{nL_b\lambda_b}\right) \equiv \beta.$$

and $\mathcal{L}(x) = \coth(x) - 1/x$ is the Langevin function. Most of case, the final two terms from saddle point expansion are not important. So we can simplify the Helmholtz free energy as

$$\psi(r) = n\varepsilon_b(\lambda_b) + 2\varepsilon_c(\lambda_c) + nk_B\vartheta\left[\ln\left(\frac{\beta}{\sinh\beta}\right) + \beta\frac{r - 2L_c\lambda_c}{nL_b\lambda_b}\right]. \tag{A.16}$$

with β is in equation (A.15).

The stretches λ_b and λ_c can be determined by equations (A.7) and (A.8). With the assumptions that all Kuhn segments are the same and the two crosslinks are the same within the single chain, we can simplify them as

$$\frac{\varepsilon_b'(\lambda_b)}{k_B\vartheta} - \left(\frac{r - 2L_c\lambda_c}{nL_b\lambda_b}\right)\frac{\beta}{\lambda_b} = 0 \tag{A.17}$$

and

$$\frac{\varepsilon_c'(\lambda_c)}{k_B\vartheta} - \left(\frac{L_c}{L_b}\right)\frac{\beta}{\lambda_b} = 0 \tag{A.18}$$

From definition, the force is given by

$$F = \frac{k_B\vartheta}{L_b\lambda_b}\beta \tag{A.19}$$

For a specific polymer chain (fixing n, L_c, L_b, $\varepsilon_b(\lambda_b)$, and $\varepsilon_c(\lambda_c)$), at any given end-to-end distance r, the λ_b and λ_c can be solved from (A.17) and (A.18), and thus the reaction force at the end of the polymer chain F can be determined. However, it is convenient to rewrite the free energy (A.16) in terms of the overall chain stretch λ instead of r. The overall chain stretch is defined as

$$\lambda = \frac{r}{r_0}, \tag{A.20}$$

where r_0, the unstretched chain length, which is now given by

$$r_0 = \sqrt{n}L_b + 2L_c. \tag{A.21}$$

From definition $r = \lambda(\sqrt{n}L_b + 2L_c)$ where λ is the overall stretch of the polymer chain with the ending cross-links and $\sqrt{n}L$ is the radius of gyration from random walk. For most of the case that we are interested in $\sqrt{n}L_b \gg 2L_c$ then $r \approx \lambda\sqrt{n}L_b$. Then

$$\begin{aligned}\psi(r) =& n\varepsilon_b(\lambda_b) + 2\varepsilon_c(\lambda_c) + nk_B\vartheta\left[\ln\left(\frac{\beta}{\sinh\beta}\right) + \left(\frac{\lambda}{\sqrt{n}\lambda_b} - \frac{2L_c\lambda_c}{nL_b\lambda_b}\right)\beta\right] \\ &\text{with } \beta = \mathcal{L}^{-1}\left(\frac{\lambda}{\sqrt{n}\lambda_b} - \frac{2L_c\lambda_c}{nL_b\lambda_b}\right)\end{aligned} \tag{A.22}$$

and λ_b and λ_c are determined by

$$\frac{\varepsilon_b'(\lambda_b)}{k_B\vartheta} = \left(\frac{\lambda}{\sqrt{n}\lambda_b} - \frac{2L_c\lambda_c}{nL_b\lambda_b}\right)\frac{\beta}{\lambda_b}; \quad \frac{\varepsilon_c'(\lambda_c)}{k_B\vartheta} = \left(\frac{L_c}{L_b}\right)\frac{\beta}{\lambda_b}. \tag{A.23}$$

As it stands, the contribution from the change in entropy to the free energy in (A.22) does not reduce to the classical freely joint chain expression in the limit $\lambda_c \to 1$. To achieve this we require that $\hat{\varepsilon}_c(1) = 0$ and modify (A.22) to read as, [2]

$$\begin{aligned}\psi(r) =& n\varepsilon_b(\lambda_b) + 2\varepsilon_c(\lambda_c) + nk_B\vartheta\left[\ln\left(\frac{\beta}{\sinh\beta}\right) + \left(\frac{\lambda}{\sqrt{n}\lambda_b} - \frac{2(\lambda_c-1)L_c}{nL_b\lambda_b}\right)\beta\right] \\ &\text{with } \beta = \mathcal{L}^{-1}\left(\frac{\lambda}{\sqrt{n}\lambda_b} - \frac{2(\lambda_c-1)L_c}{nL_b\lambda_b}\right)\end{aligned} \tag{A.24}$$

and λ_b and λ_c are determined by

$$\frac{\varepsilon_b'(\lambda_b)}{k_B\vartheta} = \left(\frac{\lambda}{\sqrt{n}\lambda_b} - \frac{2(\lambda_c-1)L_c}{nL_b\lambda_b}\right)\frac{\beta}{\lambda_b}; \quad \frac{\varepsilon_c'(\lambda_c)}{k_B\vartheta} = \left(\frac{L_c}{L_b}\right)\frac{\beta}{\lambda_b}. \tag{A.25}$$

The force is given as

$$F = \frac{k_B\vartheta}{L_b\lambda_b}\beta = \frac{k_B\vartheta}{L_b\lambda_b}\mathcal{L}^{-1}\left(\frac{\lambda}{\sqrt{n}\lambda_b} - \frac{2(\lambda_c-1)L_c}{nL_b\lambda_b}\right). \tag{A.26}$$

Let's consider two extremes: purely Kuhn segment stretch and purely cross-link stretch.

1. Purely Kuhn segment stretch. In this case $\lambda_c \equiv 1$, and the second equation in (A.25) does not exist. With these setup, all equations degenerate into the case that we discussed in Chapter 3.

2. Purely cross-link stretch. In this case $\lambda_b \equiv 1$, and the first equation in (A.25) does not exist. With these setup, all equations degenerate into the case that we discussed in section 5.3, Chapter 5.

[2]This step can be physically understood as refine of n, or omiting all entropy part from crosslink bonds.

Appendix B

Numerical implementation of the theory for fracture of polymeric gels

We build our application "Parakeet" based on MOOSE(Gaston et al., 2009). For more details on the MOOSE framework, please refer to its documentation. In this section, we display how to implement our coupled deformation-diffusion-damage theory of fracture in polymeric gels. In (C.1) we show how the solve c_{R} and λ_b from degrees of freedom. In (C.2)-(B.4) we display the Residuals and the corresponding Jacobians for each DOFs.

For simplicity, in this section we define $\lambda_{\mathrm{L}} = \sqrt{n}$, $r = \frac{\bar{\lambda}}{\lambda_{\mathrm{L}}\lambda_b}$, and $r_0 = \frac{1}{\lambda_{\mathrm{L}}\lambda_b}$. Note that the parameters r and r_0 defined here are not related to the rest length and deformed length of a single chain.

B.1 Solve ϕ and λ_b from DOFs

First of all in the class we need to calculate λ_b and c_{R} from the evolution equation of λ_b, and expression of chemical potential μ. In our specific theory, these two equations are displayed as follows,

$$g(d)\frac{N}{G_0}\frac{\partial\hat{\varepsilon}_b}{\partial\lambda_b} - \frac{\bar{\lambda}}{\lambda_L{\lambda_b}^2}\beta + \frac{1}{3}\frac{{\lambda_b}^{-2}}{\lambda_L}\left(\beta_0 + \frac{\partial\beta_0}{\partial r_0}\frac{1}{\lambda_L\lambda_b}\right)\ln J = -\frac{\xi_b{\lambda_b}^{-4}}{G_0 n}\dot{\lambda}_b \tag{B.1}$$

$$\mu = \mu_0 + R\vartheta\left[\ln(1-\phi) + \phi + \chi\phi^2\right] - g(d)\Omega J^{s-1}\left[J^e\frac{\partial\hat{\varepsilon}_{\mathrm{vol}}}{\partial J^e}\right] \tag{B.2}$$

with $\hat{\varepsilon}_b$ and $\hat{\varepsilon}_{\text{vol}}$ for the constitutive expressions of bond stretch and the volumetric part, respectively. β and β_0 are both function of r, which are

$$\beta = \mathcal{L}^{-1}(r), \quad \beta_0 = \mathcal{L}^{-1}(r_0) \tag{B.3}$$

with $\mathcal{L}(x) = \coth(x) - 1/x$ is the Langevin function. $g(d) = (1-d)^2$ is the degradation function.

Numerically, these two equations can be rewritten as

$$f_1 = g(d)\frac{\bar{E}}{G_0 n}\frac{\mathrm{d}\tilde{\varepsilon}_b(\lambda_b)}{\mathrm{d}\lambda_b}\lambda_b - r\beta + \frac{1}{3}\left(r_0\beta_0 + r_0^2\frac{\partial\beta_0}{\partial r_0}\right)\ln J + \frac{\xi_b{\lambda_b}^{-3}}{G_0 n}\dot{\lambda}_b = 0, \tag{B.4}$$

$$f_2 = \mu_0 + R\vartheta\left[\ln(1-\phi) + \phi + \chi\phi^2\right] - g(d)\Omega\frac{\phi}{\phi_0}\left[J^e\frac{\partial\hat{\varepsilon}_{\text{vol}}}{\partial J^e}\right] - \mu = 0 \tag{B.5}$$

with $\tilde{\varepsilon}_b = \hat{\varepsilon}_b/E_b$ is the normalized internal energy, and $\bar{E} = nNE_b$.

Let us first examine f_1. f_1 can be treated as a function of λ_b, $\bar{\lambda}$, J, and $\dot{\lambda}_b$. If we give a history of λ_b, within the incremental step, we can solve λ_b from equation $f_1 = 0$ numerically. Next let us focus on f_2. From our theory, $J^e = J\phi/\phi_0$, with $J = \det\mathbf{F}$ is the determinate of deformation gradient $\mathbf{F}$. Then $f_2 = \hat{f}_2(\phi, \mu, J, d)$. With the incremental step, ϕ can be solved from $f_2 = 0$ numerically. This highlights these two equations are *decoupled*, which simplifies our coding a lot.

However, $\lambda_b \in [1, \infty)$, which is not very suitable for numerical purpose. Instead of treating f_1 as function of λ_b, $\bar{\lambda}$, J, and $\dot{\lambda}_b$, we can choose r as the unknown of f_1. During the numerical procedure, we need know $\frac{\mathrm{d}f_1}{\mathrm{d}r}$, which is

$$\begin{aligned}\frac{\mathrm{d}f_1}{\mathrm{d}r} =& g(d)\frac{\bar{E}}{G_0 n}\left(\frac{\mathrm{d}\tilde{\varepsilon}_b}{\mathrm{d}\lambda_b} + \frac{\mathrm{d}^2\tilde{\varepsilon}_b}{\mathrm{d}{\lambda_b}^2}\lambda_b\right)\frac{\partial\lambda_b}{\partial r} - \left(\beta + r\frac{\partial\beta}{\partial r}\right) \\ &+ \frac{\ln J}{3}\left[\beta_0 + 3r_0\frac{\partial\beta_0}{\partial r_0} + r_0^2\frac{\partial^2\beta_0}{\partial r_0^2}\right]\frac{\partial r_0}{\partial r} + \frac{\xi_b{\lambda_b}^{-4}}{G_0 n}\left(-3\dot{\lambda}_b + \lambda_b\frac{\partial\dot{\lambda}_b}{\partial\lambda_b}\right)\frac{\partial\lambda_b}{\partial r}.\end{aligned} \tag{B.6}$$

Recall that $\lambda_b = \frac{\bar{\lambda}}{\lambda_L r} = \frac{1}{\lambda_L r_0}$ then we have

$$\frac{\partial\lambda_b}{\partial r} = -\frac{\bar{\lambda}}{\lambda_L r^2}, \quad \frac{\partial r_0}{\partial r} = \frac{1}{\bar{\lambda}}. \tag{B.7}$$

Thus $\frac{\mathrm{d}f_1}{\mathrm{d}r}$ can be written as,

$$\begin{aligned}\frac{\mathrm{d}f_1}{\mathrm{d}r} =& -g(d)\frac{E}{G_0}\left(\frac{\mathrm{d}\tilde{\varepsilon}_b}{\mathrm{d}\lambda_b}+\frac{\mathrm{d}^2\tilde{\varepsilon}_b}{\mathrm{d}{\lambda_b}^2}\lambda_b\right)\frac{\bar{\lambda}}{\lambda_L r^2}-\left(\beta+r\frac{\partial\beta}{\partial r}\right)\\ &+\frac{\ln J}{3\bar{\lambda}}\left[\beta_0+3r_0\frac{\partial\beta_0}{\partial r_0}+r_0^2\frac{\partial^2\beta_0}{\partial r_0^2}\right]+\frac{\xi_b{\lambda_b}^{-4}}{G_0 n}\left(3\dot{\lambda}_b-\lambda_b\frac{\partial\dot{\lambda}_b}{\partial\lambda_b}\right)\frac{\bar{\lambda}}{\lambda_L r^2}\end{aligned} \tag{B.8}$$

Simply, we have

$$\frac{\mathrm{d}f_2}{\mathrm{d}\phi} = R\vartheta\left(\frac{-1}{1-\phi}+1+2\chi\phi\right)-g(d)\Omega\frac{J^e}{\phi_0}\left[\frac{\mathrm{d}^2\hat{\varepsilon}_{\mathrm{vol}}}{\mathrm{d}J^{e2}}J^e+2\frac{\mathrm{d}\hat{\varepsilon}_{\mathrm{vol}}}{\mathrm{d}J^e}\right] \tag{B.9}$$

B.2 Residuals and Jacobians on displacements DOFs

Neglecting body force and possible tractions, we have the residual for the displacements (ψ^A is the test function):

$$R_i^A = -\int_{B^e}\psi^A \mathrm{Div}\,\mathbf{T}_{\mathrm{R}}\mathrm{d}v_{\mathrm{R}} = \int_{B^e}(T_{\mathrm{R}})_{im}\cdot\nabla_m\psi^A\mathrm{d}v_{\mathrm{R}} \equiv \left(\nabla_m\psi^A,(T_{\mathrm{R}})_{im}\right) \tag{B.10}$$

The Jacobians are (ϕ with the superscript is the test function here)

$$\begin{aligned}K_{ij}^{AB} &= \left(\nabla_m\psi^A,\left.\frac{\partial(T_{\mathrm{R}})_{im}}{\partial F_{j\beta}}\right|_{\mu,d}\nabla_\beta\phi^B\right);\\ K_{i\mu}^{AB} &= \left(\nabla_m\psi^A,\left.\frac{\partial(T_{\mathrm{R}})_{im}}{\partial \mu}\right|_{\mathbf{F},d}\phi^B\right);\\ K_{id}^{AB} &= \left(\nabla_m\psi^A,\left.\frac{\partial(T_{\mathrm{R}})_{im}}{\partial d}\right|_{\mathbf{F},\mu}\phi^B\right).\end{aligned} \tag{B.11}$$

By considering $\mathbf{T}_{\mathrm{R}}$ is a function of $(\mathbf{F}, c_{\mathrm{R}}(\mathbf{F},\mu,d), \lambda_b(\mathbf{F},d), d)$ in our case, then by using the chain rule, we then have

$$\begin{aligned}\left.\frac{\partial(T_{\mathrm{R}})_{im}}{\partial F_{j\beta}}\right|_{\mu,d} =& \left.\frac{\partial(T_{\mathrm{R}})_{im}}{\partial F_{j\beta}}\right|_{c_{\mathrm{R}},\lambda_b,d}+\left.\frac{\partial(T_{\mathrm{R}})_{im}}{\partial c_{\mathrm{R}}}\right|_{\mathbf{F},\lambda_b,d}\left.\frac{\partial c_{\mathrm{R}}}{\partial F_{j\beta}}\right|_{\mu,d}\\ &+\left.\frac{\partial(T_{\mathrm{R}})_{im}}{\partial \lambda_b}\right|_{\mathbf{F},c_{\mathrm{R}},d}\left.\frac{\partial \lambda_b}{\partial F_{j\beta}}\right|_{d}\end{aligned} \tag{B.12}$$

$$\left.\frac{\partial(T_{\mathrm{R}})_{im}}{\partial \mu}\right|_{\mathbf{F},d} = \left.\frac{\partial(T_{\mathrm{R}})_{im}}{\partial c_{\mathrm{R}}}\right|_{\mathbf{F},\lambda_b,d}\left.\frac{\partial c_{\mathrm{R}}}{\partial \mu}\right|_{\mathbf{F},d} \tag{B.13}$$

$$\left.\frac{\partial (T_{\mathrm{R}})_{im}}{\partial d}\right|_{\mathbf{F},\mu} = \left.\frac{\partial (T_{\mathrm{R}})_{im}}{\partial d}\right|_{\mathbf{F},c_{\mathrm{R}},\lambda_b} + \left.\frac{\partial (T_{\mathrm{R}})_{im}}{\partial c_{\mathrm{R}}}\right|_{\mathbf{F},\lambda_b,d} \left.\frac{\partial c_{\mathrm{R}}}{\partial d}\right|_{\mathbf{F},\mu} + \left.\frac{\partial (T_{\mathrm{R}})_{im}}{\partial \lambda_b}\right|_{\mathbf{F},c_{\mathrm{R}},d} \left.\frac{\partial \lambda_b}{\partial d}\right|_{\mathbf{F}} \tag{B.14}$$

The four terms

$$\left.\frac{\partial (T_{\mathrm{R}})_{im}}{\partial F_{j\beta}}\right|_{c_{\mathrm{R}},\lambda_b,d}; \quad \left.\frac{\partial (T_{\mathrm{R}})_{im}}{\partial c_{\mathrm{R}}}\right|_{\mathbf{F},\lambda_b,d}; \quad \left.\frac{\partial (T_{\mathrm{R}})_{im}}{\partial \lambda_b}\right|_{\mathbf{F},c_{\mathrm{R}},d}; \quad \left.\frac{\partial (T_{\mathrm{R}})_{im}}{\partial d}\right|_{\mathbf{F},c_{\mathrm{R}},\lambda_b} \tag{B.15}$$

are all very easy to obtain. And the expressions are as follows:

$$\begin{aligned}
\left.\frac{\partial (T_{\mathrm{R}})_{im}}{\partial F_{j\beta}}\right|_{c_{\mathrm{R}},\lambda_b,d} &= \bar{G}\delta_{ij}\delta_{m\beta} + \bar{G}_0 (F^{-1})_{\beta i}(F^{-1})_{mj} - g(d)J^e \frac{\mathrm{d}\hat{\varepsilon}_{\mathrm{vol}}}{\mathrm{d}J^e}(F^{-1})_{\beta i}(F^{-1})_{mj} \\
&\quad + g(d)J^e \left[\frac{\mathrm{d}\hat{\varepsilon}_{\mathrm{vol}}}{\mathrm{d}J^e} + J^e \frac{\mathrm{d}^2\hat{\varepsilon}_{\mathrm{vol}}}{\mathrm{d}J^{e2}}\right](F^{-1})_{\beta j}(F^{-1})_{mi} + \frac{\partial \bar{G}}{\partial F_{j\beta}} F_{im} \\
\left.\frac{\partial (T_{\mathrm{R}})_{im}}{\partial c_{\mathrm{R}}}\right|_{\mathbf{F},\lambda_b,d} &= -g(d)\Omega J^e \frac{\phi}{\phi_0}\left[\frac{\mathrm{d}\hat{\varepsilon}_{\mathrm{vol}}}{\mathrm{d}J^e} + J^e \frac{\mathrm{d}^2\hat{\varepsilon}_{\mathrm{vol}}}{\mathrm{d}J^{e2}}\right](F^{-1})_{mi} \\
\left.\frac{\partial (T_{\mathrm{R}})_{im}}{\partial \lambda_b}\right|_{\mathbf{F},c_{\mathrm{R}},d} &= \frac{\partial \bar{G}}{\partial \lambda_b} F_{im} - \frac{\partial \bar{G}_0}{\partial \lambda_b}(F^{-1})_{mi} \\
\left.\frac{\partial (T_{\mathrm{R}})_{im}}{\partial d}\right|_{\mathbf{F},c_{\mathrm{R}},\lambda_b} &= g'(d)J^e \frac{\partial \hat{\varepsilon}_{\mathrm{vol}}}{\partial J^e}(F^{-1})_{mi}
\end{aligned} \tag{B.16}$$

with

$$\begin{aligned}
\frac{\partial \bar{G}}{\partial F_{j\beta}} &= \bar{G}\bar{\lambda}^{-1}\left[-1 + \frac{r}{\beta}\frac{\partial \beta}{\partial r}\right]\frac{\partial \bar{\lambda}}{\partial F_{j\beta}}, \\
\frac{\partial \bar{\lambda}}{\partial F_{j\beta}} &= \frac{1}{3\bar{\lambda}} F_{j\beta}, \\
\frac{\partial \bar{G}}{\partial \lambda_b} &= -\bar{G}{\lambda_b}^{-1}\left(1 + \frac{r}{\beta}\frac{\partial \beta}{\partial r}\right), \\
\frac{\partial \bar{G}_0}{\partial \lambda_b} &= -\bar{G}_0{\lambda_b}^{-1}\left(1 + \frac{r_0}{\beta_0}\frac{\partial \beta_0}{\partial r_0}\right),
\end{aligned} \tag{B.17}$$

and $g'(d) = -2(1-d)$.

In addition, we also need to know the following five terms.

$$\left.\frac{\partial \lambda_b}{\partial F_{j\beta}}\right|_{d}; \quad \left.\frac{\partial \lambda_b}{\partial d}\right|_{\mathbf{F}}; \quad \left.\frac{\partial c_{\mathrm{R}}}{\partial F_{j\beta}}\right|_{\mu,d}; \quad \left.\frac{\partial c_{\mathrm{R}}}{\partial \mu}\right|_{\mathbf{F},d}; \quad \left.\frac{\partial c_{\mathrm{R}}}{\partial d}\right|_{\mathbf{F},\mu} \tag{B.18}$$

In order to obtain the first two terms,

$$\left.\frac{\partial \lambda_b}{\partial F_{j\beta}}\right|_d ; \quad \left.\frac{\partial \lambda_b}{\partial d}\right|_{\mathbf{F}} \tag{B.19}$$

we first take derivatives on the equation (B.4). Then we have,

$$\begin{aligned}
&\left[\left(\beta + r\frac{\partial \beta}{\partial r}\right)\frac{\partial r}{\partial \bar{\lambda}}\frac{\partial \bar{\lambda}}{\partial F_{j\beta}} - \frac{1}{3}\left(r_0\beta_0 + r_0^2\frac{\partial \beta_0}{\partial r_0}\right)\frac{\partial \ln J}{\partial F_{j\beta}}\right] \mathrm{d}F_{j\beta} \\
&+\left[\left(\beta + r\frac{\partial \beta}{\partial r}\right)\frac{\partial r}{\partial \lambda_b} - g(d)\frac{\bar{E}}{G_0 n}\left(\frac{\mathrm{d}^2\tilde{\varepsilon}_{\mathrm{b}}}{\mathrm{d}{\lambda_b}^2}\lambda_b + \frac{\mathrm{d}\tilde{\varepsilon}_{\mathrm{b}}}{\mathrm{d}\lambda_b}\right)\right. \\
&\quad \left.+\frac{r_0}{3\lambda_b}\left(\beta_0 + 3r_0\frac{\partial \beta_0}{\partial r_0} + r_0^2\frac{\partial^2 \beta_0}{\partial r_0^2}\right)\ln J - \frac{\xi_b {\lambda_b}^{-4}}{G_0 n}\left(-3\dot{\lambda}_b + \lambda_b\frac{\partial \dot{\lambda}_b}{\partial \lambda_b}\right)\right] \mathrm{d}\lambda_b \\
&-g'(d)\frac{\bar{E}}{G_0 n}\frac{\mathrm{d}\tilde{\varepsilon}_{\mathrm{b}}}{\mathrm{d}\lambda_b}\lambda_b \,\mathrm{d}d = 0
\end{aligned} \tag{B.20}$$

which can be simply written as $A_{j\beta}\mathrm{d}F_{j\beta} + B\mathrm{d}\lambda_b + C\mathrm{d}d = 0$. Then

$$\begin{aligned}
\left.\frac{\partial \lambda_b}{\partial F_{j\beta}}\right|_d &= -B^{-1}A_{j\beta}, \\
\left.\frac{\partial \lambda_b}{\partial d}\right|_{\mathbf{F}} &= -B^{-1}C,
\end{aligned} \tag{B.21}$$

with

$$\begin{aligned}
A_{j\beta} &= \left(\beta + r\frac{\partial \beta}{\partial r}\right)\frac{\partial r}{\partial \bar{\lambda}}\frac{\partial \bar{\lambda}}{\partial F_{j\beta}} - \frac{1}{3}\left(r_0\beta_0 + r_0^2\frac{\partial \beta_0}{\partial r_0}\right)\frac{\partial \ln J}{\partial F_{j\beta}} \\
B &= \left(\beta + r\frac{\partial \beta}{\partial r}\right)\frac{\partial r}{\partial \lambda_b} - g(d)\frac{\bar{E}}{G_0 n}\left(\frac{\mathrm{d}^2\tilde{\varepsilon}_{\mathrm{b}}}{\mathrm{d}{\lambda_b}^2}\lambda_b + \frac{\mathrm{d}\tilde{\varepsilon}_{\mathrm{b}}}{\mathrm{d}\lambda_b}\right) \\
&\quad + \frac{r_0}{3\lambda_b}\left(\beta_0 + 3r_0\frac{\partial \beta_0}{\partial r_0} + r_0^2\frac{\partial^2 \beta_0}{\partial r_0^2}\right)\ln J - \frac{\xi_b {\lambda_b}^{-4}}{G_0 n}\left(-3\dot{\lambda}_b + \lambda_b\frac{\partial \dot{\lambda}_b}{\partial \lambda_b}\right), \\
C &= -g'(d)\frac{\bar{E}}{G_0 n}\frac{\mathrm{d}\tilde{\varepsilon}_{\mathrm{b}}}{\mathrm{d}\lambda_b}\lambda_b.
\end{aligned} \tag{B.22}$$

The remaining three terms

$$\left.\frac{\partial c_{\mathrm{R}}}{\partial F_{j\beta}}\right|_{\mu,d} ; \quad \left.\frac{\partial c_{\mathrm{R}}}{\partial \mu}\right|_{\mathbf{F},d} ; \quad \left.\frac{\partial c_{\mathrm{R}}}{\partial d}\right|_{\mathbf{F},\mu} \tag{B.23}$$

can be obtained from taking derivatives on the equation (B.5), which reads as

$$\mathrm{d}\mu = \left.\frac{\partial \mu}{\partial c_{\mathrm{R}}}\right|_{d,\mathbf{F}} \mathrm{d}c_{\mathrm{R}} + \left.\frac{\partial \mu}{\partial d}\right|_{c_{\mathrm{R}},\mathbf{F}} \mathrm{d}d + \left.\frac{\partial \mu}{\partial F_{j\beta}}\right|_{c_{\mathrm{R}},d} \mathrm{d}F_{j\beta}. \tag{B.24}$$

This equation gives us

$$\begin{aligned}
\left.\frac{\partial c_{\mathrm{R}}}{\partial F_{j\beta}}\right|_{\mu,d} &= -\left(\left.\frac{\partial \mu}{\partial c_{\mathrm{R}}}\right|_{d,\mathbf{F}}\right)^{-1} \left.\frac{\partial \mu}{\partial F_{j\beta}}\right|_{c_{\mathrm{R}},d}, \\
\left.\frac{\partial c_{\mathrm{R}}}{\partial \mu}\right|_{\mathbf{F},d} &= \left(\left.\frac{\partial \mu}{\partial c_{\mathrm{R}}}\right|_{d,\mathbf{F}}\right)^{-1}, \\
\left.\frac{\partial c_{\mathrm{R}}}{\partial d}\right|_{\mathbf{F},\mu} &= -\left(\left.\frac{\partial \mu}{\partial c_{\mathrm{R}}}\right|_{d,\mathbf{F}}\right)^{-1} \left.\frac{\partial \mu}{\partial d}\right|_{c_{\mathrm{R}},\mathbf{F}}.
\end{aligned} \tag{B.25}$$

Within these expressions, we need know

$$\left.\frac{\partial \mu}{\partial c_{\mathrm{R}}}\right|_{d,\mathbf{F}}, \quad \left.\frac{\partial \mu}{\partial d}\right|_{c_{\mathrm{R}},\mathbf{F}}, \quad \left.\frac{\partial \mu}{\partial F_{j\beta}}\right|_{c_{\mathrm{R}},d}. \tag{B.26}$$

These terms can be easily read from equation (B.5) as

$$\begin{aligned}
\left.\frac{\partial \mu}{\partial F_{j\beta}}\right|_{c_{\mathrm{R}},d} &= -g(d)\Omega_{\mathrm{R}} J^{s-2}\left[\frac{\mathrm{d}^2\hat{\varepsilon}_{\mathrm{vol}}}{\mathrm{d}J^{e2}} J^e + \frac{\mathrm{d}\hat{\varepsilon}_{\mathrm{vol}}}{\mathrm{d}J^e}\right]\frac{\partial J}{\partial F_{j\beta}} \\
\left.\frac{\partial \mu}{\partial c_{\mathrm{R}}}\right|_{d,\mathbf{F}} &= \frac{\mathrm{d}f_2}{\mathrm{d}\phi}\frac{\partial \phi}{\partial c_{\mathrm{R}}} \\
\left.\frac{\partial \mu}{\partial d}\right|_{c_{\mathrm{R}},\mathbf{F}} &= -g'(d)\Omega_{\mathrm{R}} J^{s-1}\left[\frac{\partial \hat{\varepsilon}_{\mathrm{vol}}}{\partial J^e} J^e\right]
\end{aligned} \tag{B.27}$$

B.3 Residuals and Jacobians on chemical potential DOFs

The mass conservation in the reference configuration and the Fickean type law read

$$\dot{c}_{\mathrm{R}} = -\mathrm{Div}\,\mathbf{j}_{\mathrm{R}}; \quad \mathbf{j}_{\mathrm{R}} = -\mathbf{M}\nabla\mu \tag{B.28}$$

with $\mathbf{M}$ is the mobility tensor which defined as the diffusivity multiple the concentration in the simplest case.

For the diffusion equation, we have the residual

$$R^A_\mu = -\left(\psi^A, \dot{c}_{\mathrm{R}}\right) - \left(\nabla_\alpha \psi^A, M_{\alpha\gamma}\nabla_\gamma \mu\right) - \left\langle \psi^A, \mathbf{j}_{\mathrm{R}} \cdot \mathbf{n}_{\mathrm{R}} \right\rangle \tag{B.29}$$

For the case without surface flux,

$$
\begin{aligned}
K^{AB}_{\mu j} &= -\left(\psi^A, \left.\frac{\partial \dot{c}_{\mathrm{R}}}{\partial F_{j\beta}}\right|_{\mu,d} \nabla_\beta \phi^B\right) - \left(\nabla_\alpha \psi^A, \left[\left.\frac{\partial M_{\alpha\gamma}}{\partial c_{\mathrm{R}}}\frac{\partial c_{\mathrm{R}}}{\partial F_{j\beta}}\right|_{\mu,d} + \left.\frac{\partial M_{\alpha\gamma}}{\partial F_{j\beta}}\right|_{c_{\mathrm{R}},d}\right] \nabla_\beta \phi^B \nabla_\gamma \mu\right) \\
K^{AB}_{\mu\mu} &= -\left(\psi^A, \left.\frac{\partial \dot{c}_{\mathrm{R}}}{\partial \mu}\right|_{\mathbf{u},d} \phi^B\right) - \left(\nabla_\alpha \psi^A, \frac{\partial M_{\alpha\gamma}}{\partial c_{\mathrm{R}}}\left.\frac{\partial c_{\mathrm{R}}}{\partial \mu}\right|_{\mathbf{u},d} \phi^B \nabla_\gamma \mu + M_{\alpha\gamma}\nabla_\gamma \phi^B\right) \\
K^{AB}_{\mu d} &= -\left(\psi^A, \left.\frac{\partial \dot{c}_{\mathrm{R}}}{\partial d}\right|_{\mu,\mathbf{u}} \phi^B\right) - \left(\nabla_\alpha \psi^A, \left[\left.\frac{\partial M_{\alpha\gamma}}{\partial c_{\mathrm{R}}}\frac{\partial c_{\mathrm{R}}}{\partial d}\right|_{\mu,\mathbf{u}} + \left.\frac{\partial M_{\alpha\gamma}}{\partial d}\right|_{\mathbf{u},c_{\mathrm{R}}}\right] \phi^B \nabla_\gamma \mu\right)
\end{aligned}
\tag{B.30}
$$

The approximation for terms related with $\dot{c}_{\mathrm{R}}$ depends on the time integration scheme. For example, in backward Euler integration scheme, $\left.\frac{\partial \dot{c}_{\mathrm{R}}}{\partial F_{j\beta}}\right|_{\mu,d} = \frac{1}{\Delta t}\left.\frac{\partial c_{\mathrm{R}}}{\partial F_{j\beta}}\right|_{\mu,d}$ with Δt is the time-step.

For the surface flux term, we use a simple one $\mathbf{j}_{\mathrm{R}} \cdot \mathbf{n}_{\mathrm{R}} = -\kappa(\mu - \mu^\infty)$, here μ^∞ is the chemical potential of the solvent in the environment. For simplcity, set κ a constant. Thus the extra jacobian reads as

$$
K^{AB}_{\mu j} = 0; \quad K^{AB}_{\mu\mu} = -\langle \psi^A, \phi^B \rangle; \quad K^{AB}_{\mu d} = 0 \tag{B.31}
$$

B.4 Redsiduals and Jacobians on damage DOFs

For the damage evolution equation, we have the residual

$$
R^A_d = \left(\psi^A, \zeta \dot{d}\right) + \left(\nabla\psi^A, \varepsilon^f_{\mathrm{R}} \ell^2 \nabla d\right) + \left(\psi^A, \varepsilon^f_{\mathrm{R}} d - 2(1-d)\mathcal{H}\right) \tag{B.32}
$$

Then the Jacobians of the equation are

$$
K^{AB}_{dd} = \left(\psi^A, \zeta \frac{\partial \dot{d}}{\partial d}\phi^B\right) + \left(\nabla\psi^A, \varepsilon^f_{\mathrm{R}} \ell^2 \nabla \phi^B\right) + \left(\psi^A, (\varepsilon^f_{\mathrm{R}} + 2\mathcal{H})\phi^B\right) \tag{B.33}
$$

with other two off-diagonal block are,

$$
K^{AB}_{di} = -\left(\psi^A, 2(1-d)\frac{\partial \mathcal{H}}{\partial F_{i\beta}} \nabla_\beta \phi^B\right) \tag{B.34}
$$

and

$$
K^{AB}_{d\mu} = -\left(\psi^A, 2(1-d)\frac{\partial \mathcal{H}}{\partial \mu}\phi^B\right). \tag{B.35}
$$

Within the expression $\frac{\partial \mathcal{H}}{\partial F_{i\beta}}$ and $\frac{\partial \mathcal{H}}{\partial \mu}$ will evaluate numerically. As what we mentioned before, $\frac{\partial \dot{d}}{\partial d}$ depends on the time-integration scheme. In backward Euler, $\frac{\partial \dot{d}}{\partial d} = \frac{1}{\Delta t}$ with Δt is the time-step.